

Transverse Coherence of a VUV Free Electron Laser

Dissertation

zur Erlangung des Doktorgrades
des Fachbereichs Physik
der Universität Hamburg

vorgelegt von

Rasmus Ischebeck
aus Münster

Hamburg

2003

Figure on the title page: Near field diffraction pattern of crossed slits, recorded with the TTF free electron laser.

Gutachter der Dissertation	Prof. Dr. P. Schmüser Prof. Dr. M. Tonutti
Gutachter der Disputation	Prof. Dr. P. Schmüser Prof. Dr. J. Roßbach
Datum der Disputation	18. November 2003
Vorsitzender des Prüfungsausschusses	Prof. Dr. F.-W. Büßer
Vorsitzender des Promotionsausschusses	Prof. Dr. R. Wiesendanger
Dekan des Fachbereichs Physik	Prof. Dr. G. Huber

Abstract

The transverse coherence is of paramount importance for many applications of a free electron laser (FEL). In this thesis, the first direct measurement of the transverse coherence of a free electron laser at vacuum ultraviolet wavelengths is presented. The diffraction pattern at a double slit was observed and the visibility of the interference fringes was measured. The experimental near field diffraction pattern is compared with simulations, taking into account the formation of the FEL radiation, the Fresnel diffraction in the near field zone and effects of the experimental set-up. Diffraction patterns have been recorded at various undulator lengths to measure the evolution of the transverse coherence along the undulator. The highest coherence is achieved at the end of the exponential growth regime, before the onset of saturation in the FEL process.

Zusammenfassung

Die räumliche Kohärenz ist von großer Bedeutung für viele Anwendungen eines Freielektronen-Lasers (FELs). In dieser Doktorarbeit wird die erste direkte Messung der räumlichen Kohärenz eines Freielektronen-Lasers im Vakuum-Ultraviolett vorgestellt. Das Beugungsbild eines Doppelspalt wurde aufgenommen und die Sichtbarkeit der Interferenzstreifen wird bestimmt. Das Beugungsmuster wird mit Simulationen verglichen. Diese beinhaltet die Erzeugung der FEL-Strahlung, die Fresnel-Beugung im Nahfeld und Effekte des experimentellen Aufbaus. Beugungsmuster wurden mit verschiedenen Undulatorlängen aufgenommen. Auf diese Weise wird die Entwicklung der räumlichen Kohärenz entlang des Undulators bestimmt. Dabei zeigt sich, dass der höchste Kohärenzgrad am Ende des Bereiches exponentiellen Wachstums herrscht, bevor Sättigungseffekte die Kohärenz reduzieren.

Contents

I. Introduction	9
1. Introduction	11
1.1. From Röntgen's discovery to the free electron laser	11
1.2. Lasers for short wavelengths	14
1.3. Applications for X-ray lasers	14
1.4. Measurement of coherence	16
II. Theory	17
2. Physical Processes in a Free Electron Laser	19
2.1. Emission of radiation in magnetic fields	20
2.2. Undulator radiation	20
2.3. Low-gain free electron lasers	23
2.3.1. Longitudinal velocity	24
2.3.2. Energy exchange with an external electromagnetic field	25
2.3.3. The FEL amplifier	26
2.4. High-Gain Free Electron Lasers	30
2.4.1. Radiation field	31
2.4.2. Space charge field	33
2.4.3. Relation between radiation and space charge field	34
2.4.4. Steady state approximation	35
2.4.5. Vlasov equation	35
2.4.6. Current density	37
2.4.7. Equation for the field amplitude	38
2.4.8. Solution of the integro-differential equation	38
2.4.9. Summary	40
2.5. Three-dimensional FEL simulation codes	42
2.6. Requirements on the accelerator	42

3. Coherence and Interference	43
3.1. Definition of coherence properties	43
3.2. Generation of coherent light	45
3.3. Coherence of a free electron laser	46
3.3.1. Evolution of the transverse coherence	46
3.4. Analytic description of diffraction effects	48
3.5. Far field diffraction	50
3.5.1. Analytic formulae for simple apertures	51
3.5.2. Measurement of coherence by interference experiments	51
3.6. Near field diffraction	54
3.6.1. Circular aperture	54
3.6.2. Double slit	54
3.6.3. Simulation by ray tracing	56
3.6.4. Simulation by wave front propagation	58
3.6.5. Results	62
3.7. Diffraction with partially coherent light	64
III. Experimental Set-up	71
4. The TTF Accelerator and SASE-FEL	73
4.1. General concepts in particle acceleration	73
4.1.1. Acceleration with radio-frequency cavities	73
4.1.2. Emittance	74
4.1.3. Particle source	74
4.1.4. Bunch compression	74
4.2. The TESLA Test Facility	75
4.2.1. RF photo-injector	76
4.2.2. Superconducting cavities	78
4.2.3. Synchronisation and timing	79
4.2.4. Bunch compression	79
4.2.5. Collimation	81
4.3. Electron beam diagnostics	82
4.3.1. Measurements of integral properties	82
4.3.2. Measurements of the bunch structure	83
4.3.3. Indirect measurements	84
4.3.4. Planned measurements	84
4.4. Free electron laser	85
4.4.1. Permanent magnet structure	85
4.4.2. Steerers	85
4.5. Photon beam diagnostics	88
4.5.1. Intensity measurements	89

4.5.2. Measurements of the spectrum	94
5. Experimental Set-up for the Coherence Measurements at the TTF FEL	95
5.1. Apertures and slits	95
5.2. Fluorescent crystal	96
5.3. Camera	98
5.3.1. Optics	98
5.3.2. CCD sensor	99
6. Detailed Investigation of the Experimental Set-up	102
6.1. Fluorescent crystal	102
6.1.1. Uniformity	102
6.1.2. Saturation effects	102
6.1.3. Scattering effects	104
6.2. Camera	107
6.2.1. Calibration	107
6.2.2. Optical system	107
6.2.3. Deconvolution of the optical resolution	109
6.2.4. Test of the Lucy-Richardson algorithm	114
6.2.5. CCD detector	118
IV. Results	121
7. Measurements of the Transverse Coherence	123
7.1. Measurements of the FEL in saturation	123
7.2. Simulations	126
7.2.1. FEL	126
7.2.2. Diffraction	127
7.2.3. Effects of the experimental set-up	127
7.3. Image processing	130
7.3.1. Averaging	130
7.3.2. Correction for effects of the experimental set-up	130
7.3.3. Projection of the diffraction patterns	132
7.4. Analysis	133
7.4.1. Analysis method 1: visibility of the central fringe	133
7.4.2. Analysis method 2: fit to the intensity distribution	137
7.5. Discussion of measurement uncertainties	141
7.6. Summary	144

8. Evolution of coherence along the undulator	147
8.1. Measurements	147
8.2. Analysis	148
8.3. Results	161
V. Conclusion	163
9. Conclusion and Outlook	165
9.1. Coherence measurement at the TTF FEL	165
9.2. Comparison with other measurements	165
9.3. Coherence measurement at higher photon energies	166
VI. Appendices	169
A. Mathematical Symbols	171
B. Imaging with a Tilted Lens	173
C. The van Cittert-Zernike theorem	175
D. Data Acquisition	178
D.1. Overview of the control system	178
D.1.1. DOOCS	178
D.1.2. Object orientation	179
D.1.3. ROOT	179
D.2. A data acquisition for the TTF	180
D.2.1. Requirements	180
D.2.2. Choice of a database	180
D.2.3. Gateway to the existing control system	180
D.3. Implementation	181
D.3.1. Data structure	181
D.3.2. ROOT object generators	181
D.3.3. Network transfer	183
D.3.4. Tape storage	183
D.4. Synchronisation with camera image acquisition	184
D.5. Data acquisition of camera images	185
E. Circular Apertures	186
E.1. Measurements	186
E.2. Analysis	186

F. Analysis Routines for the Double Slit Diffraction Patterns	189
F.1. Image processing	189
F.2. Analysis method 1: central visibility	190
F.2.1. Finding maxima and minima	192
F.3. Analysis method 2: fit to the intensity	195
F.3.1. fitted function	198



Part I.

Introduction

Die ganze Welt ist voll von Sachen, und es ist wirklich nötig, dass jemand sie findet.
Astrid Lindgren (Pippi Langstrumpf)

Figure on the previous page: Coherence measurement using diffraction [TW57].

1. Introduction

Free electron lasers (FELs) promise to deliver intense and coherent X-ray pulses, applicable in various research areas. For one thing, X-ray FELs will exceed the brilliance of the third-generation synchrotron radiation facilities by several orders of magnitude and will additionally offer a larger transverse coherence and a shorter time structure. On the other hand, free electron lasers will complement today's lasers because they can be tuned to shorter wavelengths, corresponding to higher photon energies. The two following sections give a brief overview of the historic development in the fields of X-ray sources and lasers.

A figure of merit for radiation sources is their coherence, because it is an important feature for many applications. The coherence is a measure for the uniformity of an electromagnetic wave. A plane wave is fully coherent and a completely random radiation is said to be incoherent¹. A high coherence of the radiation source is a necessary prerequisite for interference techniques such as holography, but it also allows a smaller focal size of the beam, which results in a better resolution in scanning techniques.

In this thesis, the first direct measurement of the transverse coherence of a free electron laser at vacuum ultraviolet² (VUV) wavelengths is presented. The diffraction pattern of the FEL radiation at a double slit is observed. From the visibility of the interference fringes, one can deduce the transverse coherence of the radiation. The experimental technique provides a reliable method for quantitative measurements.

1.1. From Röntgen's discovery to the free electron laser

Since their discovery by Wilhelm Konrad Röntgen in 1895 [Rön96], X-rays have been used to reveal the hidden inner properties of objects. X-rays are photons, described classically as electromagnetic radiation. Due to their high energy, corresponding to a short wavelength, they can pass through many materials. Different attenuation in varying materials allows to observe the internal structure of an object. Röntgen

¹ formally, coherence is defined by the of the autocorrelation of the field amplitude, see chapter 3

² by vacuum ultraviolet, one understands the part of the electromagnetic spectrum with wavelengths between 100 and 300 nm; this radiation is absorbed by all materials and can propagate only in vacuum

1. Introduction

already discovered the possibility to observe bones in the human body (figure 1.1a). The X-ray technology evolved from the laboratory into widespread application in an astonishingly short time. Weeks after Röntgen's announcement of his discovery in the end of 1895, newspapers around the world reported on the mysterious "new light". It was first used to see bones in the human body in February 1896 and only one year after its discovery, the application of X-rays in medicine was a well established practice (figure 1.1b).

a)



b)



Figure 1.1.: a) One of the first radiographs, created by Röntgen himself. b) Mihran Kassabian, working in his Röntgen Laboratory.

The high photon energy is not only useful to image the inside of matter; the short wavelength allows, in principle, to achieve higher resolution in the images. Once technical difficulties in the construction of suitable optics had been overcome, microscopes with a resolution unparalleled by microscopes for visible light were constructed. Using the interference of X-rays scattered at atomic nuclei within a molecule, it was even possible to reveal the crystal structure.

In the beginning, X-rays were generated in low-pressure discharge tubes. These were succeeded by cathode ray tubes, which are still in use today. Electrons are liberated from the cathode and accelerated by a high voltage. When they impinge on the anode, the deceleration of the charge leads to emission of a continuous spectrum of radiation. Additionally, the electrons ionise the inner shell of the atoms in the anode; the electromagnetic cascade yields high energy photons at specific wavelengths, depending on the anode material. The brilliance³ of these characteristic lines is much higher than in the continuous part of the spectrum. In the last 100 years, X-ray tubes have undergone many improvements: the introduction of thermionic cathodes

³ The *brilliance* is defined as the number of photons per area, per solid angle and per wavelength interval. When comparing photon sources, the brilliance is often used as a benchmark, since it is important for experiments where an intense, monochromatic photon beam with low divergence is needed.

by Lilienfeld in 1911 made it possible to extract more electrons from the metal. Rotating anodes, designed in 1934 by Ungelenk, can sustain higher current on a smaller spot.

However, the biggest step to increase the brilliance was achieved by using electron synchrotrons for X-ray generation. Synchrotron radiation is emitted when a relativistic electron beam passes through a bending magnet. In the beginning, around 1960, the electron accelerators – built for the study of elementary particle physics – found additional use to generate synchrotron radiation. These first-generation synchrotron facilities offered a beam brilliance around 10^{12} photons/(s mm² mrad² 0.1% bandwidth), four orders of magnitude more than the brightest X-ray sources available previously. The synchrotron sources provide this high brilliance in a continuous spectrum over a very broad wavelength range, as compared to the characteristic lines of the X-ray tubes. Second-generation synchrotron radiation facilities, accelerators built or updated specifically to generate synchrotron radiation, use special magnet arrangements, undulators or wigglers. These boost the brilliance by a factor equal to the number of magnets, typically a few 100. Current, third-generation synchrotron facilities employ a magnet lattice that is optimised for a small electron beam emittance, a low coupling between horizontal and vertical betatron oscillations and insertion devices such as undulators to generate beam brilliances above 10^{23} photons/(s mm² mrad² 0.1% bandwidth). Hard X-rays can be produced by higher harmonics of the undulator radiation.

It is a widely accepted opinion that the fourth generation of synchrotron radiation facilities will be *free electron lasers* that are based on the *self-amplification of the spontaneous emission*, so-called SASE-FELs. Similarly to third-generation synchrotron sources, a free electron laser uses the alternating magnetic fields of an undulator to impose a sinusoidal motion on the electron bunch. At high beam current densities, the electromagnetic field of the radiation leads to a longitudinal modulation of the charge density. This modulation builds up along the undulator, and finally the electron bunch is divided into *microbunches*. The particles in each microbunch radiate coherently. FELs mark the transition from spontaneous to stimulated radiation. The peak brilliance of an X-ray FEL is expected to be 10^{10} times higher than the brightest sources currently in use.⁴

⁴ The brilliance of the proposed X-ray FELs rivals astronomical objects: one of the most prominent objects in X-ray astronomy, the crab nebula, contains a neutron star that rotates 30 times per second. It emits two radiation jets that have a total power of $5 \cdot 10^{31}$ W. In an interval of 0.1% bandwidth at 20 keV, $2 \cdot 10^{34}$ photons are emitted per second [Ama99]. If one assumes a diameter of 30 km [FK02] and a solid angle of 0.1 sr [UB81], one can compute a brilliance of 10^{20} photons per (s mm² mrad² 0.1% bandwidth), at the surface of the star, whereas the TESLA-FEL is expected to reach 10^{34} photons per (s mm² mrad² 0.1% bandwidth) in this wavelength range.

1.2. Lasers for short wavelengths

Conventional lasers are based on the stimulated emission of photons by electrons that are bound in atoms or molecules, by a transition between two energy levels. To create a population inversion, the atoms or molecules are pumped into the higher energy level, for example by xenon discharge lamps or by another laser. The wavelength of a laser is determined by the energy difference of the two atomic or molecular levels, typically up to a few eV.

There are several possibilities to achieve higher photon energies. The so-called *table-top X-ray lasers* extend the concept of visible lasers to the X-ray regime. The lasing medium is a plasma, created by an intensive external laser pulse. It is then heated by another, shorter pulse. Due to the optical field ionisation in the plasma, a population inversion is created. To advance in smaller wavelength regimes, the plasma is excited with extremely high flux densities [RST⁺94, NSK⁺97].

In the scheme of *high harmonic generation* a ultra short pulse laser is focused into a noble gas [KSK92]. The odd harmonics $3\omega, 5\omega \dots$ of the exciting laser frequency are produced due to a non-sinusoidal motion of the electrons in the high radiation field. The photon energies can surpass 500 eV by exciting harmonics above the 300th order.

A free electron laser can overcome the limitation to the fixed wavelength: The photons are emitted by a high-energy electron beam that is guided by an alternating magnetic field. Here, both energy pump and lasing medium are provided by a relativistic electron beam. In principle, any wavelength can be achieved. In addition, very high intensities can be achieved.

1.3. Applications for X-ray lasers

Possible applications for intense and coherent X-rays have been proposed since the middle of the last century, and in the last years, scientists have come up with a vast number of experiments for the X-FEL. These range from atomic and molecular physics over the study of solid state systems to the decipherment of large biomolecules and cover many areas of scientific research. It would exceed the scope of this work to name them all, let alone to explain the involved processes.

Therefore, the treatment will focus on techniques where the coherence of the beam is of prime importance. The technical design report [MT01] provides a comprehensive overview of the research proposed for the X-FEL. In addition to the applications that have been presented so far, it can be expected that a completely new device like the X-FEL will inspire scientists from all areas to present new applications.

The structure of a molecule can be studied by the diffraction of X-rays. A crystal of the molecule is placed in an X-ray beam. A diffraction pattern forms due to the regular arrangement of the molecules in the crystal. The diffraction pattern is

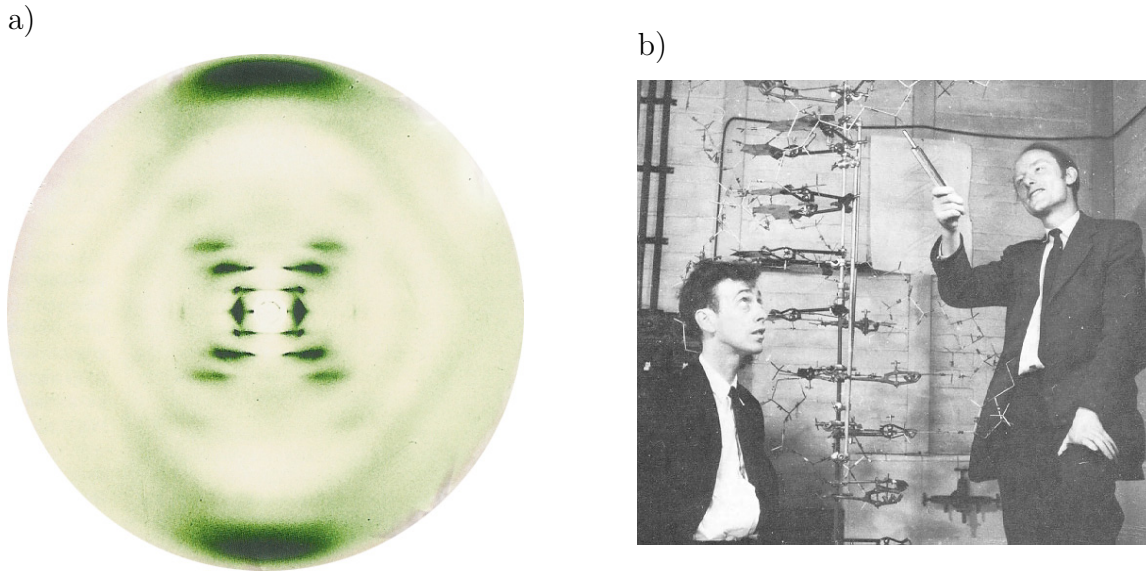


Figure 1.2.: a) Diffraction pattern and b) structure of DNA. This X-ray diffraction pattern, recorded by Rosalind Franklin allowed James Watson and Francis Crick to decipher the structure of the DNA [WC53].

recorded with a position-sensitive detector. It is the amplitude of a two-dimensional projection of the inverse crystal lattice. Historically, this method gave the final hint for the decipherment of the structure of the desoxyribo nucleic acid (DNA, see figure 1.2).

However, this method faces two difficulties: it is often demanding to obtain a sufficient quantity and to crystallise the molecule in question. Furthermore, the phase information of the diffraction pattern is lost in the detector. Various methods have been conceived to overcome these difficulties. Crystals of large molecules can be grown in space, to avoid disturbances due to gravity [DeL89]. The phase of the diffracted wave can be obtained through the interference with the anomalous diffraction of certain atoms in the molecule, a method known as *multiple wavelength anomalous diffraction* (MAD). Another method of obtaining the phase is holography, where the diffraction pattern is superimposed with the original wave. This requires a good coherence of the X-ray source. Using the high coherence and the enormous brilliance of the X-FEL, it is expected that the diffraction pattern of a nanoparticle, containing only $10^4 \dots 10^5$ molecules, can be recorded [Szö99]. Several images from differently oriented molecules have to be recorded. Similarly, diffraction patterns from surfaces can be studied.

A good coherence is also helpful to image small objects like the interior of cells. Phase contrast microscopy is superior to conventional absorption contrast microscopy for small objects. Additionally, diffraction tomography has been proposed to create

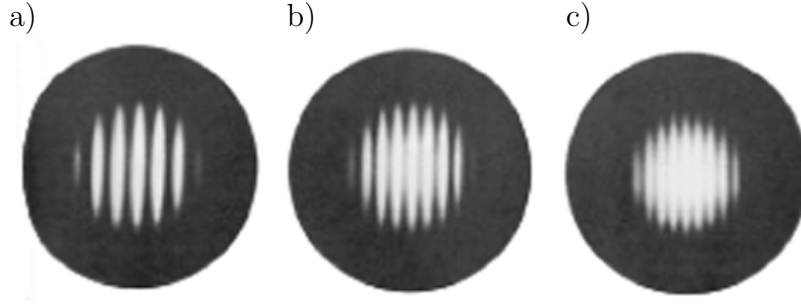


Figure 1.3.: Interference pattern of a double pinhole, measured at different pinhole separations [TW57]. A visibility of a) $\mathcal{V} = 0.593$, b) $\mathcal{V} = 0.361$ and c) $\mathcal{V} = 0.146$ is determined.

a three-dimensional image of the specimen.

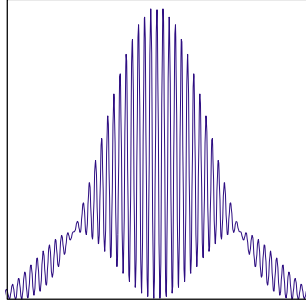
If a coherent beam reflects off a structured surface, a *speckle pattern*, the two-dimensional Fourier transform of the sample, results. Using X-rays, one can employ this technique to study the magnetic properties of a material, as the scattering depends on the magnetic moment of the atoms. This way, the fluctuations of the magnetic flux can be quantised.

When performing experiments that require a transverse coherence of the beam, one has to take care that the phases of the wave front are not distorted, e.g. by reflections on crystals with lattice errors. For example, current techniques do not allow to fabricate diamond monochromator crystals with sufficient perfection. Therefore, despite of the lower damage threshold, silicon has to be used.

1.4. Measurement of coherence

The transverse coherence of a radiation source can be measured with Young's double slit experiment [You04]. In the far field, the visibility of the diffraction pattern of a slit or pinhole pair is equal to the transverse coherence function between the two slits or pinholes, respectively. The visibility is measured at various slit separations (figure 1.3). This method has been used to measure the coherence function of visible light [TW57] and of X-rays from a third-generation synchrotron source [PAM⁺01]. Using the van Cittert-Zernike theorem (see appendix C) [Zer38], the size of a distant source can be inferred.

Recently, interference patterns have been recorded using X-ray lasers that use the high-harmonic generation of photons of a femtosecond laser [BPG⁺02] and atomic beams [BHE00]. In this thesis, the first application of a double slit experiment to measure the transverse coherence of a free electron laser in the vacuum ultraviolet, i.e. at a wavelength of 100 nm is described.



Part II.

Theory

Also zndet ein Ding dem andren Dinge das Licht an.
Lucretius (von der Natur der Dinge 1, 1094)

Figure on the previous page: The near field diffraction pattern of a double slit.

2. Physical Processes in a Free Electron Laser

The most brilliant X-ray sources are electron or positron accelerators, where the bunches generate synchrotron radiation in undulator magnets. In these sources, the radiation emitted by an electron is coherent, but there is no coherence between the radiation fields generated by different electrons, hence the intensity scales linearly with the number N of electrons per bunch. If different electrons radiate coherently, the intensity is proportional to N^2 . This is what happens in a free electron laser (FEL).

First, the emission of synchrotron radiation in a bending magnet is discussed. The next section treats the spontaneous undulator radiation, then the amplification in a low-gain free electron laser is detailed. High-gain FELs are the subject of the following section. The discussion is based on the equations of motion of a charged particle and its interaction with an electromagnetic wave, described by the Maxwell equations. From this, the following important equations are derived, which may serve for an analytic description and which are the underlying equations of FEL simulations:

- The photon wavelength of spontaneous emission: Eq. (2.14)
- The motion of the particles within the bunch are governed by the so-called pendulum equations (2.34)
- The wave equation (2.35) is simplified for the case of a one-dimensional wave, i.e. a wave of infinite extent, to Eq. (2.47)
- This leads to an integro-differential equation for the development of the radiation field amplitude: Eq. (2.78)
- In the case of a mono-energetic electron beam, this can be simplified to a third-order differential equation (2.87)
- By further imposing a beam with negligible space charge on resonance, one obtains an exponentially increasing amplitude: Eq. (2.88)
- The gain length of the FEL is given by Eq. (2.91)

Since the transverse extension of a FEL is not infinite, diffraction effects have to be considered. This results in information about the coherence of the radiation and is discussed in the following chapter, after the notion of coherence has been defined.

The discussion in this chapter is based on [SSY00b], which contains many details on FELs, and on the lectures [Sch01b], [KH00] and [DR02]. Other good books about FELs are [Bra90] and [CPR90]. A good overview is given in [Hün02]. For more details, especially about FEL simulations, the reader is referred to [Rei99]. General concepts of electromagnetic radiation are taken from [Jac98] and [Goo85].

2.1. Emission of radiation in magnetic fields

First, the radiation of a charged particle in a dipole magnet is discussed. The motion of a particle on a curved trajectory in a magnetic field \vec{B} is an accelerated motion; as a result of the *Maxwell* equations, radiation is emitted, see for example Jackson, chapter 9 [Jac98]. The radiation of a uniformly accelerated charge distribution whose extension is much smaller than the wavelength, $\Delta x \ll \lambda$, is coherent and the intensity is proportional to the square of the total charge Q^2 . If the distance between the charge carriers is larger than λ , their radiation fields add incoherently and the intensity is proportional to their number. This is usually the case in the bending magnets of an accelerator. Particles with relativistic velocities ($\gamma = (1 - v^2/c^2)^{-1/2} \gg 1$) emit radiation predominantly in the forward direction, inside a cone with opening $1/\gamma$.

2.2. Undulator radiation

Wiggler and undulator magnets are devices that impose a periodic magnetic field on the electron beam. These insertion devices have been specially designed to excite the emission of electromagnetic radiation in particle accelerators.

For the following description, the z coordinate is along the principal direction of motion of the electrons. The magnetic field on the axis of a planar wiggler or undulator is assumed to point in y direction:

$$\vec{B}(0, 0, z) = \vec{u}_y B_0 \sin(k_u z) \quad (2.1)$$

where λ_u the period of the magnetic field, $k_u = 2\pi/\lambda_u$, B_0 is the maximum field and \vec{u}_y is the unit vector in y direction. Due to the *Maxwell* equations, the curl and divergence of the static magnetic field vanish in vacuum, $\vec{\nabla} \times \vec{B} = 0$ and $\vec{\nabla} \cdot \vec{B} = 0$. Thus, the field acquires a z component for $y \neq 0$:

$$B_x = 0 \quad (2.2a)$$

$$B_y = B_0 \cosh(k_u y) \sin(k_u z) \quad (2.2b)$$

$$B_z = B_0 \sinh(k_u y) \cos(k_u z) \quad (2.2c)$$

The difference to Eq. (2.1) is small for $k_u y \ll 1$ and will be neglected in the following¹. A detailed discussion of the magnetic field, including an x dependency for the finite extent of the pole shoes, can be found in [Rei99].

Helical undulators have a magnetic field on the axis

$$\vec{B}(z) = \vec{u}_x B_0 \cos(k_u z) - \vec{u}_y B_0 \sin(k_u z) \quad (2.3)$$

A rigorous analytic discussion of helical undulators is somewhat easier since the longitudinal component of the electron velocity $v_z = \beta_z c$ is constant. A good discussion of helical and planar undulators that points out this difference can be found in [SSY00b]. In the TESLA Test Facility (TTF), a planar undulator is installed, therefore a magnetic field according to Eq. (2.1) is assumed in the following.

The magnetic field exerts a force on the electron

$$m_e \gamma \frac{d\vec{v}}{dt} = \vec{F} = -e\vec{v} \times \vec{B} \quad (2.4)$$

that results in a transverse oscillation of the particle:

$$m_e \gamma \frac{dv_x}{dt} = ev_z B_y = ev_z B_0 \sin(k_u z) \quad (2.5)$$

It is common practice in accelerator physics to replace the independent variable time by the longitudinal position z (or by the arc length, in the case of circular accelerators). Thus, equation (2.5) can be written as a derivative with respect to z , using $dz/dt = v_z$:

$$\frac{dv_x}{dz} = \frac{e}{m_e \gamma} B_0 \sin(k_u z) \quad (2.6)$$

The relativistic γ -factor of a particle is constant in a static magnetic field. Integration of Eq. (2.6) leads to

$$v_x(z) = -\frac{Kc}{\gamma} \cos(k_u z) \quad (2.7)$$

where a dimensionless undulator parameter has been introduced,

$$K = \frac{eB_0}{m_e c k_u} \quad (2.8)$$

The electron follows a sinusoidal trajectory

$$x(z) = -\frac{K}{k_u \gamma \beta_z} \sin(k_u z) \quad (2.9)$$

¹ in the undulator at the TESLA Test Facility (TTF), the correction factors were indeed quite small: at a position $10 \mu\text{m}$ off the axis, B_y changes by less than 10^{-5} , while B_z reaches 0.2% of the on-axis field.

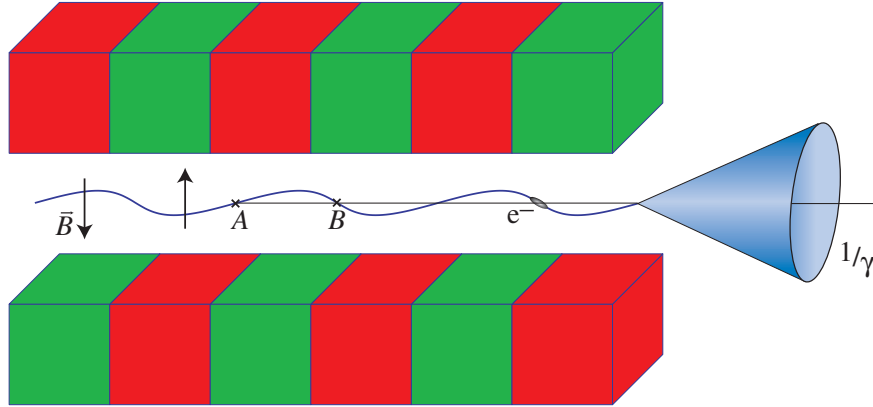


Figure 2.1.: Emission of radiation in an undulator.

In the TTF undulator, the deviation from the straight orbit is only $10\ \mu\text{m}$. Synchrotron radiation is emitted by relativistic electrons in a cone with opening angle $1/\gamma$. In an *undulator*, the maximum angle of the particle velocity with respect to the undulator axis $\alpha = \arctan(v_x/v_z)$ is always smaller than the opening angle of the radiation, therefore the radiation field may add coherently. In a *wiggler*, $\alpha_{\text{max}} > 1/\gamma$, and a broad radiation cone with lower intensity on the axis is emitted. The condition for an undulator can be rewritten for $v_z \approx c$:

$$\frac{1}{\gamma} > \arctan \frac{v_{x \text{ max}}}{v_z} \approx \frac{v_{x \text{ max}}}{v_z} \approx \frac{Kc}{\gamma c}$$

$$\implies K < 1 \quad (2.10)$$

Consider two photons emitted by a single electron at the points A and B , which are one half undulator period apart (figure 2.1):

$$\overline{AB} = \frac{\lambda_u}{2} \quad (2.11)$$

If the phase of the radiation wave advances by π between A and B , the electromagnetic field of the radiation adds coherently². The light moves on a straight line \widetilde{AB} that is slightly shorter than the sinusoidal electron trajectory \overline{AB} :

$$\frac{\lambda}{2c} = \frac{\widetilde{AB}}{v} - \frac{\overline{AB}}{c} \quad (2.12)$$

² Photons radiated by different electrons will however usually be incoherent.

The electron travels on a sinusoidal arc of length \widetilde{AB} that can be calculated (see for example [Stö99]):

$$\begin{aligned}
 \widetilde{AB} &= \int_0^{\lambda_u/2} \sqrt{1 + \left(\frac{dx}{dz}\right)^2} dz \\
 &\approx \int_0^{\lambda_u/2} \left(1 + \frac{1}{2} \left(\frac{dx}{dz}\right)^2\right) dz \\
 &= \int_0^{\lambda_u/2} \left(1 + \frac{K^2}{2\gamma^2} \cos^2(k_u z)\right) dz \\
 &= \frac{\lambda_u}{2} \left(1 + \frac{K^2}{4\gamma^2}\right) \tag{2.13}
 \end{aligned}$$

Equation (2.12) becomes

$$\frac{\lambda}{2c} = \frac{\lambda_u}{2\beta c} \left(1 + \frac{K^2}{4\gamma^2}\right) - \frac{\lambda_u}{2c}$$

with $\beta = \sqrt{1 - \gamma^{-2}} \approx 1 - \frac{1}{2}\gamma^{-2}$ for $\gamma \gg 1$

$$\implies \lambda = \frac{\lambda_u}{2\gamma^2} (1 + K^2/2) \tag{2.14}$$

This equation gives the wavelength of spontaneous undulator radiation. The photon energy is proportional to the square of the energy of the electrons. For electrons with an energy of 243 MeV, the spontaneous radiation in the undulator of the TESLA Test Facility has a wavelength of 100 nm.

As the electron travels along the undulator, the total intensity of the radiation grows proportionally to the distance travelled. The width of the radiation cone for the fundamental wavelength decreases inversely proportional to the distance, therefore the central intensity grows as the square of the undulator length. The radiation is linearly polarised in x direction.

In addition to the fundamental wavelength λ , the undulator radiation contains also its odd harmonics $\lambda/3, \lambda/5 \dots$. This can be shown by solving the equations of motion precisely in two dimensions [Sch01b]. The intensity in the higher order modes is several orders of magnitude lower.

2.3. Low-gain free electron lasers

In this section, it will be shown how an external wave with a given wavelength can be amplified by the electron bunch inside the undulator. Although this amplification

is based on a different principle than the amplification in conventional lasers, Madey named such a device a free electron laser (FEL) due to the analogy that can be drawn to the stimulated emission [Mad70]. Several types of FELs have been built:

- *FEL amplifiers* increase the amplitude of an externally generated radiation field.
- *FEL oscillators* comprise an external optical cavity that reflects the field back into the area where it overlaps with the radiation. Typically, only the fundamental transverse radiation mode is amplified.
- *Self-amplified spontaneous emission (SASE) FELs* start from the spontaneous radiation that is amplified in a single pass of the electron bunch through the undulator. No optical cavity is needed, allowing for shorter wavelengths where the reflectivity of available mirrors for normal incidence is poor.

In the discussion of the amplification of radiation in an FEL, it is appropriate to treat the photons as a continuous electromagnetic field. The charges, however, will be treated as particles to describe their motion inside the bunch more easily. Since only the ratio of mass and charge of the particles appears in the equations, the results are not changed if these two quantities are scaled by the same factor. Therefore, one can combine many electrons into one macro-particle. This will save computing time in the simulations. In the following analytic derivation however, single electrons with mass m_e and charge $(-e)$ are considered³.

2.3.1. Longitudinal velocity

From Eq. (2.7) the x component of the velocity of the electrons is $v_x = -\frac{cK}{\gamma} \cos(k_u z)$. The longitudinal velocity is calculated from

$$1 - 1/\gamma^2 = \beta_x^2 + \beta_y^2 + \beta_z^2 \quad (2.15)$$

Keeping in mind that $\beta_y = 0$ and solving Eq. (2.15) for β_z :

$$\begin{aligned} \beta_z &= \sqrt{1 - \frac{1}{\gamma^2} - \frac{K^2}{\gamma^2} \cos^2(k_u z)} \\ &\approx 1 - \frac{1}{2} \left[\frac{1}{\gamma^2} + \frac{K^2}{\gamma^2} \cos^2(k_u z) \right] \end{aligned} \quad (2.16)$$

with $\cos^2 \alpha = \frac{1}{2} + \frac{1}{2} \cos 2\alpha$

$$\beta_z = 1 - \frac{2 + K^2}{4\gamma^2} - \frac{K^2}{4\gamma^2} \cos(2k_u z) \quad (2.17)$$

³ note that in some descriptions, e.g. [Rei99], a charge $+e$ is used

The cosine term averages to zero over the passage of an undulator period, and the mean velocity in z direction is $\bar{\beta}_z c$ with

$$\bar{\beta}_z = 1 - \frac{2 + K^2}{4\gamma^2} \quad (2.18)$$

This is lower than the total velocity βc , because of the longer trajectory. Although the difference between the mean particle velocity to the velocity of light is only small, it leads to a resonance condition for the interaction between the particles and an electromagnetic field. This is derived in the next section.

2.3.2. Energy exchange with an external electromagnetic field

It is an interesting question whether a relativistic beam in an undulator can amplify an external laser beam with a wavelength in the vicinity of the wavelength of the spontaneous emission. Assume an electron bunch traversing the magnetic field of a planar undulator as in Eq. (2.1) and a plane electromagnetic wave polarised in x direction

$$\vec{E} = \vec{u}_x \tilde{E}_x \cos(kz - \omega t + \psi_0) \quad (2.19)$$

where \tilde{E}_x is the amplitude, which is regarded constant for the moment.

Compared to the undulator field, the magnetic field of the radiation is negligible. Hence, the trajectory of the electron bunch in the undulator is given by Eq. (2.9).

The interaction between the electrons and the radiation field leads to a transfer of energy dW . This is proportional to the electric field component parallel to the motion of the electrons:

$$\begin{aligned} \frac{dW}{dt} &= -e\vec{E} \cdot \vec{v} \\ &= e\tilde{E}_x \cos(kz - \omega t + \psi_0) \frac{cK}{\gamma} \cos(k_u z) \\ &= \frac{e\tilde{E}_x cK}{2\gamma} [\cos((k + k_u)z - \omega t + \psi_0) + \cos((k - k_u)z - \omega t + \psi_0)] \end{aligned} \quad (2.20)$$

The argument

$$\psi \equiv (k + k_u)z - \omega t + \psi_0 \quad (2.21)$$

of the first cosine function is called the *ponderomotive phase*. Note that ψ is periodic in z with a period that is approximately equal to the wavelength λ of the radiation, since $k_u \ll k = 2\pi/\lambda$. The second cosine term in Eq. (2.20) oscillates quickly and averages to zero [KH00]. Neglecting this term, one gets

$$\implies m_e c^2 \frac{d\gamma}{dt} \equiv \frac{dW}{dt} = \frac{e\tilde{E}_x cK}{2\gamma} \cos \psi \quad (2.22)$$

If $dW/dt < 0$, energy is transferred from the electrons to the radiation field, i.e. the electromagnetic wave is amplified:

$$dW/dt < 0 \iff \cos \psi < 0 \iff -\pi < \psi < 0 \quad (2.23)$$

If the phase ψ is constant during the passage of the electrons through the undulator, there is continuous energy transfer between the electrons and the electromagnetic field.

$$\begin{aligned} \psi &= \text{const} \\ \iff \frac{d\psi}{dt} &= (k + k_u)v_z - kc = 0 \end{aligned}$$

inserting $\bar{\beta}_z$ from Eq. (2.18)

$$\frac{d\psi}{dt} = (k + k_u) \left(1 - \frac{2 + K^2}{4\gamma^2} \right) c - kc = 0 \quad (2.24)$$

with $k_u \ll k$

$$\frac{d\psi}{dt} \approx kc \left(\frac{k_u}{k} - \frac{2 + K^2}{4\gamma^2} \right) = 0 \quad (2.25)$$

$$\iff \frac{\lambda}{\lambda_u} \equiv \frac{k_u}{k} = \frac{2 + K^2}{4\gamma_r^2} \quad (2.26)$$

This is the condition for resonant energy transfer. The relativistic factor at resonance is denoted by γ_r . For a given electron energy, the resonant wavelength λ_r is the same as the wavelength of spontaneous radiation (see Eq. (2.14)). We will see later that this allows the amplification of the spontaneous undulator radiation in a SASE-FEL and makes it possible to dispense with the external radiation source.

In most practical cases, the electron bunch is much longer than the wavelength of the radiation. Since the phases of the particles are initially homogeneously distributed (see figure 2.4a), half of the particles satisfy $dW/dt < 0$, resulting in an amplification of the electromagnetic field. For the other half, one has $dW/dt > 0$, implying an energy transfer from the electromagnetic field back to the electrons. Hence, the total gain is zero for $\gamma = \gamma_r$. In the next section, it will be shown that a small deviation from the resonance energy can lead to the net amplification of the electromagnetic wave. This principle is employed in a low-gain FEL.

2.3.3. The FEL amplifier

The energy and phase of the electrons are changed by the interaction with the radiation field. In the so-called low-gain FEL, the field amplitude \tilde{E}_x can be regarded as constant along one passage of the undulator, but the energy of an electron and its

ponderomotive phase may vary. A particle slightly above resonance is studied, with a relative energy deviation from the resonance energy $m_e c^2 \gamma_r$

$$0 < \eta = \frac{\gamma - \gamma_r}{\gamma_r} \ll 1 \quad (2.27)$$

From equation (2.26),

$$\gamma_r = \sqrt{\frac{k}{k_u} \frac{2 + K^2}{4}} \quad (2.28)$$

Inserting this in Eq. (2.27) leads to

$$(1 + \eta)^2 = \frac{\gamma^2}{\gamma_r^2} = \frac{k_u}{k} \frac{4\gamma^2}{2 + K^2} \quad (2.29)$$

The derivative of the ponderomotive phase with respect to time is not zero as in Eq. (2.25), but

$$\begin{aligned} \frac{d\psi}{dt} &= ck_u \left(1 - \frac{k}{k_u} \cdot \frac{2 + K^2}{4\gamma^2} \right) \\ &= ck_u \left(1 - \frac{1}{(1 + \eta)^2} \right) \\ &= ck_u \frac{2\eta + \eta^2}{1 + 2\eta + \eta^2} \end{aligned}$$

Since $\eta \ll 1$:

$$\frac{d\psi}{dt} \approx 2ck_u \eta \quad (2.30)$$

The time derivative of the energy deviation can be calculated from Eq. (2.27) and Eq. (2.22), keeping in mind that $d\gamma_r/dt = 0$:

$$\frac{d\eta}{dt} = \frac{1}{\gamma_r} \frac{d\gamma}{dt}$$

inserting Eq. (2.22)

$$\frac{d\eta}{dt} = \frac{e\tilde{E}_x K}{2m_e c \gamma_r^2} \cos \psi \quad (2.31)$$

Equations (2.30) and (2.31) are called *pendulum equations* because of their resemblance to the differential equations for the angle and the angular momentum of a mathematical pendulum [CPR90]. The ponderomotive phase and the energy deviation of the electron evolves according to Eq. (2.30) and (2.31). These differential

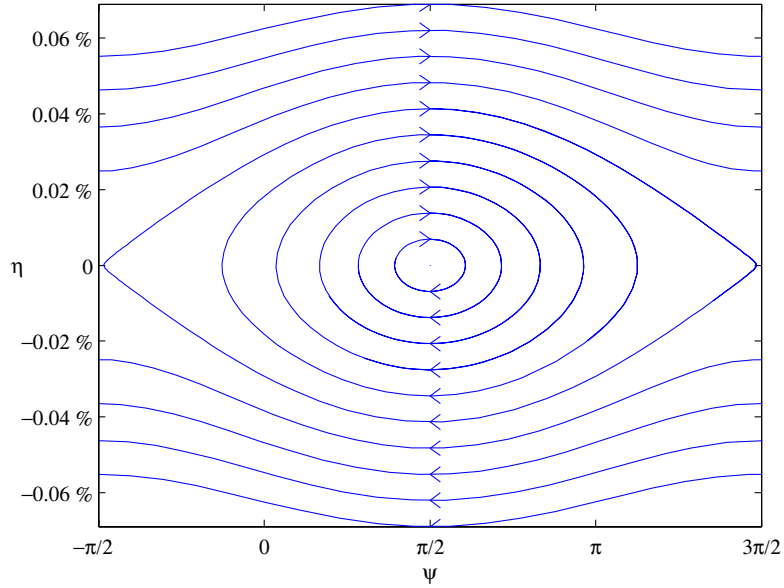


Figure 2.2.: Trajectories of selected particles in the longitudinal phase space (ψ, η) , calculated by numerically solving Eq. (2.30) and (2.31).

equations can be solved by elliptic functions. The trajectories of the particles in the (φ, η) phase space, calculated by numerical evaluation, are shown in figure 2.2.

It is customary in accelerator physics to use the longitudinal coordinate as independent variable. With

$$\frac{dz}{dt} = \bar{\beta}_z c$$

the pendulum equations read

$$\frac{d\psi}{dz} = \frac{2k_u \eta}{\bar{\beta}_z} \quad (2.32a)$$

$$\frac{d\eta}{dz} = \frac{e\tilde{E}_x K}{2m_e c^2 \bar{\beta}_z \gamma_r^2} \cos \psi \quad (2.32b)$$

A complete treatment has to take into account the periodic variation of β_z (see Eq. (2.17)), instead of just using the average velocity $\bar{\beta}$. The modification, however, turns out to be simple, the undulator parameter K has to be replaced by [Rei99]

$$\hat{K} = K \left[J_0 \left(\frac{K^2}{4 + 2K^2} \right) - J_1 \left(\frac{K^2}{4 + 2K^2} \right) \right] \quad (2.33)$$

For the TTF undulator, this means a reduction of the undulator parameter by 11%.

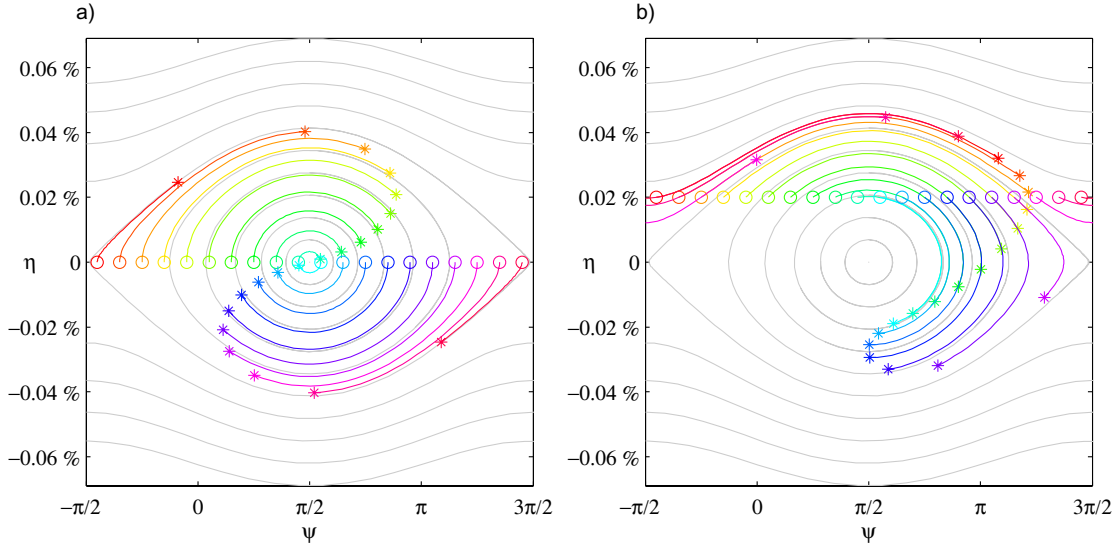


Figure 2.3.: Development of the energy deviation η and phase ψ for different initial energies. a) $\eta = 0$, b) $\eta > 0$. Initial values are marked by circles, values after the passage of the undulator by asterisks.

The pendulum equations then become

$$\frac{d\psi}{dz} = \frac{2k_u}{\beta_z} \eta \quad (2.34a)$$

$$\frac{d\eta}{dz} = \frac{e\tilde{E}_x \hat{K}}{2m_e c^2 \beta_z \gamma_r^2} \cos \psi \quad (2.34b)$$

As already mentioned, the initial distribution of the particles over the phase ψ is uniform. As the particles travel along the undulator, ψ is modified. If the electrons are injected at resonance energy, i.e. with $\eta = 0$, the phase space distribution will remain point symmetric to the origin. This is shown in figure 2.3a. There is no net energy transfer between the electron bunch and the light wave. In contrast to that, an initially positive energy deviation will result in an asymmetric distribution, leading to an average energy loss of the particles, as shown in figure 2.3b. This energy is transferred to the electromagnetic wave⁴. The amplification can be understood as stimulated emission of photons, since the transition probability is proportional to the number of photons in the incoming electromagnetic wave.

⁴ similarly, if $\gamma < \gamma_r$, energy is removed from the photon beam

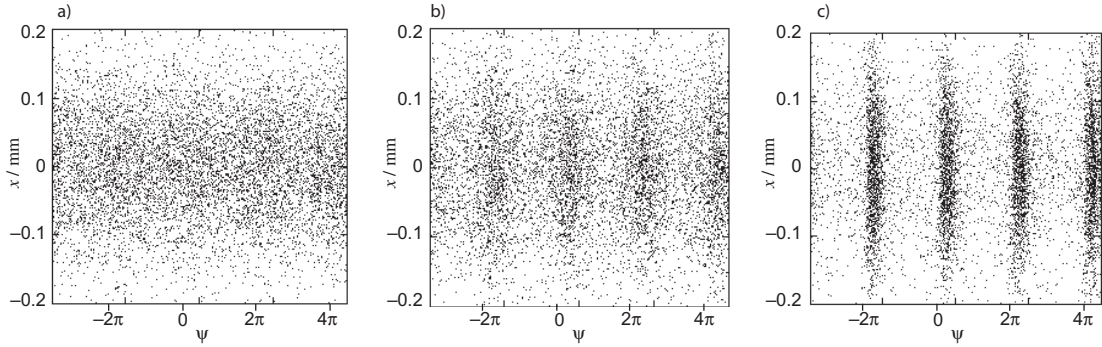


Figure 2.4.: Distribution of the electrons and radiation field in a high-gain FEL. The electric radiation induces a collective bunching of the particles [Rei99]. a) The initial situation is uniform. b) and c) Along the undulator, micro-bunching appears, with a period of 2π in the variable ψ .

2.4. High-Gain Free Electron Lasers

The particle bunches are generally much longer than the wavelength λ of the radiation. This leads to an incoherence between the emission by different particles and to a power proportional to the number N of particles per bunch. If it were possible to generate bunches whose length is less than $\lambda/2$, all particles would radiate coherently, resulting in an enormous increase in brilliance.

This is essentially the situation in a high-gain FEL. The interaction between the electrons and the photon field results in a deceleration of the particles that lose energy to the field according to Eq. (2.23) while the electrons that gain energy through the interaction are accelerated. In the undulator, the electrons with a higher energy travel on a shorter trajectory, hence a modulation of the longitudinal electron density occurs, with a period that is approximately the radiation wavelength (see figure 2.4b and c). As a result, the electrons will eventually be concentrated within slices with a distance of λ , the so-called *micro-bunches*. The emission of radiation is then coherent. This strong radiation field enhances the micro-bunching of the particles further, resulting in a collective instability and yielding an exponential growth of the radiation power. Under fortunate circumstances, the power is proportional to the square of the number of particles in a coherence volume $P \propto N_c^2$. With a typical value $N_c \approx 10^6$, the radiation power is increased one million times in comparison to the spontaneous undulator radiation. If the gain length is much smaller than the undulator length, the FEL saturates in a single pass of the particle bunch. As opposed to conventional lasers, no mirrors are needed to confine the radiation field in the interaction region.

The mathematical description of the high-gain FEL process amounts to a self-consistent solution of

- the coupled pendulum equations (2.34), describing the motion of the particles in the bunch
- the inhomogeneous wave equation for the electric field, which accounts for the diffraction of the electromagnetic wave and its interaction with the electrons. The interaction includes the emission of radiation and the micro-bunching.

The following wave equation for the electric field \vec{E} is:

$$\left[\vec{\nabla}^2 - \frac{1}{c^2} \frac{\partial^2}{\partial t^2} \right] \vec{E} = \mu_0 \frac{\partial \vec{j}}{\partial t} + \frac{1}{\varepsilon_0} \vec{\nabla} \rho \quad (2.35)$$

with the current density \vec{j} and charge density ρ of the bunch. The charge and current density are initially homogeneously distributed inside the bunch. Along the passage of the undulator, the micro-bunching effect will impose a modulation. Internal Coulomb forces⁵ counteract this bunching.

In a linear accelerator, the Coulomb repulsion of the particles within a highly relativistic bunch can be neglected due to the time dilatation. In an FEL, however, this is not justified: although the longitudinal electric field is Lorentz contracted with a factor $1/\gamma^2$, The characteristic length of the density modulation, given by the radiation wavelength, varies also as $1/\gamma^2$ according to Eq. (2.26). Therefore, even for $\gamma \gg 1$, the impact of the longitudinal Coulomb repulsion on the micro-bunching process has to be taken into consideration even in the ultra-relativistic case.

In the transverse direction, the space charge forces scale also as $1/\gamma^2$, but here the typical length scale is the transverse dimension of the bunch, which is given by the emittance and scales only as $1/\gamma$. The transverse electromagnetic field generated by the space charge can thus be neglected when compared to the radiation field.

The electric field is now decomposed into a transverse part \vec{E}_\perp , describing the radiation field and a longitudinal part \vec{E}_\parallel due to Coulomb repulsion:

$$\vec{E} = \vec{E}_\perp + \vec{E}_\parallel = E_x \vec{u}_x + E_z \vec{u}_z \quad (2.36)$$

These two parts are first considered separately in sections 2.4.1 and 2.4.2. The connection between the transverse and longitudinal fields is made in section 2.4.3 using the respective components of the current densities.

2.4.1. Radiation field

To simplify the discussion, a transverse dependency of the charge density and the electromagnetic fields is neglected in the following. This treatment is called the 1D

⁵ generally referred to as *space charge effects*

FEL theory. In the wave equation, $\vec{\nabla}^2$ can therefore be replaced by $\partial^2/\partial z^2$, so the equation reads:

$$\left[\frac{\partial^2}{\partial z^2} - \frac{1}{c^2} \frac{\partial^2}{\partial t^2} \right] E_x = \mu_0 \frac{\partial j_x}{\partial t} + \frac{1}{\varepsilon_0} \frac{\partial \rho}{\partial x} \quad (2.37)$$

Since the charge density is assumed to be independent of x , the last term is omitted. This term can in fact be neglected in the 3D treatment of the FEL, since it can be shown that $\frac{1}{\varepsilon_0} \frac{\partial \rho}{\partial x} \ll \mu_0 \frac{\partial j_x}{\partial t}$ [KH00].

The wave equation (2.37) is further simplified by writing the electric field in the *slowly varying amplitude* (SVA) approximation with a complex amplitude \tilde{E}_x :

$$E_x = \tilde{E}_x e^{ik(z-ct)} \quad (2.38)$$

Of course, the electric field described by Eq. (2.19) is a complex quantity. It is understood that only its real part is the physical field. This complex notation simplifies the calculation, since a phase offset can be included in an imaginary part of the amplitude. Furthermore, the transformation rules for the exponential function are easier than for the trigonometric functions.

As opposed to the low gain case in equation (2.19), the amplitude and phase are now allowed to vary along z and t : $\tilde{E} = \tilde{E}(z, t)$. It is however assumed⁶ that they vary slowly, compared to $e^{ik(z-ct)}$. Since $e^{ik(z-ct)}$ is a solution of the homogeneous wave equation

$$\left[\frac{\partial^2}{\partial z^2} - \frac{1}{c^2} \frac{\partial^2}{\partial t^2} \right] e^{ik(z-ct)} = 0 \quad (2.39)$$

the inhomogeneous equation (2.37) can be simplified.

Introducing the differential operators:

$$D_{\pm} = \frac{1}{c} \frac{\partial}{\partial t} \pm \frac{\partial}{\partial z} \quad (2.40)$$

it is easy to see that

$$-D_+ D_- = \frac{\partial^2}{\partial z^2} - \frac{1}{c^2} \frac{\partial^2}{\partial t^2} \quad (2.41)$$

and

$$D_+ e^{ik(z-ct)} = 0 \quad (2.42a)$$

$$D_- e^{ik(z-ct)} = -2ike^{ik(z-ct)} \quad (2.42b)$$

Using these relations, one gets

$$D_+ \left(\tilde{E}_x e^{ik(z-ct)} \right) = D_+ (\tilde{E}_x) e^{ik(z-ct)} \quad (2.43)$$

⁶ this is a good approximation even for the TTF FEL, which generates extremely short pulses of about 10^{-13} s. These are still much longer than the period of the electromagnetic wave of 10^{-16} s.

and

$$D_- \left(\tilde{E}_x e^{ik(z-ct)} \right) = D_-(\tilde{E}_x) e^{ik(z-ct)} - \tilde{E}_x 2ik e^{ik(z-ct)} \quad (2.44)$$

In the slowly varying amplitude approximation, $|D_- \tilde{E}_x| \ll |k \tilde{E}_x|$

$$\Rightarrow D_- \left(\tilde{E}_x e^{ik(z-ct)} \right) \approx -\tilde{E}_x 2ik e^{ik(z-ct)} \quad (2.45)$$

Now the wave equation (2.37) is rewritten with the derivatives defined in Eq. (2.40) and the ansatz (2.38) for the electric field. Inserting Eq. (2.41), (2.43) and (2.45) yields

$$2ikD_+ \left(\tilde{E}_x e^{ik(z-ct)} \right) = 2ikD_+(\tilde{E}_x) e^{ik(z-ct)} = \mu_0 \frac{\partial j_x}{\partial t} \quad (2.46)$$

or, inserting D_+ , the equation for the slowly varying amplitude finally reads:

$$2ik \left[\frac{1}{c} \frac{\partial \tilde{E}_x}{\partial t} + \frac{\partial \tilde{E}_x}{\partial z} \right] e^{ik(z-ct)} = \mu_0 \frac{\partial j_x}{\partial t} \quad (2.47)$$

2.4.2. Space charge field

The longitudinal electric field describes the space charge effect. For a homogeneous charge distribution, this internal field will be zero. If, however, the bunch should develop a microstructure with the periodicity of the wavelength, a longitudinal field arises showing the same period. In the following, a tiny periodic perturbation of the charge distribution in the bunch is investigated. This will be amplified by the interaction with the electromagnetic field describing the radiation. The following ansatz is made for the charge density:

$$\rho = \rho_0 + \tilde{\rho}_1 e^{i\psi} \quad (2.48)$$

From $j_z = v_z \rho$, one obtains that the current has a similar distribution:

$$j_z = j_0 + \tilde{j}_1 e^{i\psi} = j_0 + \tilde{j}_1 e^{i((k+k_u)z-\omega t)} \quad (2.49)$$

Since j_0 is constant, the derivative of the current is

$$\frac{\partial j_z}{\partial t} = -i\omega \tilde{j}_1 e^{i((k+k_u)z-\omega t)} \quad (2.50)$$

The space charge field is generated by the charge distribution (2.48), therefore it has a similar periodic modulation:

$$E_z = \tilde{E}_z e^{i((k+k_u)z-\omega t)} \quad (2.51)$$

To relate the electric field to the current density, consider the z component of the *Maxwell* equation

$$\frac{1}{\mu_0} \vec{\nabla} \times \vec{B} - \varepsilon_0 \frac{\partial \vec{E}}{\partial t} = \vec{j} \quad (2.52)$$

Inserting the current from Eq. 2.49 gives:

$$\frac{1}{\mu_0} \left(\frac{\partial B_y}{\partial x} - \frac{\partial B_x}{\partial y} \right) - \varepsilon_0 \frac{\partial E_z}{\partial t} = j_0 + \tilde{j}_1 e^{i((k+k_u)z-\omega t)} \quad (2.53)$$

The derivative of the electric field, expressed by Eq. (2.51), is:

$$\frac{\partial E_z}{\partial t} = \frac{\partial \tilde{E}_z}{\partial t} e^{i((k+k_u)z-\omega t)} - i\omega \tilde{E}_z e^{i((k+k_u)z-\omega t)} \quad (2.54)$$

In the slowly varying amplitude approximation, the first term is neglected.

The overall beam current j_0 results in a magnetic field around the beam, while the longitudinal space charge field is given by the current modulation $\tilde{j}_1 e^{i((k+k_u)z-\omega t)}$:

$$i\omega \tilde{E}_z e^{i((k+k_u)z-\omega t)} = \frac{1}{\varepsilon_0} \tilde{j}_1 e^{i((k+k_u)z-\omega t)} \quad (2.55)$$

Therefore,

$$i\omega \tilde{E}_z = \frac{1}{\varepsilon_0} \tilde{j}_1 \quad (2.56)$$

2.4.3. Relation between radiation and space charge field

To relate the space charge field E_z to the radiation field E_x , a connection between the longitudinal and transverse components of the current is made. This relation can be derived from the motion of the particles in the undulator. From $j_x = \rho v_x$ and $j_z = \rho v_z$, it follows by division

$$\frac{j_x}{j_z} = \frac{v_x}{v_z} \quad (2.57)$$

For a planar undulator, the x component of the electron velocity is given by Eq. (2.7).

$$\implies j_x = j_z \frac{v_x}{v_z} \approx j_z \frac{v_x}{\bar{v}_z} \approx j_z \frac{v_x}{c} = -j_z \frac{\hat{K}}{\gamma} \cos(k_u z) \quad (2.58)$$

This relates the currents in x and z direction. One calculates the derivative:

$$\frac{\partial j_x}{\partial t} = -\frac{\partial j_z}{\partial t} \frac{\hat{K}}{\gamma} \cos(k_u z) \quad (2.59)$$

Inserting $\partial j_z / \partial t$ from Eq. (2.50) results in the following expression for the time derivative of the transverse current density:

$$\frac{\partial j_x}{\partial t} = -\frac{i\omega \hat{K}}{\gamma} \tilde{j}_1 e^{i\psi} \cos(k_u z) \quad (2.60)$$

2.4.4. Steady state approximation

To proceed with the solution of the equations of the high-gain FEL, the *steady state approximation* is made: the electron and photon bunches are assumed to be sufficiently long, ideally of infinite extent. Also, the initial density distribution is assumed to be uniform over the bunch. This approximation implies that effects such as the slippage between the envelope of the radiation bunch and the electron bunch are neglected.

It should be noted that for the very short bunches in the TTF FEL, this slippage reduces the overlap between the electron and the photon bunches near the end of the undulator. Furthermore, the shot noise used to simulate the initial generation of spontaneous undulator radiation is in contradiction to the steady state model. These effects have to be treated numerically. Nevertheless, the analytic derivation of equations that describe the FEL process are useful to understand the general principles.

Of the four space-time dimensions, only z remains, thus the following treatment is referred to as the *one-dimensional FEL theory*.

The wave equation for the x component of the electric field becomes:

$$\begin{aligned}
 \frac{\partial \tilde{E}_x(z)}{\partial z} &= \frac{\mu_0}{2ik} \frac{\partial j_x}{\partial t} e^{-ik(z-ct)} \\
 &= -\frac{i\omega \hat{K} \mu_0}{2ik\gamma} \tilde{j}_1(z) e^{i\psi} \cos(k_u z) e^{-ik(z-ct)} \\
 &= -\frac{\mu_0 c \hat{K}}{2\gamma} \tilde{j}_1(z) e^{ik_u z} \cos(k_u z) \\
 &= -\frac{\mu_0 c \hat{K}}{2\gamma} \tilde{j}_1(z) \left(\frac{1}{2} + \frac{1}{2} e^{2ik_u z} \right)
 \end{aligned}$$

Omitting the rapidly oscillating term, one gets

$$\frac{\partial \tilde{E}_x(z)}{\partial z} \approx -\frac{\mu_0 c \hat{K}}{4\gamma} \tilde{j}_1(z) \quad (2.61)$$

2.4.5. Vlasov equation

The FEL equations can be written in terms of the independent variables⁷ (z, η, ψ) , where z is the longitudinal coordinate, η the relative deviation from the reference energy and ψ the ponderomotive phase.

An important step is to describe the evolution of the particle density distribution along the undulator, leading eventually to the micro-bunching. Under the assumption

⁷ in the Hamilton formalism, one can write this variable transformation as a canonical transformation from (z, E, t) to (z, η, ψ) [SSY00b].

that the interaction of an electron with its direct neighbours is much smaller than the interaction with the collective field generated by all electrons, one can treat the space charge field as an external field.

The ensemble of the particles is described by a continuous distribution $\tilde{f}(z, \eta, \psi)$ in the (z, η, ψ) -space. The number of particles in a phase space volume $(dz d\eta d\psi)$ is

$$dN_e = \tilde{f}(z, \eta, \psi) dz d\eta d\psi \quad (2.62)$$

To ease calculations, \tilde{f} is written as a complex function. Only its real part has physical significance.

According to *Liouville's* theorem, the phase space density is conserved along the trajectory of a particle. This leads to a generalised continuity equation which is called the *Vlasov Equation*:

$$\frac{d\tilde{f}}{dz} = \frac{\partial\tilde{f}}{\partial z} + \frac{\partial\tilde{f}}{\partial\psi} \frac{d\psi}{dz} + \frac{\partial\tilde{f}}{\partial\eta} \frac{d\eta}{dz} = 0 \quad (2.63)$$

Similarly to the charge density (section 2.4.2), the distribution f will be periodically modulated:

$$\tilde{f}(z, \eta, \psi) = \tilde{f}_0(\eta) (1 + \tilde{\varepsilon}(z) \cdot e^{i\psi}) \quad (2.64)$$

The charge density is given by $\rho = -e|f|$. Here, the assumption is made that the particle density will develop a small sinusoidal variation with the period of the ponderomotive phase along the undulator:

$$\tilde{f}_1(z, \eta) = \tilde{f}_0(\eta) \cdot \tilde{\varepsilon}(z) \quad (2.65)$$

One takes $d\eta/dz$ from the pendulum equation (2.34b), writes the trigonometric function in exponential notation and adds a term which accounts for the energy change of an electron due to the space charge force:

$$\frac{d\eta}{dz} = \frac{e\tilde{E}_x(z)\hat{K}}{2m_e c^2 \gamma_r^2} e^{i\psi} - \frac{eE_z(z)}{m_e c^2 \gamma_r} e^{i\psi} \quad (2.66a)$$

From Eq. (2.34a):

$$\frac{d\psi}{dz} = 2k_u \eta \quad (2.66b)$$

Inserting Eq. (2.64) and (2.66) in Eq. (2.63) yields:

$$\begin{aligned} \frac{d\tilde{f}}{dz} &= \tilde{f}_0 \frac{\partial\tilde{\varepsilon}}{\partial z} e^{i\psi} + i\tilde{f}_0 \tilde{\varepsilon} e^{i\psi} \cdot 2k_u \eta \\ &+ \frac{d\tilde{f}_0}{d\eta} [1 + \tilde{\varepsilon} e^{i\psi}] \cdot \left[\frac{e\tilde{E}_x(z)\hat{K}}{2m_e c^2 \gamma_r^2} e^{i\psi} - \frac{e\tilde{E}_z(z)}{m_e c^2 \gamma_r} e^{i\psi} \right] = 0 \end{aligned} \quad (2.67)$$

The sinusoidal charge density variation $\tilde{\varepsilon}$ is assumed to be small, it can hence be neglected in the term $[1 + \tilde{\varepsilon}e^{i\psi}]$. Multiplying by $e^{-i\psi}$, inserting the Eq. (2.65) and approximating $\gamma \approx \gamma_r$ results in the following equation for the space charge density:

$$\implies \frac{\partial \tilde{f}_1}{\partial z} + 2ik_u \eta \tilde{f}_1 + \left[\frac{ie\hat{K}}{2m_e c^2 \gamma^2} \tilde{E}_x(z) - \frac{e}{m_e c^2 \gamma} \tilde{E}_z(z) \right] \frac{d\tilde{f}_0}{d\eta} = 0 \quad (2.68)$$

This is a differential equation of the type

$$\frac{dF(z)}{dz} + i\alpha F(z) - G(z) = 0 \quad (2.69)$$

with general solution

$$F(z) = \int_0^z G(z') e^{-i\alpha(z-z')} dz' \quad (2.70)$$

If this formula is applied, it is possible to express \tilde{f}_1 in terms of \tilde{f}_0 :

$$\tilde{f}_1(z) = - \int_0^z \left[\frac{e\hat{K}}{2m_e c^2 \gamma^2} \tilde{E}_x(z') - \frac{e}{m_e c^2 \gamma} \tilde{E}_z(z') \right] \frac{d\tilde{f}_0}{d\eta} e^{-2ik_u \eta(z-z')} dz' \quad (2.71)$$

2.4.6. Current density

The longitudinal current density can be expressed in terms of the particle motion. As long as the deviation of a single particle from the reference orbit is much smaller than the transverse size of the electron beam, one may write:

$$\begin{aligned} j_z(z, \psi) &= v_z \rho \approx c \int_{-\infty}^{\infty} (-e) \tilde{f}(z, \eta, \psi) d\eta \\ &= -ec \left[\int_{-\infty}^{\infty} \tilde{f}_0(\eta) d\eta + e^{i\psi} \int_{-\infty}^{\infty} \tilde{f}_1(z, \eta) d\eta \right] \\ &= j_0 + \tilde{j}_1(z) e^{i\psi} \end{aligned} \quad (2.72)$$

Comparing with Eq. (2.49), one finds:

$$j_0 = -ec \int_{-\infty}^{\infty} \tilde{f}_0(\eta) d\eta \quad \text{and} \quad \tilde{j}_1(z) = -ec \int_{-\infty}^{\infty} \tilde{f}_1(z, \eta) d\eta \quad (2.73)$$

2.4.7. Equation for the field amplitude

The equation for the transverse field amplitude is given by Eq. (2.61)

$$\frac{\partial \tilde{E}_x(z)}{\partial z} = -\frac{\mu_0 c \hat{K}}{4\gamma} \tilde{j}_1(z) \quad (2.74)$$

using \tilde{j}_1 from Eq. (2.73)

$$\frac{\partial \tilde{E}_x(z)}{\partial z} = \frac{\mu_0 c^2 \hat{K} e}{4\gamma} \int_{-\infty}^{\infty} \tilde{f}_1 d\eta \quad (2.75)$$

and \tilde{f}_1 from Eq. (2.71), the equation reads:

$$\frac{\partial \tilde{E}_x(z)}{\partial z} = -\frac{\mu_0 \hat{K} e^2}{4\gamma m_e} \int_{-\infty}^{\infty} \int_0^z \left[\frac{\hat{K}}{2\gamma^2} \tilde{E}_x(z') - \frac{1}{\gamma} \tilde{E}_z(z') \right] \frac{d\tilde{f}_0}{d\eta} e^{-2ik_u \eta(z-z')} dz' d\eta \quad (2.76)$$

This equation still contains both the transverse radiation field and the longitudinal space charge field.

Combining equations (2.56) and (2.61),

$$\frac{4\gamma}{\mu_0 c \hat{K}} \frac{\partial \tilde{E}_x}{\partial z} = -i\omega \varepsilon_0 \tilde{E}_z \quad (2.77)$$

one finally obtains:

$$\frac{\partial \tilde{E}_x(z)}{\partial z} = -\frac{\mu_0 \hat{K} e^2}{4\gamma m_e} \int_{-\infty}^{\infty} \int_0^z \left[\frac{\hat{K}}{2\gamma^2} \tilde{E}_x(z') + \frac{2c}{\omega \hat{K}} \frac{\partial}{\partial z'} \tilde{E}_x(z') \right] \frac{d\tilde{f}_0}{d\eta} e^{-2ik_u \eta(z'-z)} dz' d\eta \quad (2.78)$$

This integro-differential equation describes the radiation field amplitude \tilde{E}_x produced by an electron bunch with initial energy distribution $\tilde{f}_0(\eta)$.

2.4.8. Solution of the integro-differential equation

For a few distributions \tilde{f}_0 , Eq. (2.78) can be solved analytically using the Laplace transform technique [SSY00b]. Here, we consider the case of a mono-energetic electron beam:

$$\tilde{f}_0(\eta) = n_e \delta(\eta - \eta_0) \quad (2.79)$$

The sequence of the integration can be interchanged:

$$\frac{\partial \tilde{E}_x(z)}{\partial z} = -\frac{\mu_0 c^2 \hat{K} e}{4\gamma} \int_0^z \int_{-\infty}^{\infty} \left[\frac{e \hat{K}}{2m_e c^2 \gamma^2} \tilde{E}_x(z') + \frac{e}{m_e c^2} \frac{2c}{\omega \hat{K}} \frac{\partial}{\partial z'} \tilde{E}_x(z') \right] n_e \frac{d\delta(\eta)}{d\eta} e^{-2ik_u \eta(z'-z)} d\eta dz' \quad (2.80)$$

The derivative of the δ -function is removed by partial integration:

$$\int_{-\infty}^{\infty} F(\eta) \frac{d\delta(\eta - \eta_0)}{d\eta} d\eta = \underbrace{[F(\eta)\delta(\eta - \eta_0)]_{-\infty}^{\infty}}_{=0} - \int_{-\infty}^{\infty} \frac{dF(\eta)}{d\eta} \delta(\eta - \eta_0) d\eta \quad (2.81)$$

$$= - \left. \frac{dF(\eta)}{d\eta} \right|_{\eta=0} \quad (2.82)$$

Thus,

$$\frac{\partial}{\partial z} \tilde{E}_x(z) = -\frac{\mu_0 c^2 \hat{K} e}{4\gamma} \int_0^z 2k_u(z' - z) e^{-2ik_u \eta_0(z'-z)} \left[\frac{e \hat{K}}{2m_e c^2 \gamma^2} \tilde{E}_x(z') + \frac{e}{m_e c^2} \frac{2c}{\omega \hat{K}} \frac{\partial}{\partial z'} \tilde{E}_x(z') \right] dz' \quad (2.83)$$

Introducing the gain parameter

$$\Gamma = \sqrt[3]{\frac{\mu_0 \hat{K}^2 e^2 k_u n_e}{4\gamma^3 m_e}} \quad (2.84)$$

and a wave number⁸

$$k_p = \sqrt{\Gamma^3 \frac{4\gamma^2 c}{\omega \hat{K}^2}} \quad (2.85)$$

equation (2.84) may be rewritten

$$\frac{\partial}{\partial z} \tilde{E}_x(z) = -\Gamma^3 \int_0^z i \left[\tilde{E}_x(z') + \frac{k_p^2}{\Gamma^3} \frac{\partial}{\partial z'} \tilde{E}_x(z') \right] (z' - z) dz' \quad (2.86)$$

This integro-differential equation can be transformed to a third-order differential equation [DR02]:

$$\frac{d^3 \tilde{E}_x(z)}{dz^3} - 4ik_u \eta_0 \frac{d^2 \tilde{E}_x(z)}{dz^2} + (k_p^2 - 4k_u^2 \eta_0^2) \frac{d\tilde{E}_x(z)}{dz} - i\Gamma^3 \tilde{E}_x(z) = 0 \quad (2.87)$$

⁸ which can be identified with the wave number of longitudinal plasma oscillations

This differential equation can be solved analytically for $\eta_0 = 0$ and small space charge forces ($n_e \text{small} \Rightarrow k_p \approx 0$):

$$\tilde{E}_x(z) = A_1 \exp(-i\Gamma z) + A_2 \exp\left(\frac{i + \sqrt{3}}{2}\Gamma z\right) + A_3 \exp\left(\frac{i - \sqrt{3}}{2}\Gamma z\right) \quad (2.88)$$

For $z \rightarrow \infty$, the second term dominates. This indicates the onset of a collective instability in the internal charge distribution in the bunch. The electric field grows exponentially as $\exp(\frac{\sqrt{3}}{2}\Gamma z)$, the power as $\exp(\sqrt{3}\Gamma z)$.

The gain parameter Γ is closely related to the three parameters that are in widespread use, namely Pierce parameter ρ_{Pierce}

$$\rho_{\text{Pierce}} = \sqrt[3]{\frac{e^2 \hat{K}^2 n_e}{32 \epsilon_0 \gamma^3 m_e c^2 k_u^2}} = \frac{\lambda_u \Gamma}{4\pi} \quad (2.89)$$

the power growth rate

$$\Lambda = \sqrt{3}\Gamma = \sqrt{3} \sqrt[3]{\frac{\mu_0 \hat{K}^2 e^2 k_u n_e}{4\gamma^3 m_e}} \quad (2.90)$$

and the power gain length

$$L_g = \frac{1}{\Lambda} = \frac{1}{\sqrt{3}} \sqrt[3]{\frac{4\gamma^3 m_e}{\mu_0 \hat{K}^2 e^2 k_u n_e}} \quad (2.91)$$

2.4.9. Summary

The derivation of the equations for the high-gain FEL is summarised in figure 2.5. Starting with the undulator field, Maxwell's equations, the equations of motion and an assumption on the initial particle distribution, the following equations have been derived:

- In the steady-state and one-dimensional approximation, the wave equation has been simplified in the SVA approximation.
- The radiation field has been related to the space charge field by the ratio of transverse and longitudinal current densities.
- The Vlasov equation has been used to describe the particle distribution.
- The current density in the wave equation was described by this particle distribution.

Finally, an integro-differential equation for the radiation field was derived. This was solved for the case of a mono-energetic electron beam on resonance.

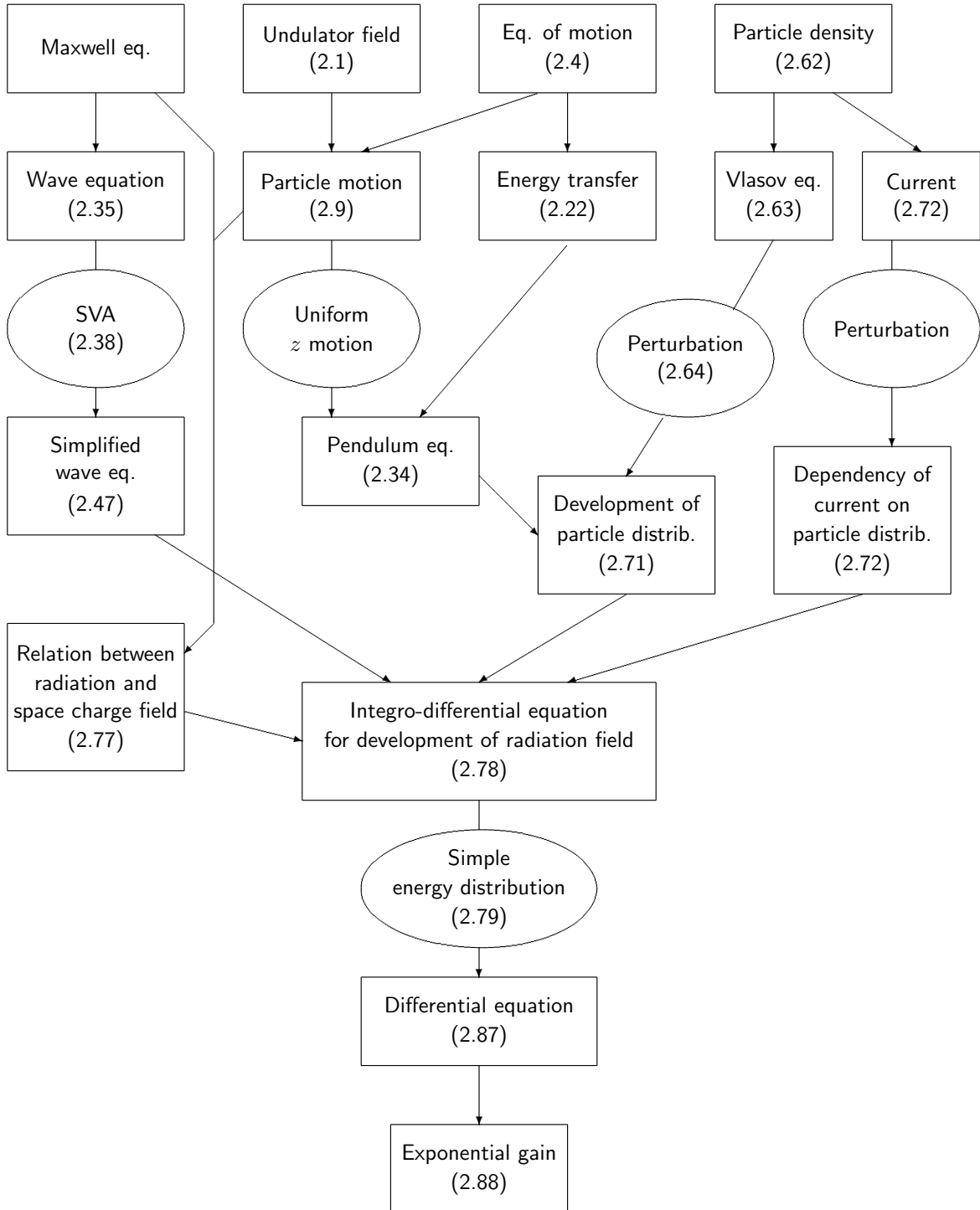


Figure 2.5.: Equations used to describe the high-gain FEL. Rectangles: equations, Ellipses: simplifications.

2.5. Three-dimensional FEL simulation codes

Up to this point, a transverse dependence of the electric fields was neglected. To study 3-dimensional effects, such as for example the transverse coherence of the radiation, a more complete model has to be used, taking into account the transverse distribution of the electrons as well as the diffraction of the radiation. This is described in details in [SSY00b] and [Rei99], where two approaches to solve the differential equations numerically are presented. The electron bunch is represented by a number of macro-particles, combining the mass and the charge of many electrons. The codes solve the *Maxwell* equations for the electromagnetic field, the equations of motion of the electrons and their mutual interaction simultaneously. The simulations are done in three spatial dimensions and include the time dependency. For this purpose, the solution of the differential equations is done in small time steps and the equations for the particle motion are interleaved with the equations for the radiated electromagnetic fields.

Unlike simulations based on the steady-state approximation, where only a slice within the bunch corresponding to one period of the ponderomotive phase ψ , i.e. only one micro-bunch, is simulated, the codes compute the differential equations for the complete bunch. This allows to treat SASE-FELs where the electron bunch envelope slips significantly behind the radiation bunch.

The simulation predicts effects as the saturation of the FEL process. Additionally, it makes predictions on the transverse variation of the radiation and thus on the coherence of the FEL radiation. This will be discussed in section 3.3.

2.6. Requirements on the accelerator

The lasing medium in a free electron laser is a high-energy electron beam provided by a particle accelerator. This has to satisfy a set of conditions. To operate a free electron laser based on the self-amplification of spontaneous emission (i.e. a SASE FEL) in the ultraviolet regime, the following approximate values have been proposed [Åbe95]:

- A particle energy of about 250 MeV: see equation (2.14)
- A peak current in the order of 1 kA
- A normalised emittance of $1\pi \mu\text{m}$ (section 4.1.2)
- An energy spread of less than 1‰

Such an electron beam can be provided by the linear accelerator at the TESLA Test Facility. It is described in chapter 4.

3. Coherence and Interference

In this chapter, the formation of diffraction patterns of an electromagnetic wave and their dependence on the transverse coherence of the wave are studied. First, the coherence properties for an electromagnetic wave are defined in terms of the cross-correlation of the field. The coherence properties of a free electron laser are discussed.

It follows a discussion of the formation of diffraction patterns on a screen behind an aperture. For a large distance to the screen, analytical formulae for the intensity distribution can be derived for a number of different apertures. At closer distances, this approximation cannot be made. This is the case for the present experimental set-up. Nevertheless, it is possible to derive a formula for a double slit that is illuminated by a plane wave.

More complex configurations can be handled with numerical methods. Two different approaches are presented.

3.1. Definition of coherence properties

The electric field vector¹ of an electromagnetic wave can be represented by its three orthogonal components:

$$\vec{E}(x, y, z, t) = E_x(x, y, z, t)\vec{u}_x + E_y(x, y, z, t)\vec{u}_y + E_z(x, y, z, t)\vec{u}_z \quad (3.1)$$

where \vec{u}_x , \vec{u}_y , and \vec{u}_z are the unit vectors. If the divergence or convergence of the wave is not too large, i.e. as long as the aperture of a focusing element is not more than $2/3$ of its focal length [App01a], an optical beam propagating in z direction can be represented to good approximation by its transverse electric fields:

$$\vec{E}(x, y, z, t) = E_x(x, y, z, t)\vec{u}_x + E_y(x, y, z, t)\vec{u}_y \quad (3.2)$$

E_x and E_y represent the two orthogonal states of polarisation. In the case of the FEL, linearly polarised light is expected, therefore one can work with E_x only:

$$\vec{E}(x, y, z, t) = E_x(x, y, z, t)\vec{u}_x \quad (3.3)$$

¹ in principle, also the magnetic field could be used. Since the fields are proportional to each other, the result would be the same.

3. Coherence and Interference

The propagation of the electromagnetic wave that is described in the *slowly varying amplitude* (SVA) approximation:

$$\vec{E}(\vec{r}, t) = \text{Re} \left[\tilde{E} \exp \left(i(\omega t - \vec{k} \cdot \vec{r}) \right) \right] \vec{u}_x \quad (3.4)$$

where \tilde{E} is the complex amplitude of the electric field whose time variation is slow in comparison with $\exp(i\omega t)$. Note that a partially coherent wave must necessarily have a time-dependent amplitude, since a constant amplitude would imply full coherence.

Coherence can be defined in terms of the correlation functions of the electric wave [Goo85]. The first-order correlation function between two points \vec{r} and \vec{r}' is defined as

$$\Gamma(\vec{r}, \vec{r}') = \left\langle \tilde{E}(\vec{r}, t) \cdot \tilde{E}^*(\vec{r}', t) \right\rangle_t \quad (3.5)$$

where \tilde{E}^* is the complex conjugate of \tilde{E} and the time average of a function $F(t)$ is defined as

$$\langle F(t) \rangle_t = \frac{1}{\Delta t} \int_{\Delta t} F(t) dt \quad (3.6)$$

Here, the time interval Δt is chosen to be much longer than the time scale of the variation of \tilde{E} . The normalised correlation function is

$$\tilde{\gamma}(\vec{r}, \vec{r}') = \frac{\left\langle \tilde{E}(\vec{r}, t) \cdot \tilde{E}^*(\vec{r}', t) \right\rangle_t}{\left[\left\langle |\tilde{E}(\vec{r}, t)|^2 \right\rangle_t \left\langle |\tilde{E}(\vec{r}', t)|^2 \right\rangle_t \right]^{1/2}} \quad (3.7)$$

By definition, the normalised correlation function is equal to 1 for $\vec{r} = \vec{r}'$. Usually, it drops to zero for large separations; the wave is then said to be incoherent between \vec{r} and \vec{r}' .

The *coherence* \mathcal{C} is defined as the absolute value of the normalised correlation function:

$$\mathcal{C}(\vec{r}, \vec{r}', z) = |\tilde{\gamma}(\vec{r}, \vec{r}', z)| \quad (3.8)$$

If the coherence between two points depends only on their distance $|\vec{r} - \vec{r}'|$, the *coherence length* can be defined as the distance where the coherence drops to a given value. Since the electric field appears quadratically in the definition, the value $1/e^2$ is chosen.

The *degree of coherence* of a wave packet can be defined as the normalised integral over the coherence function, weighted by the intensity $I = \langle \tilde{E} \tilde{E}^* \rangle_t$:

$$\mathcal{D} = \frac{\int \mathcal{C}(\vec{r}) I(\vec{r}) d^3r}{\int I(\vec{r}) d^3r} \quad (3.9)$$

Often, it is useful to study the longitudinal and transverse behaviour of a travelling wave packet separately; one can define a normalised first-order transverse correlation function

$$\tilde{\gamma}^\perp(\vec{r}_\perp, \vec{r}'_\perp, z) = \frac{\langle \tilde{E}(\vec{r}_\perp, z, t) \cdot \tilde{E}^*(\vec{r}'_\perp, z, t) \rangle_t}{\left[\langle |\tilde{E}(\vec{r}_\perp, z, t)|^2 \rangle_t \langle |\tilde{E}(\vec{r}'_\perp, z, t)|^2 \rangle_t \right]^{1/2}} \quad (3.10)$$

Similarly, a longitudinal correlation function is defined. The absolute values of longitudinal and transverse correlation functions are the longitudinal and transverse coherences, respectively. In many practical cases, the coherence length will be different in longitudinal and transverse direction. At the TTF FEL, the longitudinal coherence length is in the order of micrometres, while the transverse coherence length at the position of the double slit experiment is in the order of millimetres.

A transverse degree of coherence can be defined by integrating the coherence over the transverse dimensions, similarly to Eq. (3.9):

$$\mathcal{D} = \frac{\int \mathcal{C}(x, y) I(x, y) dx dy}{\int I(x, y) dx dy} \quad (3.11)$$

If a beam propagates in free space, the transverse coherence length increases together with the beam width. Hence the position must be specified at which the coherence length is determined. In the present experiment, this is the position of the double slits, 11.84 m downstream of the undulator exit. The longitudinal coherence length will generally not be influenced by the propagation in vacuum.

3.2. Generation of coherent light

The light emitted by thermal sources has little longitudinal coherence: the emission of photons by different atoms is uncorrelated, and their phases are random. The transverse coherence of the light from an extended source is small for the same reason. The same is true for conventional synchrotron sources, where free electrons or positrons emit photons spontaneously.

To increase the transverse coherence, one may reduce the extension of the source. Propagation in free space preserves the degree of coherence, resulting in a beam with a high transverse coherence length. In a synchrotron radiation source, the condition that the diameter of the electron beam is smaller than the diffraction limit, $\sigma_x \leq \lambda/4\pi$ is fulfilled only for the longest wavelengths. Obviously, this becomes increasingly difficult at higher photon energies. The only way to improve on the transverse coherence is then the use of a spatial filter, i.e. a pinhole aperture, to select only the central part of the beam. However, by this method the intensity is typically reduced by several orders of magnitude.

In a conventional laser, the emission of photons is stimulated by the radiation that is already present in the medium. The emission occurs in phase, resulting in a

radiation field with high longitudinal coherence. A good transverse coherence can be achieved if the optical cavity selects only the fundamental transverse optical mode.

3.3. Coherence of a free electron laser

In a SASE FEL, there is no optical cavity, hence it is interesting to study its transverse coherence. In a three-dimensional model, the radiation field in the FEL has a dependence on the transverse coordinates. Similarly to Eq. (2.88), one can write:

$$\tilde{E}(r, \vartheta, z) = A(r, \vartheta, z) \exp\left(\frac{\Lambda}{2}z\right) \quad (3.12)$$

The total energy of the beam must be finite, i.e. the following integral has to converge:

$$\int_{\mathbb{R}^2} A^2(x, y) dx dy < \infty \quad (3.13)$$

As a consequence, the development can be written with a discrete set of propagation constants Λ_i , each corresponding to a fixed distribution $A(x, y)$ [SSY00b]. This way, the photon beam is represented as a superposition of various radiation modes. These modes with transverse electric and magnetic field (TEM) are usually labelled by two indices n and m :

$$\tilde{E}(r, \vartheta, z) = \sum_{n,m} C_{nm}(z) \tilde{A}_{nm}(r, \vartheta) \quad (3.14)$$

where the complex coefficients C_{nm} are given by the respective growth rates

$$C_{nm}(z) = \exp\left(\frac{\Lambda_{nm}}{2}z\right) \quad (3.15)$$

The transverse profiles of the first modes are shown in figure 3.1. As opposed to the case of a waveguide, the modes in the FEL are not orthogonal [SSY00b]. The growth rates Λ_{nm} are determined by the overlap with the electron beam. In the case of the SASE FEL, we expect the series to converge quickly, because the beam is concentrated in a small transverse area around the optical axis.

When decomposing the spontaneous undulator radiation, many transverse modes will be present, with random magnitude and phase, as a result of the stochastic nature of spontaneous emission. Hence, the radiation has poor transverse coherence.

3.3.1. Evolution of the transverse coherence

In the case of FEL amplification, the field amplitudes of the various modes grow exponentially along the undulator. The fundamental mode TEM_{00} has the shortest gain length, due to the best overlap with the electron beam (see figure 3.2). Therefore,

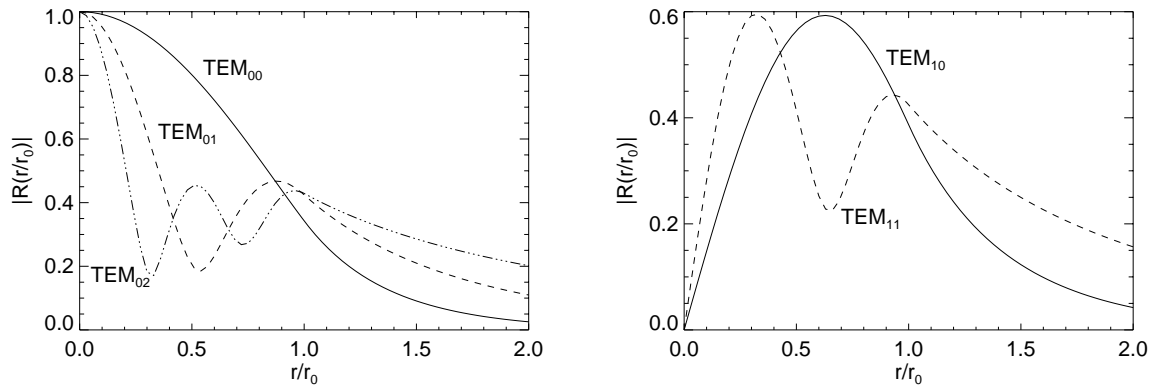


Figure 3.1.: Decomposition in transverse modes: the transverse profile of the first modes is shown [Rei99].

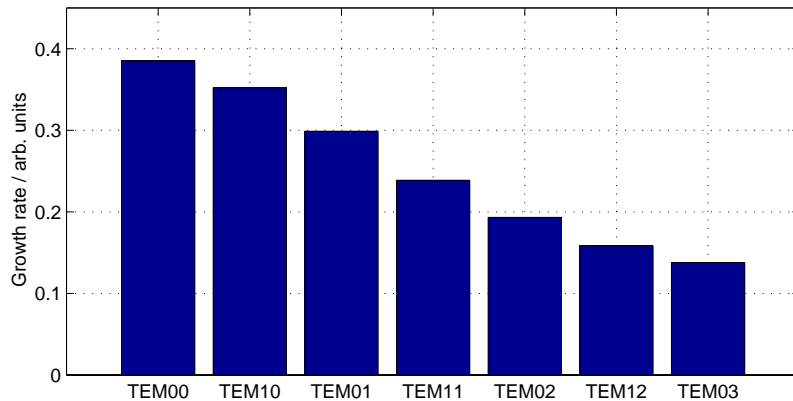


Figure 3.2.: Growth rate of the different transverse modes for an electron beam on resonance, simulated by Sven Reiche [Rei99].

this mode grows faster than the other modes. Due to the exponential increase, its intensity surpasses the total intensity in all other modes. With one mode dominating, the radiation has thus a high degree of transverse coherence.

When the fundamental mode saturates, the other modes are still growing. Since their phase generally is different from the fundamental mode, the overall transverse coherence is reduced. This decrease of transverse coherence has been predicted theoretically [SSY03]. It is shown in figure 3.3. Measurements are presented in chapter 8.

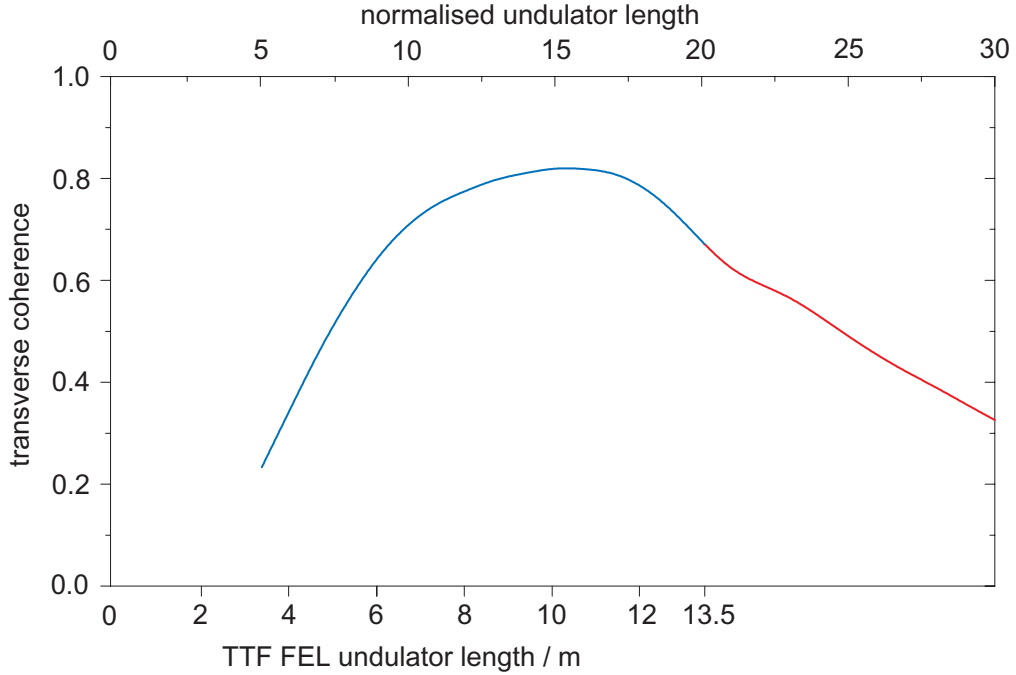


Figure 3.3.: Development of the transverse coherence in the undulator, from simulations with the code FAST3d [SSY03]. The undulator length is normalised to the gain length, which is equal to 67 cm in the case of the TTF FEL. The development was simulated up to 30 gain lengths, i.e. into deep saturation of the FEL process.

3.4. Analytic description of diffraction effects

In this section, the electric field behind an aperture \mathcal{A} of arbitrary shape [Tre01] is derived, as illustrated in figure 3.4. The distance to the plane of observation is denoted by L .

The validity of the Slowly Varying Amplitude approximation (3.4) is assumed, with a beam travelling in z direction. The field amplitude in the observation plane, denoted with index 1, is given by the propagation of the amplitudes in the aperture plane (index 0), modulated with the respective phase factor. From each point in the aperture plane inside the opening, a spherical wave emerges, according to *Huygens' principle*. The field amplitude is multiplied with the inclination factor $K(\vartheta)$, the dependence on the distance $1/\ell$, an arbitrary constant Q and the phase factor $\exp(ik\ell)$:

$$\tilde{E}(x_1, y_1) = \int_{\mathcal{A}} Q K(\vartheta) \frac{\exp(ik\ell)}{\ell} \tilde{E}(x_0, y_0) dx_0 dy_0 \quad (3.16)$$

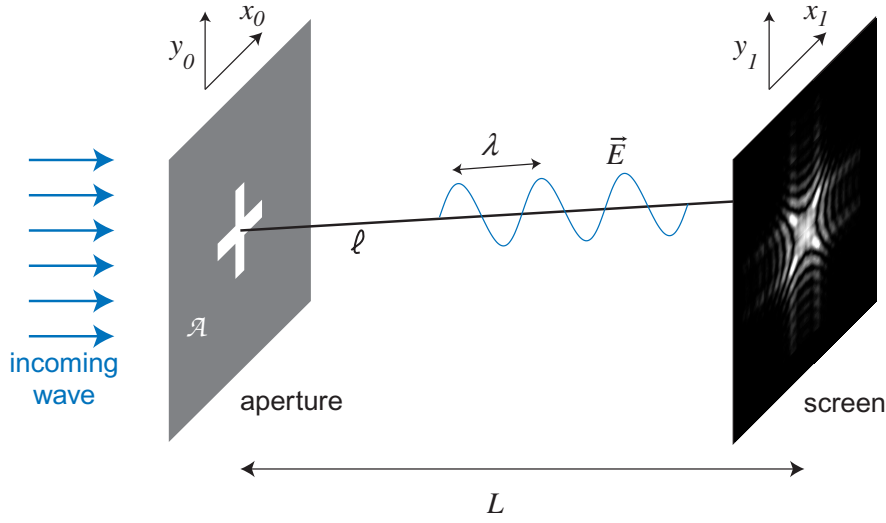


Figure 3.4.: Diffraction at an aperture. An interference pattern forms on a screen at distance L .

where

$$K(\vartheta) = \frac{1}{2}(1 + \cos \vartheta) \quad \text{with} \quad \vartheta = \arctan \frac{\sqrt{(x_1 - x_0)^2 + (y_1 - y_0)^2}}{L} \quad (3.17)$$

is the inclination factor and

$$\ell = \ell(x_1 - x_0, y_1 - y_0) = \sqrt{L^2 + (x_1 - x_0)^2 + (y_1 - y_0)^2} \quad (3.18)$$

is the distance between the points $(x_0, y_0, 0)$ and (x_1, y_1, L) . For most practical cases, $\vartheta \ll 1$ and the inclination factor can be approximated by $K \approx 1$. The constant Q ascertains that an undisturbed wave is reconstructed by equation (3.16) if no aperture is present, i.e. if the integral extends over the complete plane \mathbb{R}^2 . It can be shown that [Pér96]

$$Q = \frac{1}{i\lambda} \quad (3.19)$$

The distance ℓ in the denominator can be approximated by L . However, the term $\exp(ik\ell)$ oscillates rapidly as a function of position on the screen and gives rise to the interference pattern. For this term, the following approximation will be used:

$$\begin{aligned} \ell &= L \sqrt{1 + \left(\frac{x_1 - x_0}{L}\right)^2 + \left(\frac{y_1 - y_0}{L}\right)^2} \\ &\approx L + \frac{(x_1 - x_0)^2}{2L} + \frac{(y_1 - y_0)^2}{2L} \end{aligned} \quad (3.20)$$

assuming $\left(\frac{x_1-x_0}{L}\right)^2 \ll 1$ and $\left(\frac{y_1-y_0}{L}\right)^2 \ll 1$. Thus,

$$\begin{aligned}\tilde{E}(x_1, y_1) &= \int_{\mathcal{A}} \frac{1}{i\lambda L} \exp \left[ik \left(L + \frac{(x_1 - x_0)^2}{2L} + \frac{(y_1 - y_0)^2}{2L} \right) \right] \tilde{E}(x_0, y_0) dx_0 dy_0 \\ &= \frac{1}{i\lambda L} \exp \left[ik \left(L + \frac{x_1^2 + y_1^2}{2L} \right) \right] \\ &\quad \int_{\mathcal{A}} \exp \left[ik \left(\frac{-2x_1x_0 - 2y_1y_0 + x_0^2 + y_0^2}{2L} \right) \right] \tilde{E}(x_0, y_0) dx_0 dy_0\end{aligned}\quad (3.21)$$

If one omits the constant phase factor and defines an aperture function $A(x_0, y_0)$ that is 1 inside the opening of the aperture \mathcal{A} and 0 outside, equation (3.21) can be rewritten

$$\tilde{E}(x_1, y_1) = \frac{1}{i\lambda L} \int \exp \left[ik \left(\frac{-2x_1x_0 - 2y_1y_0 + x_0^2 + y_0^2}{2L} \right) \right] \tilde{E}(x_0, y_0) A(x_0, y_0) dx_0 dy_0\quad (3.22)$$

The integral (3.22) is called the *Fresnel integral*. It can generally not be solved analytically without further simplifications.

3.5. Far field diffraction

In this section, two simplifying assumptions are made. The incident wave is assumed to be a plane wave, that is $\tilde{E}(x_0, y_0) = \tilde{E}_0 = \text{const}$, and the observation plane is at a large distance. This will yield the formulae for *far field*, or *Fraunhofer* diffraction. Note that this simplification cannot be applied to the present experimental set-up at TTF. It is nevertheless instructive to derive analytic formulae for various types of apertures.

Let R_{\min} be the radius of the smallest circle enclosing the aperture. If the so-called *far field condition*

$$\frac{kR_{\min}^2}{2L} \ll 1\quad (3.23)$$

is fulfilled, the quadratic terms in Eq. (3.22) can be neglected and the integral becomes

$$\tilde{E}(x_1, y_1) = \tilde{E}_0 \int \exp \left[ik \left(\frac{-x_1x_0 - y_1y_0}{L} \right) \right] A(x_0, y_0) dx_0 dy_0\quad (3.24)$$

This is the *Fraunhofer integral*, which is the two-dimensional Fourier transform of the aperture.²

² the conjugate variables are x_0 and kx_1/L .

3.5.1. Analytic formulae for simple apertures

For a *circular aperture* of radius R , the diffraction pattern is described by the *Bessel* function of the first kind J_1 , the intensity varies as

$$I(r) = \left(\frac{J_1(2\pi Rr/(\lambda L))}{2\pi Rr/(\lambda L)} \right)^2 \quad (3.25)$$

with the distance r from the centre of the pattern (see figure 3.11a and d).

A *single slit* of width w and infinite length forms an intensity pattern

$$I(x) = \left(\frac{\sin(\pi wx/\lambda L)}{\pi wx/\lambda L} \right)^2 \quad (3.26)$$

in a direction x perpendicular to the slits.

If the aperture has *two slits*, separated by a distance d , an additional modulation occurs:

$$I(x) = \left(\frac{\sin(\pi wx/(\lambda L))}{\pi wx/(\lambda L)} \right)^2 \left[1 + \cos \left(\frac{2\pi d}{\lambda L} x \right) \right] \quad (3.27)$$

(see figure 3.12a and c). If one neglects the slit width,

$$I(x) = 1 + \cos \left(\frac{2\pi d}{\lambda L} x \right) \quad (3.28)$$

Maxima are located at

$$x_{\max} = \frac{n\lambda L}{d}, \quad n \in \mathbb{N} \quad (3.29)$$

3.5.2. Measurement of coherence by interference experiments

So far, a plane wave in front of the aperture has been considered, with full transverse and longitudinal coherence. If the incoming light has a only partial coherence, the contrast of the interference pattern will be reduced: the brightest areas will have a reduced intensity, the points where coherent light cancels completely will be brighter. To describe this effect, it is customary to define the *visibility* of the fringes as the modulation depth of the intensity:

$$\mathcal{V} = \frac{I_{\max} - I_{\min}}{I_{\max} + I_{\min}} \quad (3.30)$$

\mathcal{V} is not an overall feature of the pattern, but can be computed for each fringe, i.e. for each maximum of the intensity, with the adjacent minimum.

A plane wave is by definition fully coherent and generates the Fraunhofer diffraction pattern of a double slit according to Eq. (3.27). The visibility is $\mathcal{V} = 1$ for all

3. Coherence and Interference

fringes, because the minimum intensity is $I_{\min} = 0$. If the incoming wave is only partially coherent, the visibility will be lower. In the following discussion, the direction perpendicular to the slits is considered. Assuming that the slit width is small, the incoming light within each slit may be approximated by a plane wave. The coherence within each slit is $\mathcal{C} = 1$, while between separate slits, a coherence $\mathcal{C} < 1$ is assumed. In one slit, the field amplitude is called \tilde{E}_1 , in the other, \tilde{E}_2 . Such a situation occurs when the two slits are illuminated by two plane waves of equal magnitude but time-varying relative phase:

$$\tilde{E}_2 = \tilde{E}_1 e^{i\varphi(t)} \quad (3.31a)$$

$$|\tilde{E}_2| = |\tilde{E}_1| \quad (3.31b)$$

Without loss of generality, it may be assumed that the phase fluctuates around zero:

$$\langle \varphi \rangle_t = 0 \quad (3.32)$$

For a given time, the diffraction pattern obtains a time-dependent shift

$$\Delta x(t) = \frac{\lambda L}{\pi d} \varphi(t) \quad (3.33)$$

with respect to Eq. (3.28). This means that all fringes in the resulting interference pattern will fluctuate by this value (figure 3.5). Integrated over a time Δt longer than the typical fluctuation periods of the phase offset, an averaged diffraction pattern results. Because of Eq. (3.32), the positions of minima and maxima of the averaged pattern will be the same as in the case of the plane wave. They are denoted by x_{\min} and x_{\max} . The intensity in the position x_{\min} is at a given time t

$$\begin{aligned} I_{\min} &= 1 + \cos \left(-\frac{2\pi d \Delta x(t)}{\lambda L} + \pi \right) \\ &= 1 - \cos 2\varphi(t) \end{aligned} \quad (3.34)$$

The intensity at x_{\max} is:

$$I_{\max} = 1 + \cos 2\varphi(t) \quad (3.35)$$

The visibility of the averaged pattern is Eq. (3.30):

$$\mathcal{V} = \langle 2 \cos \varphi \rangle_t \quad (3.36)$$

The transverse coherence, defined by the first-order correlation function, is:

$$\mathcal{C} = \left| \frac{\langle \tilde{E}_1 \cdot \tilde{E}_2 \rangle_t}{\left[\langle |\tilde{E}_1|^2 \rangle_t \langle |\tilde{E}_2|^2 \rangle_t \right]^{1/2}} \right| = \left| \frac{\langle \tilde{E}_1 \cdot \tilde{E}_1 e^{i\varphi} \rangle_t}{\langle |\tilde{E}_1|^2 \rangle_t} \right| \quad (3.37)$$

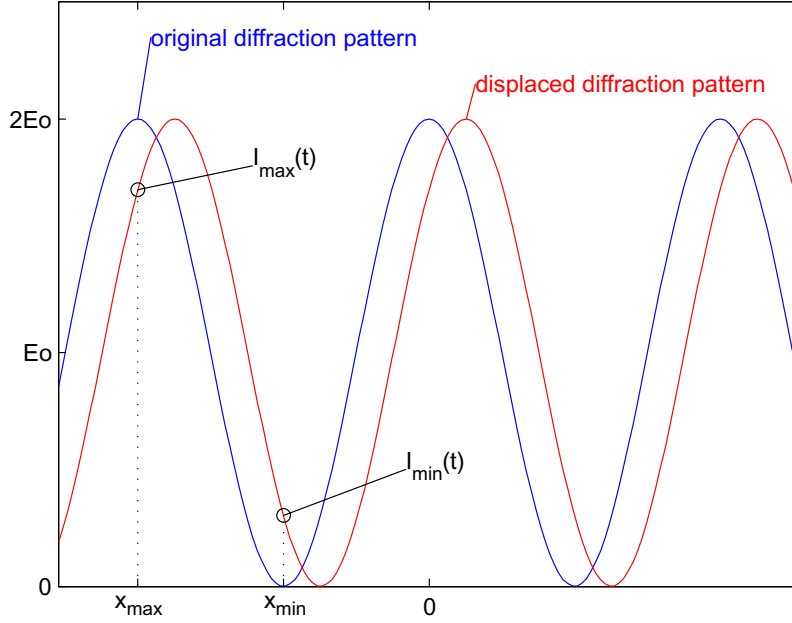


Figure 3.5.: Shifted double slit interference pattern, as a result of a phase offset in one slit.

This cannot be simplified further since the phase of \tilde{E}_1 could change with time. If perfect longitudinal coherence is assumed for one slit, i.e. constant phase for \tilde{E}_1 ,

$$\begin{aligned} \langle \tilde{E}_1^2 e^{i\varphi} \rangle_t &= \tilde{E}_1^2 \langle e^{i\varphi} \rangle_t \\ \Rightarrow \mathcal{C} &= \left| \frac{\tilde{E}_1^2 \langle e^{i\varphi} \rangle_t}{\tilde{E}_1^2} \right| = |\langle e^{i\varphi} \rangle_t| = |\langle \cos \varphi \rangle_t + i \langle \sin \varphi \rangle_t| \end{aligned}$$

Assuming a symmetric distribution $\varphi(t)$, it follows that $\langle \sin \varphi \rangle_t = 0$ and

$$\mathcal{C} = \langle \cos \varphi \rangle_t = \mathcal{V} \quad (3.38)$$

The visibility is equal to the coherence between the two slits. Note that this visibility is the same for all fringes, it is an overall property of the diffraction pattern. This is not the case in the near field, as will be discussed in section 3.6.

Equation (3.38) has been derived for the special case of a double slit slit with infinite length and negligible width and for an incident wave with perfect longitudinal coherence in the far field diffraction regime. However, a similar relationship holds in the practical case where these assumptions are only partially valid, as can be seen from the numerical simulations in section 3.7.

3.6. Near field diffraction

3.6.1. Circular aperture

For a circular aperture, a qualitative description of the near-field diffraction can be obtained by dividing the aperture into concentric rings, corresponding to path length differences of half a wavelength between source and observer. These *Fresnel zones*, illustrated in figure 3.6, contribute to the total field. The contributions of adjacent zones cancel because of their opposite phase. The area of all Fresnel zones is the same. Nonetheless, the cancellation is not complete, because the inclination factor $K(\vartheta) = \frac{1}{2}(1 + \cos \vartheta)$ is smaller for the outer zones. As the observation point is moved in transverse direction, the Fresnel zones shift across the aperture. Thus, relative maxima and minima can be observed. The total number of extrema is equal to the number of Fresnel zones, given by [Hec94]

$$N_F = \frac{r^2}{\lambda} \left(\frac{1}{D} + \frac{1}{L} \right) \quad (3.39)$$

where r is the radius of the aperture, λ the wavelength of the radiation, D the distance between source and aperture and L the distance between aperture and screen. As the problem has cylindrical symmetry, concentric fringes form on the observation plane. The outermost fringe lies near the edge of the geometric shadow of the aperture.

3.6.2. Double slit

Assume two slits of infinite length and of width w , separated by a distance d . Coherent light of wavelength λ passes the slits and forms a diffraction pattern on a screen at a distance L .

Already in the far field (section 3.5), the simple formula (3.28) may be improved by taking into account that each of the slits by itself forms a single slit diffraction pattern. Since the width w of the slits is smaller than their separation d , this pattern is broader than the double slit fringes, and the amplitude of the double slit diffraction pattern is modulated by the sum of the two single slit patterns:

$$I(x) = \mathcal{S}(x) \left[1 + \mathcal{V} \cos \left(\frac{2\pi d}{\lambda L} x \right) \right] \quad (3.40)$$

where the amplitude is

$$\mathcal{S}(x) = I_1(x) + I_2(x) \quad (3.41)$$

In the far field, the two slits form identical diffraction patterns:

$$I_1(x) = I_2(x) = \left(\frac{\sin(\pi wx/(\lambda L))}{\pi wx/(\lambda L)} \right)^2 \quad (3.42)$$

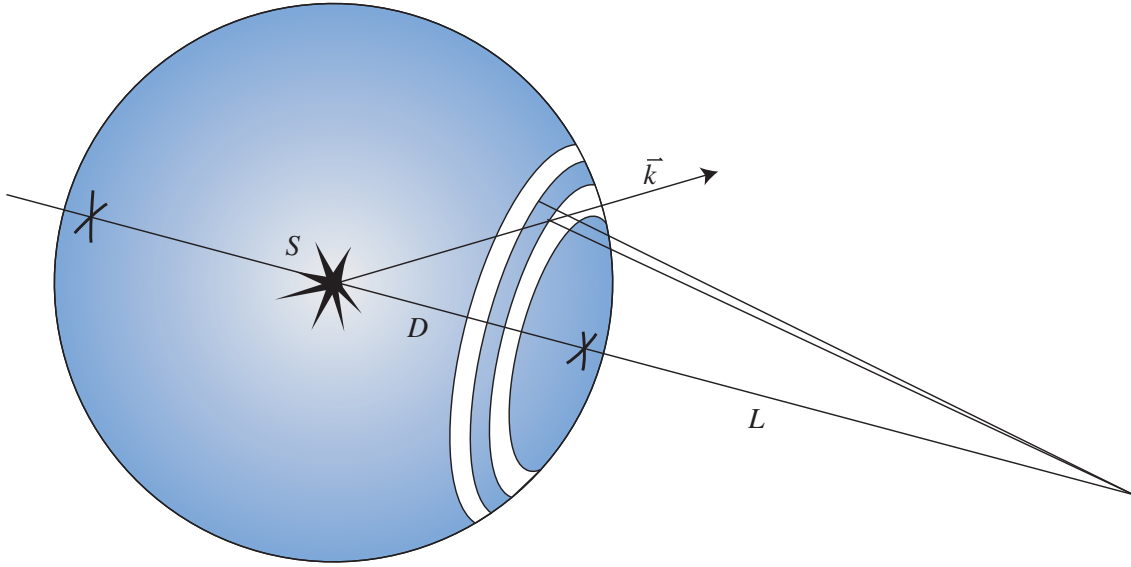


Figure 3.6.: Fresnel zones are useful to describe the diffraction on a circular aperture [Hec94]. The distance between the source S and the aperture is denoted by D , the distance from aperture to observation plane by L . The wave propagates in the direction \vec{k} .

In the case of a coherent incoming wave, the visibility is $\mathcal{V} = 1$.

In the near field, one has to take into account that the single slit diffraction patterns of the two slits are displaced by the slit separation. The two curves have minima at different positions. At these minima, only one slit is visible, and the visibility of the double slit diffraction pattern vanishes at these positions. Thus, also the visibility of the double slit interference fringes is modulated across the diffraction pattern, $\mathcal{V} = \mathcal{V}(x)$.

The double slit diffraction pattern of a plane wave, i.e. a perfectly coherent wave is now described in the near field, i.e. for $L \approx \pi d^2/\lambda$. It is assumed that the width of the slits is much smaller than their separation, such that their single slit diffraction patterns can be described by the far field approximation, $L \gg \pi w^2/\lambda$. The electric field amplitudes of the two slits are then given by

$$\tilde{E}_1(x) = \frac{\sin\left(\frac{\pi w(x+d/2)}{\lambda L}\right)}{\frac{\pi w(x+d/2)}{\lambda L}}, \quad \tilde{E}_2(x) = \frac{\sin\left(\frac{\pi w(x-d/2)}{\lambda L}\right)}{\frac{\pi w(x-d/2)}{\lambda L}} \quad (3.43)$$

It is important to note that $\tilde{E}_1(x)$ and $\tilde{E}_2(x)$ are real quantities, even when the integration is done over a complex field amplitude. In other words, the respective phase difference between the two waves is either zero or π . The field amplitudes are positive in the respective centre, i.e. at a position $-d/2$ and $d/2$, respectively,

and oscillate between negative and positive values in the outer part of the diffraction pattern, as can be seen in figure 3.7a.

The intensities $I_1(x)$ and $I_2(x)$ are the absolute square of the electric field amplitudes:

$$I_1(x) = |\tilde{E}_1(x)|^2, \quad I_2(x) = |\tilde{E}_2(x)|^2 \quad (3.44)$$

The amplitude of the double slit diffraction pattern is modulated by their sum (shown in figure 3.7b):

$$\mathcal{S}(x) = I_1(x) + I_2(x) \quad (3.45)$$

The visibility of the the double slit diffraction pattern is determined by the relative intensities that are contributed by the two single slit diffraction patterns, it is a function of the coordinate x . The total electric field at a point x is the sum of the two contributions. The extrema of the intensity are

$$I_{\text{ex1}}(x) = (\tilde{E}_1(x) + \tilde{E}_2(x))^2 \quad \text{and} \quad I_{\text{ex2}}(x) = (\tilde{E}_1(x) - \tilde{E}_2(x))^2 \quad (3.46)$$

In the middle of the double slit diffraction pattern, there is no phase difference between the contributions from the two slits and $\tilde{E}_1(x)$ and $\tilde{E}_2(x)$ have the same sign. The intensity $I_{\text{ex1}}(x)$ is a maximum and $I_{\text{ex2}}(x)$ is a minimum. In the outer parts, there may be a relative phase difference, leading to a maximum in $I_{\text{ex2}}(x)$ and to a minimum in $I_{\text{ex1}}(x)$.

This is the difference to the far field case, where the single slit diffraction patterns from the two slits are taken to coincide and the electric fields from the two slits have always the same sign. In the near field, the visibility of the double slit diffraction fringes is

$$\mathcal{V}(x) = \frac{I_{\text{ex1}}(x) - I_{\text{ex2}}(x)}{I_{\text{ex1}}(x) + I_{\text{ex2}}(x)} \quad (3.47)$$

The visibility is shown in figure 3.7c. A negative visibility occurs when $\tilde{E}_1(x)$ and $\tilde{E}_2(x)$ have opposite sign. In this case, maxima and minima are interchanged, which is equivalent to a phase shift of π .

The double slit diffraction pattern is given by:

$$I(x) = \mathcal{S}(x) \left[1 + \mathcal{V}(x) \cos \left(\frac{2\pi d}{\lambda L} x \right) \right] \quad (3.48)$$

The visibility is plotted for a slit separation of $d = 2 \text{ mm}$, a slit width of $w = 100 \text{ }\mu\text{m}$ and a distance to the screen of $L = 3.1 \text{ m}$ in figure 3.7

3.6.3. Simulation by ray tracing

To obtain a quantitative description of an arbitrarily shaped aperture, the near field diffraction pattern has to be computed numerically. This has been done by propagation of the wave front of the electromagnetic field with the code GLAD [App01b],

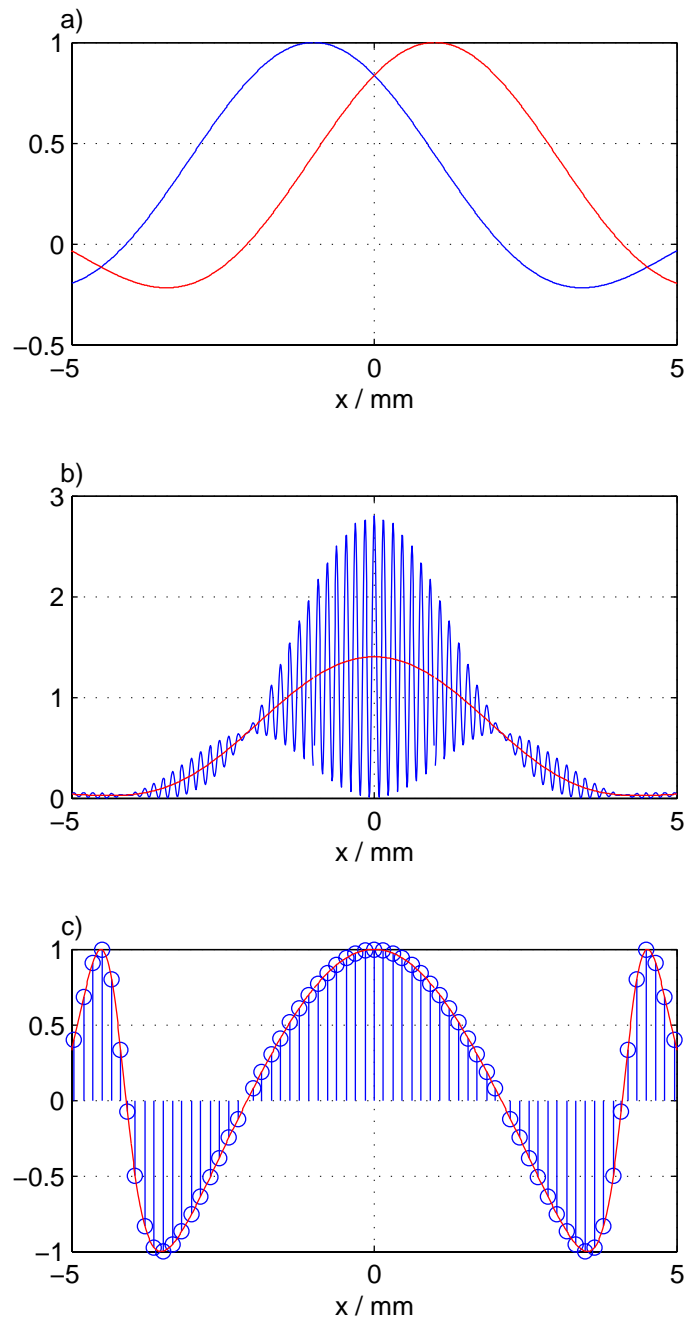


Figure 3.7.: Formation of a double slit diffraction pattern in the near field. a) electric field amplitude of the left slit only (red) and the right slit only (blue), b) amplitude modulation (red) and double slit diffraction pattern (blue) c) visibility of the double slit interference fringes, as a function of x (red line) and at the position of the maxima (blue circles).

described in section 3.6.4. To verify the results, the case of the circular aperture was also simulated by ray tracing from the source to the observation plane. This is described in this section.

The field amplitude at a given point on the detector plane can be calculated by summing the amplitudes of all spherical waves originating at the points inside the aperture; in other words, by tracing the rays from all points in the source to all points in the destination. One evaluates Eq. (3.22) numerically by subdividing the aperture into sufficiently fine segments, such that the path difference from neighbouring segments to the detector is much smaller than the wavelength (see also figure 3.8):

$$\Delta g = s \sin \alpha = \frac{s\rho}{L} \ll \lambda \quad (3.49)$$

Choosing $\Delta g < \lambda/100$ and a distance of 3.1 m to the observation plane, the sampling width has to be $s < 0.3 \mu\text{m}$. An aperture of 3 mm has to be sampled at 10^8 points.

Often, one can make use of the symmetry by combining all rays that travel the same distance. For a point (x_1, y_1, L) on the observation plane, these lie on a circle that is centered around the point $(x_1, y_1, 0)$ on the aperture. One can decompose the area in the aperture into thin circular rings of width s and radius ρ . If a ring lies completely inside the aperture, it is straightforward to add the electric field with the respective phase. Some of the circles intersect the rim of the aperture, these contribute only partially to the total wave. The number of terms that have to be added to obtain the total electric field is significantly reduced to about 10^4 .

It has to be noted that this simplification cannot be applied when the intensity or the phase are not constant across the aperture, i.e. when the incoming wave is not plane. In the next section, a more efficient algorithm that propagates the complete wave front is presented. The results for the plane wave at the circular aperture are the same (see for example figure 3.11).

3.6.4. Simulation by wave front propagation

An algorithm, based on the propagation of wave fronts is implemented in the code GLAD (General Laser Analysis and Design, [App01b]). The code solves Maxwell's equations numerically for a wave front that propagates in z direction, applying simplifications that greatly speed up the calculations.

To derive the differential equations, one starts with *Maxwell's* Equations:

$$\vec{\nabla} \times \vec{E} = -\frac{d\vec{B}}{dt} \quad (3.50a)$$

$$\vec{\nabla} \times \vec{H} = \vec{j} + \frac{d\vec{D}}{dt} \quad (3.50b)$$

A non-conducting medium with linear magnetisation and current density is as-

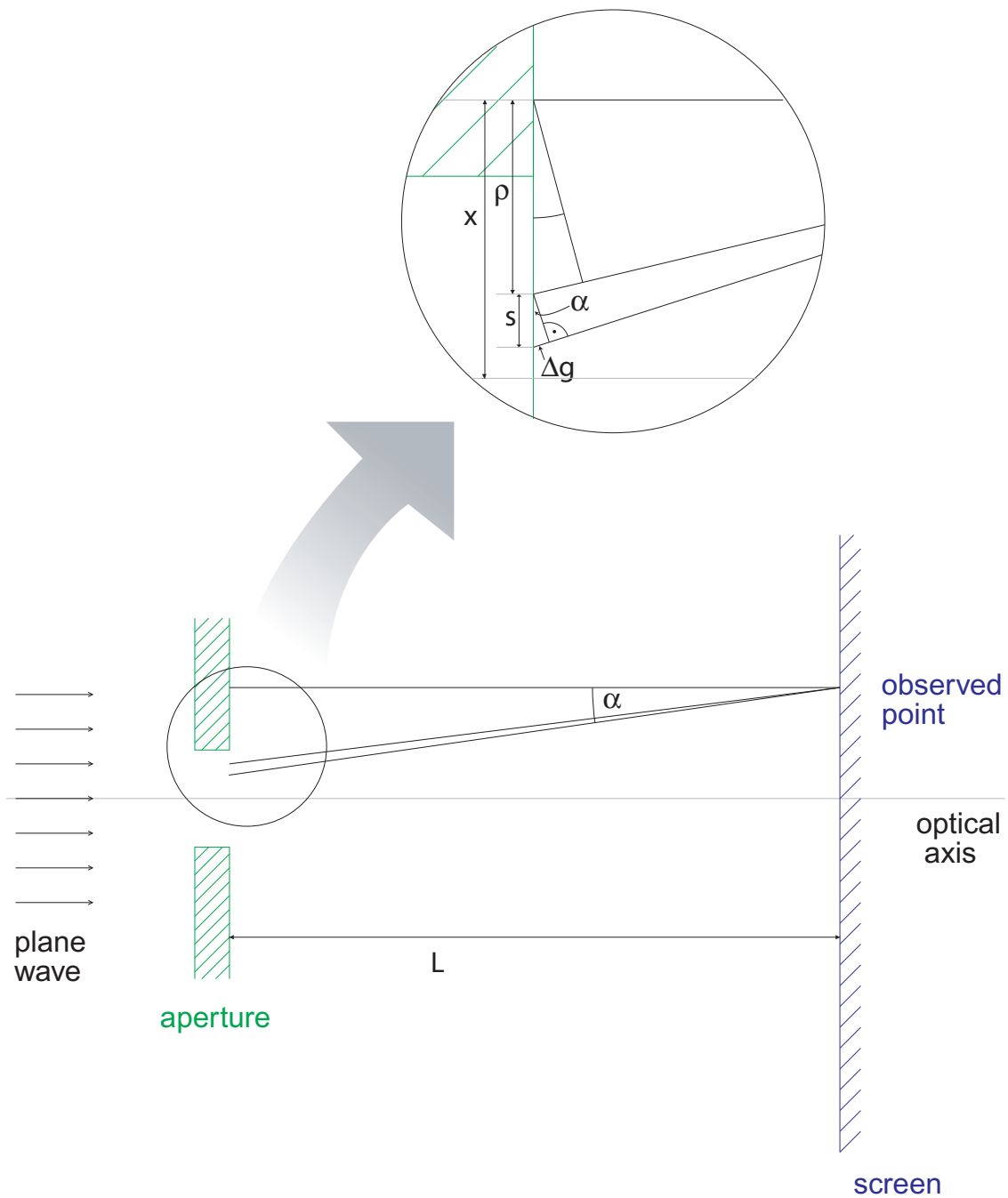


Figure 3.8.: Simulation by ray tracing. A plane wave enters a circular aperture from the left. The screen is located a distance L to the right. To calculate the intensity on the screen, at a distance x from the centre of the aperture, the contributions from circles with radius ρ around this point are added.

3. Coherence and Interference

sumed:

$$\vec{B} = \mu_0 \mu_r \vec{H} \quad (3.51a)$$

and a polarisation of the form

$$\vec{D} = \varepsilon_0 \vec{E} + \vec{P} = \varepsilon_0 \vec{E} + \varepsilon_0 \chi \vec{E} \quad (3.51b)$$

Taking the time derivative of Eq. (3.50b) and substituting in the curl of Eq. (3.50a), one obtains

$$\vec{\nabla} \times \vec{\nabla} \times \vec{E} = -\mu_0 \mu_r \varepsilon_0 \frac{\partial^2 \vec{E}}{\partial t^2} - \mu_0 \mu_r \frac{\partial^2 \vec{P}}{\partial t^2} \quad (3.52)$$

Which can be simplified under the assumption $\vec{\nabla} \cdot \vec{D} \approx 0$ and $\vec{\nabla} \cdot \vec{P} \approx 0$ and assuming a non-conducting material ($\sigma = 0$) to

$$\vec{\nabla}^2 \vec{E} = \mu_0 \mu_r \varepsilon_0 \frac{\partial^2 \vec{E}}{\partial t^2} + \mu_0 \mu_r \frac{\partial^2 \vec{P}}{\partial t^2} \quad (3.53)$$

Again, the slowly varying amplitude (SVA) approximation is used, this time with a complex amplitude that may also depend on the transverse coordinates:

$$E_x(x, y, z, t) = \text{Re} \left(\tilde{E}_x(x, y, z, t) e^{ik(z-ct)} \right) \quad (3.54)$$

Here, k is z component of the wave vector. The wave front of the beam at a given position z and at time t is represented by a complex function $\tilde{E}_x(x, y; z, t)$.

The following equation for a wave travelling in z direction can be deduced [App01a]:

$$\frac{\partial \vec{E}}{\partial z} = -i \frac{1}{2k} \nabla^2 \vec{E} - i \frac{\vec{k} \chi}{2n^2} \cdot \vec{E} \quad (3.55)$$

where χ is the linear electric susceptibility and $n = \sqrt{(1 + \chi) \mu_r}$ the index of refraction in the medium.

In numerical calculations, only discrete points in space and time may be represented. We sample the field amplitude \tilde{E} on an $M \times N$ grid on the rectangle of size $X \times Y$, centered on the optical axis. The sampling points are separated by $\Delta x = X/M$ and $\Delta y = Y/N$, respectively. In our case, a square region of $(20.48 \text{ mm})^2$ is divided into $2048 \cdot 2048$ points. Note that the sampling of the field amplitude at a given point (x, y) is not exactly the same as the averaged field amplitude over a small rectangle $\Delta x \times \Delta y$ around this point, which for example is done by a CCD detector. If however the sampling interval is much smaller than the distance where \tilde{E} changes significantly, the distinction can be neglected.

To solve the differential equation (3.55), it is useful to perform the calculations in the Fourier domain, taking advantage of the simpler representation of harmonic waves. The two-dimensional Fourier transform of the field amplitude is denoted by $\mathcal{E}(f_x, f_y)$, the spatial frequencies are f_x and f_y .

To do numerical calculations in Fourier space, one needs a discrete frequency distribution. It is most efficient to use the Fast Fourier Transform (FFT) algorithm, which requires that N and M are powers of two. The same number of sampling points in the Fourier domain will be used, and the frequency range is:

$$\frac{1}{2\Delta x} \leq f_x \leq \frac{1}{2\Delta x} \left(1 - \frac{2}{M}\right); \quad \frac{1}{2\Delta y} \leq f_y \leq \frac{1}{2\Delta y} \left(1 - \frac{2}{N}\right) \quad (3.56)$$

The upper limit of the frequency range is called the *Nyquist frequency*.

To propagate the electric field amplitude along z according to Eq. (3.55), one separates the two terms on the right hand side, advancing the first term with an implicit finite difference approximation and the second one by means of the FFT [HT73]. The two algorithms are iterated using small steps Δz up to the observation plane. This algorithm is implemented in the code GLAD [App01b].

The proper choice of sampling interval $\Delta x \times \Delta y$ and region $[-X/2, X/2] \times [-Y/2, Y/2]$ is essential to avoid numerical errors. If the separation of the sampled points is too large, maxima of the amplitude falling in between the sampling points are underestimated. Similarly, minima are overestimated.

The representation of the transverse field distribution by its Fourier transform implies periodic boundary conditions, whereas the actual distribution is not periodic and drops to zero for x or $y \rightarrow \pm\infty$. As a result, any propagated beam which leaves the simulated range is folded back and interferes then with the other rays (figure 3.9). If the sampling region is too small (and the resolution is high enough), the interference with the mirror source is visible (see for example figure 3.10e and f). To avoid this effect, the matrix has to be large enough that the field remains concentrated in the central part of the matrix.

The simulation has converged when the results do not change if the density of sampling points is increased and the field size is enlarged simultaneously. This has been verified for the present experimental set-up. The results are shown in figure 3.10. In the present experiment, the simulation is most difficult for a double slit with large separation, since here the diffraction fringes show the finest detail. Furthermore, the total extension of the diffraction pattern is larger than for the other slit pairs. The computer used for the simulations has a memory of 384 MB. The largest array that can be propagated has a dimension of $8192 \cdot 8192 = 67108864$ points. The simulation using this array for a field of $4.096 \cdot 4.096 \text{ mm}^2$ with a pixel size of $5 \mu\text{m}$ looks smooth, i.e. the computed intensity does not vary significantly from one pixel to the next. It has been used as a reference (blue curves in figure 3.10).

In a simulation with $512 \cdot 512 = 262144$ pixels with $20 \mu\text{m}$ edge length (red crosses in figure 3.10a, b), the grid is too coarse to sample the field in the minima correctly, it is therefore not sufficient for the slit distance of 3 mm. The situation is somewhat more relaxed for 1 mm slit separation. Decreasing the distance between the pixels and increasing the simulated area simultaneously improves the simulation (figure 3.10c and d): also the slits with 3 mm separation are accurately modelled.

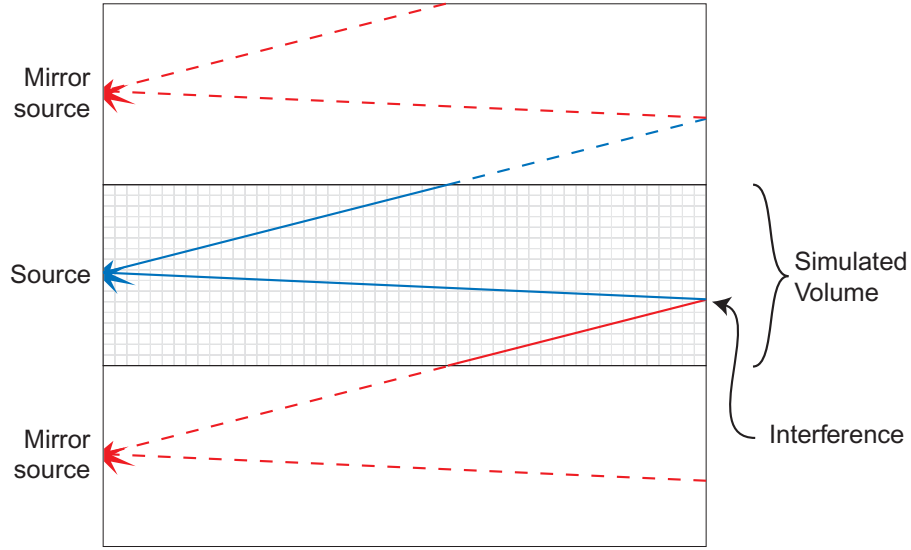


Figure 3.9.: Periodic boundary conditions, as imposed by the numerical solution of the wave equation in frequency space, imply the interference of radiation with mirror sources.

One can see that misleading results are produced if the resolution is increased without simultaneously enlarging the field size: in figure 3.10e and f, artefacts from interfering mirror sources appear. To double the resolution in both directions, one has to double also the field size, resulting in 16 times as many points to be computed.

3.6.5. Results

The computed diffraction pattern of a circular aperture is shown in figure 3.11. The two different codes, based on ray tracing and on wave front propagation are in excellent agreement. For the selected wavelength of 100 nm, the aperture diameter of 3 mm and the distance to the observation plane $L = 3.1$ m, the far field condition Eq. (3.23) is not fulfilled. As anticipated, the diffraction pattern calculated in the Fraunhofer approximation is completely different, it contains only the central peak.

A double slit with 1 mm separation yields the diffraction pattern shown in figure 3.12. The differences between the numerical simulation in the near field and the analytic far field approximation manifest themselves not only in the vertical coordinate, also the horizontal dependency is different. In the far field case, the minima have zero intensity, yielding a visibility $\mathcal{V} = 1$ for all fringes. This is no longer the case in the near field, here the cancellation of the electric field due to destructive interference is not perfect. Only the minima near the centre have $I_{\min} \approx 0$ and $\mathcal{V} \approx 1$. For the outer fringes, the visibility is reduced, as compared to the far field case. This is due to an incomplete cancellation of the contributions from the two slits.

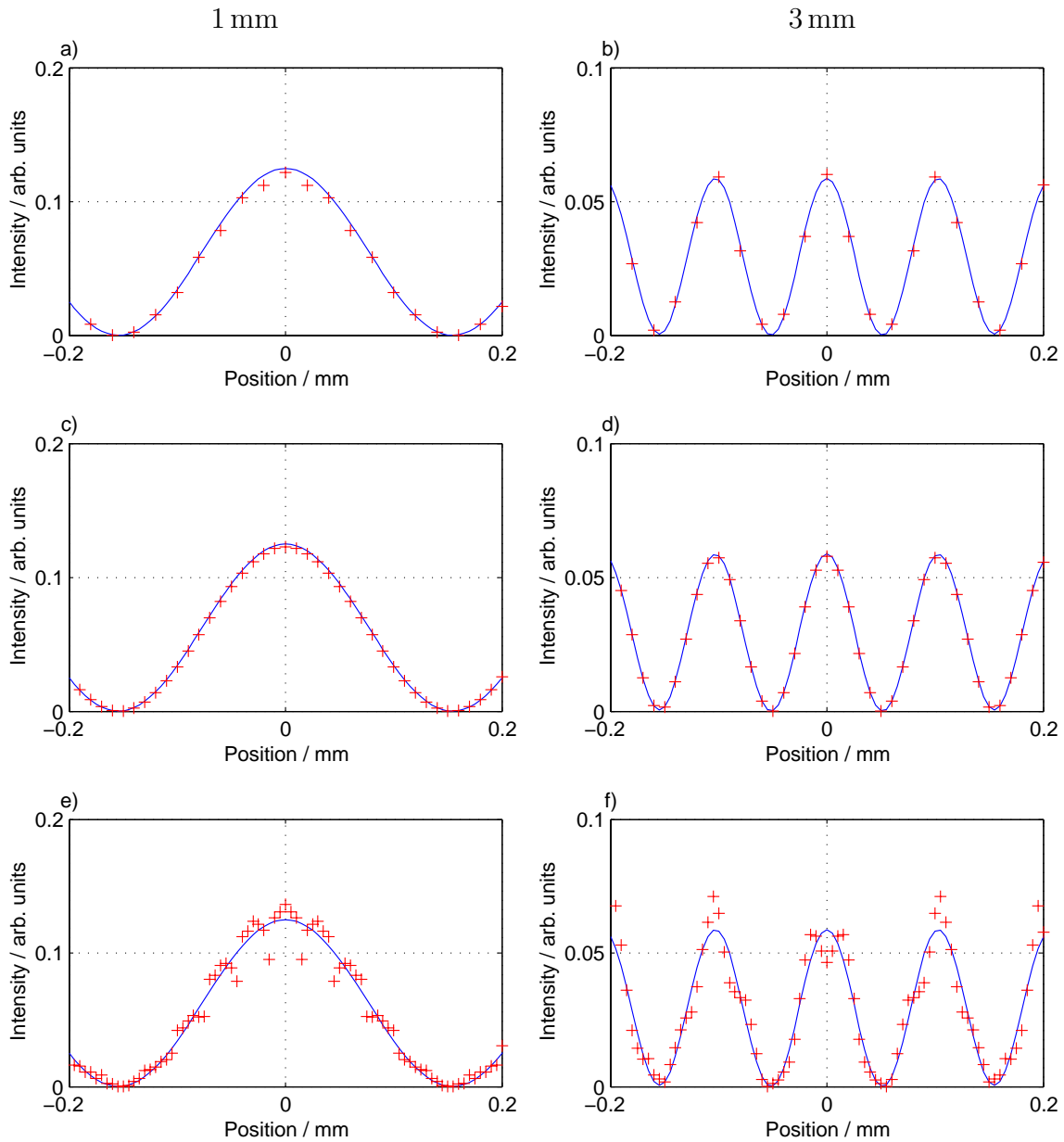


Figure 3.10.: Central fringes of double slit diffraction patterns, with various simulation parameters, a), c) and e) for 1 mm, b), d) and f) for 3 mm slit separation. The blue line represents the intensity on a grid with $8192 \cdot 8192 = 67108864$ pixels with $5 \mu\text{m}$ edge length and is used as a reference. The simulations indicated by red crosses use the following parameters: a) and b) $512 \cdot 512 = 262144$ pixels with $20 \mu\text{m}$ edge length, c) and d) $2048 \cdot 2048 = 4194304$ pixels with $10 \mu\text{m}$ edge length, e) and f) $2048 \cdot 2048$ pixels with $5 \mu\text{m}$ edge length.

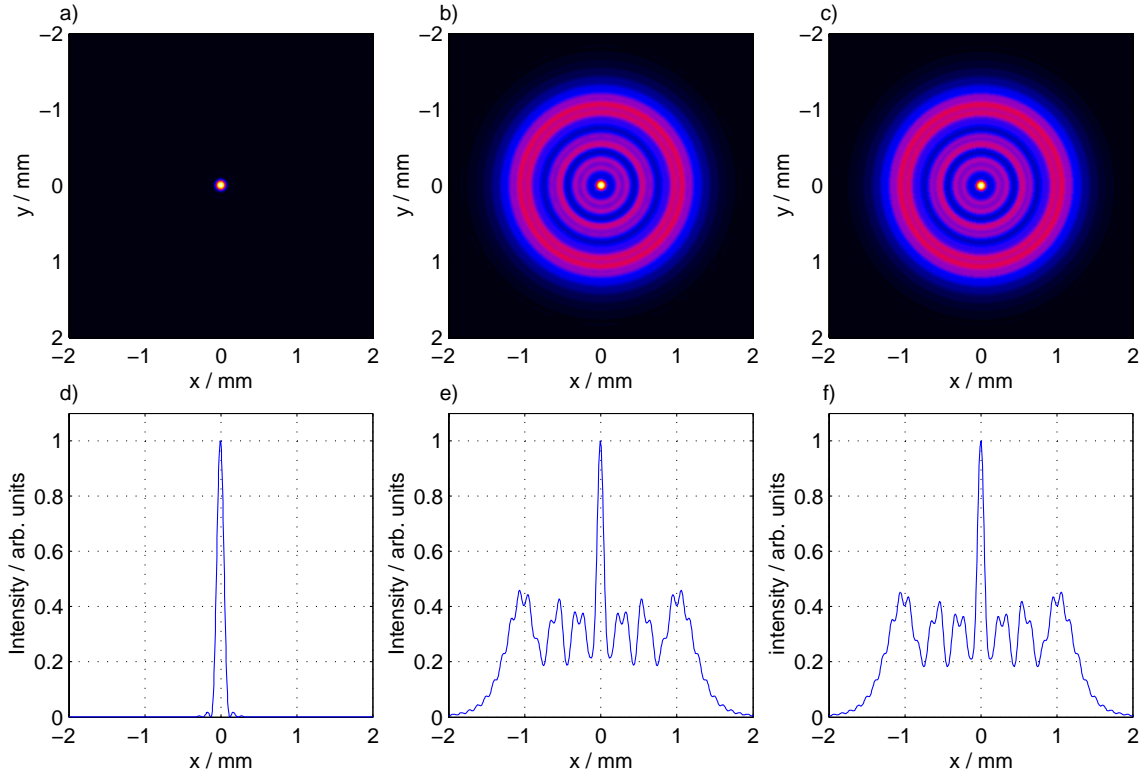


Figure 3.11.: Comparison of different computation methods for the diffraction pattern of a circular aperture of 3 mm diameter, illuminated by a plane wave with $\lambda = 100$ nm. a) Far field approximation, b) propagation algorithm (GLAD), c) ray tracing, for a distance of 3.1 m. d. . . f) Central slices of the above distributions.

An interesting diffraction pattern is produced by crossed slits (figure 3.13). Again, the far field approximation yields different results than the numeric calculation in the near field, where the pattern is dominated by hyperbolic fringes.

3.7. Diffraction with partially coherent light

More realistic than a plane incoming wave is a Gaussian beam, whose intensity depends on the transverse coordinates as $\exp(-x^2/\sigma_x^2 - y^2/\sigma_y^2)$. A Gaussian of full coherence is characterised by a time independent field amplitude for each point in space, thus $|\tilde{\gamma}(\vec{r}, \vec{r}')| = 1$ for all \vec{r}, \vec{r}' . A partially coherent beam, on the other hand, has distorted wave fronts, which can be simulated by multiplying $\tilde{E}(x, y)$ with a phase aberration $\exp(ih(x, y))$. If this distortion varies with time, the coherence acquires values $\mathcal{C}(\vec{r}, \vec{r}') < 1$ for $\vec{r} \neq \vec{r}'$. To take into account this variation, a finite photon bunch has to be simulated on a three-dimensional grid.

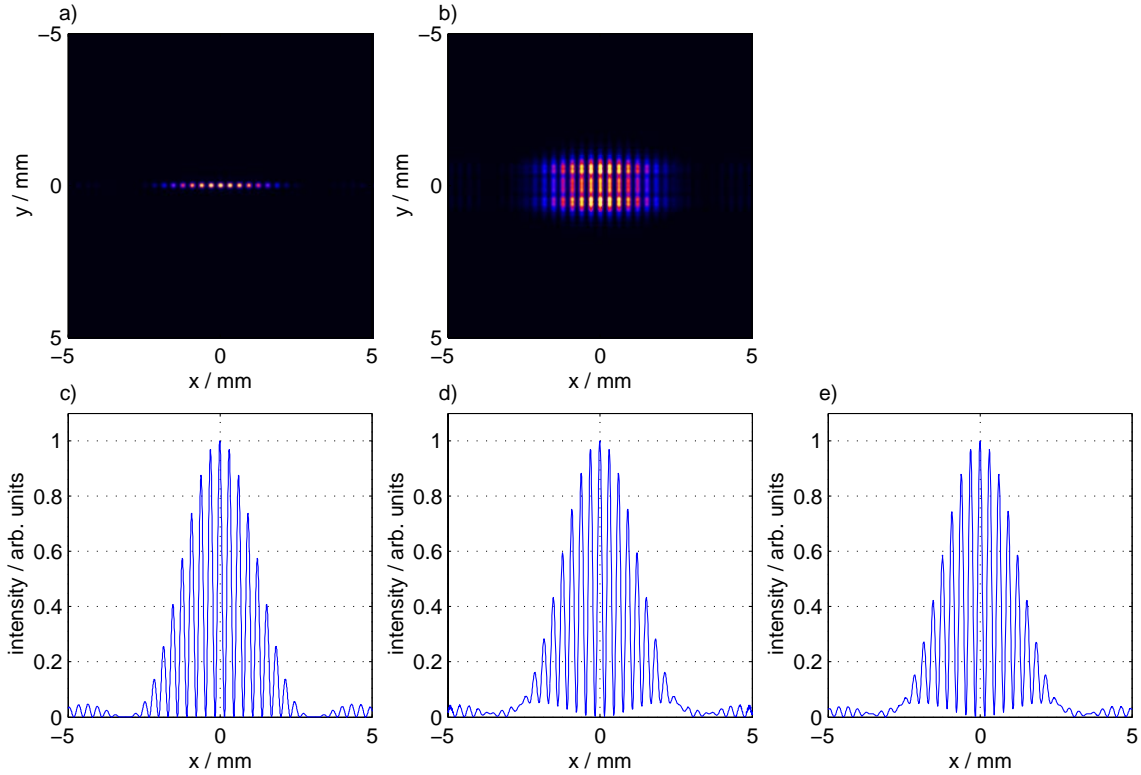


Figure 3.12.: Double slit diffraction pattern: a) diffraction pattern in far field approximation and b) in near field simulation. c), d) Cross sections of the above distributions. e) Cross section calculated using Eq. (3.48).

For the present simulation, 100 grid points in z direction are considered. A random phase aberration $h(x, y)$ with a Gaussian spatial frequency spectrum was calculated with the code GLAD.

The propagation of such a beam through the double slits and the formation of the near field diffraction pattern can be computed with the code GLAD. However, the total number of grid points in GLAD is limited and a beam given on $100 \times 512 \times 512$ points cannot be propagated. A reduction of the number of points in the transverse plane would result in too coarse a grid to sample the diffraction fringes. Therefore, each slice of the beam is propagated separately and the intensities of the resulting diffraction patterns are added.

This is obviously a simplification to the general case, where the formation of diffraction patterns involves the interference of different wave fronts, which were initially separated longitudinally. In the middle of the interference pattern, the path length difference to the two slits is zero and the two field amplitudes are given by the wave front in the same slice. For the outer fringes however, different wave fronts interfere,

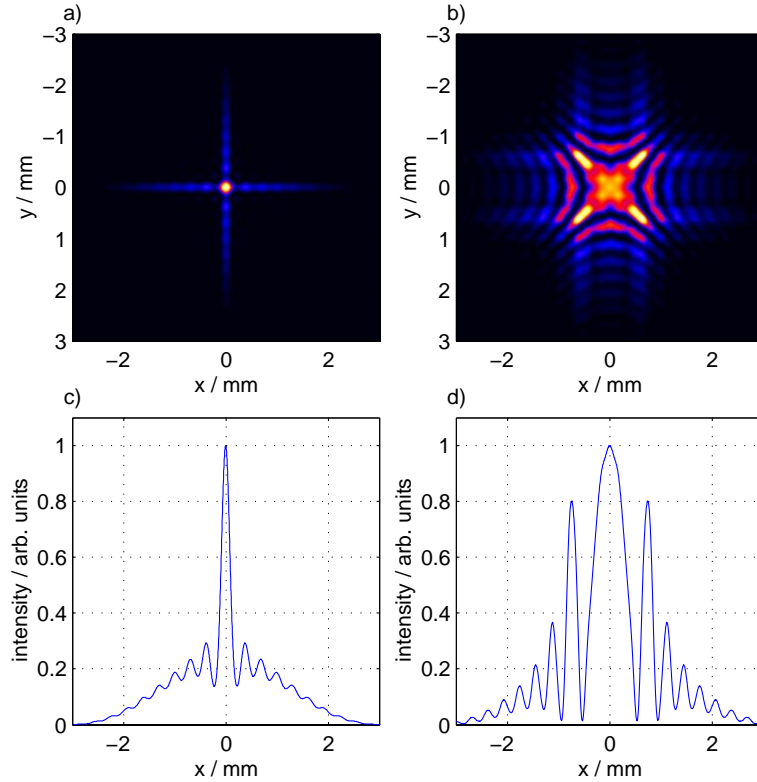


Figure 3.13.: Diffraction pattern of crossed slits, a) calculated in the far field approximation and b) in near field simulation. c and d) Cross sections of the above distributions.

the ordinal number of the fringe is equal to the path length difference in units of the wavelength. In the present case, a grid spacing of $1 \mu\text{m} = 10\lambda$ in z direction has been used. Therefore, the amplitude of the tenth interference fringe would have to be calculated from the intensities from two different slices of the FEL beam. In using the same slice, a longitudinal variation of the phase or amplitude of the electric field is neglected. In a quasi-monochromatic beam such as the FEL, the longitudinal coherence length is much larger than ten wavelengths and the simplification is justified.

The transverse correlation function of the wave packet is calculated with respect to the centre of the beam, performing the time average in Eq. (3.7) over the 100 slices. The absolute value of $\tilde{\gamma}(x, y)$ is shown in figure 3.14a. It is mapped to radial coordinates (r, φ) and averaged over the angle φ . The resulting function is shown in figure 3.14b.

Different coherence functions can be achieved by varying the magnitude of the phase aberration function $h(x, y)$. The result for four different magnitudes is shown in figure 3.15. At a separation of 1 mm, a coherence function of 1.00, 0.86, 0.55 and 0.05

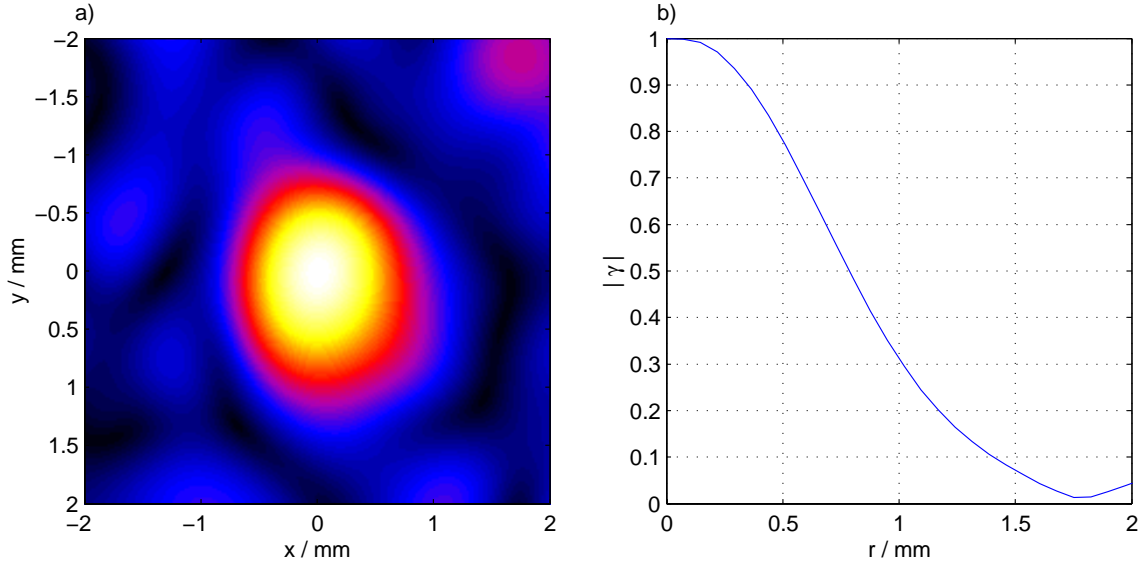


Figure 3.14.: Absolute value of the correlation function of the simulated wave packet, calculated with respect to the centre of the beam. a) Plotted as a function of x and y and b) as a function of r .

is computed from Eq. (3.8). In the last case, a very small phase aberration leads to a practically coherent wave. There is a certain uncertainty of the coherence function, due to the randomised phase aberration function. Different starting parameters for the random number generator that is used for the phase aberration function lead to coherence functions that differ by about 0.05. This can account for the fact that the coherence function is not always monotonous, as for example in figure 3.15a.

From the diffraction patterns, the visibility \mathcal{V} of the interference fringes, defined in Eq. (3.30), can be calculated. The visibility of the central fringe is compared to the absolute value of the correlation function \mathcal{C} at a distance equal to the slit separation. For the far field diffraction pattern of a plane wave, $\mathcal{V} = \mathcal{C}$, as given by Eq. (3.38). For the four diffraction patterns shown in figure 3.15, values $\mathcal{V}_{\text{central}} =$ The present simulation shows that this is also the case for the near field diffraction of a Gaussian beam, as can be seen in figure 3.16.

The simulation can be improved by taking into account the formation of the FEL radiation and the influence of the measurement devices on the recorded images. The FEL radiation has been simulated by Saldin, Schneidmiller and Yurkov [Yur03] using the code FAST. The measurement devices are discussed in chapter 6. This simulation is described in section 7.2.

3. Coherence and Interference

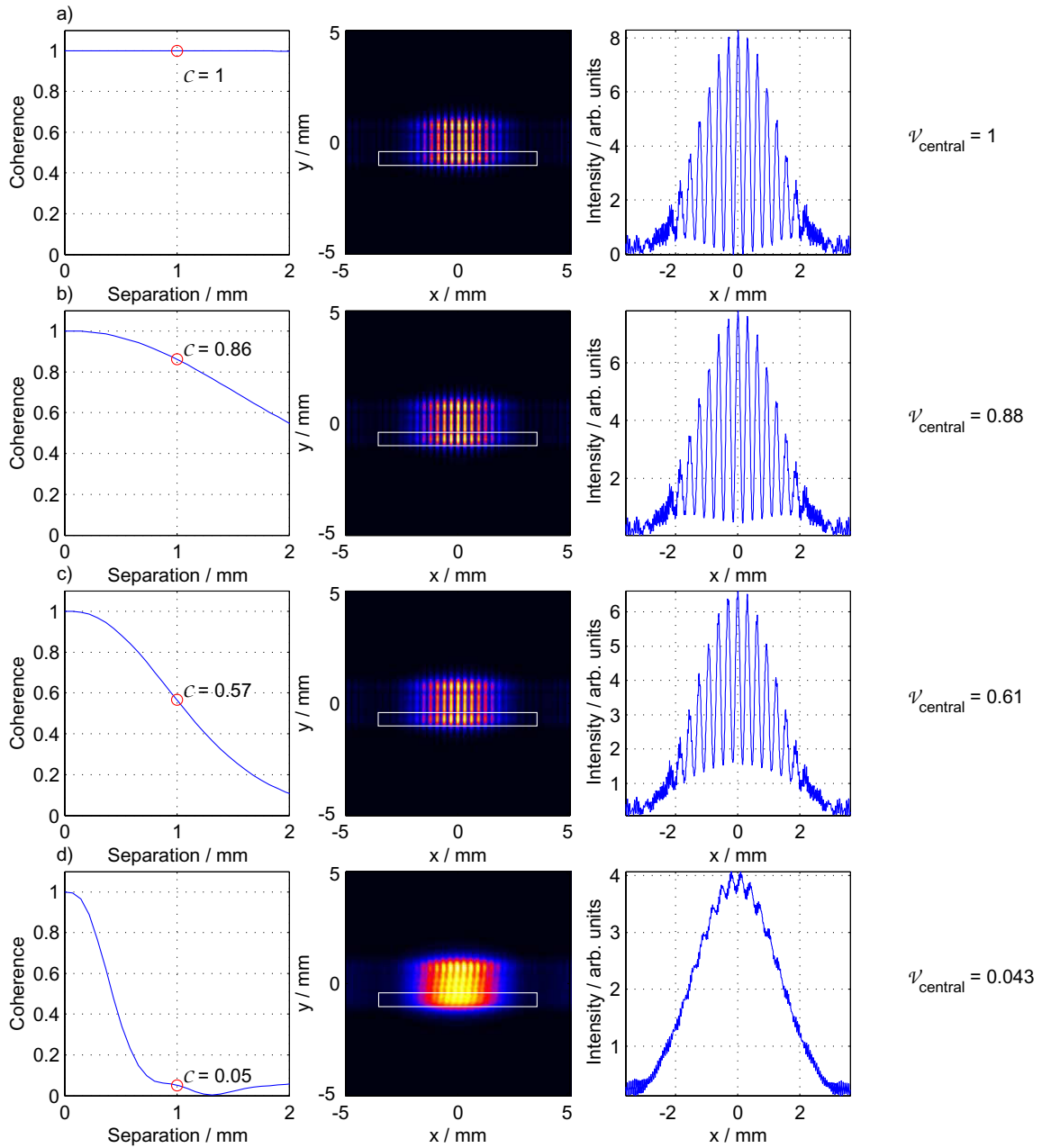


Figure 3.15.: Simulated double slit diffraction patterns of a distorted Gaussian beam. Left column: Absolute value of the correlation function as a function of distance. The value for 1 mm separation is marked by a red circle. Middle column: Diffraction pattern of vertical double slits of 2 mm length and $100 \mu\text{m}$ width, separated by 1 mm. Right column: projection of the selected area of the diffraction pattern. The wave front distortion results in a transverse coherence of See also figure 3.16b.

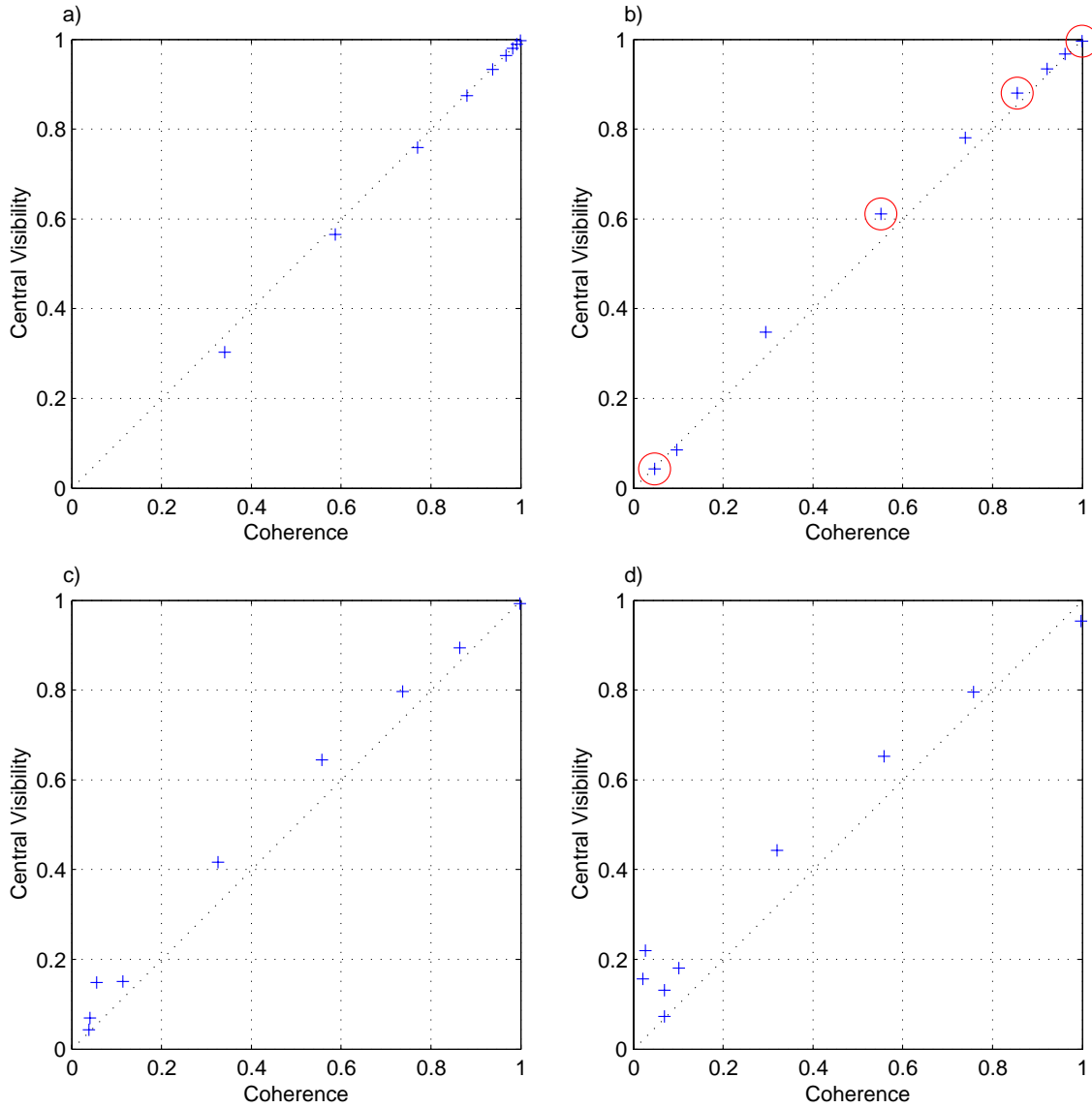
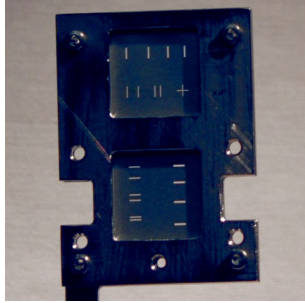


Figure 3.16.: Simulation of the visibility of the central fringes as a function of the coherence. The transverse correlation function was evaluated at a distance equal to the slit separation of a) 0.5 mm, b) 1 mm, c) 2 mm and d) 3 mm. The circled points in b represent the cases shown in figure 3.15.

The present simulation shows that the central visibility of the near field diffraction pattern is in good agreement with the transverse coherence at the slit distance.

3. *Coherence and Interference*



Part III.

Experimental Set-up

The Fly

Little Fly

Thy summer's play,
My thoughtless hand
Has brush'd away.

Am not I
A fly like thee?
Or art not thou
A man like me?

For I dance
And drink & sing:
Till some blind hand
Shall brush my wing.

If thought is life
And strength & breath:
And the want
Of thought is death;

Then am I
A happy fly,
If I live,
Or if I die.

William Blake

Figure on the previous page: the double slits.

4. The TTF Accelerator and SASE-FEL

The measurements presented in this thesis have been performed at the linear accelerator (linac) of the TESLA Test Facility (TTF) at DESY. Before this accelerator is described in detail, general concepts in electron acceleration are briefly reviewed.

4.1. General concepts in particle acceleration

4.1.1. Acceleration with radio-frequency cavities

Charged particles are accelerated by electric fields. Alternating fields can be stored in resonant cavities, either made from a good conductor like copper or from a superconductor, for example niobium. For reasonable dimensions of the cavity, the frequency of the field ranges from about 100 MHz to 10 GHz. This range is referred to as radio frequency (RF). The energy gain of the particles is the product of their charge with the path integral of the longitudinal electric component of the field. The accelerating field of the resonator is defined as the energy gain per unit charge, divided by the length of the structure.

A superconducting material has vanishing resistance for direct currents if it is cooled below its critical temperature, which is a function of the applied magnetic field. The critical temperature of elementary superconductors is typically a few Kelvin, hence liquid helium is needed as a coolant. Although there is a resistance R_{BCS} for alternating currents, the losses are many orders of magnitude lower than for normal-conducting materials. Resonant cavities manufactured from superconducting material therefore allow the construction of energy efficient accelerators, even when taking into account the energy needed for cryogenics. The ratio of frequency to bandwidth of a resonator without external coupling is called unloaded quality factor Q_0 . The losses are inversely proportional to the quality factor. Superconducting cavities can reach a value of $Q_0 \approx 10^{10}$, in normal-conducting resonators, Q_0 is typically a few times 10^4 .

To reduce the effects of wake fields, superconducting accelerators use generally cavities with a larger aperture than their normal-conducting counterparts. This results in a lower resonant frequency, typically around 1 GHz. The frequency is chosen to optimise production and operation costs: a higher frequency allows to reduce

the production cost, as less material is required. However, electric losses scale with $R_{BCS} \propto \omega^2$ [Sch03a], limiting the use of superconducting cavities to frequencies below 3 GHz. These losses are due to the oscillation of electrons that are not bound in Cooper pairs. As the number of free electrons drops exponentially with the temperature, the quality factor of the cavity resonator can be increased by cooling the cavity far below the critical temperature.

The RF power is supplied by an external source, for example a klystron. The wave is transmitted through a wave guide and coupled to the resonating cavity. In storage rings as well as linear accelerators made from superconducting cavities, one creates a standing wave in the resonators, while normal-conducting linear accelerators often employ travelling wave structures.

4.1.2. Emittance

The transverse emittance is defined as the product of the rms bunch size with the angular divergence. The emittance shrinks with increasing energy, because the longitudinal momentum component is increased while the transverse component remains the same. Hence it is convenient to define a normalised emittance by multiplication with the relativistic γ factor. A small beam diameter can be achieved by focusing the beam using quadrupole magnets of alternating polarity.

The normalised emittance is a constant of motion under linear beam optics. Space charge forces increase the emittance in the first part of the accelerator. In the highly relativistic regime, the repulsive Coulomb forces are effectively counteracted by attractive magnetic forces.

4.1.3. Particle source

Free electrons can be produced by different methods. A conventional source, based on a thermionic cathode provides too small bunch charges. A photo cathode driven by an ultraviolet laser deliver higher charges. However, the emittance of the bunch blows up due to internal Coulomb forces. To reduce this effect, three measures are taken: the electrons are rapidly accelerated to relativistic energies, the bunches are not excessively short (around 10 ps) and a longitudinal magnetic field imposes a spiraling trajectory on the particles. Thus, it is possible to achieve a bunch charge of several nanocoulombs with a normalised transverse emittance of a few micrometres.

4.1.4. Bunch compression

To increase the peak current to the value of several kA required for the SASE-FEL process, the bunch is compressed at relativistic energies. To do this, one adjusts the phase of the accelerating field such that the bunch passes the cavities when the electric field is increasing. The particles in the tail of the bunch acquire a higher energy than

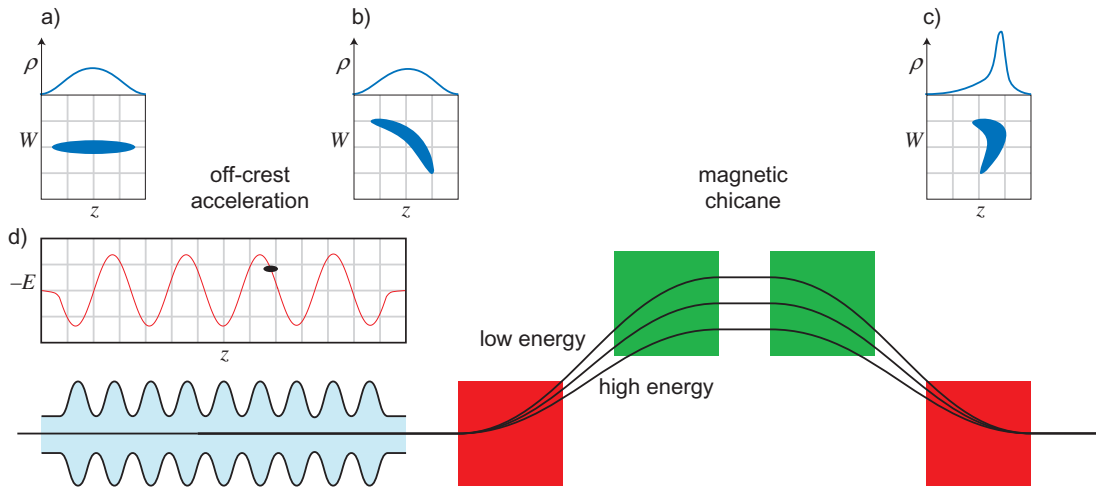


Figure 4.1.: Schematic drawing of a bunch compressor. The off-crest acceleration introduces a correlated energy spread. The phase space is sheared by the magnetic chicane. Symbols: W : energy, z : longitudinal position, ρ : charge density, E : electric field. a) The particle distribution as a function as a function of z and as a function of W and z , before the acceleration, b) the particle distribution after off-crest acceleration, c) the particle distribution behind the magnetic chicane. The peak current is increased. d) The electric field in the accelerating cavity.

the particles in the head, a so-called *energy chirp* is imposed on the bunch (figure 4.1). In a magnetic chicane behind the accelerating section, the tailing particles follow a shorter trajectory, allowing them to catch up with the leading particles. The rms bunch length is shortened, the peak current increased. The principle is similar to the optical pulse compression in lasers.

The accelerating field has a sinusoidal time dependency. Therefore, the chirp is not linear. This translates to a distorted phase space distribution with a sharp front peak followed by a long tail. Obviously, the non-linearities in the field become more important for larger initial bunch lengths. Therefore, the effect can be reduced if the bunch is pre-compressed at a lower energy. The emission of coherent synchrotron radiation in the chicanes has to be considered.

4.2. The TESLA Test Facility

Planned originally as a test facility for the TESLA¹ collider, the TESLA Test Facility (TTF) linear accelerator has been equipped at a later stage with an undulator that generates FEL radiation at 100 nm wavelength. The TTF has demonstrated

¹Teraelectronvolt Energy Superconducting Linear Accelerator

- the performance of superconducting cavities at high gradient,
- the pulsed operation of the cavities and the compensation of beam loading of long pulse trains,
- the controlled beam transport with low emittance from the gun to the end of the accelerator,
- the RF regulation concept to stabilise the field amplitude and phase,
- a proof-of-principle of a SASE FEL in the VUV, and finally
- first experiments using this radiation [Wab02].

As a test facility, the accelerator undergoes a constant modification and expansion. The state referred to in this chapter is of 2001/2002, when the measurements were done. This state is called *TTF Phase I*. It is schematically presented in figure 4.2.

The set-up of this accelerator is only briefly summarised here. For more details, the reader is referred to the design report of the TTF [Edw95], the conceptual design report for the Free Electron Laser [Åbe95] and the technical design report for TESLA [RSTW01] a report on the performance [Cas02] and to the papers mentioned in each section.

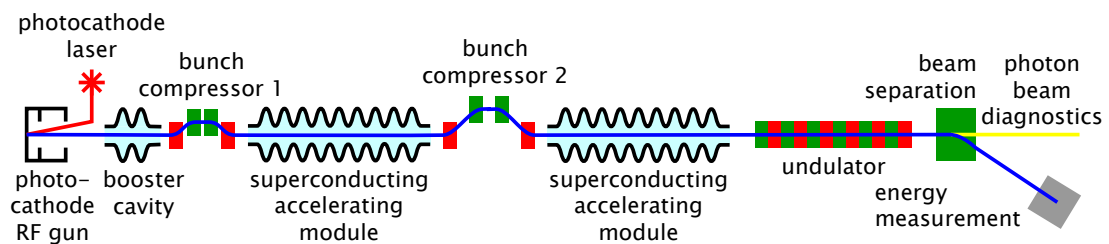


Figure 4.2.: Schematic view of the TTF Linac, in its state 2001/2002.

4.2.1. RF photo-injector

To achieve the high current together with the low transverse emittance and the small energy spread required for SASE FEL operation, the injector of the TTF linac consisted of a laser-driven RF photo-cathode gun [Sch00, SCG⁺02], shown in figure 4.3.

A high-power Nd:YLF laser generated a pulsed infra-red beam. Two nonlinear crystals reduced the wavelength to 262 nm, corresponding to a photon energy of 4.7 eV. The energy of each laser UV pulse was up to 50 μ J. The longitudinal pulse shape was approximately Gaussian, with a standard deviation of $\sigma = (7 \pm 1)$ ps. This has been determined with streak camera measurements (figure 4.4).

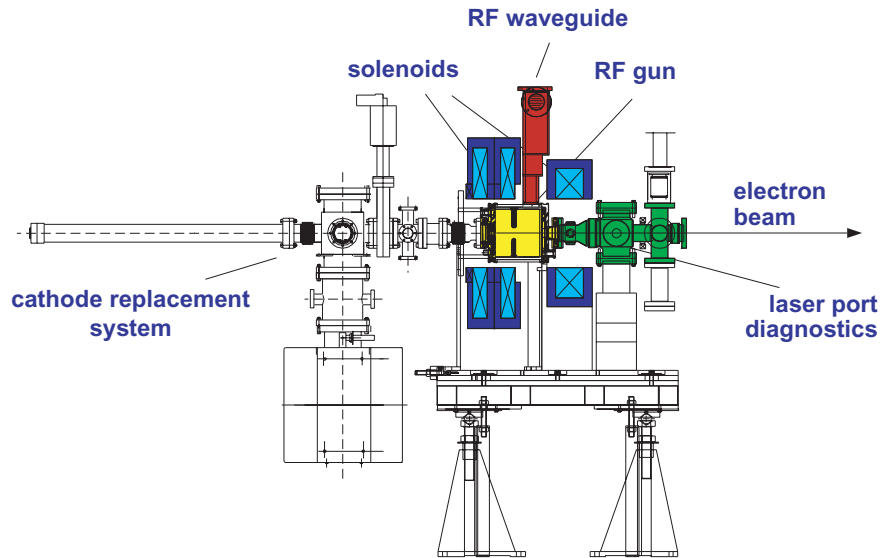


Figure 4.3.: Radiofrequency (RF) gun of the TTF linac. The cathode replacement system is used to exchange the photo cathode under ultra high vacuum. The beam is emitted at the right side with an energy of 4.5 MeV [Col97].

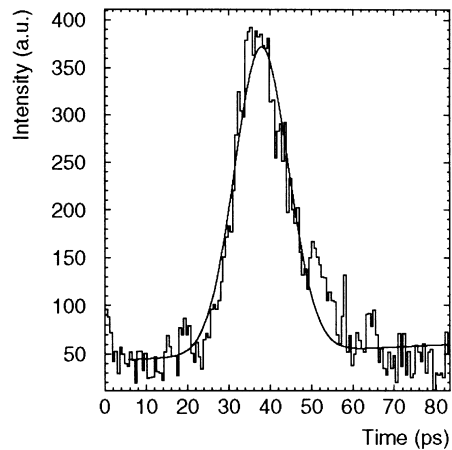


Figure 4.4.: A typical longitudinal pulse shape of the injection laser, measured with a streak camera at 262 nm [SWS⁺00]. In this measurement, the Gaussian fit yields a width of $\sigma = 8.0$ ps.

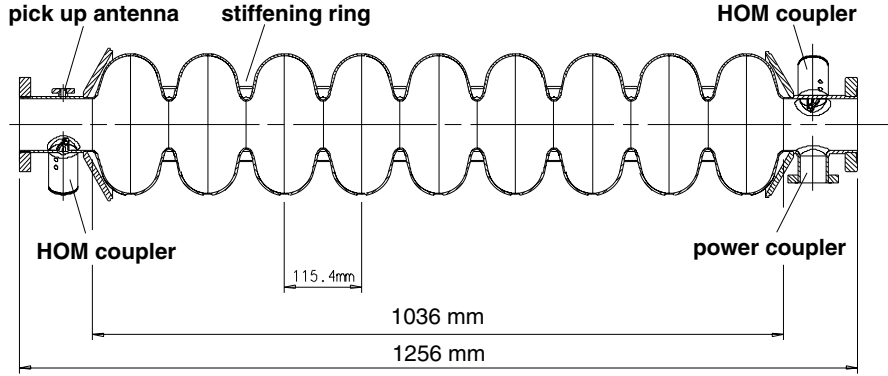


Figure 4.5.: Cross section of a superconducting RF cavity installed in the TTF linac [Aun00]. The power coupler is connected by a wave guide to the klystron. Higher-order mode (HOM) couplers remove resonant fields of higher order, a pick-up antenna is used to measure the field.

This laser pulse liberated electrons from a caesium telluride (Cs_2Te) cathode by photo-emission. The cathode resided on the axis of a normal-conducting $1\frac{1}{2}$ -cell radio-frequency (RF) cavity, operated at a frequency of 1.3 GHz and with an accelerating field of up to 42 MV/m. Two solenoidal coils surrounded the cavity to create a longitudinal magnetic field of ≈ 0.1 T on the axis. A third coil behind the cavity compensated this field to zero on the surface of the cathode. The presence of a magnetic field in the cavity is one of the reasons why a normal-conducting cavity is used.

The electrons left the gun with an energy of 4.5 MeV. The injector of the TTF achieved a peak current of 130 A with a normalised transverse emittance of $3 \pm 0.2 \mu\text{m}$ in the horizontal and $3.5 \pm 0.5 \mu\text{m}$ in the vertical plane. The energy spread of the core of the bunch was 5 keV, measured behind the first superconducting cavity [HS03].

4.2.2. Superconducting cavities

While the gun had a normal-conducting RF cavity, further acceleration of the electron bunch was achieved by superconducting cavities. These are operating also at 1.3 GHz and with an accelerating field of up to 22 MV/m [Aun00]. One cavity is shown in figure 4.5. The nine-cell cavities are operated in the π -mode, i.e. the phase of the field advances by π in each cell. The cavities were made from ultra-pure niobium that becomes superconductive at a temperature of 9.2 K in the absence of a magnetic field.

The TTF cavities achieved a quality factor $Q_0 \approx 10^{10}$ for $T = 2$ K. This temperature was maintained by cooling the cavities with superfluid helium. A module contained cryostats and couplers for eight cavities. Two of these modules were in-

stalled in the TTF linac in 2001/2002. The first cavity directly behind the gun, called booster cavity, had its own cryostat.

The linac was operated in pulsed mode. The amplitude of the electromagnetic field in the cavities had a flat top of up to 850 ps. During this time, a large number of electron bunches could be accelerated, with a repetition frequency of 1 or 2.25 MHz. These bunch trains are called macropulses. The repetition frequency of the macropulses is between 1 and 10 Hz. The accelerating field was controlled by adjusting the amplitude and phase of the incoming RF wave. A pick-up antenna in each cavity was used to measure the field.

Amplitude and phase can be represented as a complex field vector. A digital feedback system stabilised the vector sum of the field amplitude in all cavities in the first module, taking into account the load of the beam. Details on the RF regulation system can be found in [Lie98]. An interesting issue is the detuning of the cavities due to Lorentz forces of the electromagnetic field.

4.2.3. Synchronisation and timing

Various timing signals were generated by a master oscillator with a frequency $f = 9.027775$ MHz. The RF field for the cavities and the injection laser were synchronised within 1 ps (rms). Figure 4.6 shows an overview of the timing in the accelerator.

For the measurements presented in this thesis, a bunch repetition rate of 1 MHz was chosen. Up to 30 bunches per macropulse were used during the studies presented here.

4.2.4. Bunch compression

A two-stage bunch compression was used at the TTF linac. The first chicane was installed behind the booster cavity at an energy of 16 MeV, the second behind the first module at an energy of 120 MeV.

Initially, only the second bunch compressor was in operation. The nonlinearity of the sinusoidal electric field in the cavities resulted in a bunch with a very short peak at the front and a relatively long tail. Only the short peak reaches the current density required for FEL operation. From measurements of the photon pulse (see section 4.5) and simulations of the FEL process, the length of this peak was derived to be in the order of 100 fs [Sal03]. The fragmentation of the electron beam has also been observed directly [HPS01]. The direct measurements done so far yield a peak length of 600 ± 100 fs, which is in the order of the resolution of these devices. They are summarised in figure 4.7.

The commissioning of the first bunch compressor allowed to reduce the nonlinearity to some extent. Hence, it was possible to adjust the bunch shape, allowing to increase the amount of the charge that contributes to the FEL process. This increased the FEL pulse energy and effectively lengthened the pulse.

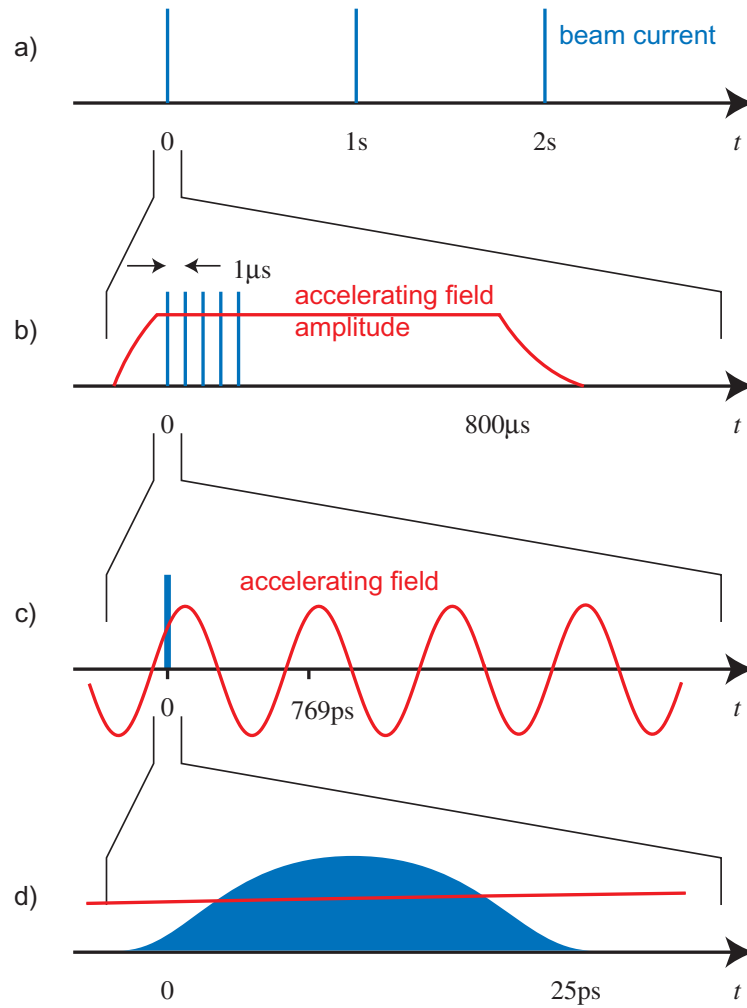


Figure 4.6.: Timing in the TTF linac. a) The macropulses are separated by 1 s. b) Detailed view of a macropulse: the envelope of the accelerating field has a flat top of up to $800\ \mu\text{s}$. The electron bunches are spaced by $1\ \mu\text{s}$. c) The accelerating RF field has a frequency of 1.3 GHz, corresponding to a period of 769 ps. d) An electron bunch with a length of $20\ \text{ps}$ is shown. (Drawings are not to scale.)

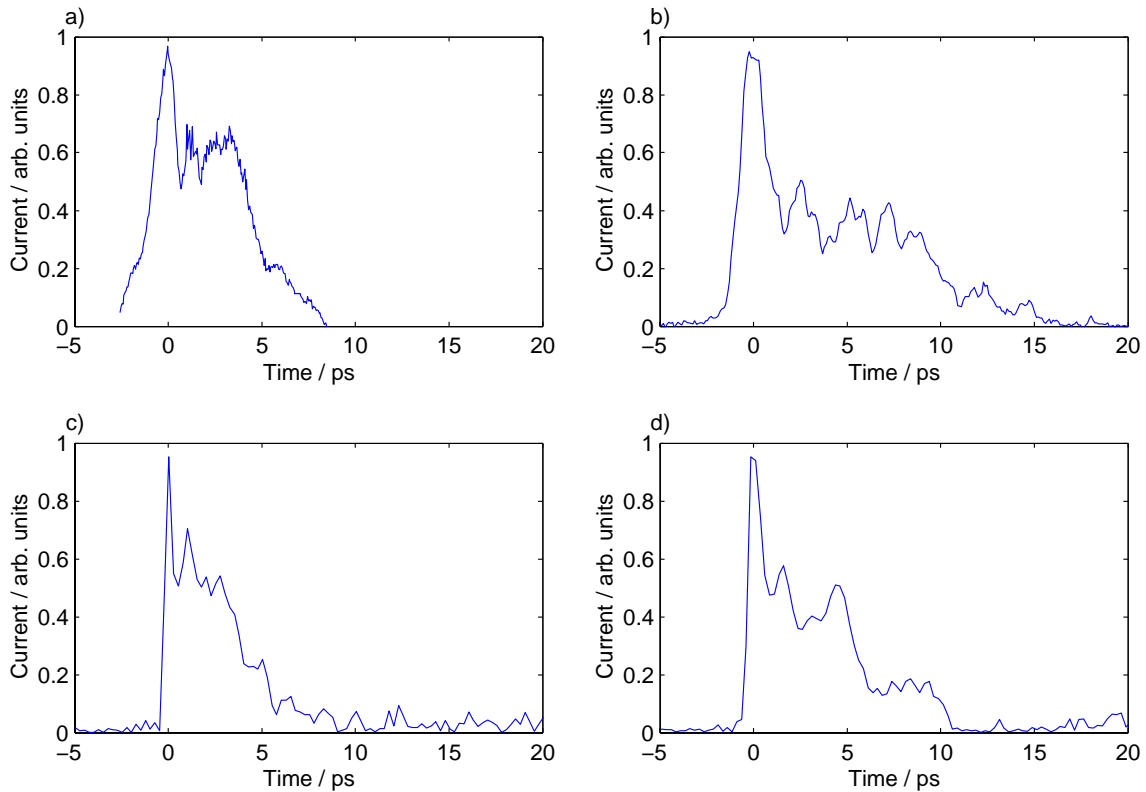


Figure 4.7.: Longitudinal electron bunch shape in the TTF linac, measured with different methods. a) Reconstruction by tomographic methods from the energy distribution [Hün02], b) measured with the synchrotron radiation from a dipole with a streak camera [GFH⁺03]. c) interferometric measurements of coherent transition radiation (CTR) with Golay cells [Men03]. These three measurements were done at maximum compression with the second bunch compressor, the first bunch compressor was not used. d) Interferometric measurements of CTR, using pyroelectric detectors [Men03]. For this measurement, both bunch compressors were activated.

4.2.5. Collimation

Collimators were installed in front of the undulator to protect the permanent magnets from radiation damage [Sch01a]. A small aperture removed most of the beam halo and dark current, which would otherwise be lost in the narrow beam tube of the undulator. Additionally, an active protection system was installed.

Table 4.1.: Parameters of the electron bunch at the undulator entrance [And00, Sch03b, Yur03, Hün02].

Parameter	Measured value
Beam energy	adjustable: 180 . . . 300 MeV
rms energy spread (without compression)	0.3 ± 0.2 MeV
rms transverse beam size (without compression)	100 ± 30 μm
Normalised projected emittance	(7 ± 2) μm
Total bunch charge	adjustable: 1.5 . . . 3 nC
Bunch charge in the radiating part of the beam	1 nC
	0.15 ± 0.05 nC*
Peak current	600 A
	1.3 ± 0.3 kA*

* not a direct measurement, but inferred from the FEL radiation

4.3. Electron beam diagnostics

Various devices were installed in the TTF linac to investigate the beam properties. Some measure integral properties of the electron bunch, e.g. the position or the total charge, others allow to determine the distribution inside the electron bunch.

It is important to note that the requirements for the operation of the free electron laser are more stringent than achievable with today's beam diagnostics. Therefore, the fine tuning of the accelerator was done using also the measurements from the photon beam. The physics of electron and photon beam are much more interleaved than in conventional synchrotron sources.

Measured properties of the electron bunches are summarised in table 4.1.

4.3.1. Measurements of integral properties

- The *total charge* of the electron bunch is measured with toroidal coils around the beam [FJ96] or with Faraday cups.
- The transverse *beam position* is measured by *beam position monitors (BPMs)*. Various types are installed in the TTF accelerator:
 - Button BPMS [Che95] and stripline BPMs [Lor97] measure the electric field of the passing bunch on four electrodes in the beam tube.
 - Wave guide BPMs extract part of the electromagnetic field into little wave guides which are equipped with antennae [Kam00].
 - The beam trajectory monitor [Ng96] was intended to measure the trajectory of the bunch in the undulator by imaging its spontaneous undulator

radiation. However, this device did not work satisfactorily due to an occlusion of the optical path by the beam tube mount and because of severe electromagnetic pick-up noise in the preamplifiers.

- Cavity BPMs measure a transverse mode in a pillbox cavity that is excited by an excentric beam [Lor97].
- Re-entrant cavity BPMs have the same operating principle, but a different cavity layout [Mag98].
- The electron *momentum* is measured by a beam position monitor installed behind a dipole magnet. For a single bunch measurement, the resolution is $\Delta p/p = 10^{-4}$ [Stu02].
- *Beam loss monitors* record electrons that are lost from the bunch, as well as secondary particles [Sch02].

4.3.2. Measurements of the bunch structure

To gain a deeper insight into non-linear processes as the amplification in the FEL, it is helpful to measure the distribution of the electrons in (phase) space. There were various devices installed in the TTF accelerator. They measured the electron density:

- *As a function of x and y* : the transverse distribution was measured by inserting a Kapton foil or silicon wafer that had been coated with a thin aluminium layer. The electrons generated optical transition radiation (OTR), which was imaged onto a CCD [Cas96].
- *As a function of x, y, p_x and p_y* : the distribution in the transverse phase space is rotated by quadrupole magnets. By adjusting the strength of these magnets, and by using tomographic reconstruction algorithms, the phase space distribution could be reconstructed by the measured projections on the (x, y) plane [Gei99].

Due to the analogue data transfer from the cameras, the orientation perpendicular to the primary read-out direction of the CCD was affected by noise and could not be used: the camera was rotated by 90° to measure vertical beam profiles, such that the projection is done perpendicularly to the read-out. Therefore, only a two-dimensional distribution, i.e. in the (x, p_x) or (y, p_y) phase space could be measured up to now. An improved read-out of the cameras, as well as advanced reconstruction algorithms, will be used in future experiments [HBF⁺03].

- *As a function of t and E :* similar tomographic methods can be applied to the (t, E) phase space: the particle distribution was sheared by accelerating the bunch off crest, the bunch was imaged behind a dipole magnet [Hün02].
- *As a function of z :* there are different methods to measure the longitudinal charge distribution in the bunch (see also figure 4.7):
 - The synchrotron radiation in a dipole magnet was measured with a streak camera [HSGP03].
 - The transition radiation from a thin aluminium layer extends to the far infrared. For wavelengths longer than the bunch, the electrons emit this radiation coherently. This coherent transition radiation (CTR) has a high intensity as it scales with the square of the number of electrons. Using an interferometer to measure the auto-correlation of this pulse, one can reconstruct the bunch shape [LBS⁺99, Men03].

4.3.3. Indirect measurements

Several properties of the electron bunch have been derived from the radiation that is produced in the undulator (see next section). These include the energy of the electrons, inferred from the wavelength of the radiation. From simulations of the FEL process, and by comparing to the measurements of the FEL intensity and its fluctuation, it was also possible to infer the peak current and the length of this peak, and from the gain length and the peak current, the emittance of the electron beam.

4.3.4. Planned measurements

- *Electro-optic Sampling:* The electromagnetic field of the bunch induces birefringence in a zinc telluride crystal. This can be measured by the polarisation change of a femtosecond laser. A proof-of-principle experiment of this electro-optic effect has been done using the transition radiation from a thin metal layer [Tür02, BGG⁺03], the construction of a set-up to measure the direct field of the bunch is under way [Ste03].
- *Transverse mode Cavity:* The electron bunch can be deflected by a rapidly varying transverse electric field. This can be done in an RF cavity which is excited in a transverse mode. The bunch is sheared in the (x, t) plane, an observation of the (x, y) plane with optical transition radiation gives the desired longitudinal distribution [ABE02]. However, synchronisation of this cavity with the accelerating structures is still an issue.



Figure 4.8.: Side view of the three undulator modules.

- *FIR Spectroscopy using Undulator radiation:* There are ideas to measure the longitudinal pulse shape with coherent synchrotron radiation from a far infrared undulator [GSSY03].

4.4. Free electron laser

4.4.1. Permanent magnet structure

The electron bunch passed the undulator (figure 4.8) at energies between 180 and 300 MeV. To enhance and shape the field, pole shoes had been attached to the permanent magnets (figure 4.9). Three undulator modules of 4.472 m length each were installed. On the axis, the field was to a good approximation sinusoidal, with a period of 27.3 mm and a peak induction of 0.46 T; table 4.2 lists further parameters.

4.4.2. Steerers

For the amplification of the radiation, it is necessary to ensure good overlap between the electron and the photon beam along the undulator. Small deviations lead to a drastic decrease in the output power (figure 4.10). The position of the electron was

Table 4.2.: Undulator parameters [And00, Faa03].

Parameter	Design value
Number of modules	3
Gap	12 mm
Module length	4.472 m
Effective total length	13.5 m
Period	27.3 mm
Peak dipole field	0.46 T
Undulator Parameter K	1.17
Corrected undulator parameter \hat{K}	1.04
Pierce Parameter ρ_{Pierce}	$2.5 \cdot 10^{-3}$
Average horizontal betatron function	1.2 m
Average vertical betatron function	1.1 m
FEL gain	$3 \cdot 10^3$
gain length	67 cm

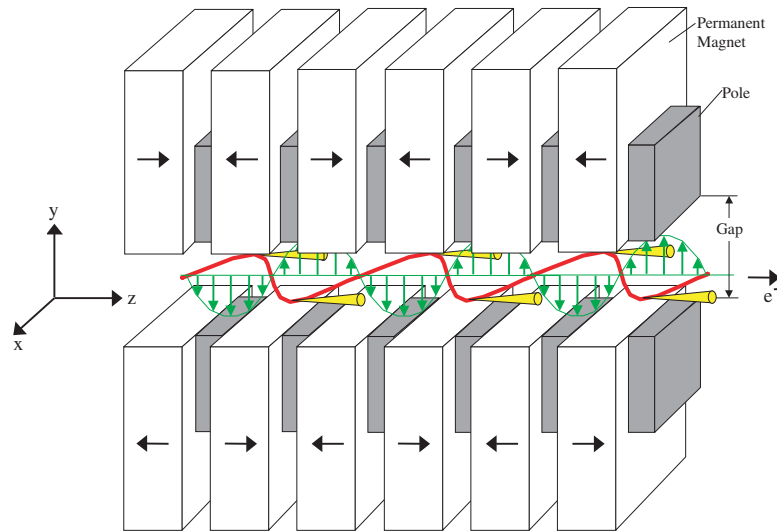


Figure 4.9.: Arrangement of the magnets in the undulator that creates a sinusoidal field on the beam axis [FP99]. The drawing is not to scale. The quadrupole magnets are not shown.

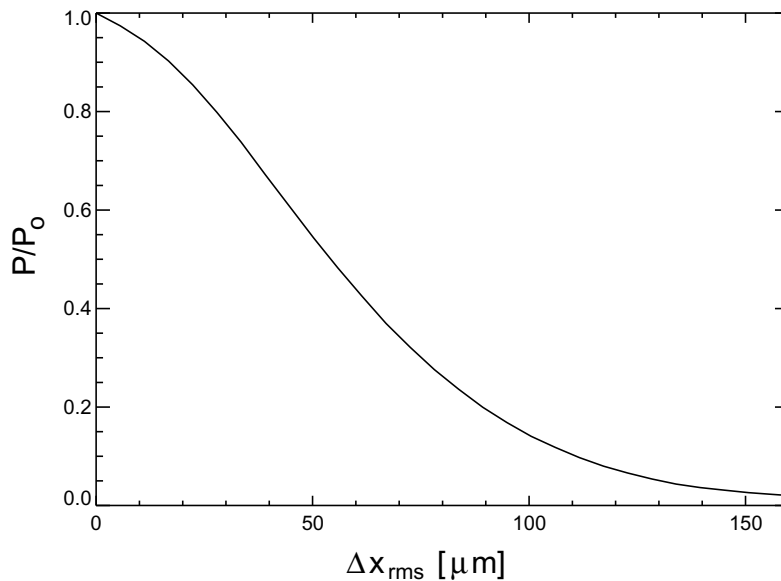


Figure 4.10.: Degradation of the FEL output power as a function of the rms misalignment of electron and photon beam [Rei99, Kam00].

Table 4.3.: Parameters of the FEL pulse [And00, RGK⁺03, Ayv02b].

Parameter	Measured value
wavelength	87 ... 109 nm
pulse length	0.4 ... 1 ps*
pulse energy	30 ... 100 μJ
spectral width	1 nm (FWHM)
intensity in 2nd harmonic	< 1% of fundamental
peak brilliance	$4 \cdot 10^{28}$ photons/(s · mm ² · mrad ² · 0.1% bandwidth)
angular divergence	260 μrad

* inferred from the number of longitudinal modes of the radiation

be measured with BPMs. To correct for misalignment, nine steerer magnets were installed in each of the three undulator modules.

These steerers consisted of four coils with one winding each (figure 4.11). Depending on the interconnection of the coils, they could be used as horizontal, vertical or combined-function steerer. The last steerer in each undulator module was connected to two power supplies to act as a combined-function steerer. The permanent magnets and their poles acted as a yoke that strengthened the field for the horizontal and weakened the field for the vertical steerers.

The parameters of the FEL pulse are listed in table 4.3.

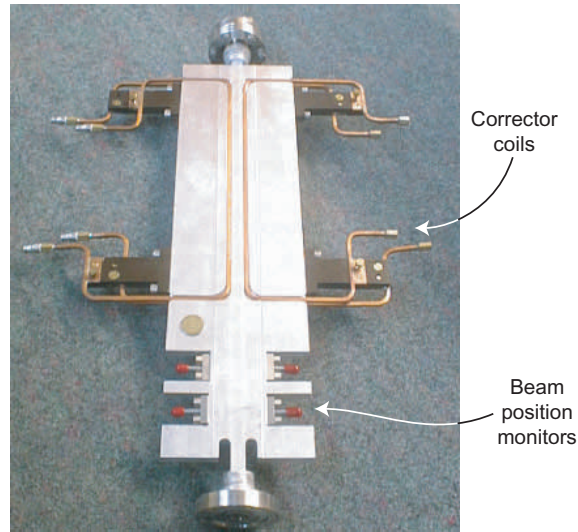


Figure 4.11.: Prototype of the undulator vacuum chamber with a steerer. Each of the four correction coils consists of only one winding [Hah00]. In the front, a BPM is installed.

4.5. Photon beam diagnostics

In the FEL process, the radiation is amplified by five orders of magnitude, as compared to the spontaneous emission. Many different detectors were installed to cover this dynamic range (figure 4.12) [TLX⁺00, TLF98]. The intensity was monitored over a wide range with a calibrated microchannel plate (MCP) [Faa01], detecting the light which is scattered from a thin wire. A grating spectrometer [GFL⁺01], equipped with a CCD camera with an image intensifier, was used to measure the spectral distribution. A fluorescent crystal could be inserted to measure the spatial distribution of the FEL light as well as interference patterns. The detectors had been aligned with the help of a helium-neon (HeNe) laser that was collinear with the FEL beam. Circular apertures of 0.5, 1, 3 and 5 mm diameter could be inserted to reduce the cross section of the beam. They were mounted on a water cooled frame that could be moved to an arbitrary horizontal and vertical position (figure 4.12, Nb. 3).

The CCD cameras were protected against radiation damage by a 20 cm thick lead shielding. This corresponds to 40 radiation lengths, which is sufficient to block the radiation showers completely².

²if the shielding has a thickness of only a few radiation lengths, the number of particles is increased by scattering processes, resulting in a higher damage

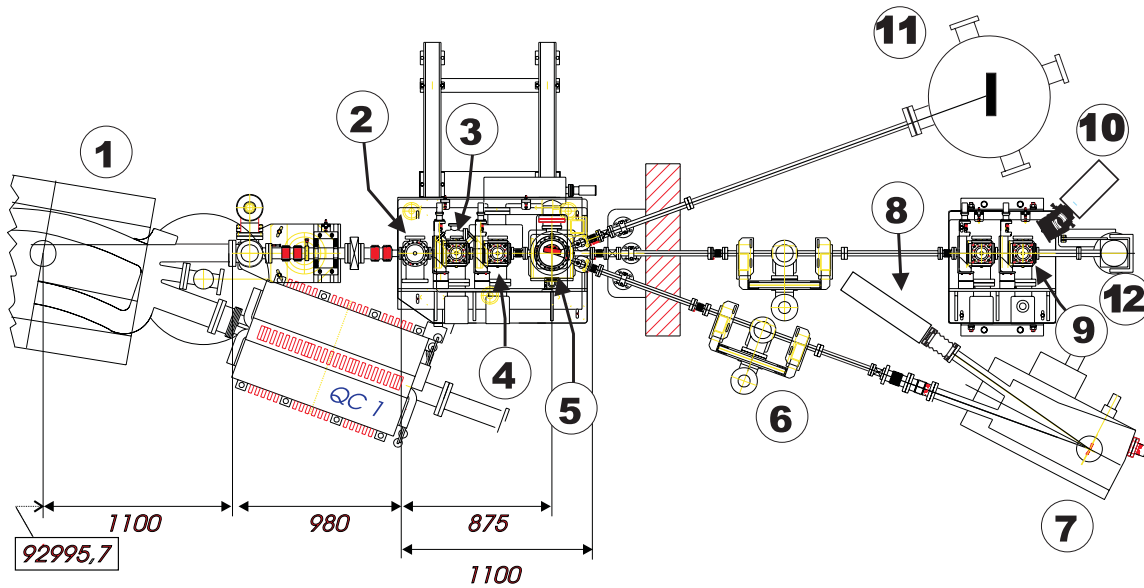


Figure 4.12.: Experimental set-up for the SASE FEL photon diagnostics at the TTF linac. 1: bending magnet to deflect the electron beam, 2: alignment laser port, 3: aperture unit, 4: unit with the first MCP detector and the double slits, 5: deflecting mirror, 6: TSP and ion getter pumps, 7: grating monochromator, 8: monochromator camera, 9: fluorescent crystal, 10: CCD camera, 11: laser ablation or cluster experiment, respectively, 12: second MCP detector.

4.5.1. Intensity measurements

The intensity of the photon beam has been measured to demonstrate the successful operation of the SASE-FEL and to compare with theoretical models for the formation of FEL radiation. Furthermore, the measurement is important for the optimisation of the accelerator.

The intensity varies by four orders of magnitude from spontaneous radiation to the saturation of the FEL, where it reaches intensities close to the damage threshold of many materials. For these two reasons, it is not a trivial task to measure the intensity of the FEL radiation.

Photodiodes

Semiconductor detectors are commonly used to detect VUV radiation. However, radiation damage had been observed in *pn* junction detectors consisting of silicon or gallium arsenide phosphide (GaAsP) when exposed to radiation of a wavelength $\lambda < 150$ nm already at an exposure level of a few mJ/cm^2 . This is due to the formation of traps in the oxide layer on top of the semiconductor, resulting in a degradation of the quantum efficiency [SMK⁺96].

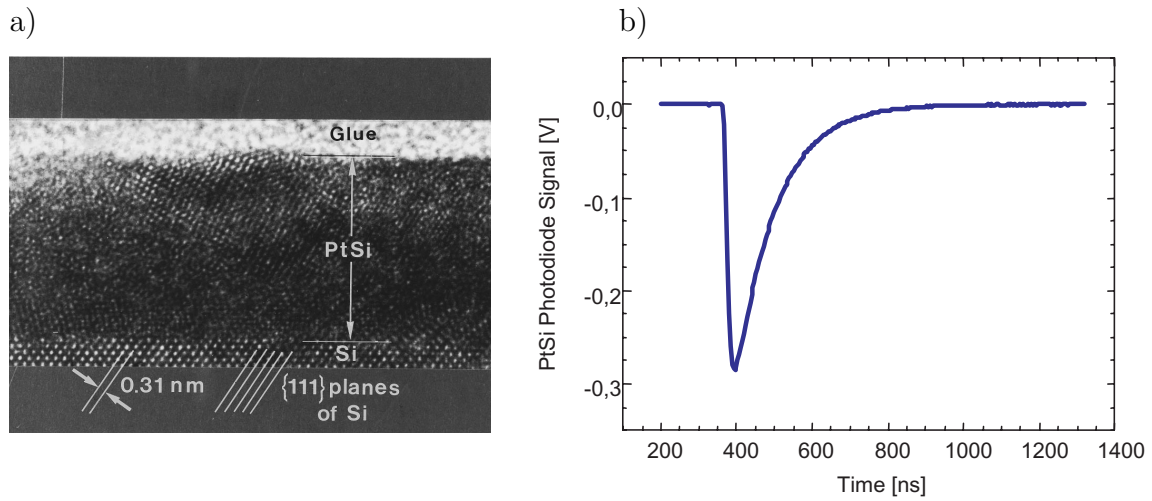


Figure 4.13.: Platinum silicide detector. a) Micrograph of a PtSi film [SMK⁺96], b) signal of the PtSi detector, as measured at the FEL [Ger03].

As opposed to *pn* junction diodes, where the incident photons create electron-hole pairs in a depletion zone between a *p* and an *n* doped semiconductor, a Schottky-barrier photodetector employs a junction between a metal and a doped semiconductor [RR96]. The difference in work functions between the two materials creates an electrostatic barrier, which can be overcome by the energy from the absorption of photons. At the TTF FEL, platinum silicide photodiodes (PtSi) have been used. By depositing platinum on a silicon crystal and annealing, the platinum diffuses into the silicon and the platinum silicide had been formed in-situ. As a result, the PtSi–Si Schottky contact had been formed inside the bulk material, at some distance below the original surface of the crystal (figure 4.13a). Therefore, it could be made atomically clean, resulting in a spatially uniform response that is stable under VUV exposure up to doses of 150 mJ/cm² [SMK⁺96].

The high sensitivity of this detector was suitable for low to intermediate power densities of the FEL, from spontaneous emission up to two orders of magnitude below saturation. Figure 4.13b shows a signal from this detector.

Thermopiles

A Thermopile detector is based on the *Seebeck* effect. The electrical potential in the joints between two dissimilar conductors at the presence of a temperature difference between the junctions is measured. Incident radiation establishes a temperature gradient $\vec{\nabla}T$ perpendicular to the surface of the detector (figure 4.14a). The present detector was composed of a YBa₂Cu₃O_{7- δ} film and is operated at room temperature. The crystallographic film *c*-axis was tilted to the film surface normal resulting in a transverse voltage. This had been shown to be proportional to the power of the

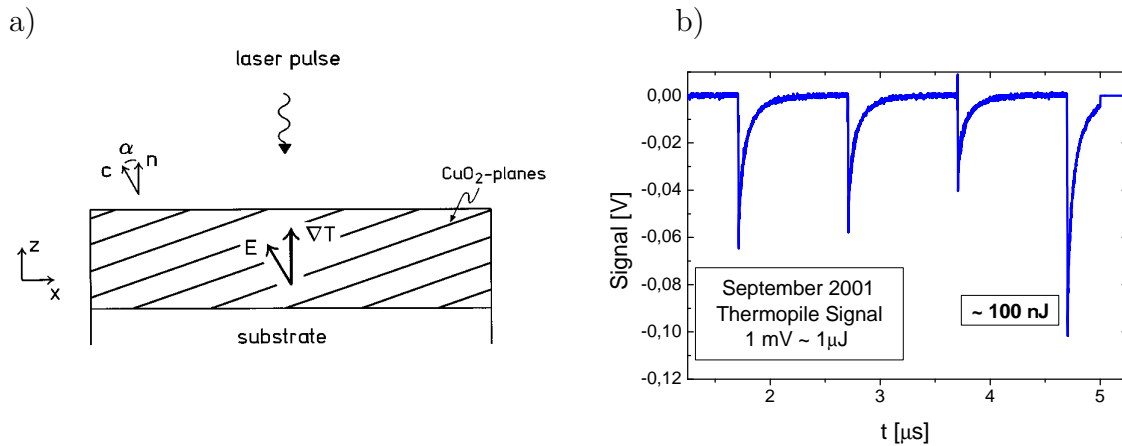


Figure 4.14.: Thermopile detector. a) Schematic cross section of a $\text{YBa}_2\text{Cu}_3\text{O}_{7-\delta}$ film [ZPL95]. b) Signals from the detector [Ger03].

radiation over more than 11 orders of magnitude [LZPR94]. The signal has a fast rise time of 1 ns. Signals obtained at the TTF FEL are shown in figure 4.14b.

Microchannel plate detector

Two microchannel plate (MCP) detectors [Faa01] were installed (figure 4.15), one in front of the other detectors, one at the very end of the set-up. They were not inserted directly into the beam, but measured the FEL radiation scattered to the side on a thin wire. A variation of the amplifying voltage allows to adapt the measuring range by several orders of magnitude and to cover the full range from spontaneous emission to the saturation of the FEL. These detectors had been cross-calibrated with other detectors. The energy growth in the radiation pulse as it passes the undulator is shown in figure 4.16.

Gas monitor detector

The gas monitor detector (GMD) [RGK⁺03] measures the atomic photo-ionisation of a noble gas at a particle density of about 10^{17} m^{-3} , corresponding to a pressure of 10^{-3} Pa . It was separated from the accelerator vacuum of 10^{-7} Pa by a differential pumping stage. About 10^6 to 10^9 electrons and ions are created from each FEL pulse. They are separated by a homogeneous electric field (figure 4.17). Positive and negative charge carriers were collected in Faraday cups. The ions passed through an acceleration section, which allows to determine their charge through their time of flight ($q \propto t^{-1/2}$). It has been verified that no second-order effects lead to a double ionisation of the xenon atoms.

Due to the low particle density and the absence of an input window, the detector was almost transparent, even for VUV radiation. However, one has to keep in mind

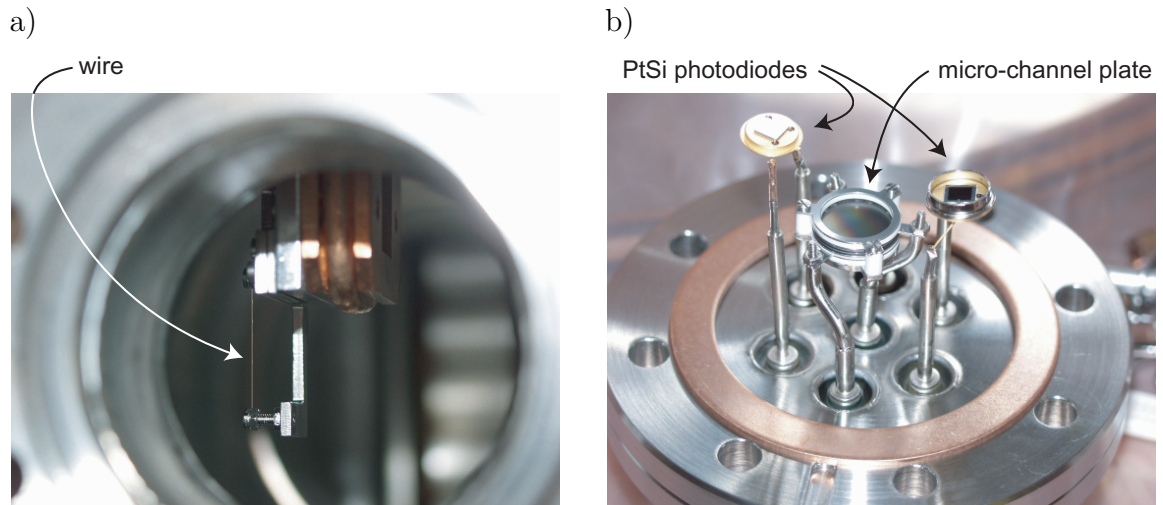


Figure 4.15.: Microchannel plate detector. a) wire that can be inserted into the beam and reflects a part of it into the actual detector. b) microchannel plate and two photo-diodes.

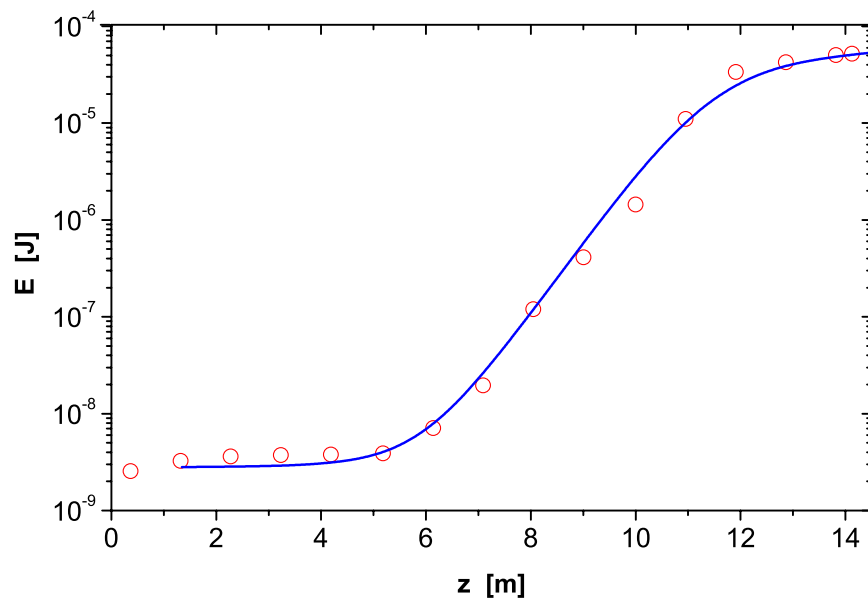


Figure 4.16.: Average energy in the FEL pulse as a function of the active undulator length [Ayv02b]. In this plot, the length comprises the space between the undulator modules. From this, one can infer a gain length of 67 cm. Circles: experimental results. Solid curve: numerical simulations with the code FAST [SSY99].

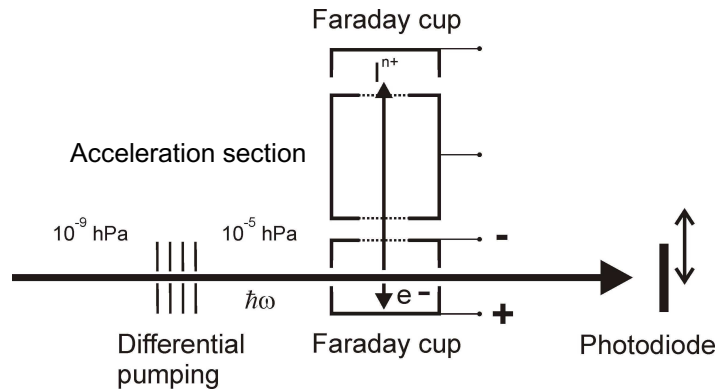


Figure 4.17.: Schematic diagram of the gas monitor detector

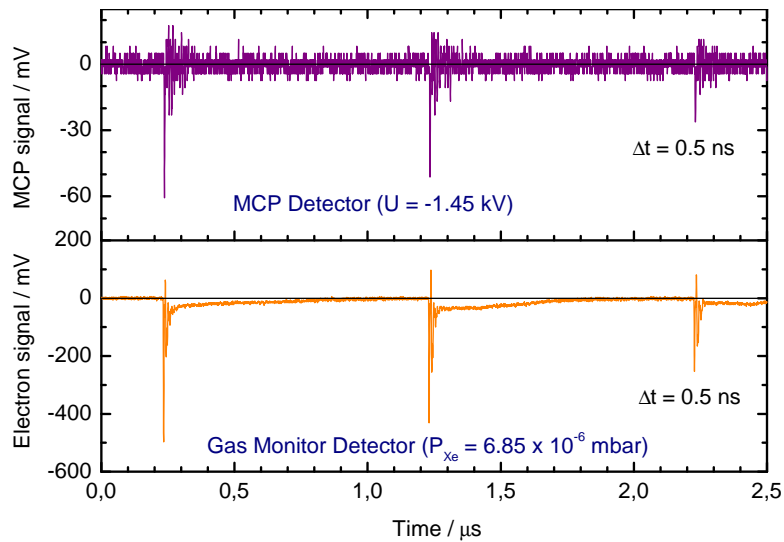


Figure 4.18.: Signals from the microchannel plate (top) and the gas monitor detector (bottom).

that diffraction occurs at the aperture of the differential pumping stage. The detector medium is not affected by radiation damage, even at a radiation level of 10^{20} W/m². It had been calibrated to a primary standard in the Radiometry Laboratory of the Physikalisch-Technische Bundesanstalt (PTB). Signals from the MCP detector and the gas monitor are shown in figure 4.18.

4.5.2. Measurements of the spectrum

The spectral distribution of the radiation pulse could be measured with a spectrometer [GFL⁺01]. It consisted of a normal incidence grating with 1 m focal length; the diffraction pattern which was produced on a fluorescent screen was imaged with tandem optics providing a very large aperture. This set-up collects 5.3% of isotropically emitted light from the screen. The image intensifier was coupled to a CCD, which is digitised directly in the device. It was controlled and read out by a fibre optical link from the control room. A wavelength resolution of 0.2 nm has been measured with this spectrometer, while the covered wavelength range is 7 nm [GFL⁺01]. Single-shot spectra could be recorded using the short exposure times of the image intensifier (figure 4.19).

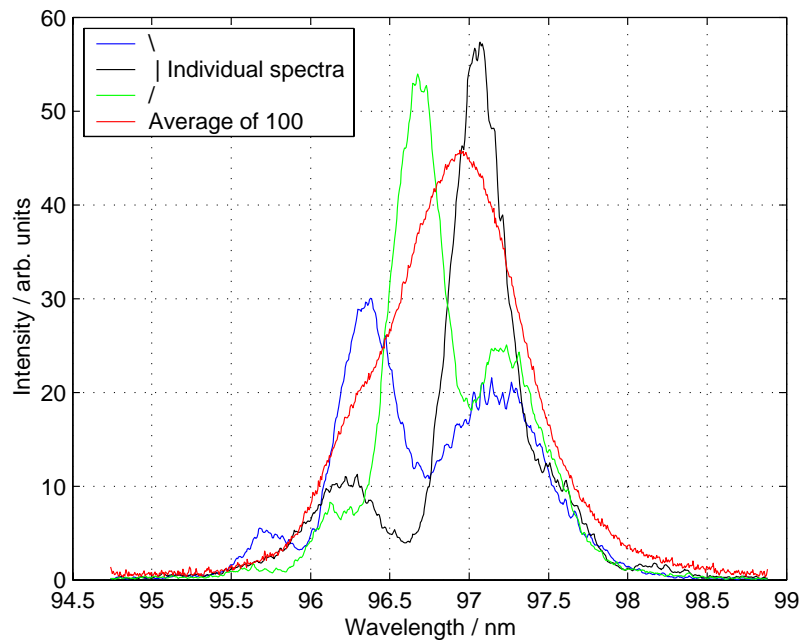


Figure 4.19.: Measured spectra of FEL pulses. Individual electron bunches produce different spectral distributions. An averaged spectrum is also shown.

5. Experimental Set-up for the Coherence Measurements at the TTF FEL

The transverse coherence of the TTF Free Electron Laser has been measured with double slit experiments, installed in the ultra high vacuum of the accelerator. The diffraction pattern was observed on a fluorescent crystal. This chapter contains a technical overview of the set-up, describing the slits, the fluorescent crystal and the CCD camera. The devices were installed in the photon diagnostics area, shown in figure 4.12: the circular apertures and slits in positions 3 and 4, the fluorescent crystal in position 9 and the CCD camera in position 10.

Due to the high absorption of 100 nm radiation by almost any material, it is not possible to extract the radiation from the accelerator beam tube through an optical window. Therefore, the entire set-up was incorporated into the accelerator vacuum system. As a consequence, the slit arrangement and the distance between slits and screen could not be varied during the measurements described in this thesis. To fulfil the far field condition (3.23) for an aperture with 3 mm diameter, the distance to the screen would have to be much larger than 70 m, which is not feasible in the present set-up. Therefore, near field (Fresnel) diffraction patterns were recorded.

5.1. Apertures and slits

Different apertures have been moved into the beam at a distance 11.84 m behind the undulator exit and 3.1 m in front of the fluorescent crystal. Double slits with different separations were cut into the same metal foil, shown in figure 5.1. The arrangement could be moved horizontally and vertically with respect to the beam axis by stepper motors. For the measurement of the double slit diffraction patterns, the desired slit pair was selected by centring it with respect to the FEL beam and by introducing a circular aperture 0.23 m in front of the slits that let only the central part of the beam pass. Slit pairs of 0.5, 1, 2 or 3 mm horizontal separation, 1, 2 or 3 mm vertical separation or crossed slits could be selected.

The slits were 2 mm long. The slit pairs with 0.5, 1 and 2 mm had a width of 100 μm , the width of the pairs with 3, 3.5 and 4 mm was 200 μm . At 3.1 m distance, the diffraction pattern of a single slit with 200 μm width is only a few millimetres

wide. Two such slits separated by 3 mm produce two separated single slit diffraction patterns and no double slit interference is visible. However, two of the slits belonging to the 1 and 2 mm pairs, which have a width of 100 μm have a separation of 3 mm. The overlap was small but sufficient, and measurements have been recorded successfully.

The slits were manufactured from 50 μm thick stainless steel foil by laser cutting [Mey00]. The crossed slits can be seen in figure 5.2. The precision of the edges is 2.5 μm rms. The foil is completely opaque at a wavelength of 100 nm.

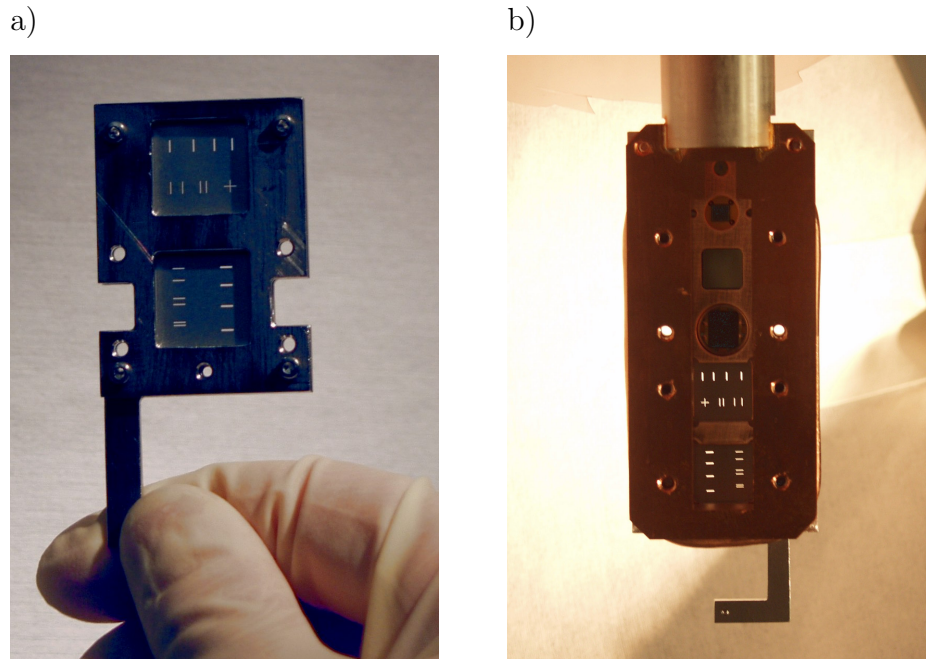


Figure 5.1.: a) *The double slits cut into stainless steel foil in a support frame and b) the complete unit.*

5.2. Fluorescent crystal

Cerium doped yttrium aluminium garnet (Ce:YAG, $\text{Y}_3\text{Al}_5\text{O}_{12} : \text{Ce}$) is a fast scintillator, its decay time constant is 80 ns. It is mechanically robust and suitable for ultra high vacuum applications. Due to its good radiation hardness and high quantum efficiency, it is widely used in the diagnostics of electron and photon beams [MRY⁺00]. A Ce:YAG crystal with a thickness of 2 mm was used for observation of the interference patterns.

In addition, a lead tungstenate (PbWO_4) crystal was installed. This material has a lower sensitivity but features a linear response towards higher radiation intensities. Due to the low light yield, it could not be used for measurements of double slit diffraction patterns. Table 5.1 summarises the properties of the two scintillators.

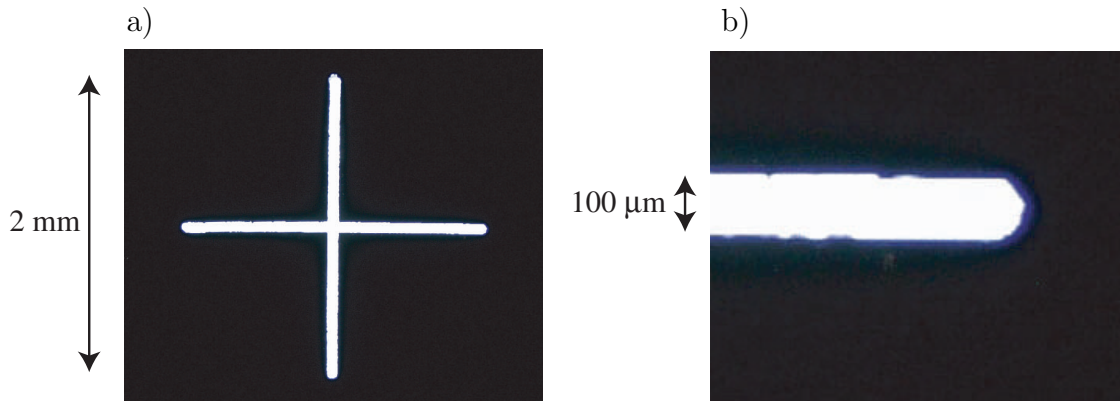


Figure 5.2.: Microscopic view of the crossed slits. The slits are 2 mm long and 100 μm wide. The right image shows a detail.

Table 5.1.: Properties of CeYAG and PbWO₄ [Tec02, CL99, Det00, Sug01]

	CeYAG	PbWO ₄
chemical formula	Y ₃ Al ₅ O ₁₂ : Ce	PbWO ₄
refractive index	1.8	2.16
density	4.6 g/cm ³	8.29 g/cm ³
wavelength of max. emission	550 nm	520 nm
decay constant	80 ns	2... 3 ns

The two crystals were mounted on an actuator to be inserted into the photon beam line (Figure 5.3, located at position 9 in Figure 4.12). The Ce:YAG crystal had some scratches (Figure 5.4) that degraded the quality of the image. The area selected for the analysis of the horizontal slit diffraction patterns was fortunately not affected (see section 6.1.1).

At the present intensities of approximately 10^{12} W/m², the Ce:YAG crystal shows saturation effects, which have been measured and were included in the analysis of the recorded images. The procedure is described in section 6.1.2.

Figure 5.5 shows the absorption spectrum of Ce:YAG. The FEL photons with a quantum energy of 12.4 eV and the 4.7 eV photons used for determining the crystal resolution (Chapter 6.1.3) are absorbed in the surface layer of the crystal and excite fluorescence. The emission spectrum is also shown in figure 5.5.

The resolution of the fluorescence image is limited by diffuse light scattering in the crystal. Furthermore, electron-hole pairs can travel in the crystal before recombination. In the section 6.1.3, a measurement of the scattering is described.

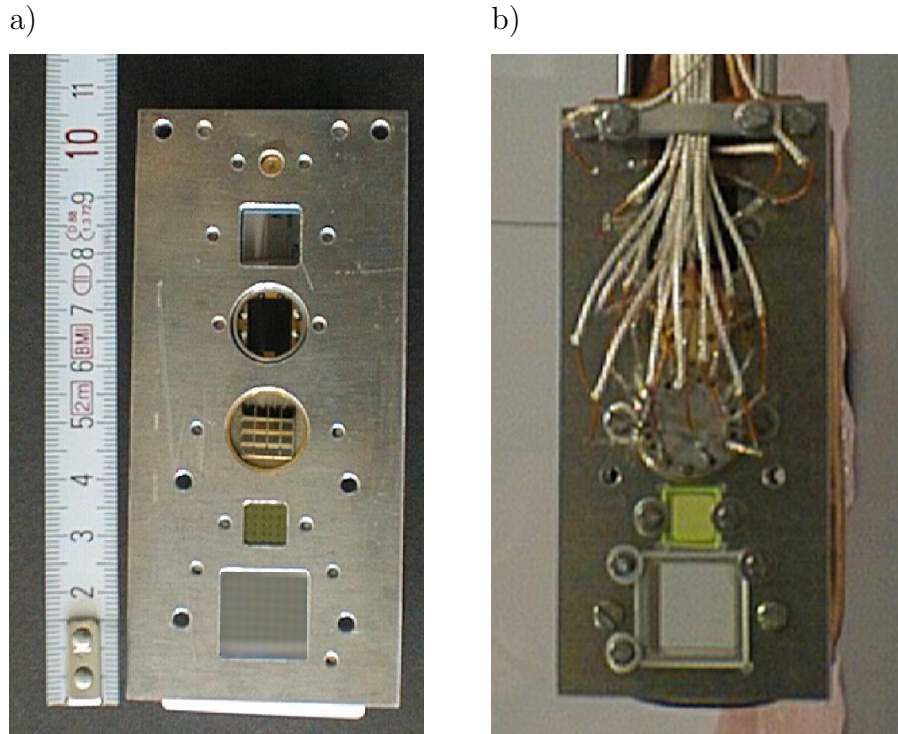


Figure 5.3.: The frame that holds the PBWO_4 crystal (bottom) and the Ce:YAG crystal (second from bottom), a) seen from the beam side and b) from the back side.

5.3. Camera

5.3.1. Optics

Since an MCP detector (position 12 in figure 4.12) was situated immediately downstream of the fluorescent crystal, the CCD camera for the observation of the diffraction patterns had to be mounted at an angle of approximately 35° with respect to the normal of the crystal. The depth of field of a conventional camera lens would have been insufficient to produce a sharp image of the entire crystal. For this reason, the Nikon shift/tilt lens Nikkor 85mm f/2.8 D was used. Using such a tilted lens, the image is focused over the complete plane when the three planes through the object, the lens and the detector intersect in one line¹. The lens could be tilted by 8.3° , which was not completely sufficient given the present distances and angles: using the equations derived in appendix B, a tilt angle of 16.2° would have been ideal. Nevertheless, the focusing was much improved, compared to the case of a rectilinear set-up. Detailed measurements on the optical system are presented in section 6.2.2.

The mechanical set-up permitted a distance of approximately 150 mm between the crystal and the front of the lens body. The distance g between the object and the

¹This criterion is derived in appendix B.

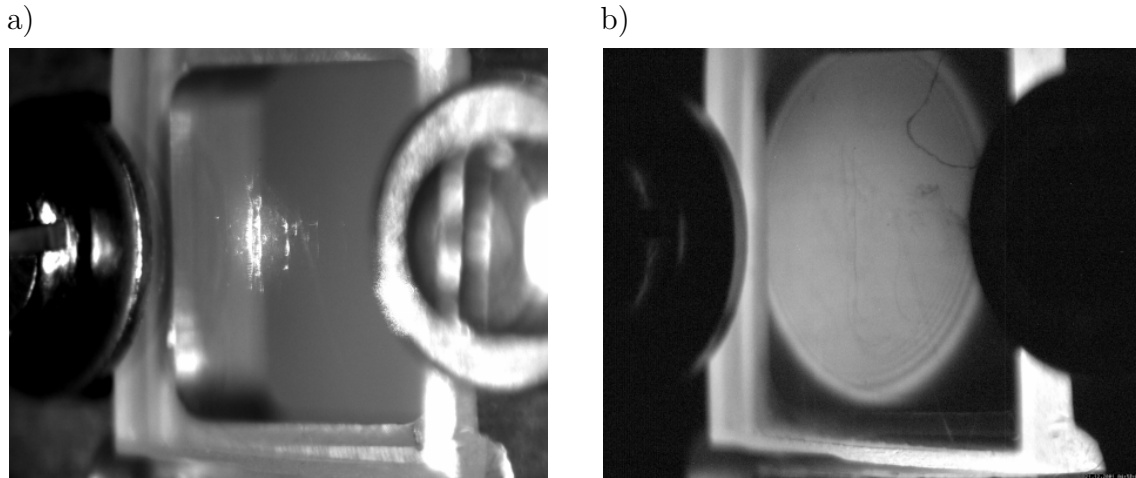


Figure 5.4.: Images of the Ce:YAG crystal, taken with the CCD camera that was used to record the diffraction patterns. Two M3 screws and washers hold the crystal in its frame. a) The crystal during installation. The set-up is illuminated by diffuse light; in the middle of the crystal, some scratches are made visible by a red alignment laser. b) The crystal is illuminated by the FEL. The shape of the beam tube in front of the crystal is visible; at the edge, diffraction effects can be seen. Fluorescence light that is internally reflected leaves the crystal at the edges.

actual lens is 205 mm. This is less than the smallest foreseen focal distance of the lens, therefore an intermediate ring was mounted between lens and camera body. The image distance measured between the centre of the lens and the CCD sensor is 145 mm.

5.3.2. CCD sensor

The image is recorded with a CCD (charge coupled device) camera. A SONY CCD chip is installed in the SensiCam FastShutter, a camera manufactured by PCO Computer Optics [PCO02]. The CCD has 1280×1024 pixels with a size of $(6.7 \mu\text{m})^2$ each. The camera features a *full frame* read-out where all pixels are exposed simultaneously, the *interline transfer* technique to achieve short exposure times and *digital data acquisition* to ensure reliable operation. The quantum efficiency of the chip is shown in figure 5.6.

the full-frame CCD exposes all pixels synchronously, while in CCIR cameras with interlaced read-out, the odd and even lines of the array are exposed and read out with a time difference of 20 ms and in the case of very short light pulses only half of the picture elements contain image data.

For the CCD chip, the interline transfer technique is employed to achieve exposure times below one microsecond: each active pixel is connected to an additional

5. Experimental Set-up for the Coherence Measurements at the TTF FEL

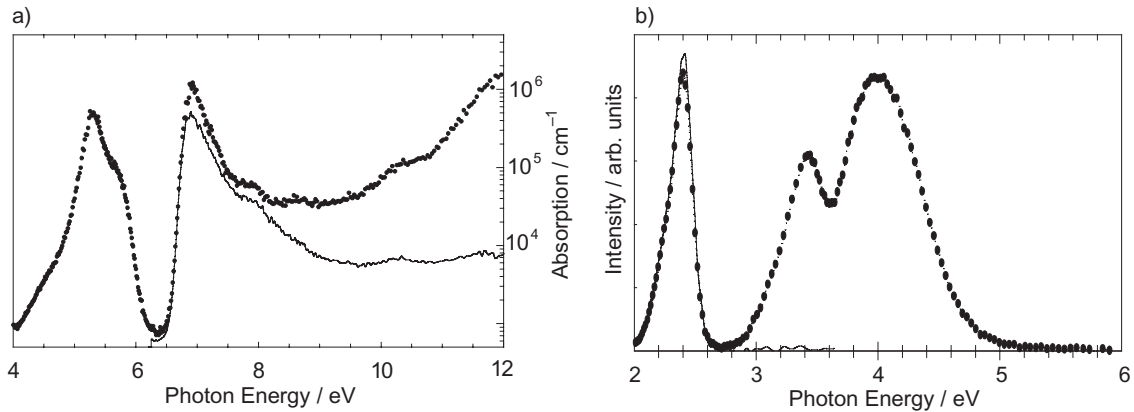


Figure 5.5.: a) Absorption spectrum of Ce:YAG, for the 2.38 eV Ce³⁺ emission (dots) and for the direct 4.13 eV YAG emission (solid line) [KLLZ00].
b) Emission spectrum of Ce:YAG, when excited by 7 eV photons (dots) and excited by 5.2 eV photons (solid line) [KLLZ00].

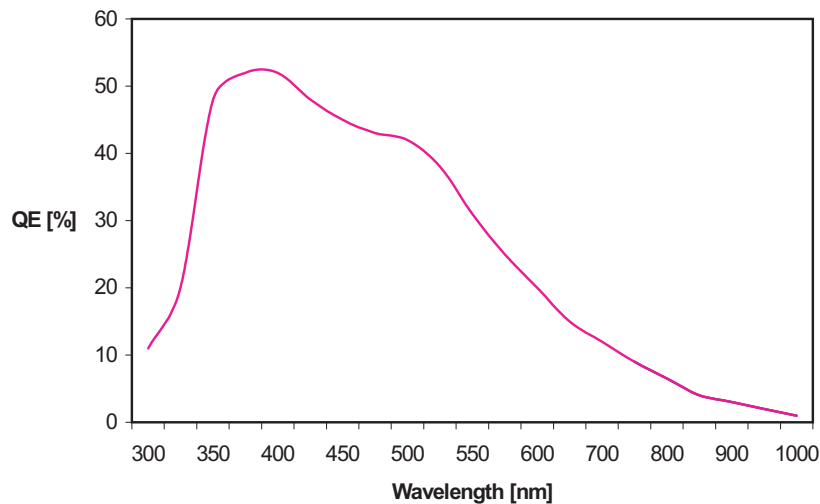


Figure 5.6.: Quantum efficiency of the CCD sensor [PCO02].

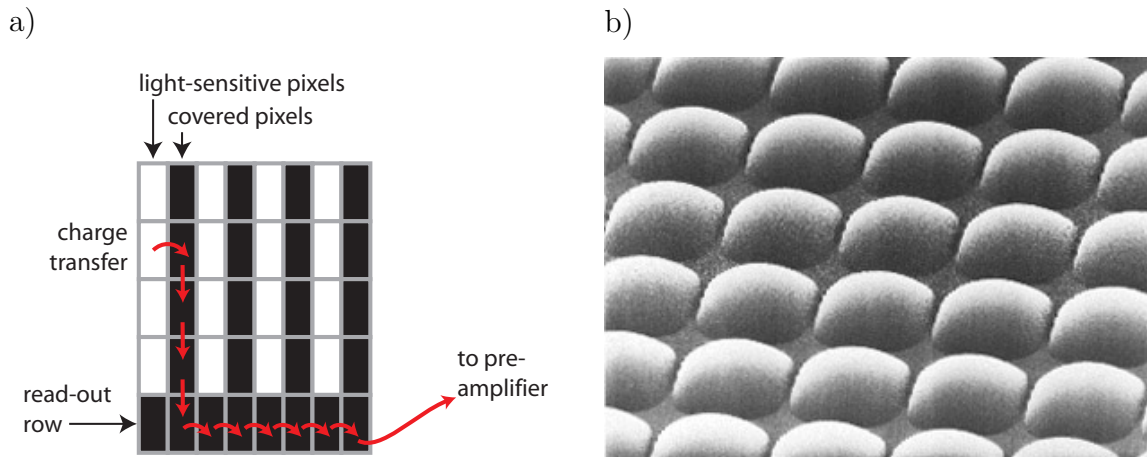


Figure 5.7.: An interline transfer charge coupled device. This technique is used to allow short exposure times without a mechanical shutter. a) Schematic drawing of the interline transfer read-out, b) microscopic view of the microlenses on an interline transfer CCD chip [N.02].

shift register cell, which is protected against direct light exposure (figure 5.7a). The charges from the exposed pixels can be transferred to these repositories within less than $0.1 \mu\text{s}$; they can then be read out. The shift registers are located on the surface of the CCD and reduce the sensitive area of the chip. To maintain a good quantum efficiency, the lens-on-chip technique is used: a layer of microlenses just above the detector elements focus the light to the active pixels (figure 5.7b).

A Peltier thermoelectric element cools the CCD down to -12°C , which reduces the noise in the detector to make use of the full range of the 12 bit ADC. The quantum efficiency is around 40% for the light emitted by the fluorescent crystal (Figure 5.6).

The CCD signal is digitised in the camera itself. In comparison with conventional CCIR video technology, where an analogue signal is transmitted to a frame grabber outside of the accelerator area, the digital readout reduces crosstalk to a minimum and assures that the read-out cycle of the ADC is synchronised to the pixel clock of the CCD. The camera was controlled and read out through a fibre optical link, a very reliable communication in areas of high electromagnetic noise such as the accelerator.

6. Detailed Investigation of the Experimental Set-up

In this chapter, the components of the experimental set-up are described in more detail and their effects on the measurements are discussed. There are two main factors that limit the resolution of the measured diffraction patterns: the fluorescent crystal and the optical system of the camera. Measurements to determine their point spread function have been done.

There are methods to reconstruct images that have been acquired with a limited resolution. The Lucy-Richardson algorithm is described and tested on images acquired in a laboratory set-up. The careful use of this procedure allows to improve the images.

6.1. Fluorescent crystal

6.1.1. Uniformity

As visible in figure 5.3, there were some scratches on the fluorescent crystal. A projection of a central area of this image on the y axis (the same area that will be used in the analysis of the horizontal double slit diffraction patterns in chapter 7) is shown in figure 6.1. A Gaussian has been fitted to the centre of the intensity distribution. The deviation from this Gaussian is in the order of 2.5% rms.

6.1.2. Saturation effects

The Ce:YAG crystals go into saturation at high intensities [MRY⁺00, LBYW98]. The light output of the Ce:YAG crystal is then a non-linear function of the incident photon pulse energy. In the present experiment, an energy deposition of 10 μJ is expected within 100 fs on an area of approximately 10 mm^2 .

The saturation curve has been measured by comparing the intensity of the fluorescence light to the signal of the microchannel plate detector as a reference. The set-up is depicted in figure 6.2. A wire was inserted into the FEL beam in front of the fluorescent crystal to reflect part of the beam into the MCP detector.

Three measurement series were recorded at different operating voltages of the MCP detector. The intensity of the FEL has been calculated according to a previous

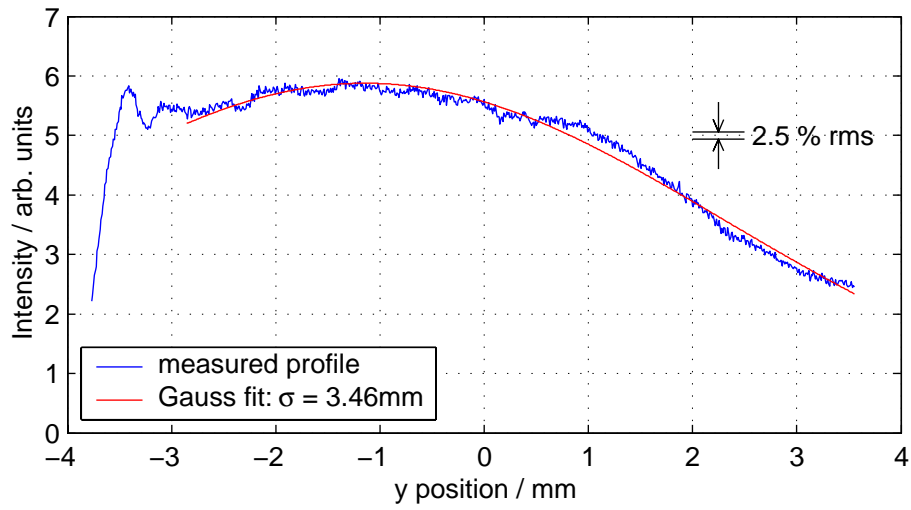


Figure 6.1.: Projection of the central area of the crystal that has been used for the measurements of the transverse coherence. The illumination is not completely uniform, but is apparent that no major scratches lie in the selected area.

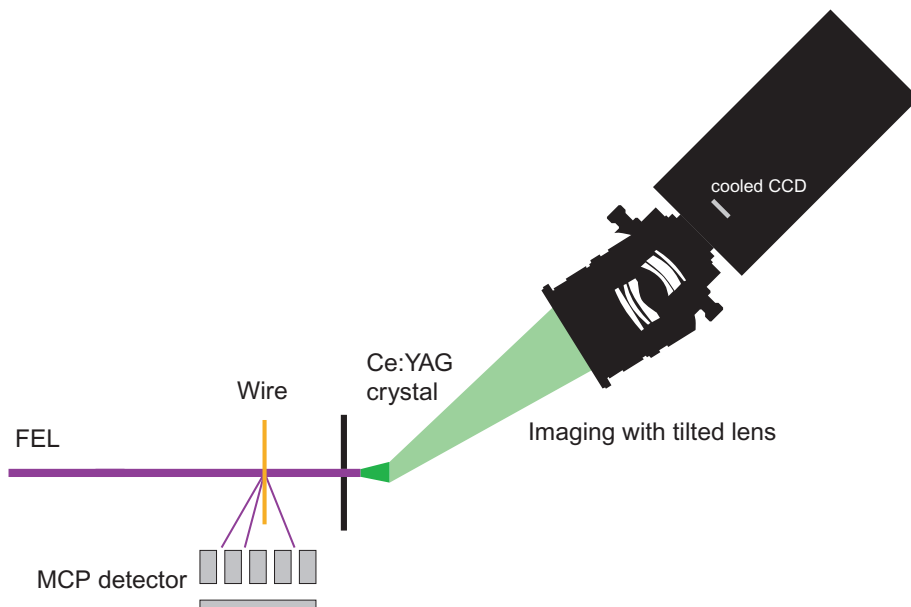


Figure 6.2.: Set-up to measure the saturation of the Ce:YAG crystal. The yield of fluorescence light is compared to the signal of a microchannel plate detector.

calibration [Faa01]. The gain of the MCP detector varies exponentially with the voltage across the micro-channels, it doubles every 50 V.

The light output of the crystal, as measured with the CCD camera, is shown in figure 6.3 as a function of the FEL pulse energy. Fluctuations of the FEL beam positions affect the coverage of the wire and therefore influence the amount of light that is reflected onto the microchannel plate. Its measurement depends therefore not only on the intensity of the FEL, but also on the direction of the beam. This can be measured with the fluorescent crystal and a correction can be applied. The wire creates a diffraction pattern on the crystal. For the present comparison of the signal from the MCP detector with the intensity on the fluorescent crystal, a region in the centre of the image was chosen to record fluctuations of the beam position in a similar manner with both detectors.

The fluorescent light yield of the crystal can be approximated by a function of the type

$$I_f = A (1 - e^{-I_i/I_0}) \quad (6.1)$$

where I_i is the incoming intensity, I_f the intensity of the fluorescence light and the parameters A and I_0 can be determined by a fit.

Equation (6.1) has been fitted to the three data sets from the different operating voltages for the MCP detector, as shown in figure 6.3. At intensities relevant for the present set-up, the three data sets are in good agreement. The inverse of the fit function to all data has been used to correct the images.

If $I_f > A$, equation (6.1) cannot be inverted, and already for $I_f \approx A$, the inversion results in very large values for I_i . This problem occurred a few times, because of X-rays hitting directly a single pixel of the CCD. These values have been eliminated and replaced by the value of an adjoining pixel.

6.1.3. Scattering effects

An ultraviolet photon entering in the Ce:YAG crystal can be absorbed by the Cerium ions, or, if it has sufficient energy, directly excite electronic transitions. Both processes result in the generation of electron-hole pairs. Their recombination yields visible photons. However, this does not happen immediately, the electrons and holes can travel a distance of a few micrometres in the crystal.

Photons created by fluorescence are emitted uniformly in all directions. Only a small fraction enters the camera directly, many are scattered inside the crystal. Those that are emitted with a large angle to the direction of the incident beam are internally reflected and leave the crystal at the edges. This can be seen for example in the images acquired with the FEL in figure 5.4.

As a consequence, the fluorescence photons may be emitted from a different location than the original conversion point, which leads to a degradation of the resolution.

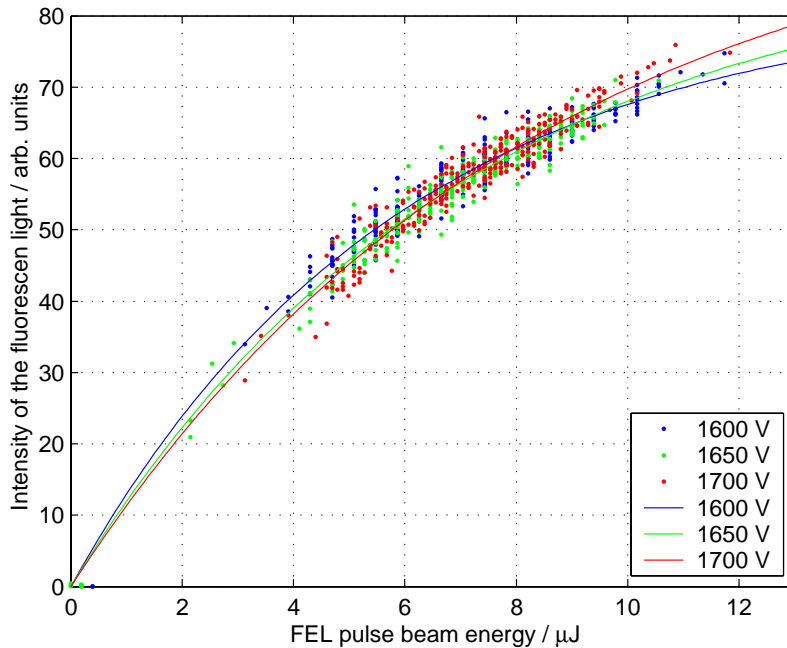


Figure 6.3.: Light yield of the Ce:YAG crystal as a function of the FEL pulse energy. The measured fluorescence light output is plotted as a function of the FEL pulse energy, which has been measured with a multichannel plate detector. Three data sets at different operating voltages of the MCP detector show good agreement. The lines are fits of the form $a(1 - e^{-bx})$ to the three data sets.

In addition, a uniform background of scattered photons is expected. The effects depend to a large extent on the impurities in the crystal.

The broadening of the image details was measured by imaging the fluorescent light of a point-like UV source. A slit of $10\ \mu\text{m}$ width was placed 1 mm in front of the crystal. It was illuminated by the photoinjector laser of the TTF linac (figure 6.4). The wavelength is 262 nm, corresponding to a photon energy of 4.73 eV. These photons are absorbed by the cerium ions; the direct YAG emission is not excited. The image was recorded with a microscope, a Leica MZ 7.5 with an objective lens $0.32\times$ and a zoom set to $5\times$, equipped with a CCD with $4.65\ \mu\text{m}$ pixel size. The resolution of this device in the object plane has been determined to $5\ \mu\text{m}$ by measuring its point spread function.

The broadening effect of the scattering is shown in figure 6.5. The profile of the slit is compared to the profile of the fluorescence light, which shows a slight asymmetry due to inhomogeneities of the crystal surface. A Gaussian fit is a good approximation of this profile. Its standard deviation is $22.5\ \mu\text{m}$, the full width at half maximum (FWHM) is $53.0\ \mu\text{m}$. Subtracting the contribution of the width of the slit and the resolution of the microscope, the FWHM for the scattered light is $52\ \mu\text{m}$.

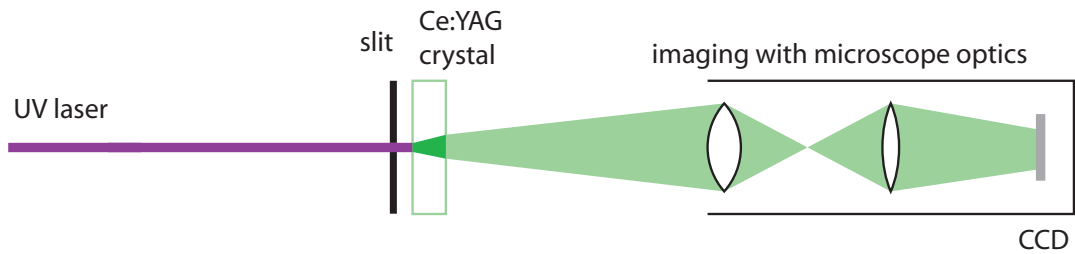


Figure 6.4.: Set-up to measure the broadening of the image due to the scatter of fluorescence photons in the Ce:YAG crystal.

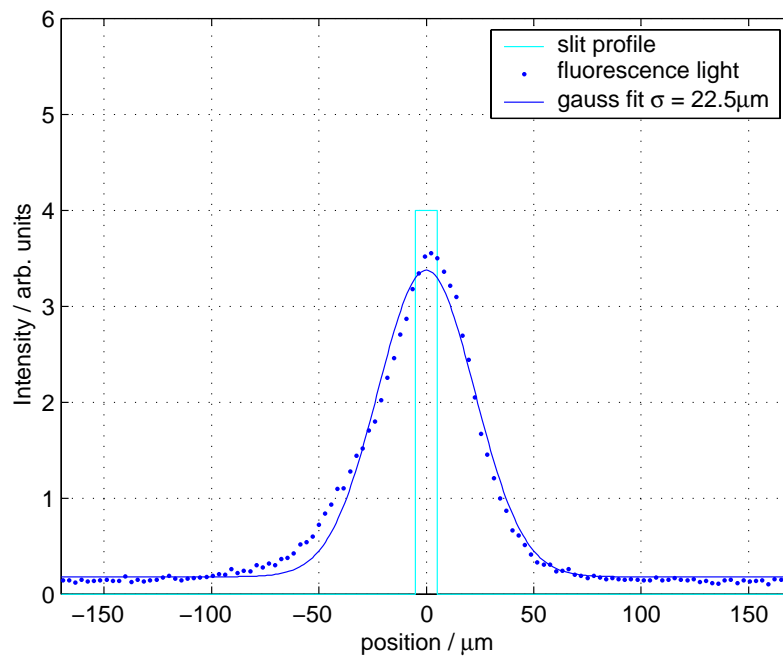


Figure 6.5.: Profile of the fluorescent light behind a slit. The actual slit profile is broadened by the scatter in the crystal. A Gaussian curve has been fitted to the data.

6.2. Camera

The imaging process in a camera involves usually a re-scaling with a certain magnification factor, but also distortions and blur are introduced. While distortion effects are small in the present set-up, the blur has to be considered in detail, as it reduces the visibility of the double slit diffraction patterns, apparently lowering the coherence of the FEL.

6.2.1. Calibration

The magnification of the camera was calibrated in the FEL by moving a small aperture directly in front of the crystal by a given distance and observing the movement of the spot of the FEL radiation on the crystal. The CCD had square pixels with a size of $(6.7\ \mu\text{m})^2$. The projection of this size onto the object plane yields a horizontal size of $13.1\ \mu\text{m}$. Due to the inclined plane of the object with respect to the optical axis of the camera, the vertical projected pixel size is different; it has been determined to be $9.1\ \mu\text{m}$.

6.2.2. Optical system

The resolution of an imaging lens system is limited by the diffraction at the aperture (which is increasing with small apertures) and by various lens errors (generally increasing with large apertures).

The resolution of an optical system can be expressed by its *modulation transfer function* (MTF), defined as the ratio between measured contrast in the image and actual contrast in the object as a function of the spatial frequency. In frequency space, the measured image is the product of the MTF with the scaled image. To measure the MTF, it is convenient to use test patterns that are segmented in areas with one pure spatial frequency, i.e. with a sine-like variation of the transmission, illuminated by diffuse light. Generally, the MTF gets smaller with higher spatial frequencies, because the smaller details are smeared out by the imaging process. The modulation transfer function is closely related to the *contrast transfer function* (CTF) [Nil01], which is determined by measuring the contrast of a square wave (bar) object as a function of spatial frequency.

The resolution of an optical system can also be characterized by the *point spread function* (PSF), defined as the distribution in the image plane produced by a point-like light source in the object plane. The variables u, v will be used in the object plane and x, y in the image plane a magnification factor of 1 will be assumed. Because the photons of incoherent light are emitted independently, the image Φ that an extended object creates with a given optical system is the convolution of the ideal image Ψ

with the point spread function P of the imaging system:

$$\Phi(x, y) = \int_{-\infty}^{\infty} \int_{-\infty}^{\infty} P(x - u, y - v) \cdot \Psi(u, v) du dv \quad (6.2)$$

or, using discrete distributions with indices m, n in the object plane and i, k in the image plane:

$$\Phi_{i,k} = \sum_{m,n} P_{i-m,k-n} \cdot \Psi_{m,n} \quad (6.3)$$

The image of a point-like object $\delta(x) \cdot \delta(y)$ will simply be $P(x, y)$, hence the name *point spread function*. For a perfect lens with finite aperture, the PSF is a Bessel function:

$$P(r) = \left(\frac{J_1\left(\frac{2\pi R}{\lambda b} r\right)}{\frac{2\pi R}{\lambda b} r} \right)^2 \quad (6.4)$$

where $r = \sqrt{u^2 + v^2}$, R is the radius of the aperture, λ the wavelength of the light and b the distance between lens and image. In the present case, $2R = 85 \text{ mm}/2.8$ and the factor $\frac{2\pi R}{\lambda b} = 1.2 \cdot 10^6 \text{ m}^{-1}$. The FWHM of the central peak of the Bessel function is $2.7 \mu\text{m}$ in the image plane, much smaller than the pixel size of the CCD.¹ Generally, lens errors dominate and P is much broader.

In frequency space, a convolution is just a multiplication; the point-like source corresponds to the unit function, its multiplication with the Fourier transform of the Point Spread Function describes the effect of the lens; thus, the Modulation Transfer Function is just the Fourier transform of the Point Spread Function.

It should be noted that this discussion of imaging system takes for granted that the light that comes from the object is incoherent. Coherence would introduce additional diffraction effects at all apertures in the lens. Indeed, fluorescent light is incoherent, as well as the light produced by an tungsten halogen lamp for the measurement of MTF and PSF. Therefore the image produced by different parts of the object can be treated independently. The total image is the sum of the intensities.

Measurement of the modulation transfer function

The modulation transfer function of the Nikkor 85mm f/2.8 D shift/tilt lens was directly measured with a test slide [Lam83], using the same distances between lens and object and the same aperture as in the accelerator. The tilt of the lens was set to 8.3° . The slide was illuminated from the back with incoherent, diffuse light created on a screen with a gooseneck lamp. The image was exposed for 1 ms, the longest exposure time possible. Figure 6.6 shows the recorded image.

¹If one reduced the aperture of the lens to f/22, the FWHM of the PSF would be $21 \mu\text{m}$, which is well above the pixel size.

A background (“black”) image was subtracted. To analyse the image, rectangles within the different zones of the slide were selected and a sine curve was fitted to their projections. The amplitude of these fits, divided by the reference amplitude given by the manufacturer of the slide, is the modulation transfer function of the given spatial frequency. As expected, the MTF decreases with increasing spatial frequency (figure 6.8).

Following the definition of ISO 12233 of limiting resolution as the “value where the imaged response equals 5% of the reference response or the value of the Nyquist limit, whichever is lower” [McD99], the following statements can be made:

- In horizontal direction, the modulation transfer function of the lens reaches a value of 0.05 for a spatial frequency of 17 mm^{-1} (figure 6.8a), corresponding to a limiting resolution of one line pair per $58 \mu\text{m}$.
- In vertical direction, the Nyquist limit of the CCD detector is reached, with a projected pixel size of $9 \mu\text{m}$. The limiting resolution is thus one line pair per $18 \mu\text{m}$.

Measurement of the point spread function

The PSF was directly measured by imaging a pinhole of $1 \mu\text{m}$ diameter, illuminated with incoherent light. Again, the tilt of the lens was set to 8.3° and the distances and aperture were the same as in the accelerator set-up. The size of this pinhole is much smaller than the diffraction limit of the lens, it can be regarded as a point-like source. Ten images were added to reduce noise, and a background image was subtracted. Due to the tilt of the lens, the PSF is not axisymmetric (figure 6.7). The FWHM of its x -projection is $5.6 \text{ pixels} = 37 \mu\text{m}$ in the image plane and $51 \mu\text{m}$ in the object plane (measured along the direction of the tilted object). In y direction, the FWHM is $2.2 \text{ pixels} = 15 \mu\text{m}$ in the image plane and $29 \mu\text{m}$ in the object plane.

The absolute value of the Fourier transforms of the projections are shown in figure 6.8. They correspond to the direct measurement of the MTF with the test slide.

6.2.3. Deconvolution of the optical resolution

The knowledge of the lens errors that limit the resolution in an imaging system can be used to reverse the detrimental effects to some extent. Recall that the measured image Φ can be described by a convolution of the ideal image Ψ with the point spread function P (see Eq. (6.3)). Due to the convolution, Φ is a much smoother function than Ψ . In the Fourier space, the high spatial frequencies will be generally reduced.

The system of equations (6.3) can in principle be solved for Ψ if the point spread function P is accurately known; in Fourier space, a convolution is simply a multiplication, so the solution can be found by division. However, the measured image is

6. Detailed Investigation of the Experimental Set-up

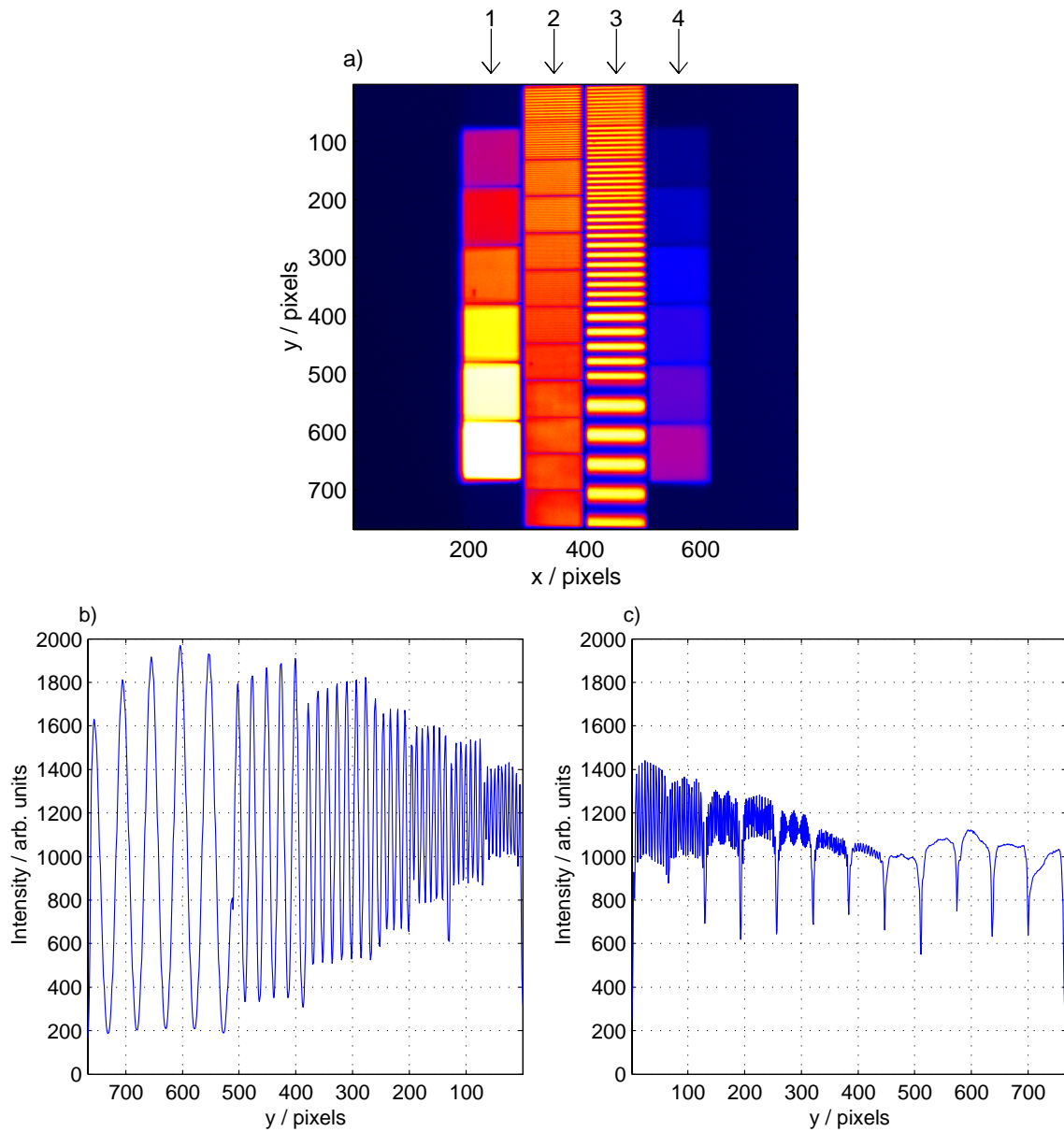


Figure 6.6.: a) Test slide with sinusoidal density modulation. 1) and 4) different levels of grey, 2) sinusoidal density modulation with a period of 3.9 to 50 μm , 3) with a period of 62.5 to 500 μm . The slide has been imaged with the Nikkor 85mm f/2.8 D shift/tilt lens at the same distance and with the same tilt as in the set-up for the TTF linac. b) projection of the sine pattern 3, c) projection of the sine pattern 2. In reality, the amplitude of the oscillation is constant, in the image, it decreases with higher spatial frequency.

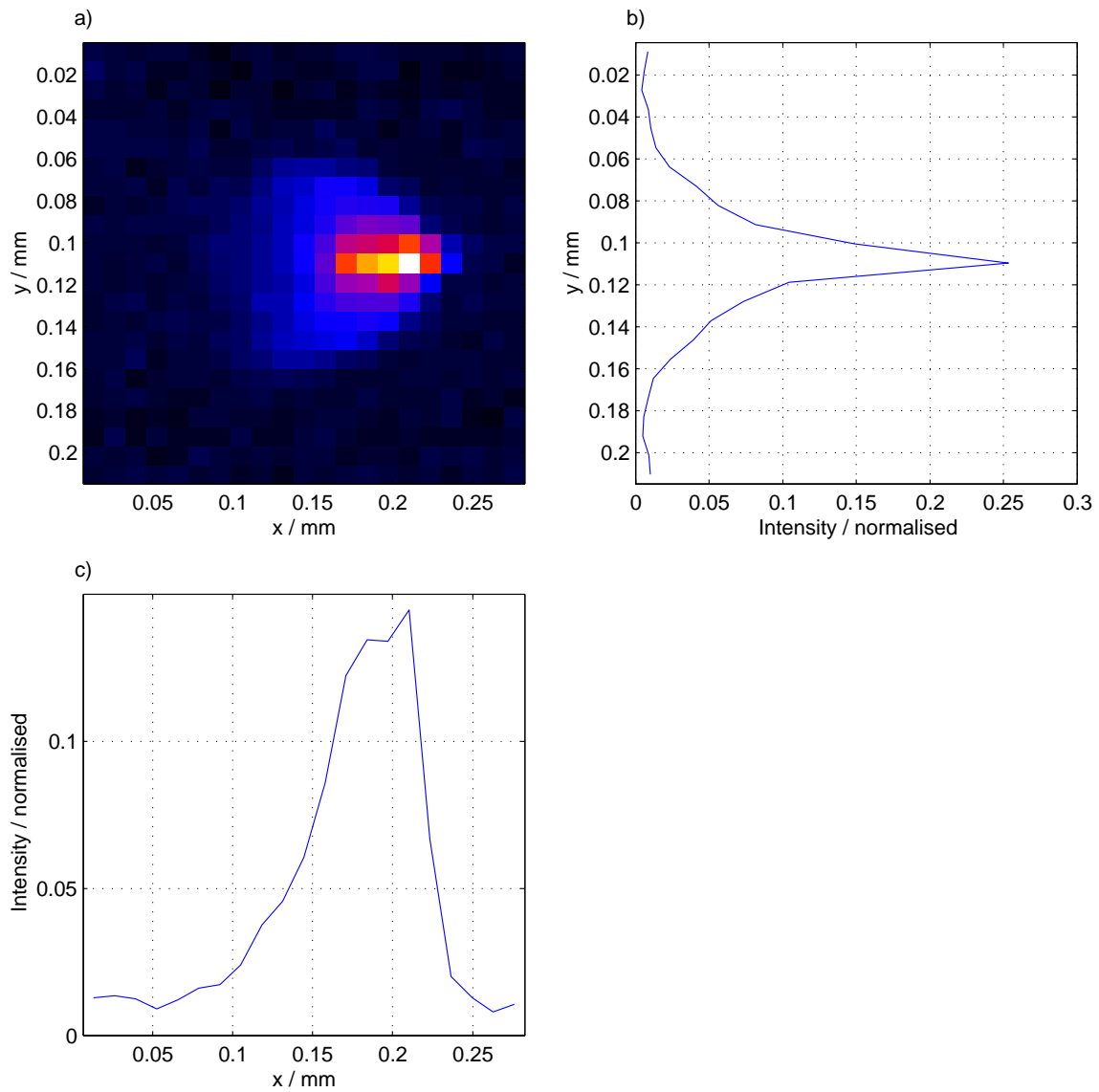


Figure 6.7.: a) Measured Point Spread Function of the Nikon 85mm f/2.8 D shift/tilt lens. Only the central part of the image is shown. The lens was tilted around a vertical axis, in clockwise direction seen from the top; the PSF shows a long tail to the left of the image. b) and c) Projections along the x and y direction.

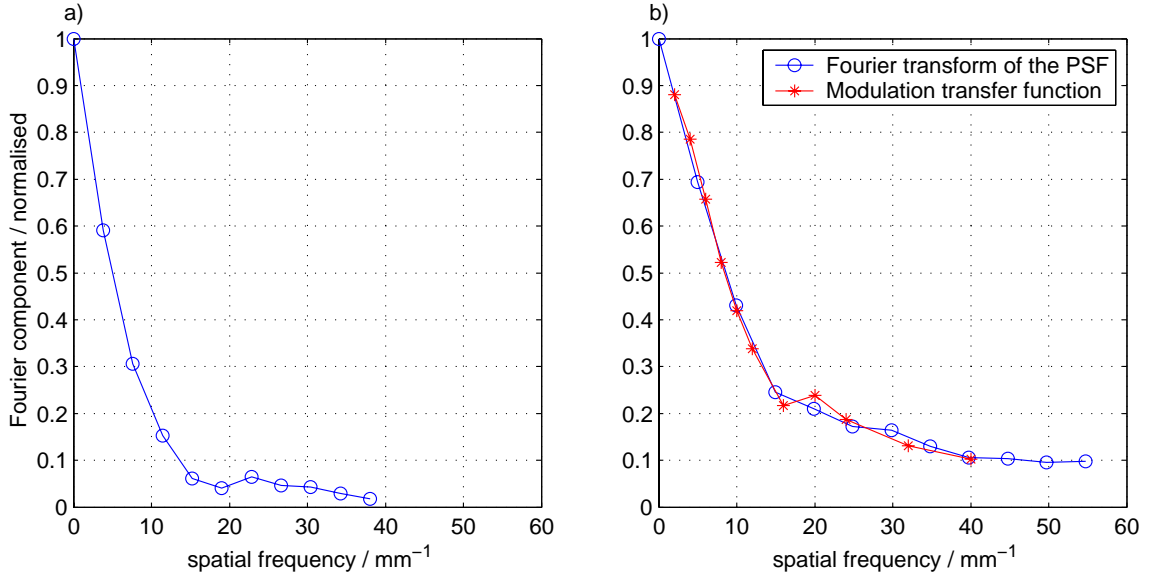


Figure 6.8.: Fourier transform of the projections of the PSF in figure 6.7, a) in x direction, b) in y direction. The modulation transfer function, measured with the sinusoidal density pattern (see also figure 6.6) is shown for comparison. This curve has been measured in two parts, from 2 to 16 and from 20 to 40 mm⁻¹, respectively. This accounts for the discontinuity between 16 and 20 mm⁻¹.

always affected by noise:

$$\Phi_{i,k} = \sum_{m,n} P_{i-m,k-n} \cdot \Psi_{m,n} + \mathbf{N}_{i,k} \quad (6.5)$$

where \mathbf{N} is a random noise matrix. Such noise could be read-out noise of the CCD, or even photon statistics for low intensities. This varies typically from pixel to pixel, two adjacent pixels are not correlated.² The Fourier spectrum of this noise is evenly distributed over the complete spectrum. If one now neglects the noise and solves Eq. 6.5 with $\mathbf{N} = 0$, the high-frequency part of this noise will be amplified; furthermore, this will inevitably lead to negative values for Ψ . (For an example, see figure 6.10.)

It could now appear suitable to smooth the function Φ prior to solving Eq. (6.3) by lowering the high-frequency Fourier components. However, keeping in mind that this smoothing can be regarded in object space again as a convolution with some appropriate function, it becomes obvious that nothing is gained, the original difficulty simply reappears.

²This is not true if the image is acquired with an analogue camera. In this case, electromagnetic disturbances in the analogue signal transmission lead to a correlated noise for horizontally adjacent pixels.

More appropriate are methods based on the maximum likelihood principle, imposing additional constraints on the smoothness and non-negativity of the reconstructed distribution. Originally developed in the 1970's by Lucy [Luc74] and Richardson [Ric72], this method (and the numerically accelerated version [BA97]) are widely used to correct for lens errors.

The Lucy-Richardson algorithm is derived in the following. For the sake of clarity, the treatment is restricted to a one-dimensional distribution and a magnification factor of 1.

The point spread function is the probability $P(x|\xi)dx$ that a photon originating in ξ is detected at the point x :

$$\Phi(x) = \int \Psi(\xi)P(x|\xi)d\xi \quad (6.6)$$

This is the same as equation (6.3), written in the language of probability theory: If Eq. (6.6) is applied for a large number of photons, Eq. (6.3) results. Introducing the inverse probability $Q(\xi|x)$ that the real value is in the interval $[\xi, \xi + d\xi]$, when the measured value has been in the interval $[x, x + dx]$; from the normalisation of the probability $P(x|\xi)$, it follows that

$$\Psi(\xi) = \int \Phi(x)Q(\xi|x)dx \quad (6.7)$$

Unfortunately, one cannot simply solve this equation for $\Phi(x)$ because $Q(\xi|x)$ depends on $\Psi(\xi)$. This can be calculated from Bayes' theorem on conditional probabilities

$$Q(\xi|x) = \frac{\Psi(\xi)P(x|\xi)}{\int \Psi(\xi)P(x|\xi)d\xi} \quad (6.8)$$

The equations (6.7) and (6.8) suggest the following method of iteration:

1. Use the measured distribution Φ as a first guess $\Psi^{(0)}$
2. With the known point spread function $P(x|\xi)$, take Eq. (6.8) to calculate a first estimate $Q^{(1)}(\xi|x)$:

$$Q^{(1)}(\xi|x) = \frac{\Psi^{(0)}(\xi)P(x|\xi)}{\int \Psi^{(0)}(\xi)P(x|\xi)d\xi} \quad (6.9)$$

3. Insert this estimate for $Q(\xi|x)$ in Eq. 6.7 to calculate an improved estimation of Ψ :

$$\Psi^{(1)}(\xi) = \int \Phi(x)Q^{(1)}(\xi|x)dx \quad (6.10)$$

4. The iteration continues by calculating $Q^{(2)}$ using $\Psi^{(1)}$ and $\Psi^{(2)}$ using $Q^{(2)}$. The procedure is repeated as long as necessary.

This procedure is called the *Lucy-Richardson* algorithm.

It has been shown that this method conserves the total intensity, avoids negative solutions, converges to a distribution and the likelihood that $\Psi^{(n)}$ is imaged with Eq. (6.6) as Φ increases with each iteration [Luc74]. However, this likelihood does not reach its absolute maximum. Instead, the smoothness of the reconstructed image is better than of the one that maximizes the likelihood. This is seen as an advantage since very high spatial frequency contributions to the measured distribution can be generally attributed to noise.

The Lucy-Richardson deconvolution algorithm can be accelerated by evaluating the change each pixel is subject to due to the iteration instruction. The change from the two last iterations is evaluated to predict the direction of the following step; one achieves thus a faster convergence of the reconstructed image [BA97]. An implementation of the accelerated Lucy-Richardson algorithm can be found in the MATLAB Image Processing Toolbox³ [Mat01a].

The point spread function may depend on the position in the image. Lens errors, for example, are more important in the outer part of the observed field, thus the width of the PSF increases as one moves the aperture away from the centre or out of the focal plane. However, a deconvolution with a spatially varying point spread function is numerically elaborate since it cannot be done in Fourier space [BRHM96]. Here, the narrow PSF of the centred, focused aperture has been used in the data analysis in order to avoid that an image is reconstructed with a higher contrast than is present in the real diffraction pattern.

6.2.4. Test of the Lucy-Richardson algorithm

The Lucy-Richardson algorithm has been applied to measurements with a simulated defocusing of the image [Ric72, Mat01a], but it seemed useful to demonstrate its effectiveness on images that have been acquired with a real lens, producing actual lens errors. Thus, an experiment was set up with the same lens and CCD that were installed in the FEL (figure 6.9), using the same aperture, distances and angles. An image of a fly's wing, showing structures on a sufficiently small scale, was taken with the Nikkor 85mm f/2.8 D shift/tilt lens.⁴ The point spread function of this lens, with the given distances, has been described in section 6.2.2.

To demonstrate that the direct inversion of the convolution (6.5) is not applicable in practice, this is demonstrated with the image. Figure 6.10 shows the result. The noise of the image is amplified to a point where it appears as a checkerboard pattern, spurious details are reconstructed.

Therefore, the image has been deconvoluted using the Lucy-Richardson algorithm. The result is shown in figure 6.11. The visual improvement of the image quality

³the function name is `deconvlucy`

⁴The fly was found dead on the windowsill in the office. No animal was harmed in the preparation of this PhD thesis.

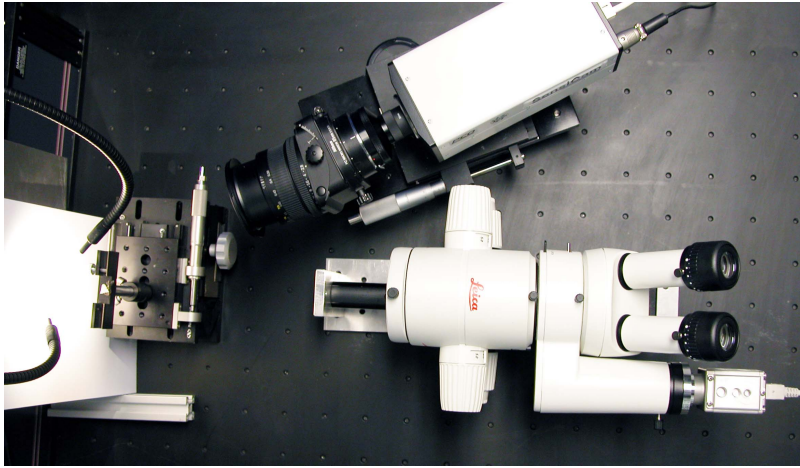


Figure 6.9.: Experimental set-up to demonstrate the Lucy-Richardson algorithm. The test object is on the left, illuminated by a gooseneck lamp. At the top of the photo, the camera with the Nikon lens is shown, at the bottom, the microscope that is used to take a reference image.

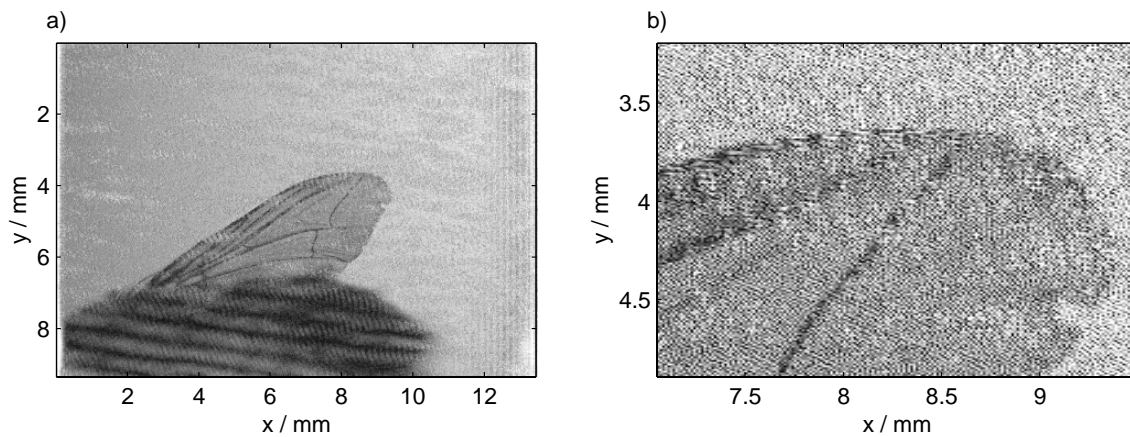


Figure 6.10.: Deconvolution of the resolution of the imaging system by inversion of the convolution equation 6.3. a) Complete image, b) detail. Compare with figure 6.11.

6. Detailed Investigation of the Experimental Set-up

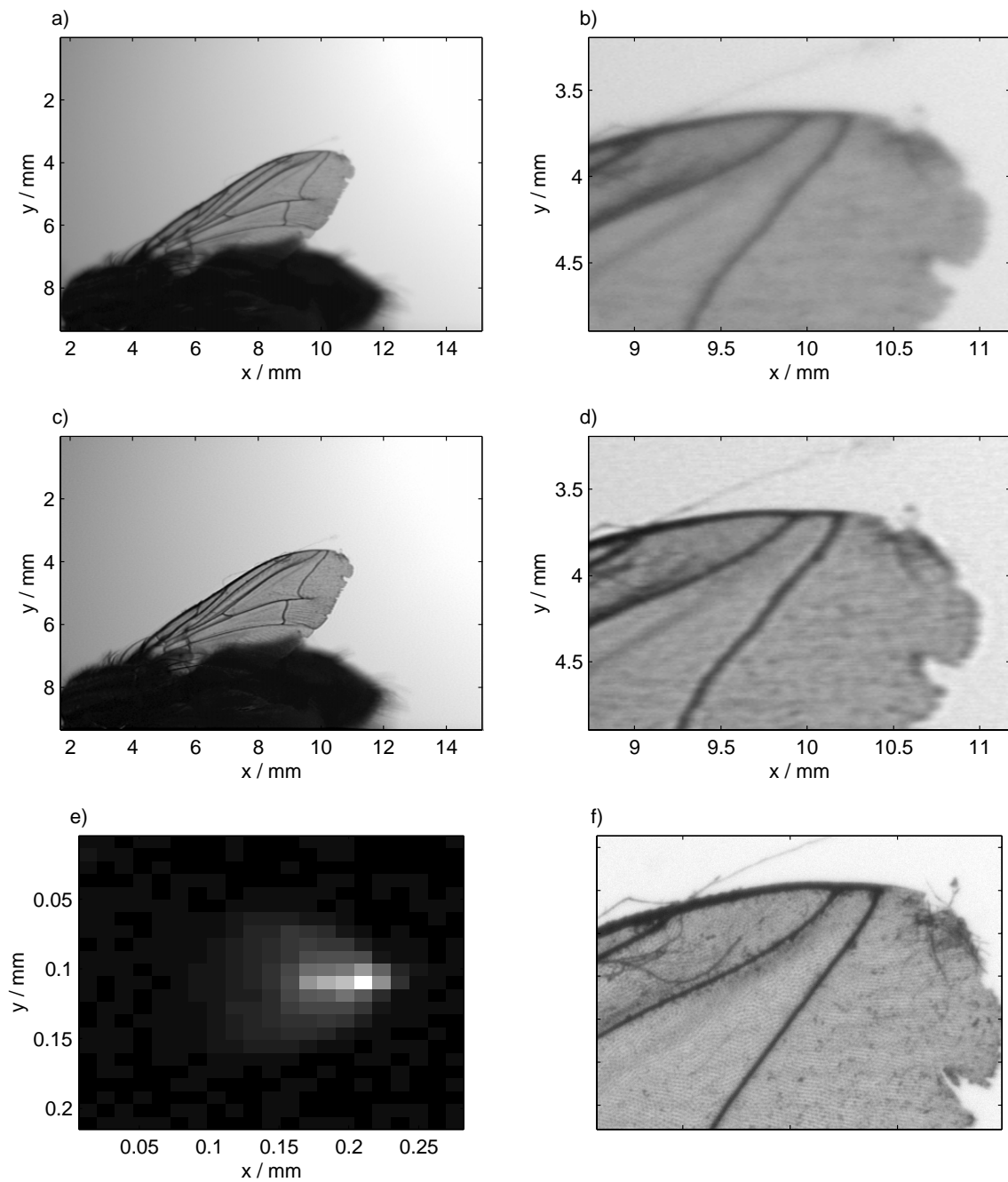


Figure 6.11.: Image of a fly's wing, processed with the Lucy-Richardson algorithm. a) Raw image, acquired with the Nikkor 85mm $f/2.8$ D shift/tilt lens, b) magnified detail, c) image processed with 10 iterations of the accelerated LR-algorithm, d) magnified detail, e) point spread function used for the deconvolution and f) reference image, acquired with the Leica microscope.

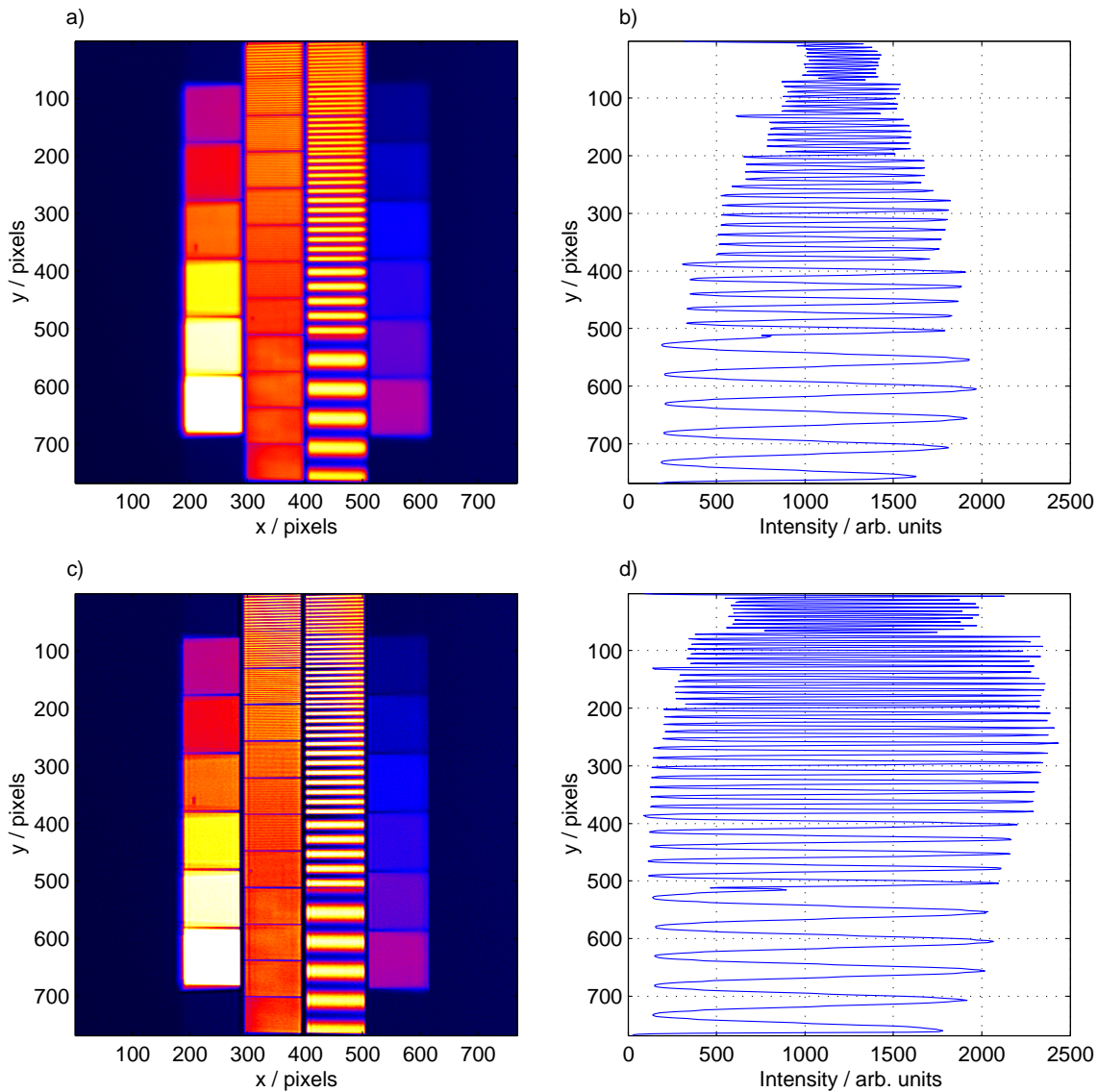


Figure 6.12.: Image of the resolution test pattern, processed with the Lucy-Richardson algorithm. a) Raw image, acquired with the Nikkor 85mm f/2.8 D shift/tilt lens, b) projection of the right column of sine patterns, c) image processed with 10 iterations of the accelerated LR-algorithm and d) projection.

is obvious. A comparison with an image taken with a high-resolution microscope (figure 6.11f) shows that the reconstructed details are actually present in the object.

A more quantitative analysis is possible with the resolution test pattern that has been used for the measurement of the modulation transfer function in section 6.2.2. The raw and the processed images are shown in figure 6.12. From the measured

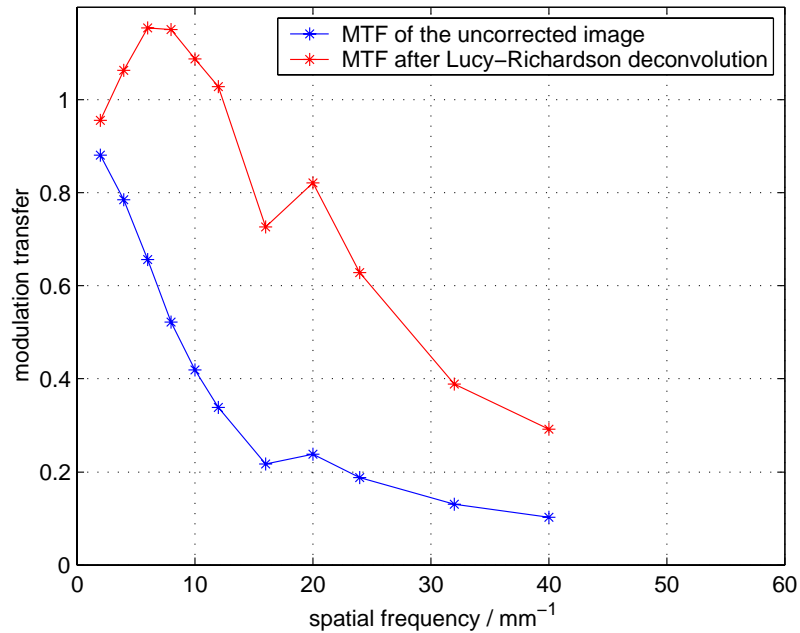


Figure 6.13.: Modulation transfer function after application of the Lucy-Richardson algorithm. Compare to figure 6.8.

modulation depth, one obtains the modulation transfer function of the total imaging system, including the reconstruction. This is shown in figure 6.13. The value of the MTF surpasses one in the frequency range of 4 to 12 mm^{-1} . This means that details with a size of few hundred micrometres are exaggerated by this process.

This may be due to an overestimated point spread function: for the imaging of the pinhole, the focusing was not trivial since the shape of the image changed with the focus. Indeed, the ideal focus distance for the horizontal and vertical direction were not the same, but displaced by a few hundred micrometres. A compromise between the two had to be made. Focusing on the slide with the sinusoidal density modulation was more straightforward, since the optimum focus distance could be seen easily: the focus was adjusted until more and more of the fields were visible. Thus, the vertical modulation transfer function was optimised. Another reason for an overestimation of the contrast might be the binning of the point spread function by the CCD chip. The pixel size is not much smaller than the width of the PSF in vertical direction.

6.2.5. CCD detector

In this section, the influences of the CCD detector on the measurements are discussed. The linearity of the CCD is better than 0.1% [PCO02], due to the purely digital read-out. As opposed to images acquired with an analogue data transfer, a common offset of all pixels in a row, due to charge induced in the signal cables, was not observed.

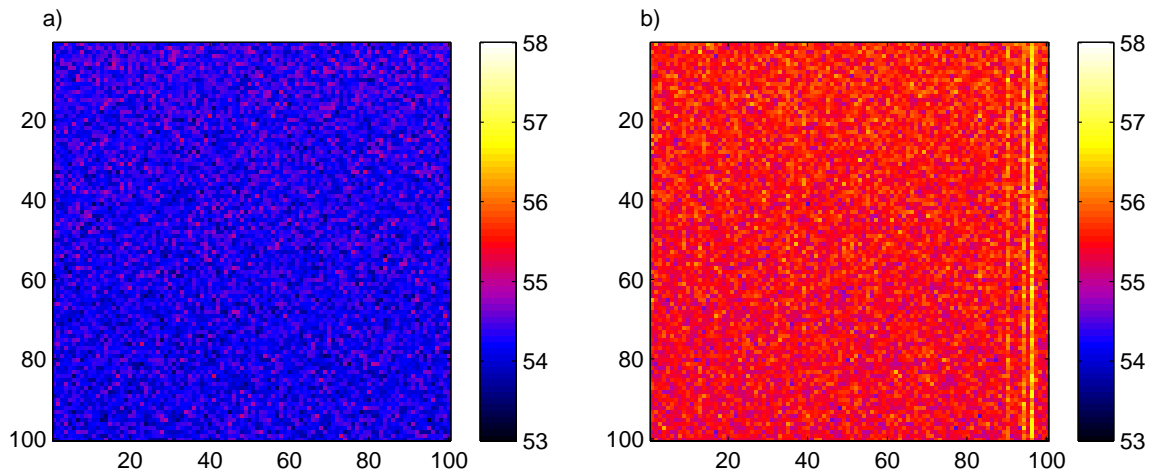


Figure 6.14.: Dark level of the CCD, a) directly after installation and b) after four months of operation. A region of $100 \cdot 100$ pixels, located in the upper left corner of the images of the diffraction patterns, is shown. The vertical lines are due to radiation damage in the read-out pixel row. Fifty measurements have been averaged.

The radiation damage to the CCD chip can be quantised by measuring the pixel noise, i.e. the dark charge accumulated without irradiation. During four months of operation, the dark charge increased by 1.3 LSB of the ADC, corresponding to approximately 30 electron-hole pairs, during the four months of operation.

In addition to the overall noise, an increase in the dark charge is also observed on individual pixels and on complete columns. Three of these are shown in figure 6.14. It is conjectured that the read-out is done in vertical direction and that transfer pixels have degraded due to the radiation.

The pixel noise, a common measure for the radiation damage to semiconductor detectors, has not changed significantly during four months of operation. Its distribution is roughly Gaussian (figure 6.15). It can be concluded that the radiation has not degraded the overall detector performance. The effect of single noisy detector and transfer pixels can be

The noise originates for one part in thermally generated electron-hole pairs within the pixels of the CCD, for the other part in the transfer and ADC. The CCD noise decreases exponentially with the temperature of the chip. Therefore, it was cooled by double-stage Peltier thermoelectric cooling element to -12°C . The signal-to-noise ratio (SNR) could be improved, at the expense of resolution, by adding the charge from several pixels: while the signal increases linearly with the number of pixels, the pixel noise increases only as the square root of the number. If the charge is added directly in the CCD chip before passing it to the ADC this is called *hardware binning*. This is advantageous compared to *software binning* where the pixels are combined after digitisation, because the noise of the ADC affects the signal only once. The

6. Detailed Investigation of the Experimental Set-up

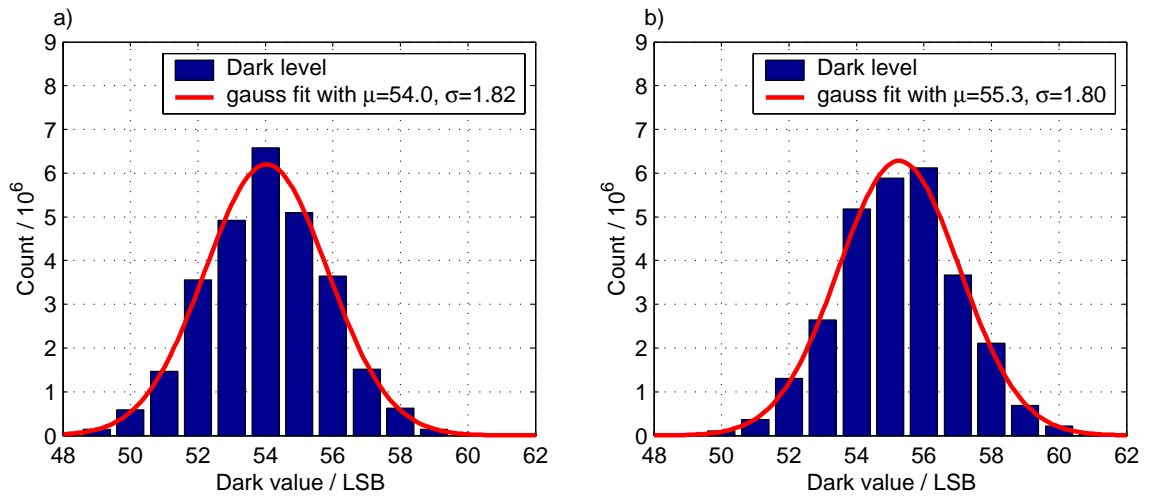


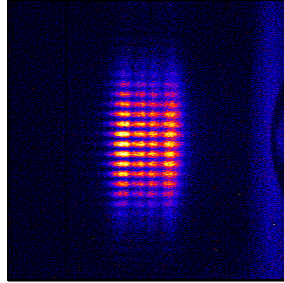
Figure 6.15.: Histograms of the dark level, a) directly after installation and b) after four months of operation. A Gaussian has been fitted to the data. The mean dark current has increased only slightly, its standard deviation is not changed significantly.

PCO SensiCam supports hardware binning of up to 8 pixels in horizontal and 32 pixels in vertical direction.

This dark level was subtracted from the measured images. This corrects for individual offsets of the pixels, but introduces an additional noise. The background has been averaged over 50 measurements, yielding a relative noise increase in the image of 0.26 LSB. If a single image had been used as a background, the noise increase would be 1.82 LSB.

For the measurements of the diffraction patterns of horizontal slits, vertical resolution is more important than horizontal. Therefore, the horizontal binning has been set to 4, while the vertical binning was disabled. For the vertical slits, the interchanged binning was used.

To increase the signal-to-noise ratio (SNR) in the images, the measurements of a few hundred FEL pulses have been added for each configuration.



Part IV.

Results

We must all hang together, or assuredly we shall all hang separately.
Benjamin Franklin

Figure on the previous page: double slit diffraction pattern of the TTF FEL.

7. Measurements of the Transverse Coherence

The double slit diffraction patterns recorded at the TESLA Test Facility FEL allow a straightforward determination of the transverse coherence, as discussed in chapter 3. Diffraction patterns from different slit separations show the dependency of the transverse coherence on the distance. Two methods are used to determine the transverse coherence from the measurement data: for one thing, the visibility of the central fringe is used as a measure of the coherence at the slit separation. Furthermore, the intensity distribution of a double slit diffraction pattern is computed in Fresnel theory and compared to the data. The results of these two methods are verified on diffraction patterns that have been simulated with numerical methods.

Measurements have been performed under different accelerator conditions, i.e. with different properties of the electron bunch. First, a measurement at 100 nm FEL wavelength with a slit separation of 1 mm is presented and its analysis is described in detail.

7.1. Measurements of the FEL in saturation

Measurements of double slit diffraction patterns were performed on February 22, 2002 (figure 7.1). The TTF FEL was running reliably with a bunch charge of 1.95 nC. Before the actual coherence measurements were started, the performance of the FEL was optimised by adjusting the electron trajectory in the undulator and the respective phases of the beam and the RF systems.

As a result of these optimisations, the FEL process was saturated, i.e. maximum output power was reached. This was confirmed by observing the bunch-to-bunch fluctuations of the FEL pulse energy. Saturation leads to a smaller variance in the otherwise purely stochastic FEL process. The wavelength of the radiation was measured to be 100 nm. The middle of the two slits was aligned with respect to the centre of the beam.

The images have been recorded by the computer that is connected to the camera. They were saved on a network drive and synchronised with auxiliary data from the accelerator, which were recorded by a distributed data acquisition system. The data acquisition system is detailed in appendix D.

Image series with 0.5, 1, 2 and 3 mm slit separation were recorded. The averages of

7. Measurements of the Transverse Coherence

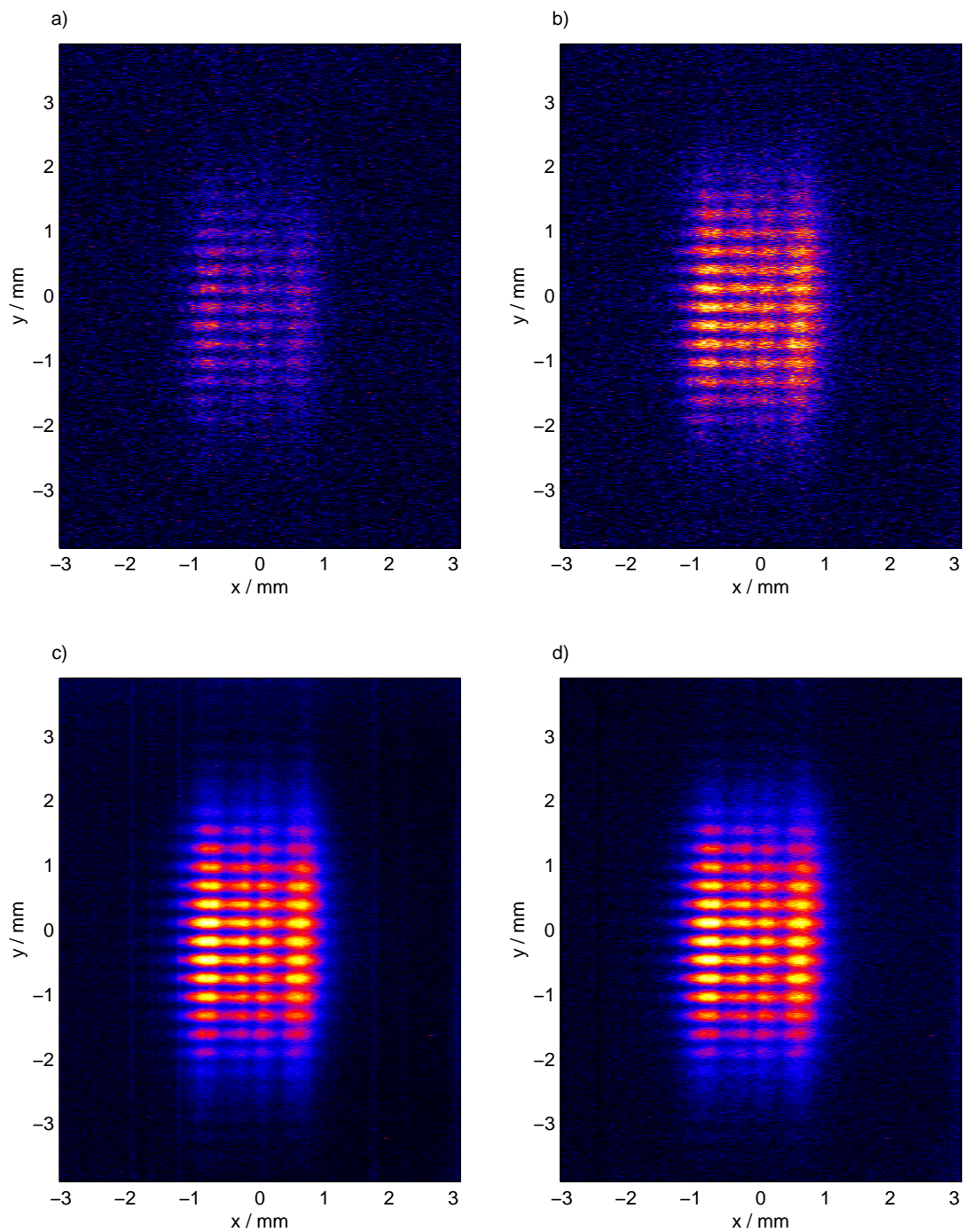


Figure 7.1.: Measured diffraction patterns for 1 mm slit separation: a) a typical image, b) the brightest image in a series of 100 measurements, c) the average of 100 measurements, and d) the average, with dark current subtracted.

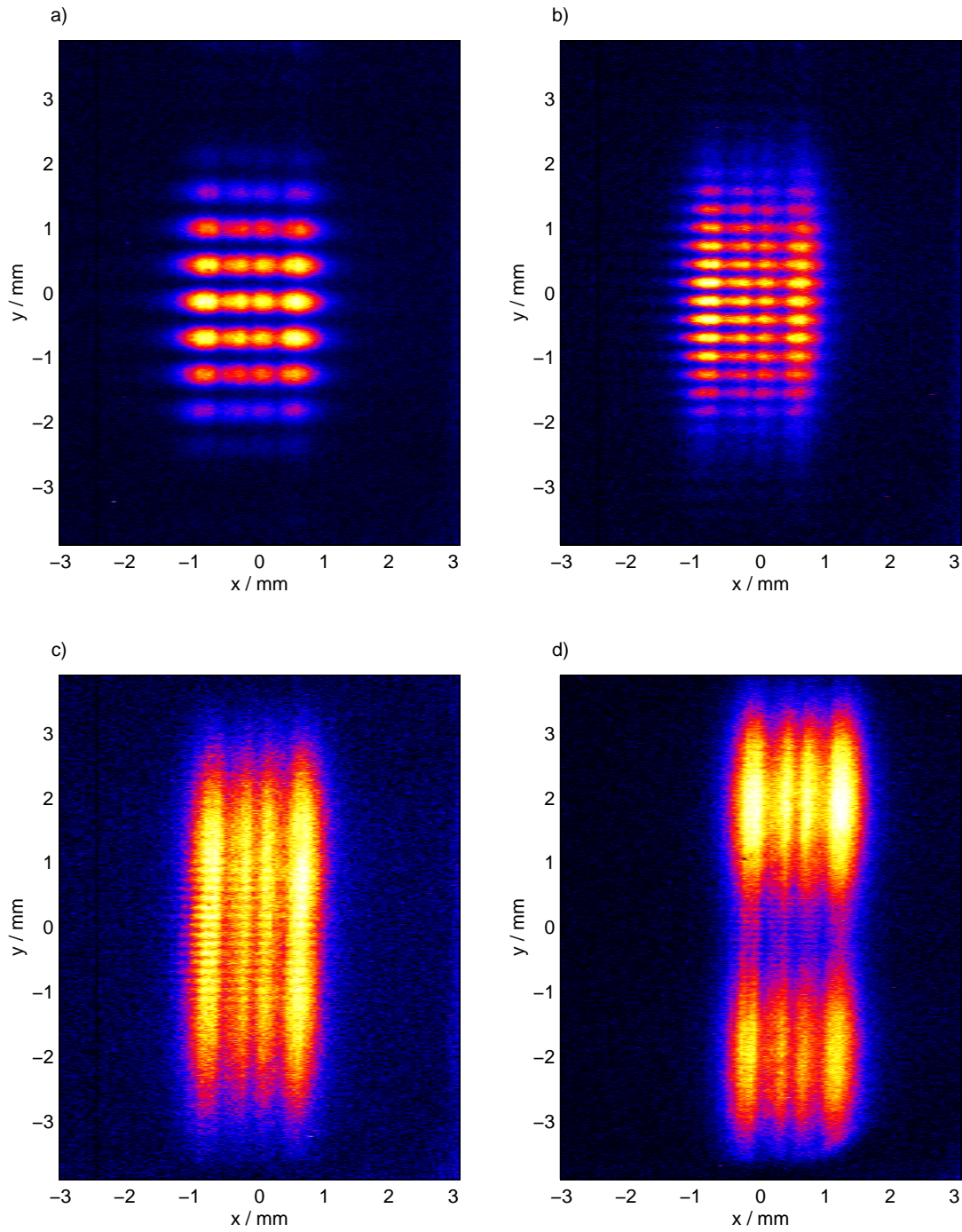


Figure 7.2.: Measured horizontal double slit diffraction patterns at 100 nm FEL wavelength. a) 0.5 mm, b) 1 mm, c) 2 mm and d) 3 mm slit separation.

100 images are shown in figure 7.2. The horizontal double slit diffraction fringes are clearly visible, their distance is inversely proportional to the separation of the slits. An intensity variation is also visible along the direction of the slits, i.e. the horizontal axis. Two absolute maxima near the end of the slit and two smaller relative maxima in the middle are visible. This pattern is due to the finite slit length.

Due to the short distance between the slits and the observation plane, the Fresnel diffraction theory has to be applied. The effects of near field diffraction manifest themselves especially in the diffraction pattern with 3 mm slit separation (figure 7.2 d): the single slit diffraction patterns of the two slits overlap barely and the intensity in the middle of the image is much lower than at $y = \pm 1.5$ mm. Furthermore, the visibility varies across the diffraction pattern. It is highest in the middle and decreases outwards. This effect is best visible in the patterns of 2 and 3 mm slit separation (figure 7.2c and d).

7.2. Simulations

The formation of the FEL radiation in the undulator, the diffraction at the double slits and the propagation to the fluorescent crystal, the conversion of VUV photons to visible light and the imaging of the latter onto the CCD have been simulated. The resulting images are subjected to the same analysis routines as the measured data. The amplitude and phase of the computed electromagnetic field are precisely known. Thus, the theoretical value for the coherence function can be compared with the coherence that is determined from the images with the two analysis routines. That way, it is possible to gain information on the accuracy of the analysis.

7.2.1. FEL

The wave front of the 100 nm FEL beam at the exit of the undulator was computed by Saldin, Schneidmiller and Yurkov with the code FAST3d (see section 2.5). The beam is represented in the SVA approximation by a complex field amplitude.

The FEL bunch is separated longitudinally in 118 slices with a thickness of 1 μ m (measured in the laboratory system). In each of these slices, the electric field amplitude is calculated on a square grid of 201×201 points. The code FAST models the SASE process as closely as possible. In particular, the stochastic nature of the spontaneous undulator radiation, which initiates the SASE process, is incorporated. This leads to distorted wave fronts at the exit of the undulator.

The coherence of the FEL beam may be varied by adjusting the distortion of the wave fronts. This may seem unnecessary, as FAST3d takes effects that influence the coherence into account, such as the formation from spontaneous undulator radiation and the divergence of the beam. However, the present analysis will show that the current version of FAST3d overestimates the coherence of the TTF FEL. This may

be an indication that too optimistic assumptions have been made on the electron beam properties: it was presumed to be round and having a Gaussian distribution. In reality, the transverse phase space distribution of the beam is distorted by the longitudinal compression. This disagreement between the simulation and the measurements is currently being investigated, and a new version of FAST3d results in a lower transverse coherence of the radiation [Yur03]. However, it is not yet published, hence a different approach is followed in this thesis.

The complex field amplitude in front of the slits is multiplied with a space-dependent phase aberration. This decreases the transverse coherence function. The method is the same that has been applied to the Gaussian beam in section 3.7. The phase aberration is randomised for each slice of the FEL bunch and the intensities of the diffraction patterns are added. Hereby, the visibility of the interference fringes is lowered.

The reduction of the coherence of the FEL beam improves the agreement between the measured and the computed diffraction patterns. The magnitude of the aberration is adjusted to optimise this agreement.

7.2.2. Diffraction

The propagation of the wave fronts from the exit of the undulator through the double slit to the observation plane is computed with the code GLAD (section 3.6.4). To take into account the expansion of the beam, a larger grid of 512×512 points is used. As in section 3.7, the slices are propagated individually, and the resulting intensities at the observation plane are added.

The distortion of the wave fronts computed by FAST results in distorted diffraction patterns for each slice. In the overall pattern, the visibility is lowered, as compared to the coherent case (see section 3.7).

7.2.3. Effects of the experimental set-up

For a comparison of simulated and measured diffraction patterns, the effects of the experimental set-up on the diffraction patterns (see chapter 6) are taken into account. This is shown in figure 7.3.

- The image is convoluted with the scattering function of the crystal. A two-dimensional Gaussian distribution with a standard deviation $\sigma = 22.5 \mu\text{m}$ is used, as it has been determined in section 6.1.3.
- The nonlinear response function of the Ce:YAG crystal is taken into account by applying a function (6.1) with parameters as determined by comparison with a calibrated reference detector in section 6.1.2.

7. Measurements of the Transverse Coherence

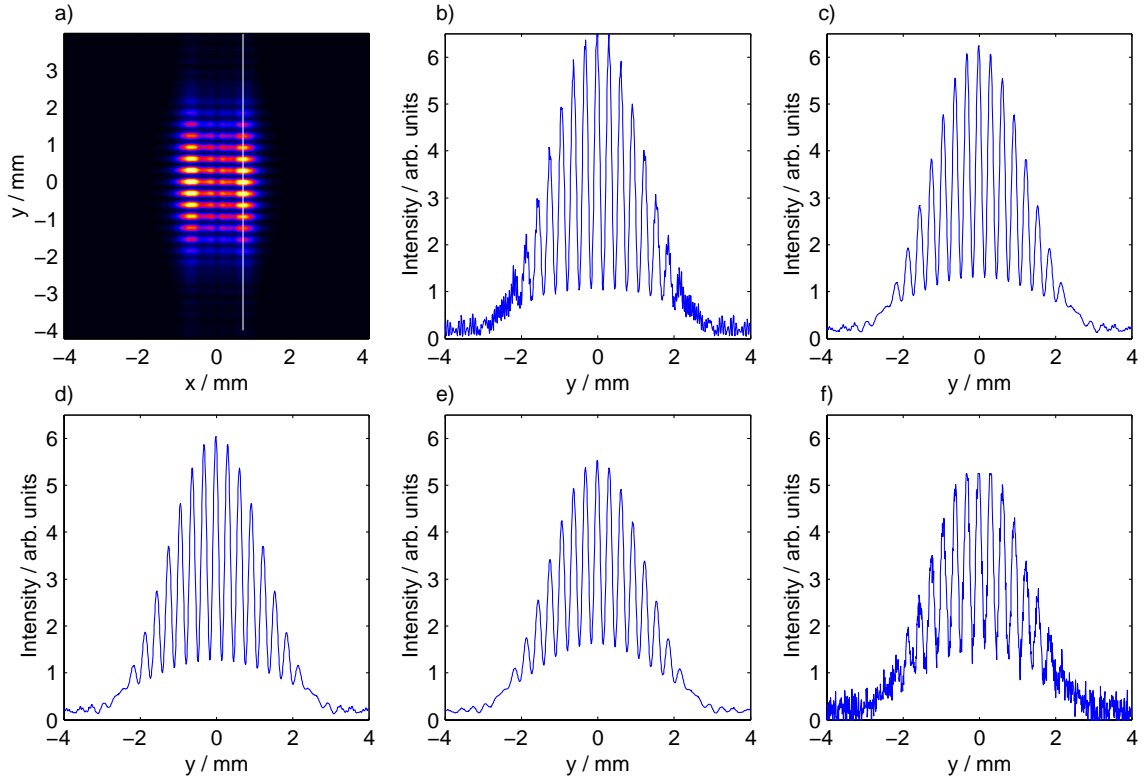


Figure 7.3.: a) Simulated diffraction pattern for 1 mm slit separation, b) intensity distribution along the white line in a. c) Convolution with the scattering function of the fluorescent crystal. d) Application of the non-linear response curve of the Ce:YAG crystal. e) Convolution with the point spread function of the lens. f) Addition of Gaussian pixel noise in the CCD chip.

- The imaging process of the fluorescent light is simulated by convoluting the pattern with the point spread function of the optical system. The asymmetric PSF of the tilted Nikkor lens is used as determined in section 6.2.2.
- Noise is added to the image, using the Gaussian distribution of section 6.2.5, to obtain the same signal-to-noise ratio as for the experimental data.

The resulting images should be equivalent to the measured images and are subjected to the same analysis procedure. The images are shown in figure 7.4.

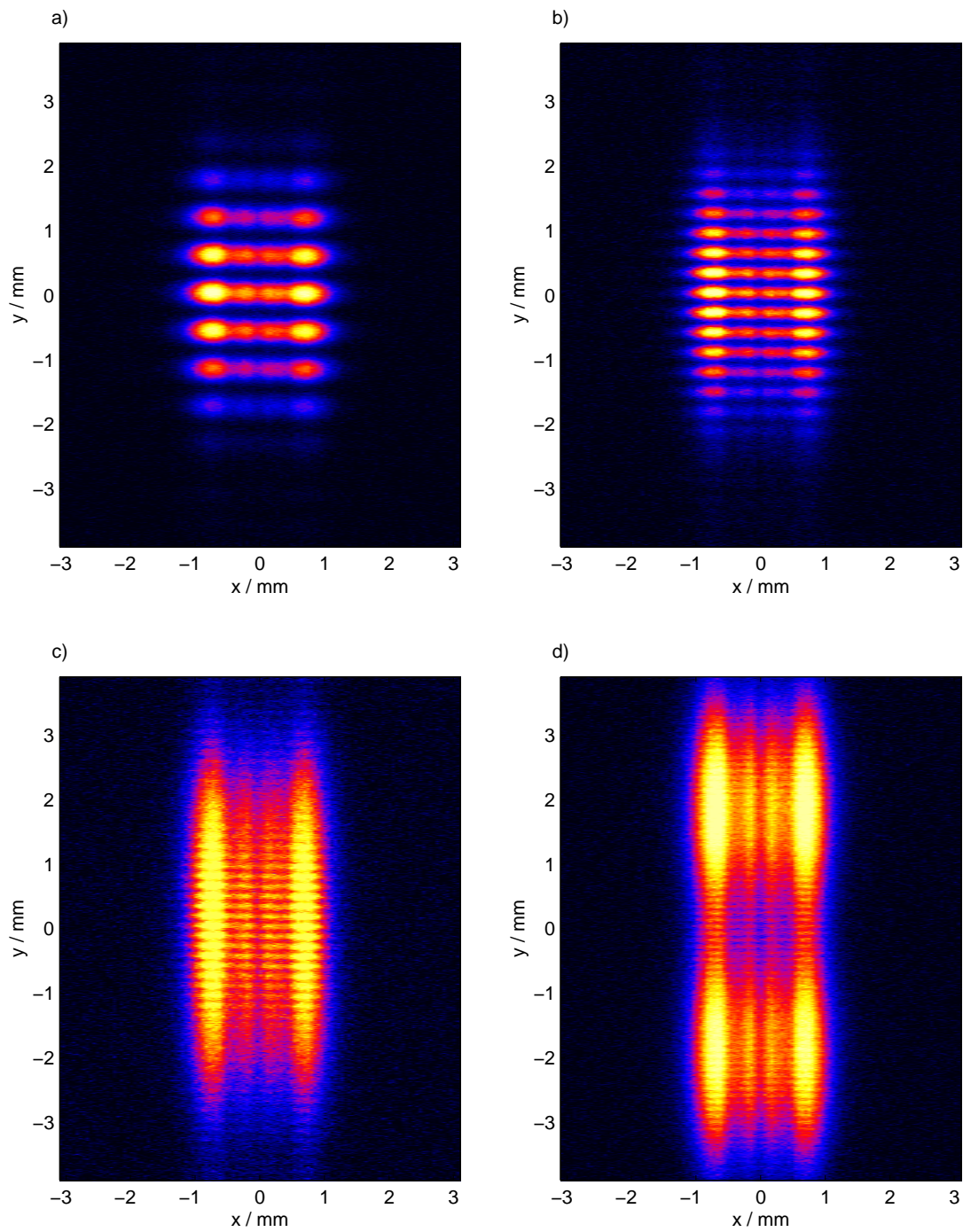


Figure 7.4.: Simulation of the diffraction pattern, including the effects of the experimental set-up, a) 0.5 mm, b) 1 mm, c) 2 mm, and d) 3 mm slit separation.

7.3. Image processing

The analysis of the double slit diffraction patterns is illustrated for 1 mm slit separation. The same procedure is applied to the measured patterns (shown in the left column of figures 7.5, 7.7, 7.9, 7.10 and 7.11) and the simulated patterns (shown in the right column).

7.3.1. Averaging

To improve the signal-to-noise ratio of the images, in the order of 100 measurements made under identical conditions are averaged. One calculates thus the intensity-weighted average of the coherence.

It has to be ensured that the position of the diffraction pattern does not jitter from measurement to measurement, as this would reduce the visibility. The position and intensity of the diffraction pattern is shown in figure 7.6. The intensity-weighted rms variation of the fringe position is $3.4\ \mu\text{m}$, while the next fringes are located at a distance of $290\ \mu\text{m}$.

For a slit separation of 0.5, 1 and 2 mm, 100 images were averaged. In the case of 3 mm slit separation, 404 images were averaged to account for the low intensity in the middle of the diffraction pattern.

It is also possible to process the images of a single FEL bunch. This is however more difficult, as the signal-to-noise ratio is not as good. The two analysis methods described in sections 7.4.1 and 7.4.2 are first applied to the average image. The positions of the diffraction fringes determined this way are used as start values for the analysis of single bunch images.

7.3.2. Correction for effects of the experimental set-up

The interference pattern of the FEL is broadened by light scattering in the fluorescent crystal and by the limited resolution of the lens system. The non-linear response function of the crystal decreases the contrast further. Therefore, the images are corrected for these effects, as discussed in chapter 6.

For the simulated images, these corrections should in principle remove the smearing which was applied in section 7.2.3. However, due to the noise that has been added to the images, it is not possible to reverse the convolution with the optical resolution of the fluorescent crystal and the camera.

The Lucy-Richardson algorithm, described in section 6.2.3, has been used to deconvolute the images, using the measured point spread function (section 18). This maximum-likelihood algorithm reconstructs an image that has a high probability of resulting in the measured image when convoluted with the given point spread function. The reconstruction does however not result in an image that is exactly identical

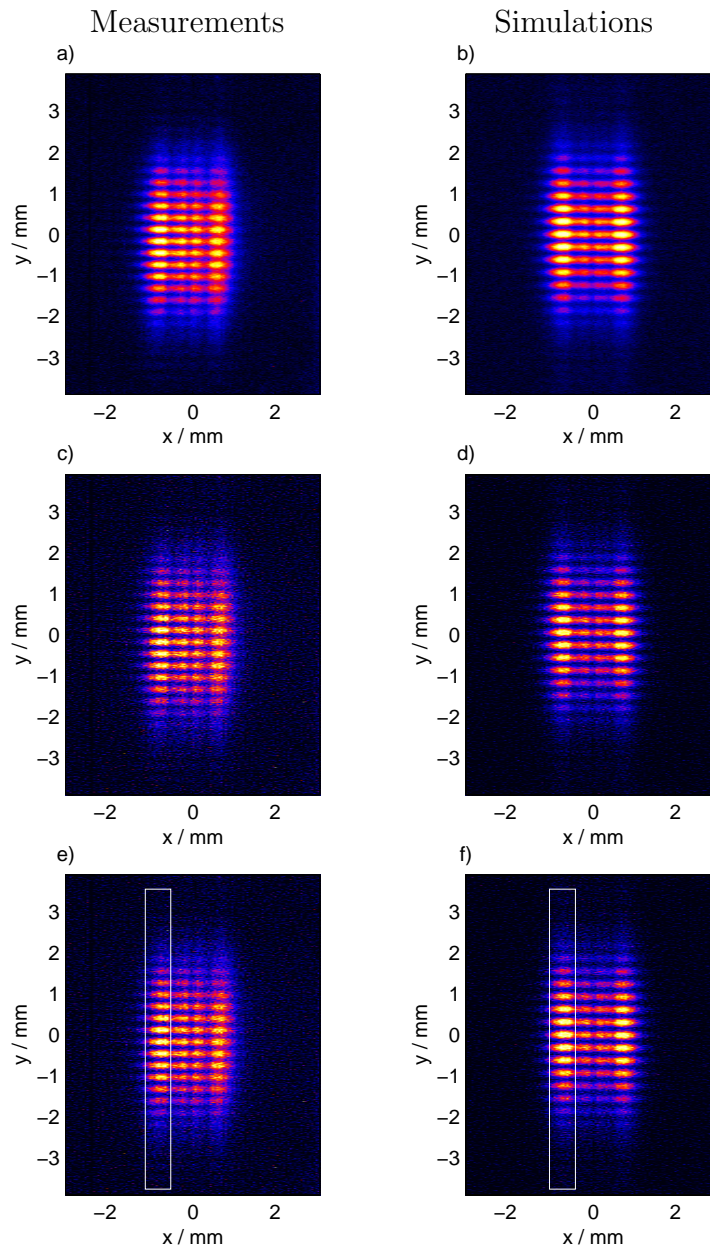


Figure 7.5.: Image Processing of the measured (left) and simulated (right) double slit diffraction patterns for 1 mm slit separation. a) Average of 100 measurements, background subtracted, as in figure 7.1d. b) Simulated image, including the effects of the experimental set-up. c) and d) These images has been deconvoluted with the Lucy-Richardson algorithm, using the measured point spread function (figure 6.7). e) and f) Correction for the nonlinear response of the fluorescent crystal. The selected area for further processing is shown by a white rectangle.

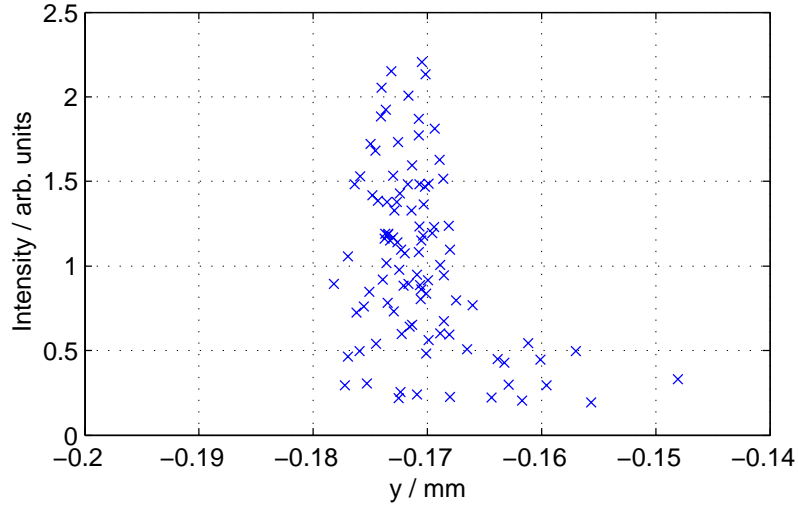


Figure 7.6.: Vertical position and intensity of the central fringe of the 100 double slit diffraction patterns, recorded under identical conditions. The FEL intensity fluctuates due to the stochastic nature of the SASE process. The fluctuations of the position are $3.4 \mu\text{m}$ rms.

to the original image. Correspondingly, the coherence function that can be determined from the reconstructed images is not exactly equal to the coherence that could be seen in the original images. The present simulation shows thus the validity of the analysis routines.

The response function of the Ce:YAG crystal was corrected with the inversion of Eq. (6.1). This improves the overall contrast of the image, since the brighter parts of the image are enhanced with respect to the background.

7.3.3. Projection of the diffraction patterns

A region in the images is selected for further processing. Careful inspection of the observed diffraction pattern shows that the sharpness of the focusing varies a little bit from left to right; it is conjectured that this is due to the insufficient tilt of the lens (see section 5.3.1). The focusing appears slightly better in the left part of the diffraction pattern (see figure 7.2). The uniformity of the fluorescent crystal in this area is good (see figure 6.1).

The leftmost quarter of the diffraction pattern (see figure 7.5e and f) was projected onto a vertical axis. The two-dimensional interference pattern is represented by a curve with approximately 800 points. The intensity variation can be seen nicely in this projection, the bright interference fringes appear as maxima of the curve.

7.4. Analysis

The measured and simulated intensity distributions are analysed with two different methods:

- *Method 1*: the visibility of the interference fringes is determined from the maxima and minima of the smoothed intensity distribution. The central visibility of the diffraction pattern is equal to the transverse coherence of the beam (see section 3.7).
- *Method 2*: a function parametrising for the near field double slit interference (see section 3.6.2) is fitted to the intensity distribution. One of the fit parameters is the transverse coherence of the incoming beam.

The MATLAB code of the analysis routines is given in appendix F.

7.4.1. Analysis method 1: visibility of the central fringe

This method is illustrated in figure 7.7.

Smoothing of the curve

The image recorded by the CCD chip is affected by read-out noise. Taking the pixels with the highest and lowest contents as maxima and minima respectively overestimates the modulation, as the maxima and minima of the diffraction pattern extend over several pixels: the highest pixel within a maximum overestimates the peak, the lowest pixel within a minimum underestimates the latter. It is therefore necessary to reduce the noise by smoothing the curve before the extrema are determined.

A common method is to apply a median filter, i.e. to average each value with its neighbours to flatten the curve. However, this unavoidably decreases the modulation between minima and maxima and lowers the visibility of the diffraction fringes below its true value. The aim is to reduce the noise but to maintain the modulation depth.

It is helpful to look at the problem in the Fourier space. The noise in the images originates from photon statistics and the read-out electronics, there is no correlation between a pixel and its neighbours¹. The noise can hence be considered as *white noise* which is characterised by a flat Fourier spectrum. The double slit diffraction pattern, on the other hand, occupies only a limited region in the frequency domain, with a strong peak at the spatial frequency corresponding to the fringe separation and smaller peaks at its harmonics. These are located in the low-frequency part of the spectrum (figure 7.8).

¹ Note that this is not true for images acquired with an analogue video camera, where electromagnetic pick-up on the data transfer line leads to different noise distributions in the horizontal and vertical plane

7. Measurements of the Transverse Coherence

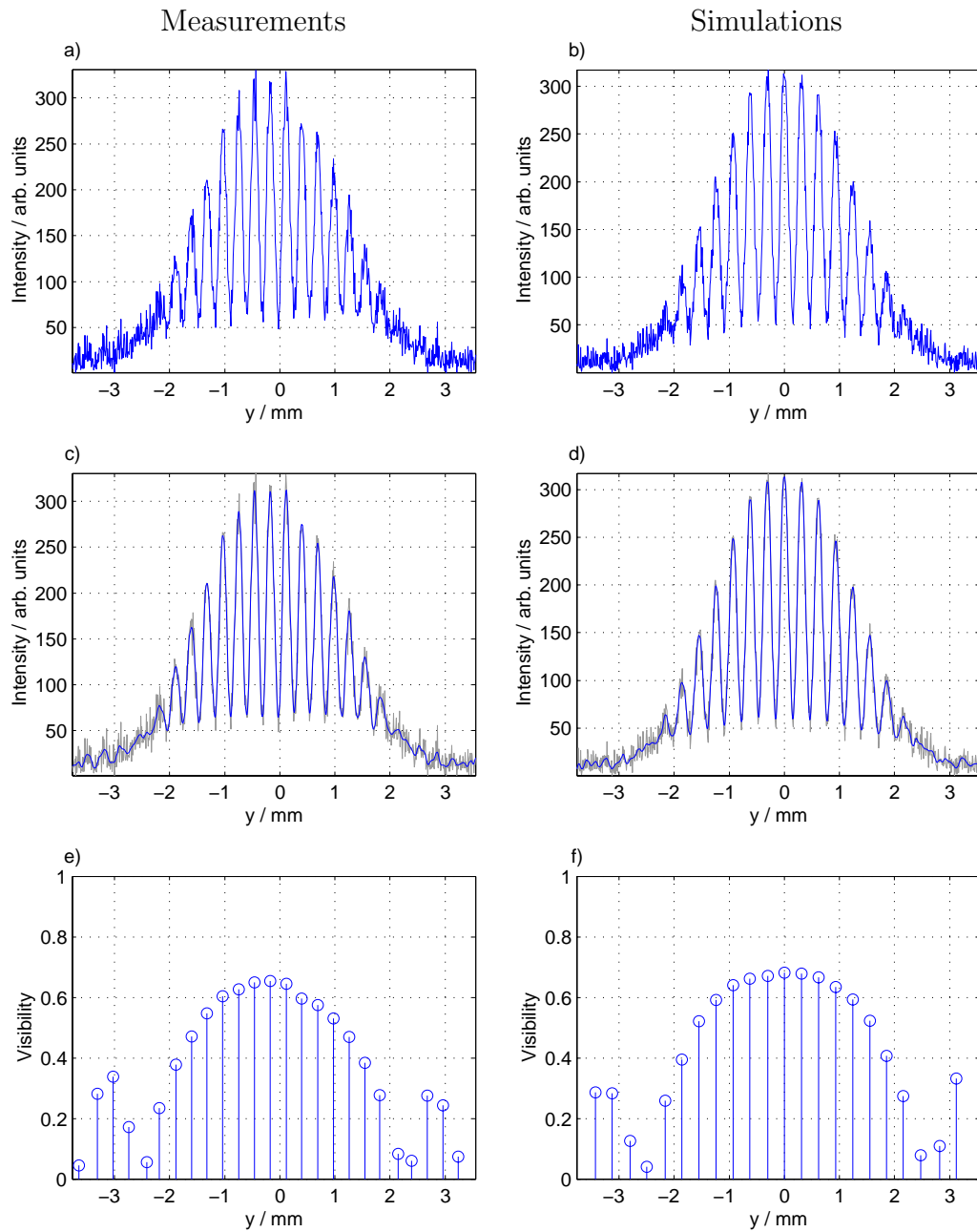


Figure 7.7.: Analysis method 1 of the measured and simulated double slit diffraction patterns, continued from figure 7.5. Left: measurements, right: simulations. a) and b) horizontal projection of the selected area, c) and d) smoothed with a Butterworth filter, e) and f) visibility of the diffraction pattern, at the position of the maxima of the smoothed curve.

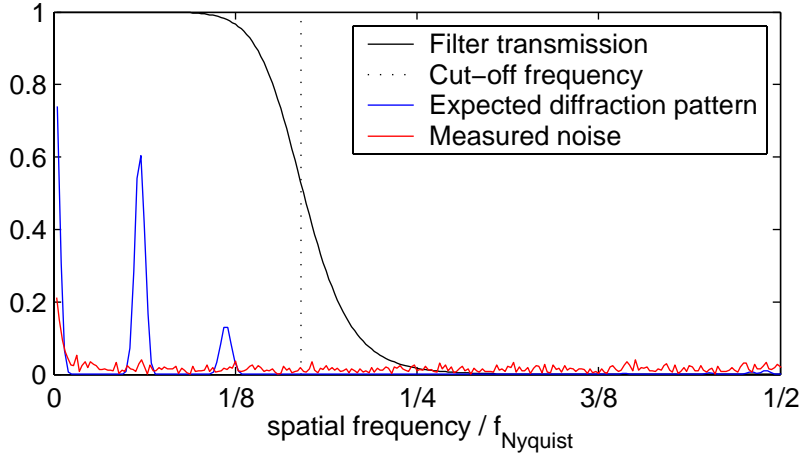


Figure 7.8.: Transmission Spectrum of a fifth order Butterworth filter with a cut-off frequency of 17% of the Nyquist frequency (indicated by the dotted line). The square of the transmission is shown, since the filter is applied twice. The Fourier transform of the expected picture and the measured noise are also shown.

One can therefore suppress the high frequency part by applying digital filtering. Filters can be characterised by their frequency response. A high transmission below a given cut-off frequency ω_c and a low transmission for higher frequencies is achieved with a low-pass Butterworth filter. Its squared frequency response is given by

$$|H(\omega)|^2 = \frac{1}{1 + (\omega/\omega_c)^{2N}} \quad (7.1)$$

where $N \in \mathbb{N}$ is called the order of the filter. Here, a fifth order Butterworth filter was chosen.

A digital filter with the desired transmission function can be constructed by evaluating the roots of the transfer function in the complex plane and using a bilinear transformation of the frequency axis to the unit circle. Details of this procedure can be found in [OS92]. The algorithm results in two filter vectors, \mathbf{a} and \mathbf{b} , that are inserted in the following difference equation. Call $x(m)$ the measured curve before filtering and $y(m)$ the filtered curve. Its m^{th} element is:

$$y(m) = b_1 x(m) + z_1(m-1) \quad (7.2)$$

with

$$\begin{aligned} z_1(m) &= b_2 x(m) + z_2(m-1) - a_2 y(m) \\ z_j(m) &= b_{j+1} x(m) + z_{j+1}(m-1) - a_{j+1} y(m) \end{aligned}$$

for $j = 1 \dots N-1$ and

$$z_N(m) = b_{N+1} x(m) - a_{N+1} y(m)$$

As one can see in equation (7.2), the filter acts only to the left side, i.e. an element $y(m)$ depends on $x(m), x(m-1)$ etc. The resulting directional bias can be avoided by applying the filter twice, coming once from the left and once from the right side. This double application of the filter twice leads to a squared transmission function. The algorithm of the Butterworth filter is implemented in the MATLAB Signal Processing Toolbox² [Mat01c].

The cut-off frequency was chosen to accommodate the given diffraction pattern. For 1 mm slit separation, 17% of the Nyquist frequency was chosen. As can be seen in figure 7.8, this filter has a transmission of more than 0.96 for the expected diffraction pattern but suppresses the frequencies above the cut-off frequency strongly.

The filtered projections are shown in figure 7.7 c) and d). The pixel noise is significantly reduced, while the intensity modulation is not affected.

Finding maxima and minima

The maxima and minima are determined from the smoothed diffraction curve. In the central part of the curve, this is easily done by comparing each point with its neighbours. In the outer range, where the modulation of the curve is lower, this method may be affected by the remaining noise in the data.

To make sure that the real extrema of the diffraction curve are found, one may make use of the fact that they are to a good approximation equidistant. The position of a maximum or minimum that has been determined this way is compared with the position that is expected from the extrapolation of the inner extrema. If the deviation is higher than a quarter of the fringe separation, the value of the smoothed curve at the expected position is used. This method has proven successful even for images with low intensity, for example those that were obtained at a reduced undulator length (see chapter 8).

For each maximum, the arithmetic mean of the two adjacent minima is formed and the visibility

$$\mathcal{V} = \frac{I_{\max} - I_{\min}}{I_{\max} + I_{\min}} \quad (7.3)$$

is calculated. As Fresnel diffraction theory has to be applied, the visibility is different for each interference fringe (see section 3.6).

It has been shown in simulations that the *central visibility* is a good measure for the coherence at the given slit separation (see section 3.7, figure 3.16). In the near field, the visibility of the central fringe is higher than the visibilities of the neighbouring fringes. As the FEL beam is not always perfectly centered with respect to the double slits, the maximum value of the visibility is usually not achieved exactly in the middle.

Therefore, the maximum of visibility of all fringes in the central area of the diffraction pattern is taken as a measure for the central visibility.

² the MATLAB function names are `butter` and `filtfilt`

Results

The resulting visibilities are shown in figure 7.9. In the present measurement series, the central visibility of the averaged pattern reaches 0.82 for a slit separation of 0.5 mm.

The central visibility for a slit separation of 1 mm is 0.65, for 2 mm slit separation, the value is 0.24. The diffraction pattern of the slits with 3 mm separation has a very low intensity in the centre. Nevertheless, the analysis routine is successful, as it can be seen in figure 7.9g. The central visibility is 0.23.

7.4.2. Analysis method 2: fit to the intensity distribution

The theoretical intensity distribution of a double slit in the near field, derived in section 3.6, can be fitted to the projected diffraction patterns, varying the coherence of the incoming wave. This method is illustrated in figure 7.10.

Fitted function

The intensity distribution of a double slit diffraction pattern in the near field is given by Eq. (3.48). For the present fit, some differences to the ideal case discussed in section 3.6 are allowed:

- A coherence $\mathcal{C} < 1$ reduces the modulation globally, the visibility $\mathcal{V}(x)$ is the product of the coherence \mathcal{C} with the position-dependent modulation of the near field diffraction pattern:

$$\mathcal{V}(x) = \mathcal{C} \cdot \frac{I_{\text{ex1}}(x) - I_{\text{ex2}}(x)}{I_{\text{ex1}}(x) + I_{\text{ex2}}(x)} \quad (7.4)$$

- To take into account a misalignment between the FEL beam and the centre of the double slits, the fit allows for unequal magnitudes \mathcal{E}_1 and \mathcal{E}_2 of the electric field amplitude at the two slits. This reduces the visibility further [Hec94]:

$$\mathcal{V}(x) = \frac{2\mathcal{E}_1\mathcal{E}_2}{\mathcal{E}_1^2 + \mathcal{E}_2^2} \cdot \mathcal{C} \cdot \frac{I_{\text{ex1}}(x) - I_{\text{ex2}}(x)}{I_{\text{ex1}}(x) + I_{\text{ex2}}(x)} \quad (7.5)$$

- The curvature of the wave front of the diverging beam in front of the slits displaces the two single slit diffraction patterns with respect to Eq. (3.43). If the angle between the wave vector \vec{k} and the normal of the aperture plane is called ϑ and the distance between the aperture and the observation plane is L , the displacement of the single slit diffraction pattern is equal to ϑL . Different angles ϑ_1 and ϑ_2 are assumed for the two slits. A typical value for the angle is 10^{-4} .

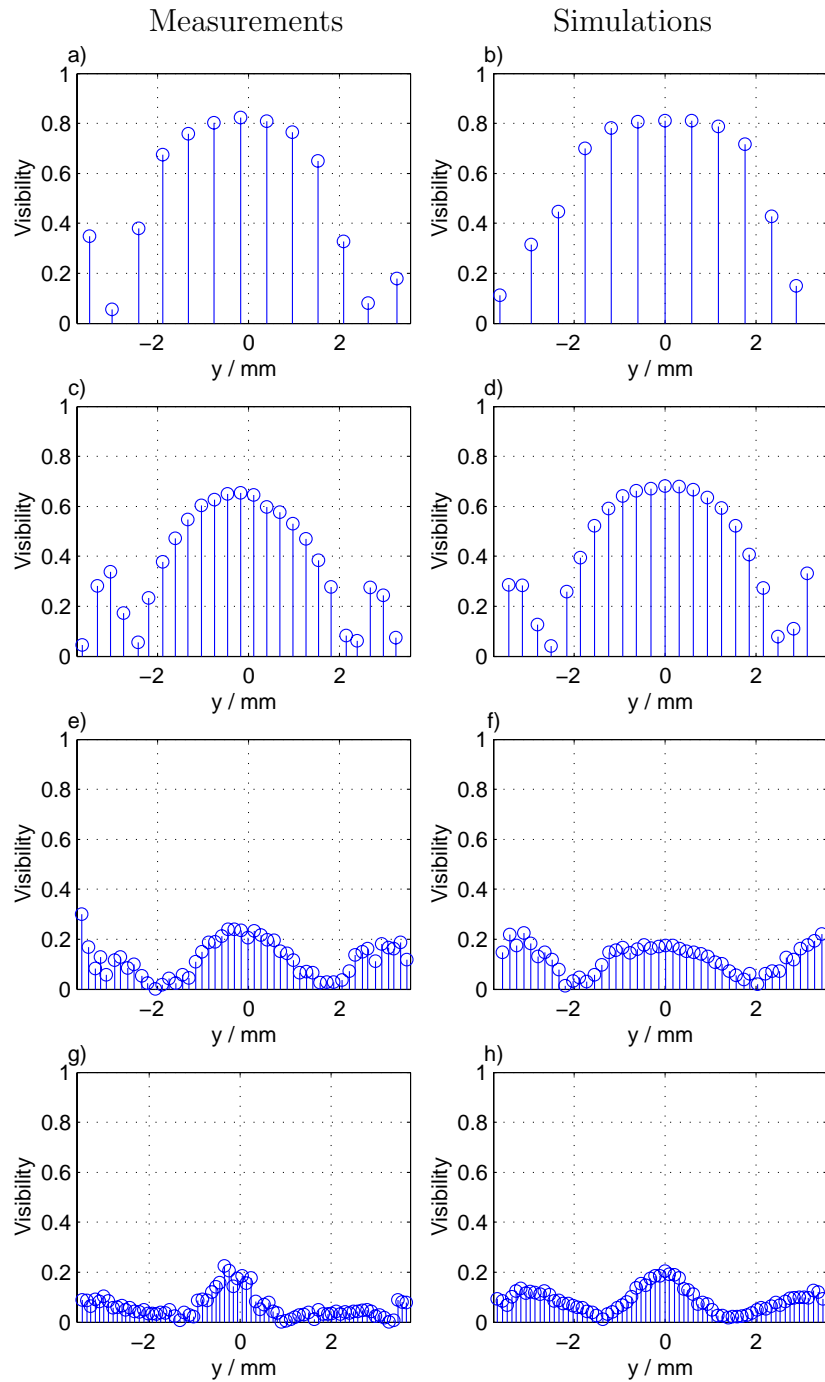


Figure 7.9.: Results of the first analysis method: the visibilities of the diffraction patterns at various slit separations. Left column: measurements, right column: simulations. a) and b) slit separation $d = 0.5$ mm, c) and d) $d = 1$ mm, e) and f) $d = 2$ mm and g) and h) $d = 3$ mm.

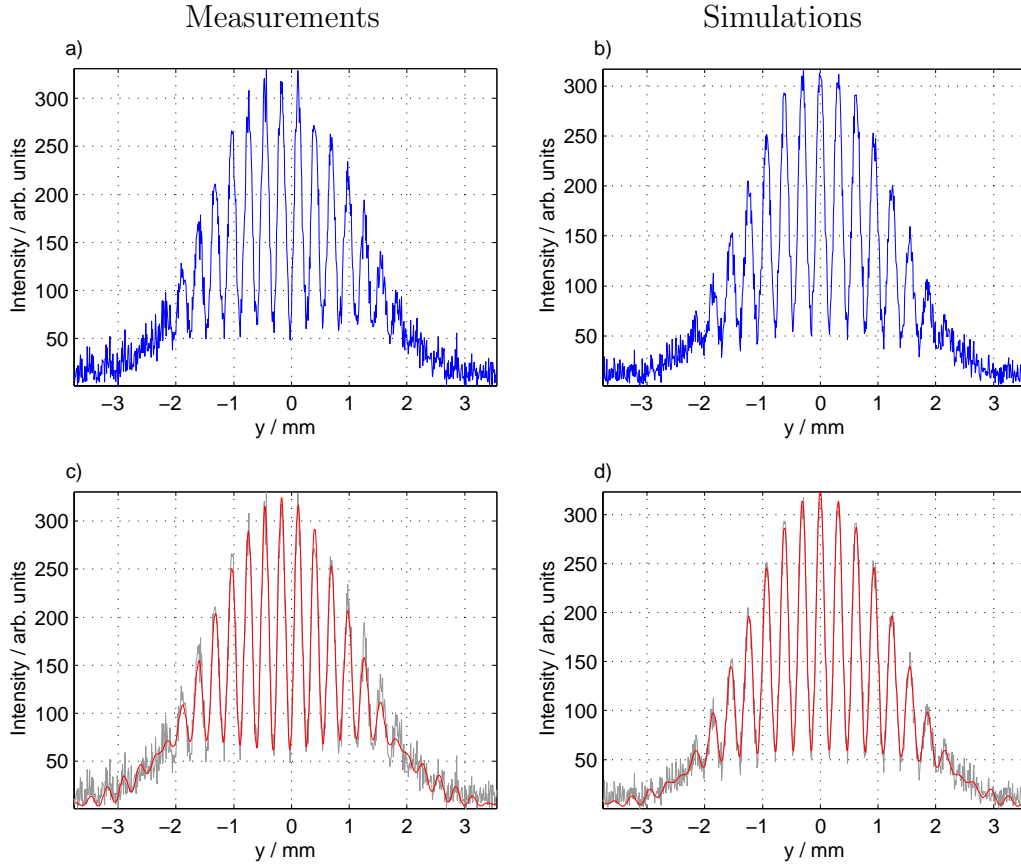


Figure 7.10.: Analysis method 2 of the measured and simulated double slit diffraction patterns, continued from figure 7.5. Left: measurements, right: simulations. a) and b) horizontal projection of the selected area, c) and d) fitted curve.

- The centre of the pattern may be shifted by a distance μ with respect to the origin. The electric field amplitudes of the two single slit contributions are thus given by

$$\tilde{E}_1(x) = \mathcal{E}_1 \frac{\sin(\alpha_1)}{\alpha_1} \quad \text{where} \quad \alpha_1 = \frac{\pi w(x + d/2 + \vartheta L - \mu)}{\lambda L} \quad (7.6)$$

$$\tilde{E}_2(x) = \mathcal{E}_2 \frac{\sin(\alpha_2)}{\alpha_2} \quad \text{where} \quad \alpha_2 = \frac{\pi w(x - d/2 - \vartheta L - \mu)}{\lambda L} \quad (7.7)$$

From the absolute square of the electric field amplitudes, the intensities I_1, I_2 and $I_{\text{ex}1}, I_{\text{ex}2}$ can be computed as in Eq. (3.44) and (3.46), respectively. The double slit diffraction pattern is

$$I(x) = \mathcal{S}(x) \left[1 + \mathcal{V}(x) \cos \left(\frac{2\pi d}{\lambda L} (x - \mu) \right) \right] \quad (7.8)$$

where the overall amplitude $\mathcal{S}(x)$ is computed as in Eq. (3.45) and $\mathcal{V}(x)$ is given by Eq. (7.5).

- Finally, the wavelength λ of the radiation is used as a fit parameter. It influences the overall scaling of the diffraction pattern and accounts also for small uncertainties in the measured distances in the set-up.

Seven parameters are fitted: the transverse coherence \mathcal{C} , the wavelength λ of the radiation, the electric field amplitude at both slits as $\sqrt{\mathcal{E}_1 \mathcal{E}_2}$ and $\mathcal{E}_1/\mathcal{E}_2$, the angles ϑ_1 and ϑ_2 of the wave fronts to the aperture plane and the displacement μ of the diffraction pattern. To allow the fit routine to select reasonable step sizes and convergence criteria, the parameters are normalised.

Fit algorithm

The algorithm used to fit the expected function to the data is based on the *reflective Newton* method on *trust-regions* [CL94, CL96]. It is implemented in the MATLAB Optimization Toolbox³ [Mat01b].

The least-squares fitting of a function $f(x; p_1, \dots, p_N)$ of the variable x with a set of parameters $\mathbf{p} \equiv p_1, \dots, p_N$ to a data set $g(x)$ consists in minimising the square of the difference of the function with the data:

$$\min_{p_1, \dots, p_N} h(p_1, \dots, p_N) \quad \text{where} \quad h(\mathbf{p}) = \int [f(x; \mathbf{p}) - g(x)]^2 dx \quad (7.9)$$

or, in the typical case of a function measured at discrete points x_i :

$$h(\mathbf{p}) = \sum_i [f(x_i; \mathbf{p}) - g(x_i)]^2 \quad (7.10)$$

It is often useful to constrain the parameters in intervals $[p_{i,\min}, p_{i,\max}]$. For example, in the present case, the coherence has to be between 0 and 1, and the centre of the diffraction pattern may not be displaced by more than a few millimetres.

Finding the minimum in a multi-dimensional parameter space is a non-trivial task, and no method can guarantee that the global minimum of $h(\mathbf{p})$ is found, except in the simplest cases. The minimisation starts with a set of initial parameters \mathbf{p}_0 , obtained by guessing the best values.

In the reflective Newton method, the function $h(\mathbf{p})$ is first approximated by a simpler function $q(\mathbf{p})$ around \mathbf{p}_0 , for example by taking the first-order and second-order terms of the Taylor expansion of $h(\mathbf{p})$ around \mathbf{p}_0 .

Next, one calculates the minimum of $q(\mathbf{p})$ in a trust-region, i.e. a neighbourhood \mathcal{N} around \mathbf{p}_0 . The position of this minimum is denoted \mathbf{p}_m . The original function $h(\mathbf{p})$ is now evaluated at \mathbf{p}_m . If $h(\mathbf{p}_m) < h(\mathbf{p}_0)$, the iteration step is successful and

³ MATLAB function name `lsqnonlin`

\mathbf{p}_m is the new starting point. Otherwise, one decreases the size of the trust region and repeats the iteration with \mathbf{p}_0 .

To minimise the quadratic function $q(\mathbf{p}_m)$, one has to factorise the matrix \mathbf{H} of second derivatives. A lot of computing time is spent for this step, especially if the number N of parameters is large. The algorithm can be accelerated by constraining the problem to a two-dimensional subspace (i, j) . In this case, the factorisation of the sub-matrix $[H_{ii}H_{jj}; H_{ij}H_{ji}]$ and thus the minimisation of $q(\mathbf{p})$ is trivial. This minimisation has to be repeated for all possible subspaces (i, j) with $i, j \in \{1, \dots, N\}$, $i \neq j$.

For the present case of seven optimisation parameters, the trust-region reflective Newton algorithm is superior to the commonly used simplex search method⁴, especially since the fitted parameters can be constrained in reasonable intervals.

Results

The resulting intensity fits for the four slit separations are shown in figure 7.11.

A coherence $\mathcal{C} = 0.84$ was determined for the diffraction pattern of the slits separated by 0.5 mm. The fitted curve agrees well with the measurements, as can be seen in figure 7.11. For 1, 2 and 3 mm slit separation, the values are $\mathcal{C} = 0.68$, $\mathcal{C} = 0.25$ and $\mathcal{C} = 0.21$ respectively. The agreement with the first analysis routine is remarkable.

To fit the diffraction pattern of individual FEL bunches, the parameters determined from the averaged patterns are used as starting parameters for the fit. The fit is constrained to narrow intervals around these starting values. Only the transverse coherence is allowed to vary between zero and one. The fit then has a good chance to converge, even in the case of a low signal-to-noise ratio.

7.5. Discussion of measurement uncertainties

Systematic uncertainties of the presented analysis procedures are due to the formation of the near field diffraction pattern, the scattering in the fluorescent crystal, the limited resolution of the optical system and to noise in the CCD image. These can be quantified with the simulations, which include these effects.

Here, the amplitude and the phase of the electric field at the position of the double slit are known and it is thus possible to determine the transverse correlation function between the two slits by the definition in Eq. (3.8). Its absolute value can be compared to the results of the two analysis procedures. The values for the four slit separations are shown in figure 7.12.

The deviation of the analysis results from the theoretical coherence function is about 0.03 at 0.5 mm slit separation. At 1 mm slit separation however, the deviations

⁴ MATLAB function name `fminsearch`

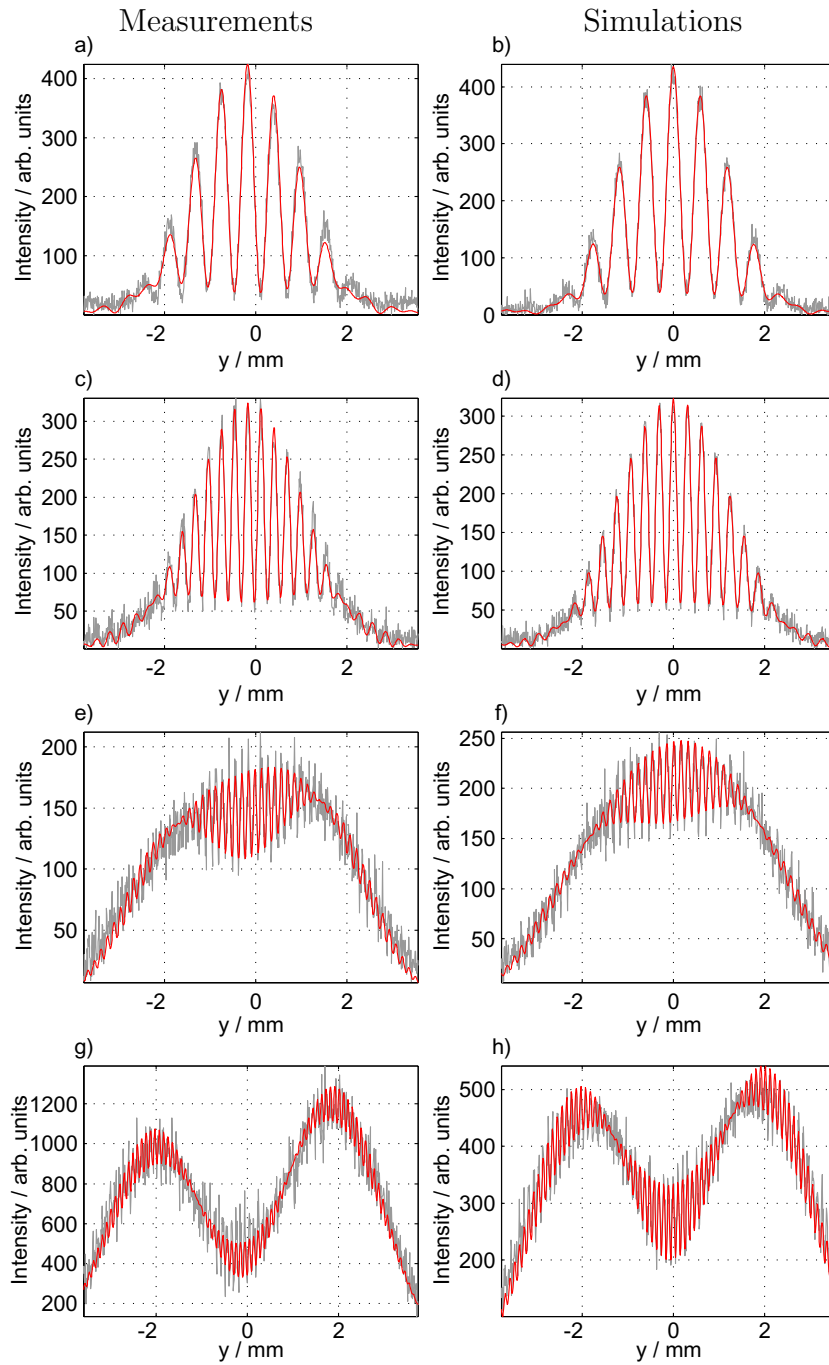


Figure 7.11.: Fit to the intensity at various slit separations. Left column: measurements, right column: simulations. a) and b) slit separation $d = 0.5$ mm, c) and d) $d = 1$ mm, e) and f) $d = 2$ mm and g) and h) $d = 3$ mm.

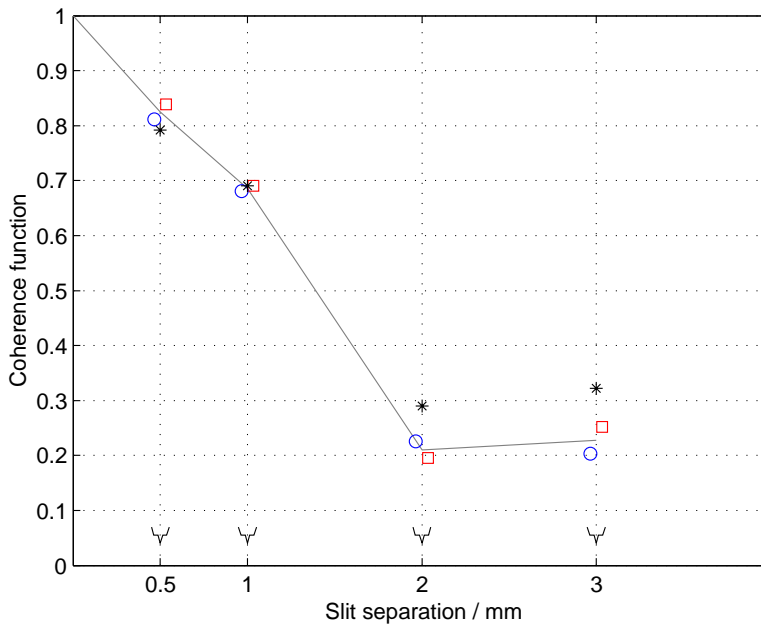


Figure 7.12.: Simulation results for the four slit separations. The value of the theoretical coherence function at a distance equal to the slit separation is shown with an asterisk. The blue circles show the result of the first analysis method, the visibility of the central fringe of the averaged image. The red squares show the result of the second analysis method, the coherence of the fitted intensity distribution. For the clarity, the points have been slightly displaced horizontally in the plot.

between the theoretical coherence function and the result of the analysis are only 0.0005 for the first and 0.0001 for the second analysis method. These small deviations cannot be reasonably taken as the systematic uncertainty. Therefore, a value of 0.03, as found for 0.5 mm slit separation, is used. At 2 and 3 mm slit separations, the deviations are 0.08 and 0.10, respectively. The systematic uncertainties are shown in the outer error bars in figure 7.13.

The statistical errors of the measurements are determined by analysing the single-bunch images in each measurement series. The processing of these images is analogous to the averaged images. In the first analysis method, the positions of the maxima and minima are taken from the analysis of the averaged image. At these positions, the smoothed curve from the single images is evaluated. In the second analysis method, the fit parameters of the averaged projection are used as start values for the fit of the single bunch images. The parameters are constrained to a narrow interval around these values. This results in a reliable convergence of the fit even when the noise level is high.

The uncertainty of the mean value is given by σ/\sqrt{N} , where σ is the standard deviation of the single measurements and N is the number of measurements.

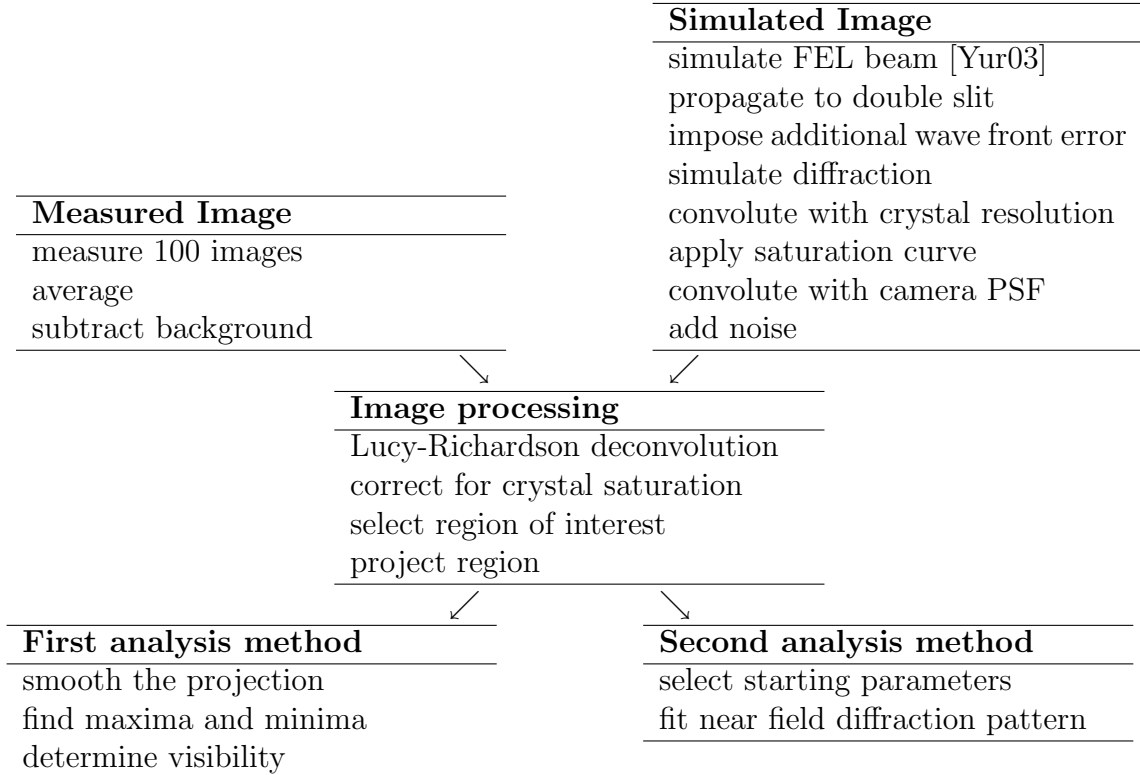
7.6. Summary

The transverse coherence of the TTF FEL has been measured with Young’s double slit experiment. Two methods have been used to analyse the diffraction patterns, determining the central visibility of the projected pattern and fitting the near field diffraction function to the measurements. The analysis is summarised in table 7.1.

The results of the two methods are in good agreement. A simulation of the experimental set-up shows that the central visibility and the fitted coherence are in good agreement with the transverse coherence function of the electromagnetic wave. The results are shown in figure 7.13. The shaded band indicates the confidence interval of the measurements. As expected, the transverse coherence decreases as a function of the distance.

The profile of the beam intensity has been measured at the position of the fluorescent crystal. The central part, which can be seen on the crystal, is approximately Gaussian with $\sigma = 3.5$ mm. This corresponds to an rms beam width of $\sigma = 2.7$ mm at the position of the double slits. This intensity profile is used to calculate the degree of coherence of the FEL, which is defined as the intensity-weighted average of the coherence function, Eq. (3.11). It is assumed that the coherence function has

Table 7.1.: Analysis procedures for the double slit diffraction patterns.



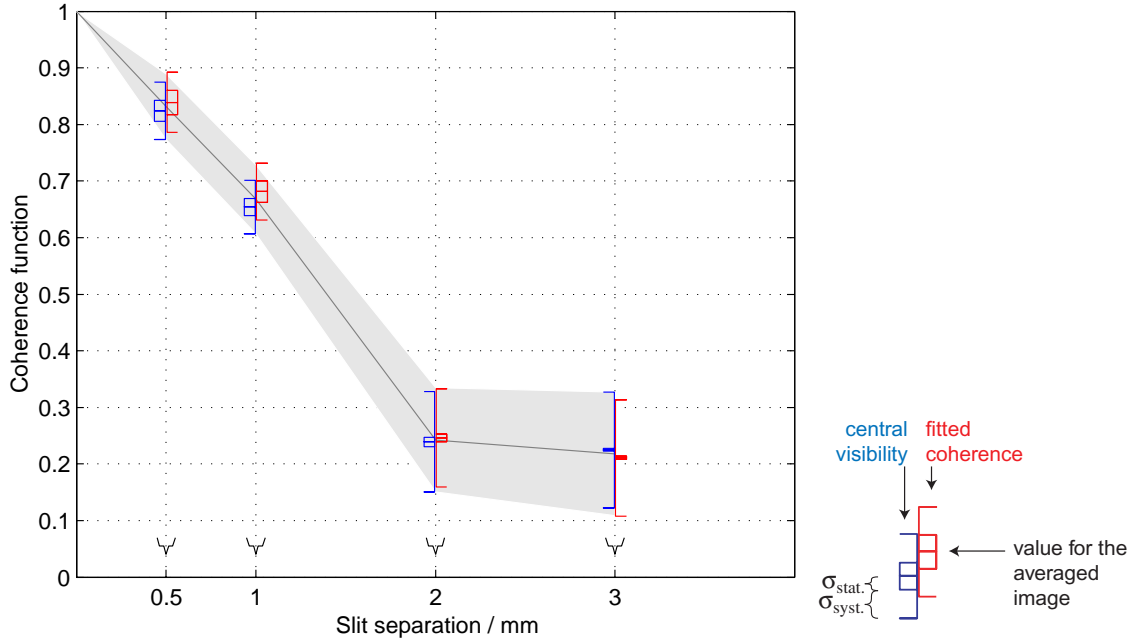


Figure 7.13.: Central visibility and fitted coherence as a function of slit separation. The blue symbols show the result of the first analysis method, the visibility of the central fringe of the averaged image. The red symbols show the result of the second analysis method, the coherence of the fitted intensity distribution. The error bars show $\pm\sigma$ statistical fluctuations of analysis of the single bunch images and the systematic uncertainty. The shaded area gives the confidence interval of the measurements.

circular symmetry, i.e. that it depends only on the distance from the centre. In the present experiment series, measurements have been made for slit separations of 0.5, 1, 2 and 3 mm. For a distance of 0, the coherence is equal to 1 by definition. The coherence function is linearly interpolated between these values. No measurements at larger distances are available, therefore the degree of coherence within a circle of 3 mm radius is calculated:

$$\mathcal{D}_{3\text{mm}} = \frac{\int_0^{3\text{mm}} \mathcal{C}(r)I(r)2\pi r \, dr}{\int_0^{3\text{mm}} I(r)2\pi r \, dr} = 0.64 \pm 0.06 \quad (7.11)$$

An aperture at the position of the double slits improves the degree of coherence by selecting only the central part of the beam, which has a higher coherence. If one chooses an aperture radius of 2 mm, i.e. one selects the cone of the radiation within an opening angle of $\pm 170 \mu\text{rad}$, the degree of coherence is improved to

$$\mathcal{D}_{2\text{mm}} = 0.70 \pm 0.06 \quad (7.12)$$

7. Measurements of the Transverse Coherence

A reduction of the aperture size increases the degree of coherence further, for example for a radius of 0.5 mm, more than 90% coherence can be achieved.

8. Evolution of coherence along the undulator

The transverse coherence varies with the evolution of the FEL pulse along the undulator. As described in section 3.3, the coherence is expected to increase continuously in the regime of exponential growth, because the amplification in an FEL favours the central mode TEM_{00} , due to its best overlap with the electron beam. The situation is changed in the last part of the undulator, as the amplification process for the central mode begins to saturate. Other radiation modes, uncorrelated to the central mode, gain importance and a decreasing transverse coherence is expected.

8.1. Measurements

To study the evolution of the transverse coherence in the undulator, double slit diffraction patterns have been recorded at effective undulator lengths between 9.37 and 13.5 m. Using the analysis routines described in chapter 7, the transverse coherence of the radiation can be determined.

In the TTF FEL, it is not possible to extract the radiation from a given point in the undulator. The effective length of the undulator is varied as follows. The generation of FEL radiation depends critically on the overlap of electron and photon beam (see figure 4.10): an offset of a few hundred micrometres is sufficient to inhibit the FEL amplification. Although the photon beam follows the electron beam to a certain extent due to the beam guiding effect [SSY00b], a deviation of 1 mm results in a separation of the two beams.

By operating one of the horizontal steering magnets (section 4.4.2) at maximum strength, the electron beam is kicked away from the ideal trajectory. Behind the selected steerer, the bunch follows a betatron trajectory, due to the focusing quadrupoles (see figure 8.1). The overlap of the electron and photon beams is then too small to contribute to the FEL process. Only spontaneous undulator radiation is emitted, whose intensity is several orders of magnitude lower.

Using this intentional orbit perturbation, measurements of double slit diffraction patterns could be performed at effective undulator lengths of 9.37, 10.32, 11.28, 12.23, 13.19, and 13.5 m. Thereby, the exponential gain regime of the FEL and the onset of saturation could be studied.

For each effective undulator length, horizontal double slits with separations of

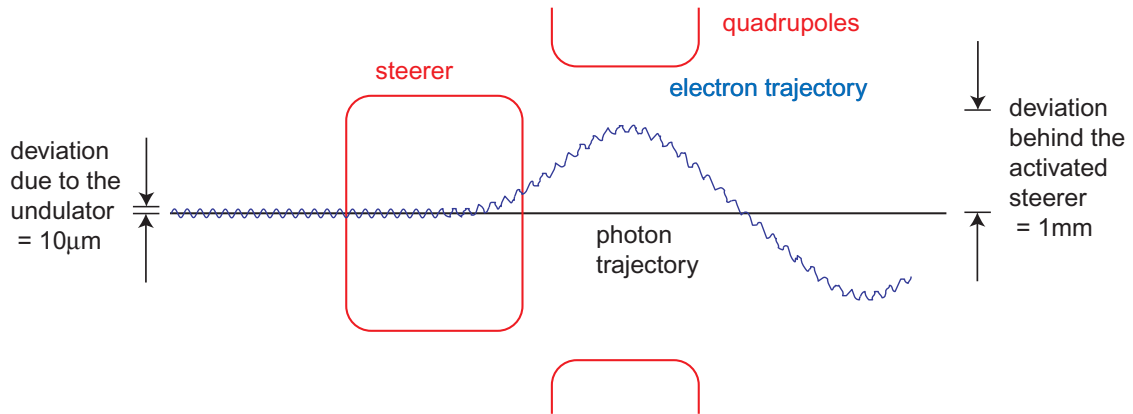


Figure 8.1.: Principle of the adjustment of the effective undulator length. The electron beam is kicked away from the photon beam by a steerer magnet. The sinusoidal undulator motion is also shown. Schematic view, drawing not to scale.

0.5, 1 and 2 mm have been inserted into the FEL beam. The slit pair with 3 mm separation was omitted, because the intensity in the middle of the diffraction pattern is too low. For each configuration, 50 images were acquired. Below an undulator length of 9 m, the diffraction patterns have too little intensity to be recordable with the present set-up.

8.2. Analysis

The images of the double slit diffraction patterns have been corrected for the effects of the experimental set-up: the resolution, affected by the scattering in the crystal and the imaging by the camera lens has been improved with the Lucy-Richardson deconvolution and the non-linear response of the fluorescent crystal has been corrected. The processed images are shown in figures 8.2 and 8.3.

These measured diffraction patterns have been analysed with the two methods that have been described in chapter 7. Minima and maxima of a smoothed projection allow to determine the visibility of the interference fringes, and a near field diffraction curve has been fitted to the measurement data. The projection of the selected area is shown in figures 8.4 and 8.5, the resulting fringe visibilities are shown in figures 8.6 and 8.7. The fits to the intensity distributions are shown in figures 8.8 and 8.9.

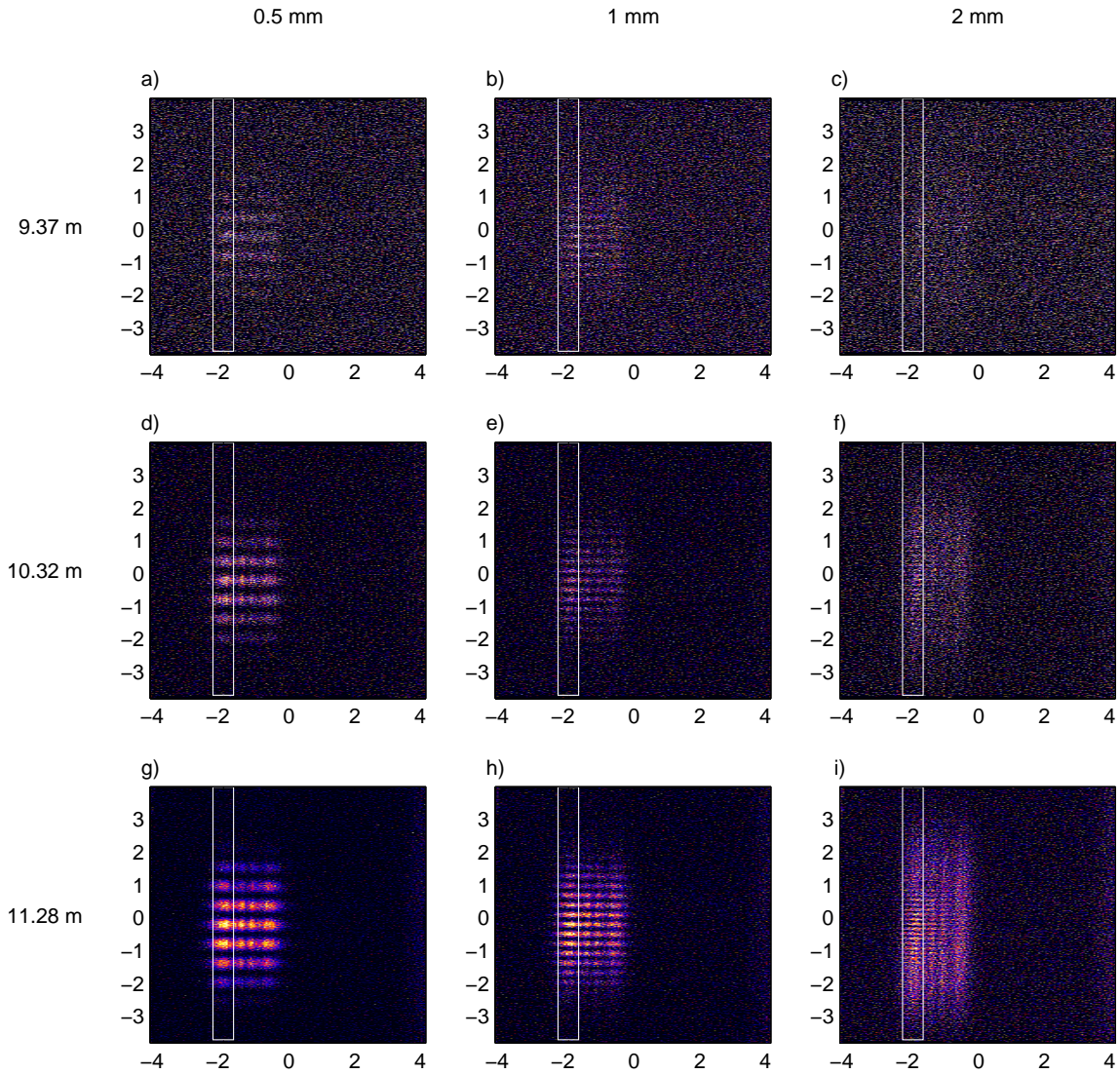


Figure 8.2.: Measured diffraction patterns of double slits with 0.5, 1 and 2 mm slit separation at an effective undulator length between 9.37 and 11.28 m. The recorded images have been corrected for the effects of the experimental set-up. The images have been scaled to the same intensity. The white box indicates the area that has been selected for further processing.

8. Evolution of coherence along the undulator

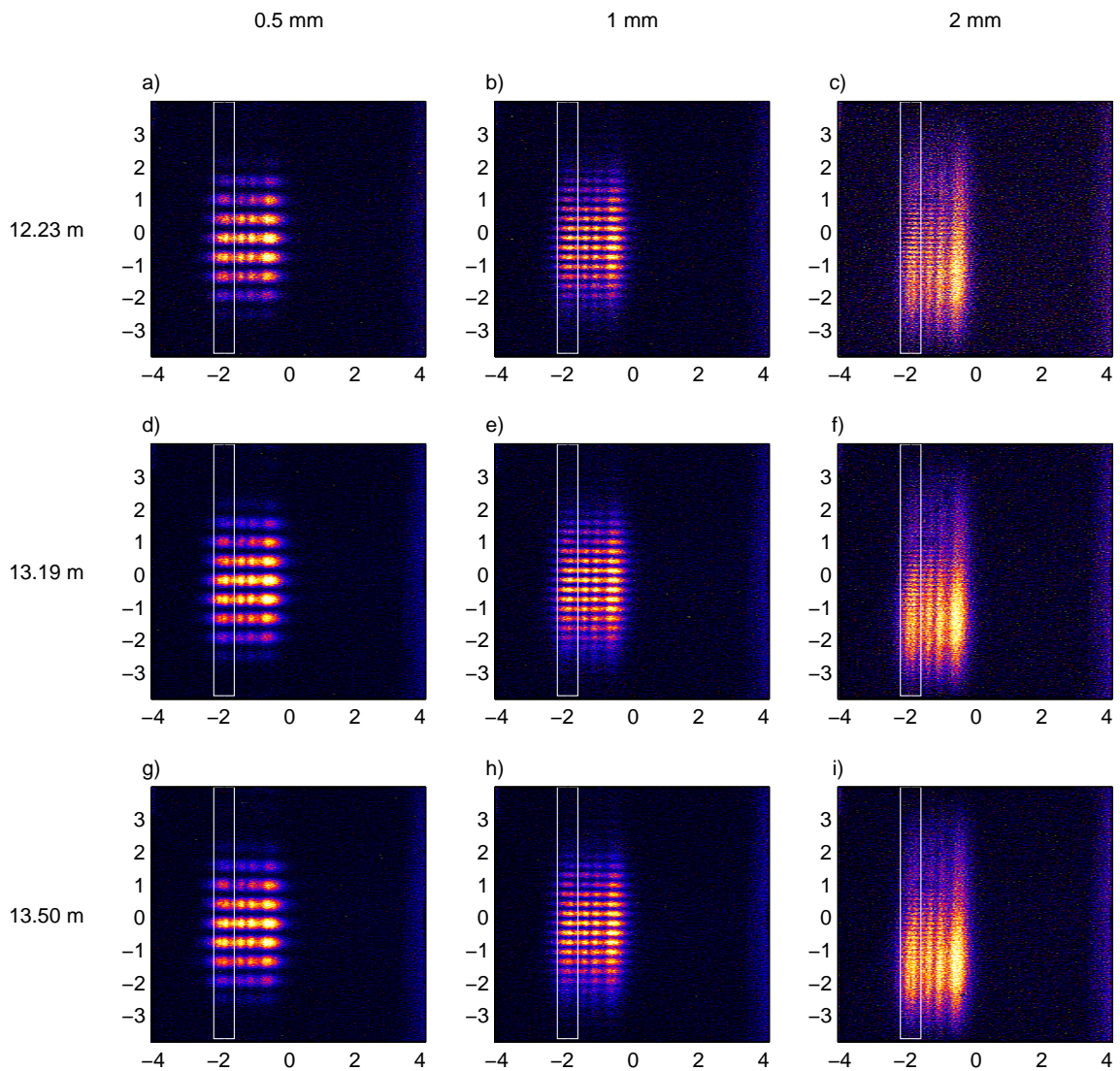


Figure 8.3.: Measured diffraction patterns of double slits with 0.5, 1 and 2 mm slit separation at an undulator length between 12.23 and 13.50 m.

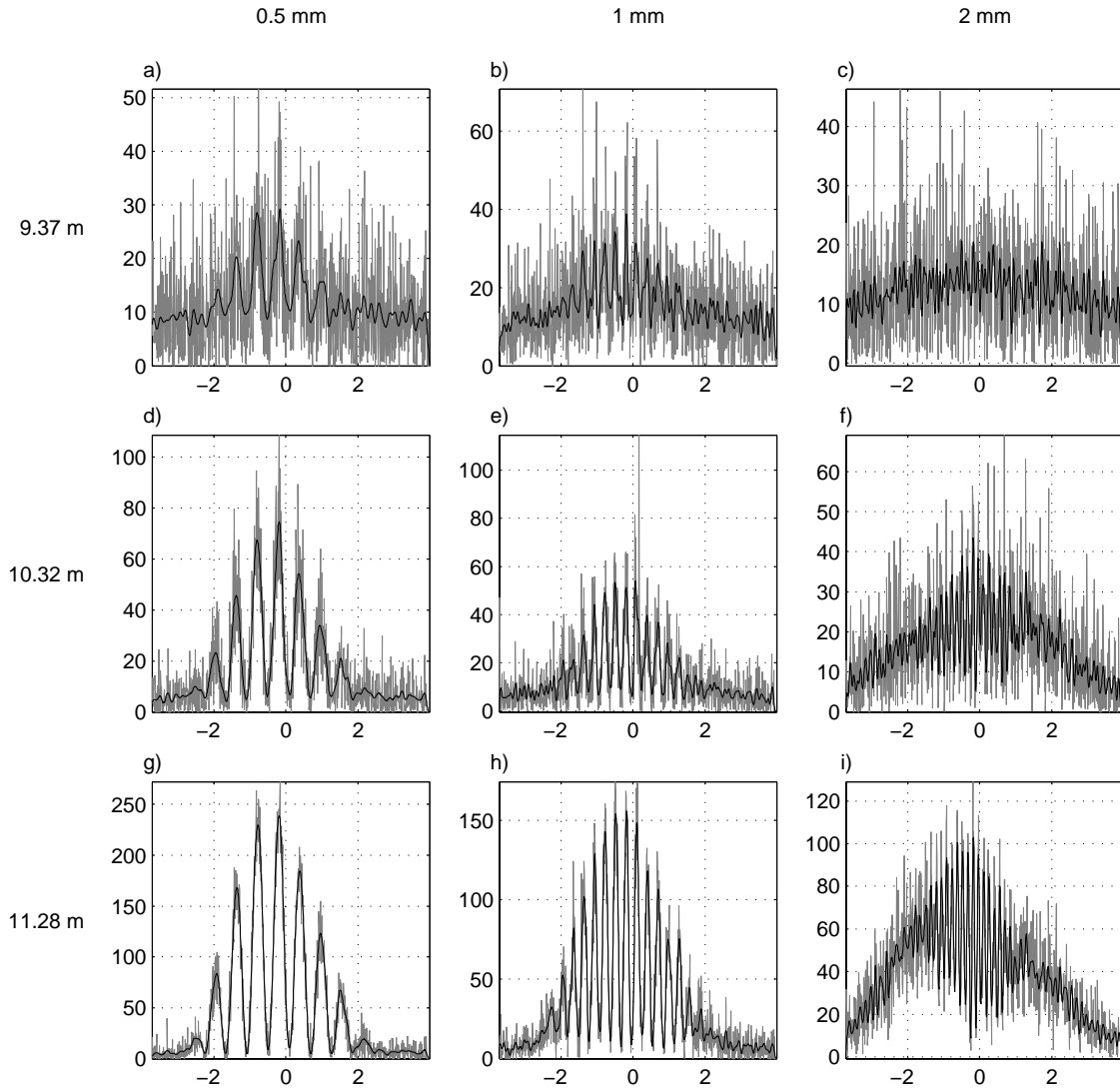


Figure 8.4.: Projection of the selected area in the measured double slit diffraction pattern, shown with a grey line. This has been smoothed with a Butterworth filter, the smoothed projection is shown in black. Measurements with slit separations of 0.5, 1 and 2 mm at an effective undulator length between 9.37 and 11.28 m are shown.

8. Evolution of coherence along the undulator

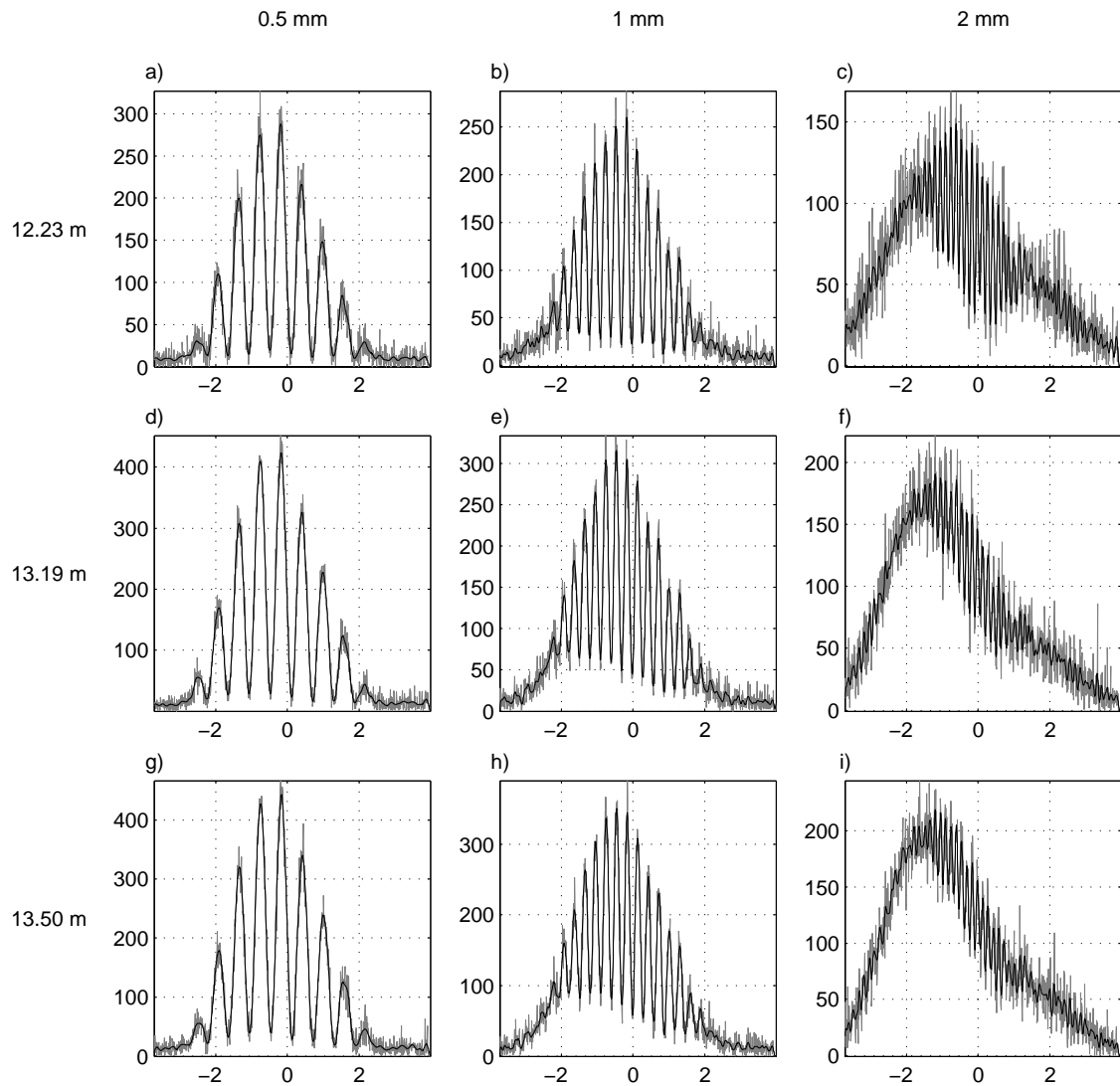


Figure 8.5.: Projection of the selected area in the measured double slit diffraction pattern at an effective undulator length between 12.23 and 13.50 m.

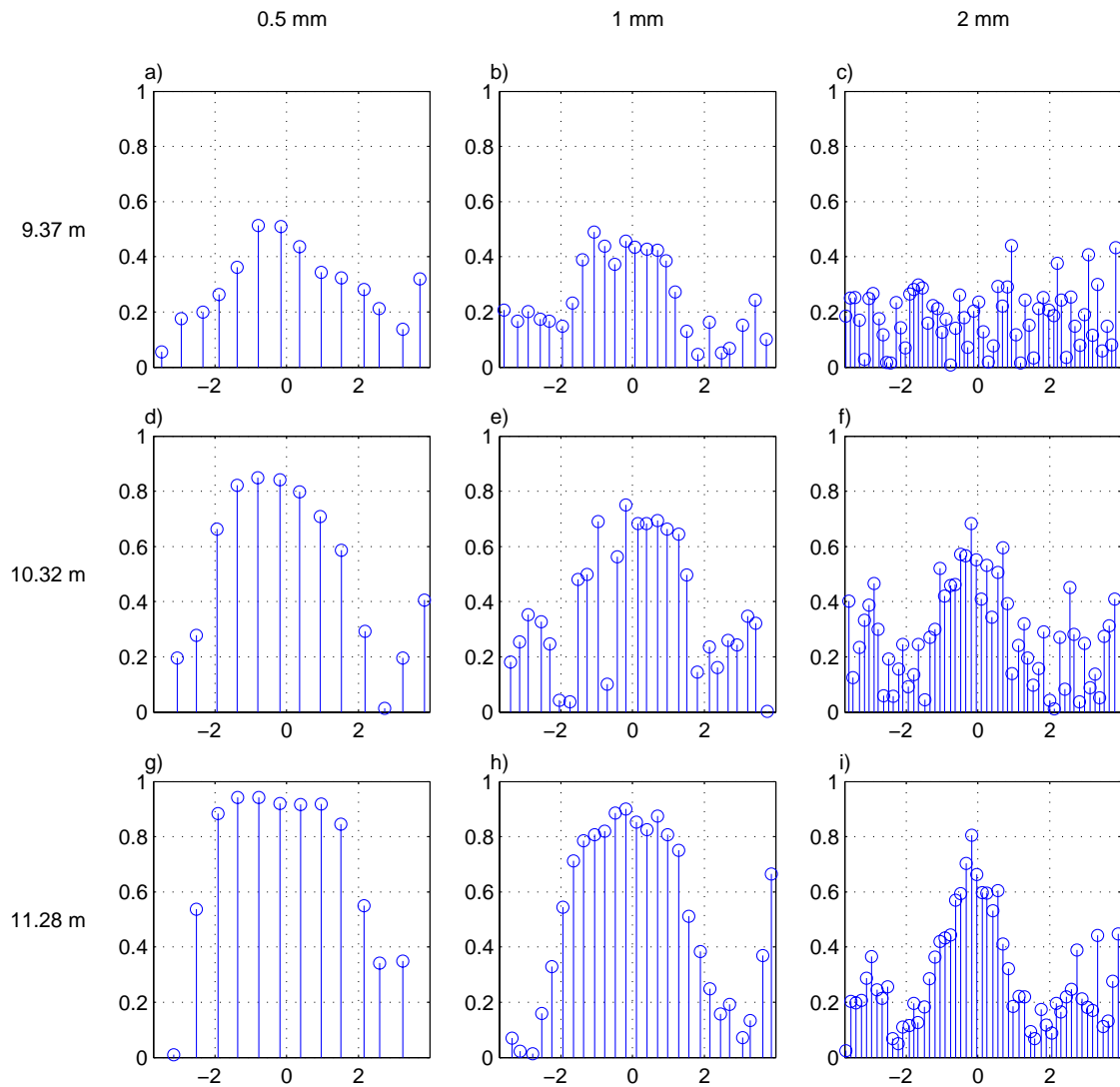


Figure 8.6.: Results of the first analysis method: from the maxima and minima of the measured diffraction patterns, the visibility of each fringe has been determined. The visibilities are shown for slit separations of 0.5, 1 and 2 mm, the effective undulator length has been varied between 9.37 and 11.28 m.

8. Evolution of coherence along the undulator

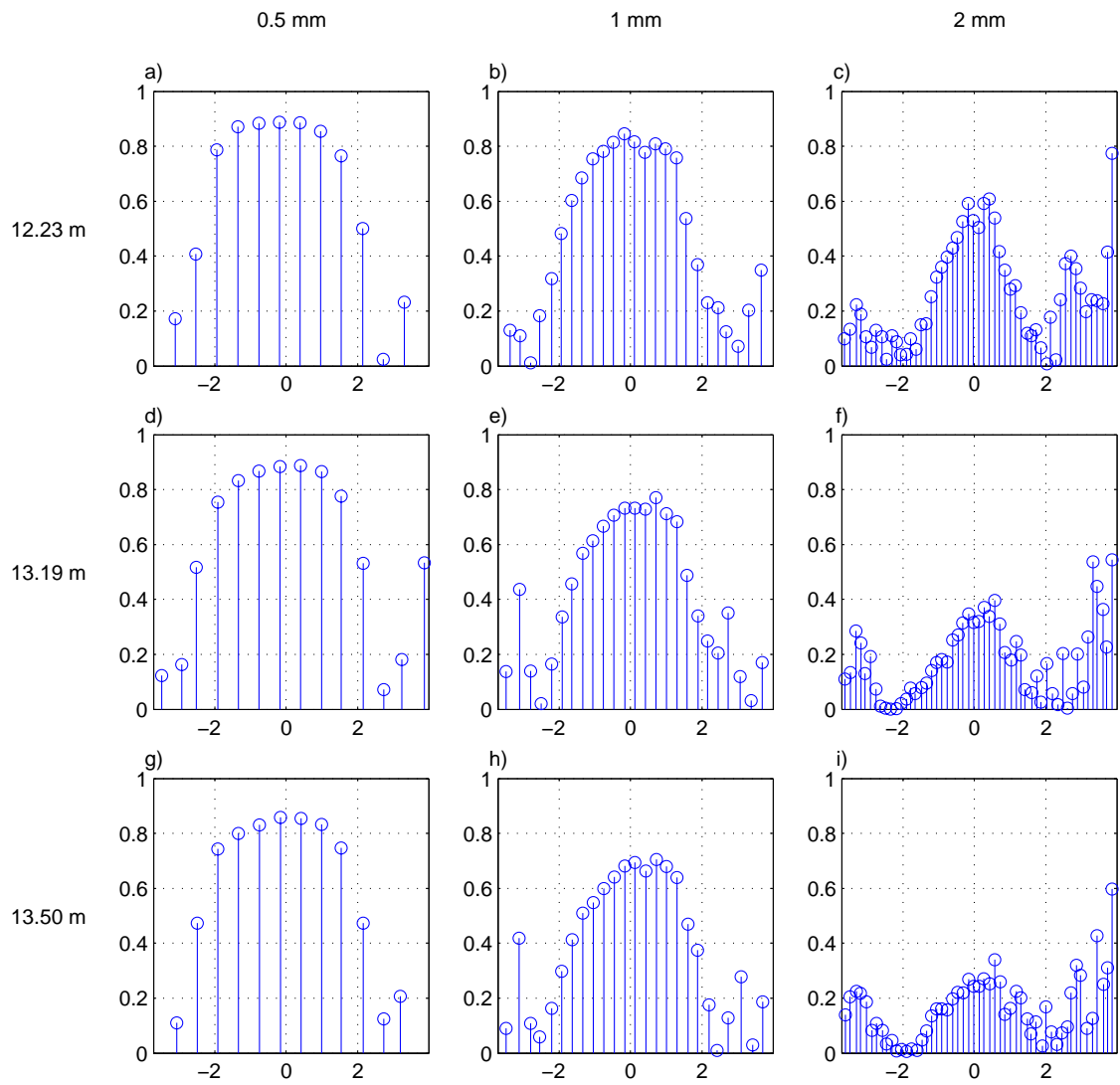


Figure 8.7.: Results of the first analysis method: visibility of the measured diffraction fringes at an undulator length between 12.23 and 13.50 m.

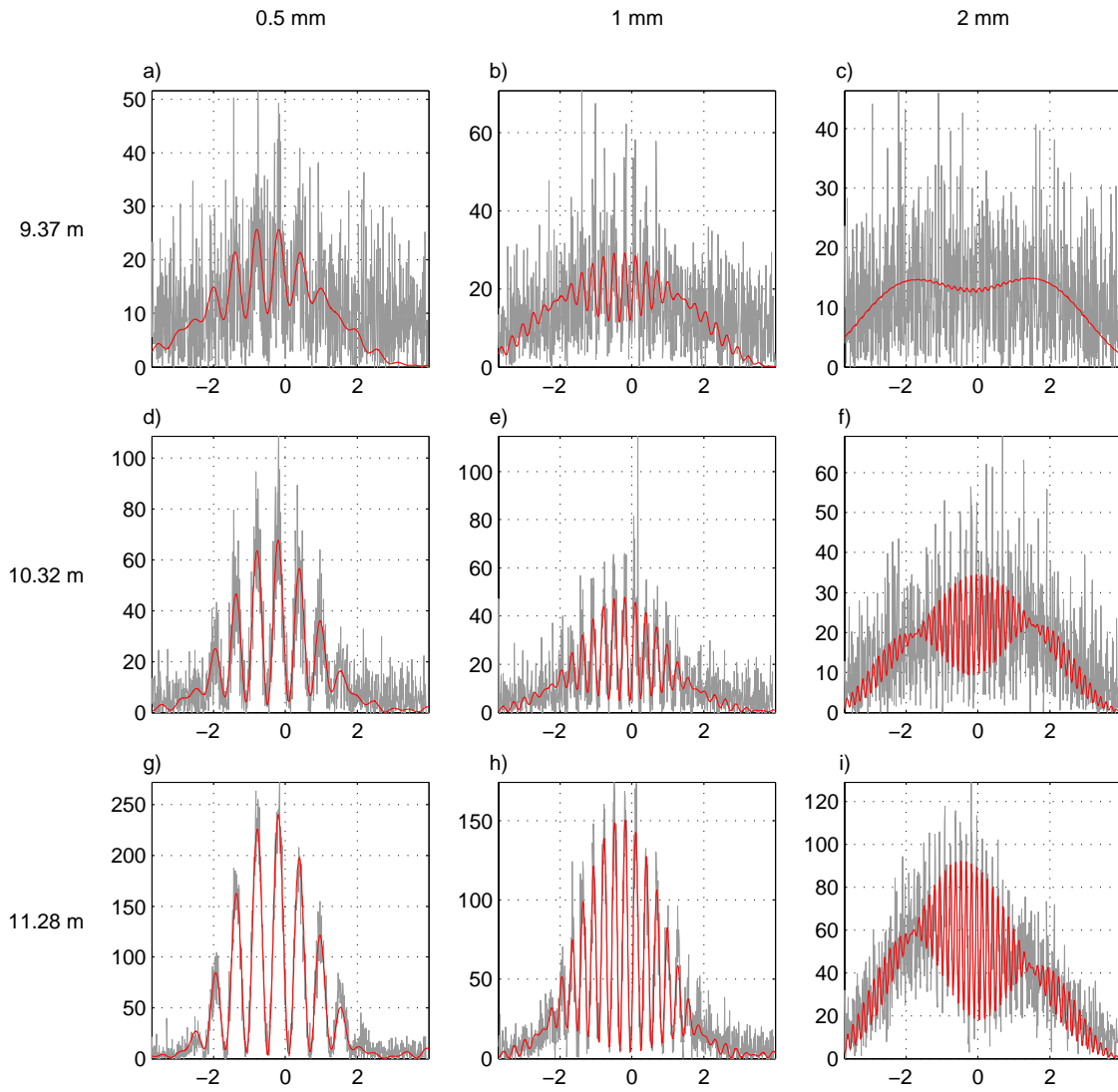


Figure 8.8.: Second analysis method: the intensity distribution in the near field has been fitted to the projection of the measured diffraction patterns. The projected diffraction pattern is shown in grey, the fit is shown in red. Measurements for slit separations of 0.5, 1 and 2 mm are shown at effective undulator lengths between 9.37 and 11.28 m.

8. Evolution of coherence along the undulator

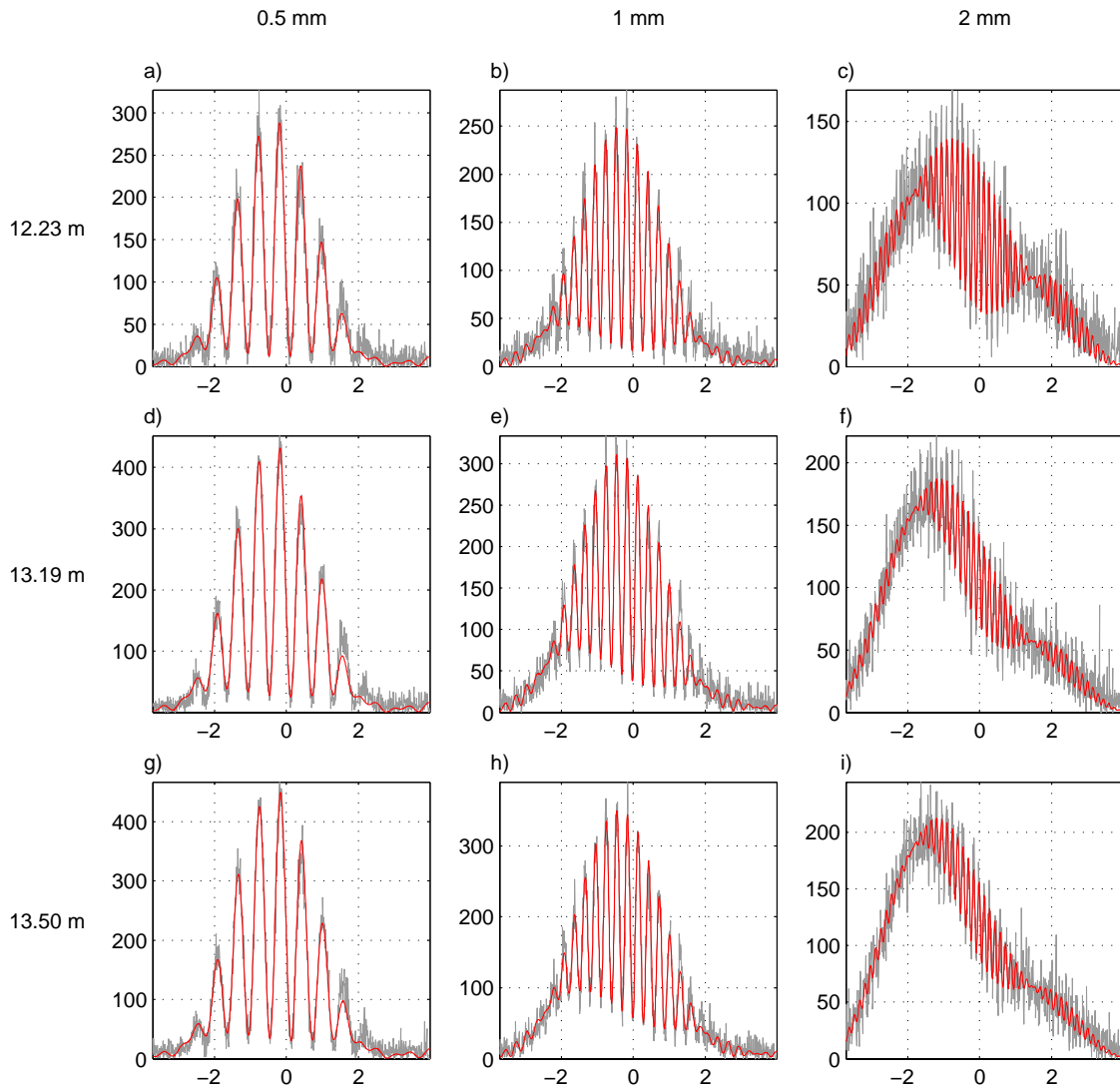


Figure 8.9.: Second analysis method: the intensity distribution in the near field has been fitted to the projection of the measured diffraction patterns. Measurements for slit separations of 0.5, 1 and 2 mm are shown at effective undulator lengths between 12.23 and 13.50 m.

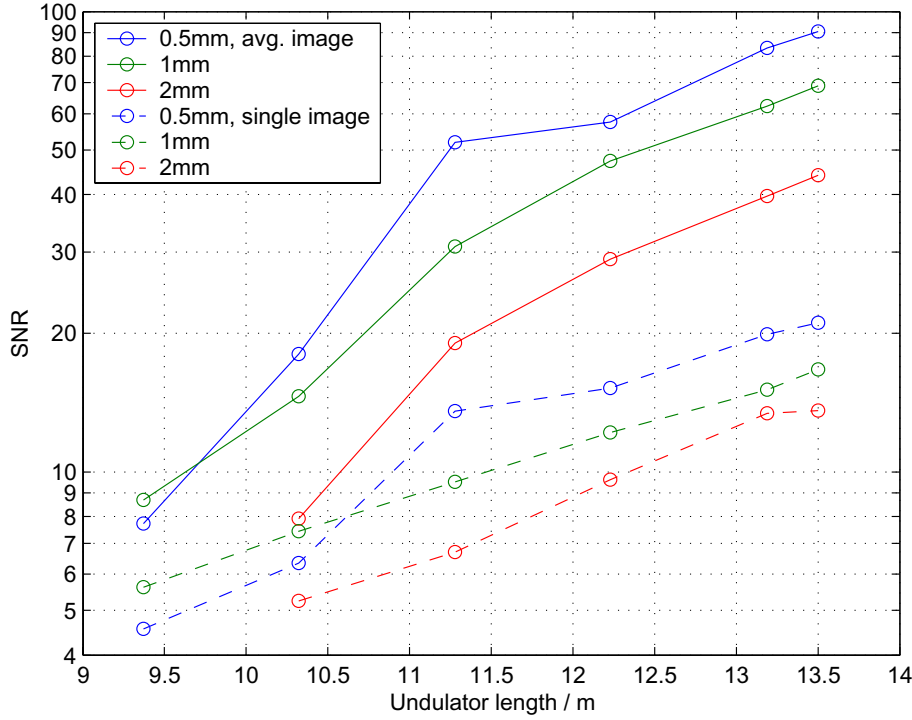


Figure 8.10.: Signal-to-noise ratio of the measurements as a function of undulator length. The SNR of the average of 50 images and the average SNR of the 50 single images are shown.

The dependency of the analysis results on the signal-to noise ratio of the measurements is of special interest, because the intensity of the images varies significantly for undulator lengths between 9.4 and 13.5 m. The signal-to-noise ratio of a point in the projection is defined as

$$\text{SNR} = \frac{1}{\overline{R}\sqrt{N}} \sum_{k=1}^N I_k \quad (8.1)$$

where N is the number of pixels that are added when the diffraction pattern is projected, I_k the intensity in a pixel, \overline{R} the average pixel noise, determined in an area of the image beside the diffraction pattern. The SNR in the brightest diffraction fringe is plotted in figure 8.10 as a function of the undulator length.

At an undulator length of 9.37 m, the diffraction pattern is indiscernable in the individual images and only barely visible in the averaged image (figure 8.2a...c). Nevertheless, the projection of the selected area and the subsequent smoothing reveals the modulation. The fit converges if reasonable starting parameters are selected and the parameters are constrained in small intervals around these values. Only the transverse coherence is left free to vary between 0 and 1.

To understand how the varying intensity in the images influences the result of the analysis routines, simulations have been performed, using a signal-to-noise ratio between 8 and 100. All images were analysed as described in section 7.4. The resulting central visibilities and the fitted coherence are shown in figure 8.11. For an increasing signal-to-noise ratio, the results converge to the coherence function at the slit separation, determined by Eq. (3.8). For a signal-to-noise ratio above 20, a good agreement with the theoretical coherence is observed, within the uncertainties determined in section 7.5. However, for a SNR below 20, larger deviations occur. For the slit separations of 0.5 and 1 mm, both analysis methods underestimate the actual coherence at a low SNR.

At 2 mm slit separation, the first analysis method yields a central visibility that is higher than the actual coherence function. Since the distance between the interference fringes is about 15 pixels, only a few pixels contribute to one fringe, and the detrimental effect of the noise is stronger than for the smaller slit separations. Furthermore, a higher cut-off frequency has been chosen for the Butterworth filter, since the diffraction patterns contain components with higher spatial frequency. This enlarges the influence of the noise further. It appears that noise clusters with a typical size of 7 pixels can be mis-interpreted as interference fringes. The highest of these clusters determines the maximum of the visibility and hence the analysis result. Indeed, as can be seen in figure 8.6f, the visibility at the position of the maxima does not follow the typical curve predicted by Eq. (3.47) and shown in figure 3.7c, but appears to be more randomly distributed. The second analysis method, the fit to the intensity, results in an underestimated value for the coherence.

Besides the described deviations at the low intensities, the values for the transverse coherence obtained by the two analysis methods are in good agreement. The central visibility and the fitted coherence are shown as a function of undulator length in figure 8.12. The variations of the single-bunch measurements have been used to determine the statistical uncertainties.

It appears that the centre of the FEL beam moves downwards with increasing undulator length. The photon beam in the FEL follows the electron beam to a certain extent, therefore this could have been corrected individually with the vertical steerers. However, it was decided to keep the standard settings in order to obtain a better consistency between the measurements. The fitted function accounts for the asymmetry of the slit illumination by assuming different field amplitudes and wave front curvatures at the positions of the two slits, and the visibility has been corrected according to Eq. (7.5).

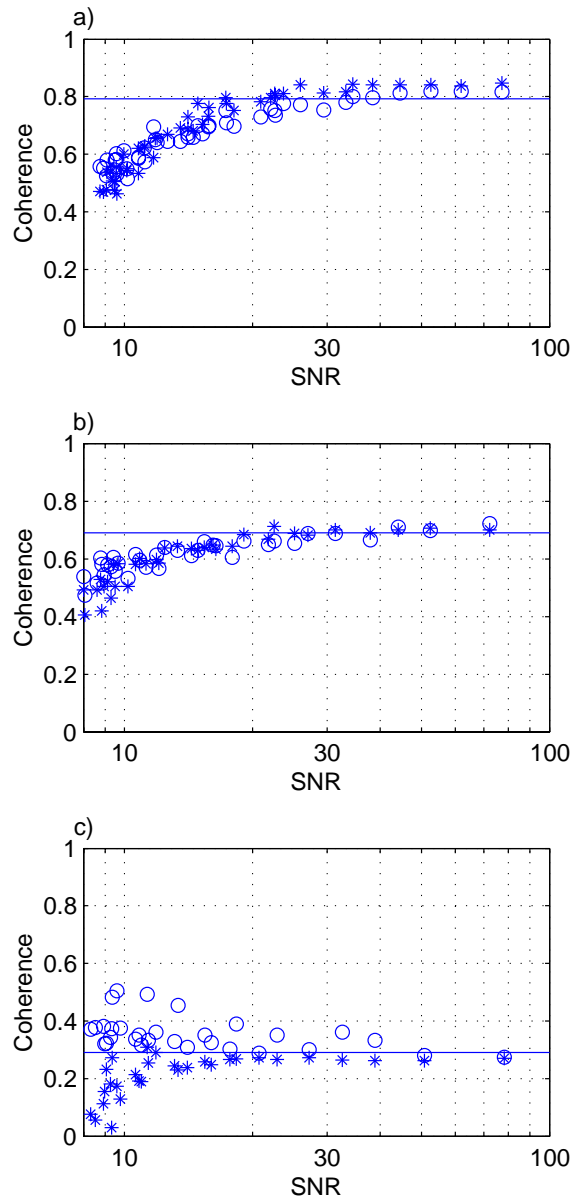


Figure 8.11.: Numerically computed diffraction patterns allow to estimate the systematic uncertainties of the analysis as a function of the signal-to-noise ratio. The slit separations are a) 0.5, b) 1 and c) 2 mm, respectively. The result of the first analysis method, the visibility of the central diffraction fringe is shown with circles, the result of the second analysis method, the fitted coherence is shown with asterisks. The theoretical coherence function for all simulations at the respective slit separation is indicated by the line.

8. Evolution of coherence along the undulator

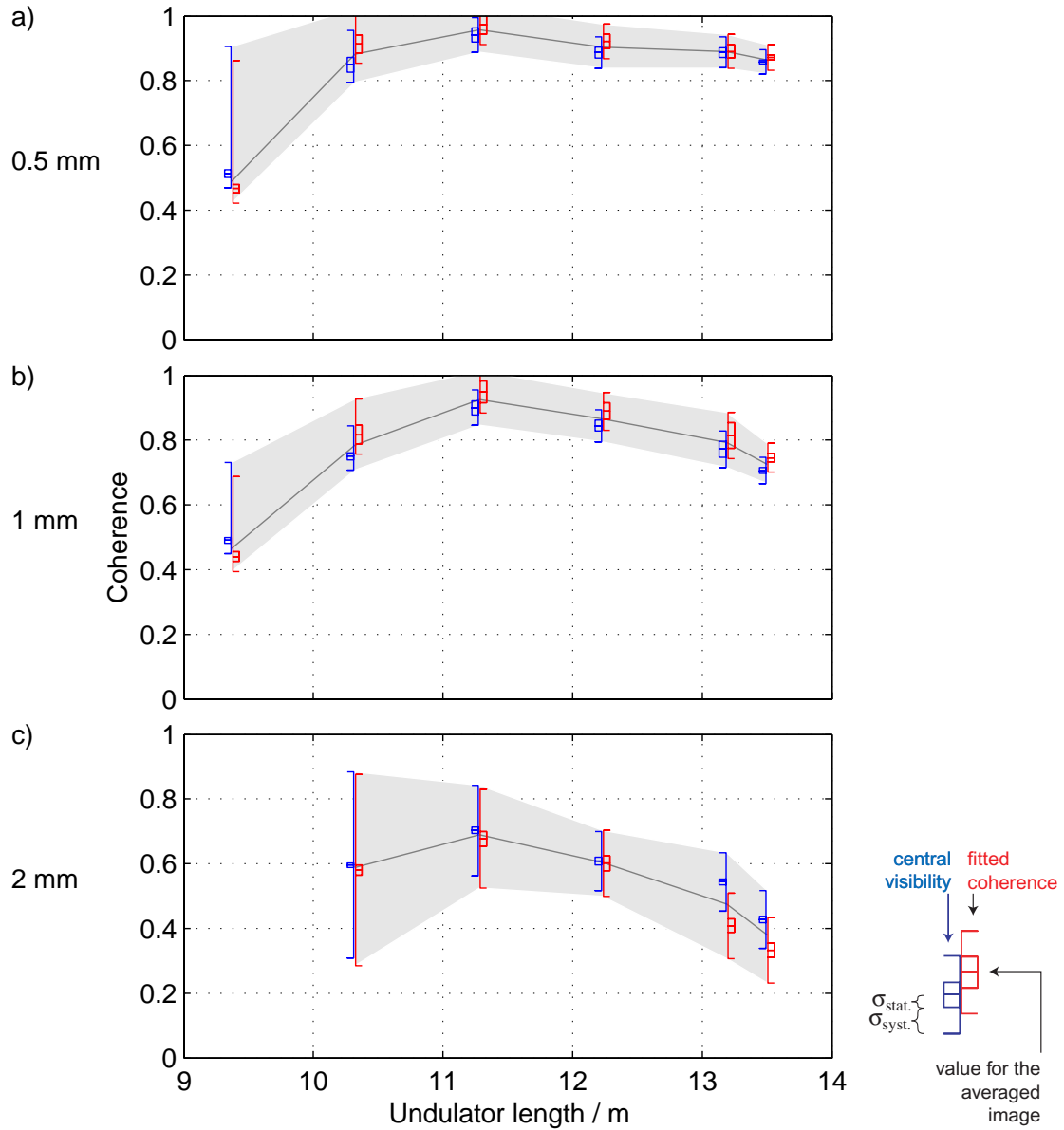


Figure 8.12.: Transverse coherence of the FEL as a function of undulator length, at slit separations of a) 0.5, b) 1 and c) 2 mm. The curves have a maximum around 11 m. The central visibility of the measured diffraction patterns is shown in blue, the fitted coherence in red. The error bars show statistical fluctuations and systematic uncertainties, as shown in the legend.

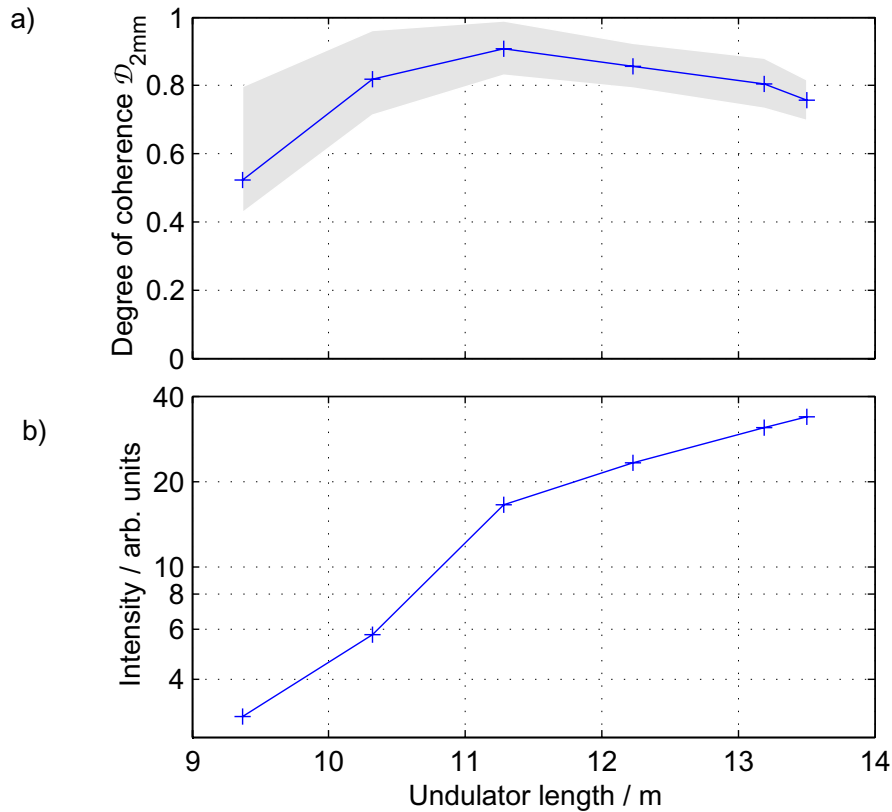


Figure 8.13.: a) The degree of transverse coherence as a function of the undulator length. The values of the transverse coherence up to a separation of 2 mm have been taken into account. b) From the total intensity of the diffraction patterns, it can be seen that the measurements extends over an interval that covers the end of the exponential gain regime of the FEL (from 9 to 11 m) to the beginning of saturation (above 11 m).

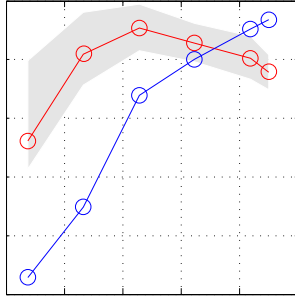
8.3. Results

The degree of transverse coherence is the intensity-weighted average of the coherence function on the observation plane. The measurements described in this chapter have been done up to a slit separation of 2 mm. Figure 8.13 shows the degree of coherence within a circle of 2 mm radius.

The transverse coherence of the FEL increases in the regime of exponential gain, between virtual undulator lengths between 9 and 11 m. It reaches a value of 0.91 ± 0.08 at 11.28 m. The growth rate of the FEL intensity decreases behind 11 m: the plot on a logarithmic axis (figure 8.13b) has a smaller slope above 11 m. This indicates the onset of the saturation in the FEL process. It is expected that the transverse coherence starts to decrease in saturation, because the fundamental transverse radi-

8. *Evolution of coherence along the undulator*

ation mode cannot grow further (see section 3.3.1). This can be in fact observed in figure 8.13a. For experiments that require a high transverse coherence of the FEL, it is thus mandatory to operate the FEL such that the fundamental mode does not saturate.



Part V.

Conclusion

Speed: But tell me true, will't be a match?

Launce: Ask my dog: if he say ay, it will! if he say no,
it will; if he shake his tail and say nothing, it will.

Speed: The conclusion is then that it will.

William Shakespeare, *The Two Gentlemen of Verona*, Act II, scene V

Figure on the previous page: Measured intensity (red) and coherence (blue) of the TTF FEL, as a function of the undulator length. See figure 8.13.

9. Conclusion and Outlook

9.1. Coherence measurement at the TTF FEL

The coherence of the free electron laser at the TESLA Test Facility has been measured with Young's double slit experiment. The double slits and a fluorescent crystal were installed in the ultra high vacuum of the accelerator. The diffraction pattern on the crystal was observed by a gated CCD camera. Measurements on single FEL pulses were possible. Diffraction patterns were recorded with different slit separations. The acquired images were corrected for detrimental effects of the fluorescent crystal and the camera.

Two methods were used to extract the transverse coherence of the FEL beam from the near field diffraction patterns: the central visibility of the pattern was determined, and a function for the near field diffraction was fitted to the measured intensity distribution. The results are in good agreement. The degree of coherence within a circle of 3 mm radius is $\mathcal{D}_{3\text{mm}} = 0.64 \pm 0.06$ for a saturated FEL.

A comparison to simulations has been made. These simulations include the formation of the photon bunch in the FEL [Yur02], a variable transverse coherence, the near field diffraction, the non-linearity of the fluorescent crystal at the high intensities, the scatter in the crystal, the imaging of the tilted lens and the noise in the CCD. The resulting images show good agreement with the measurements.

The development of the coherence along the undulator was observed, using steering magnets to adjust the effective undulator length to values between 9.4 and 13.5 m. The highest coherence is achieved at a length of 11 m, where the FEL process is still in its exponential gain regime and before the saturation of the central radiation mode sets in. Here, a degree of coherence within a circle of 2 mm radius $\mathcal{D}_{2\text{mm}} = 0.91 \pm 0.08$ has been measured.

9.2. Comparison with other measurements

The FEL radiation can be decomposed in its longitudinal and transverse modes, as described in section 3.3. As the electric field amplitude in different modes is uncorrelated, a high number of modes lowers the coherence of the beam. The number of longitudinal modes depends on the bunch length, which can be varied with the first bunch compressor (see section 4.2.4). While this influences many other parameters

of the electron beam, it has been shown that in the saturation regime of the FEL electron bunch parameters have only a weak influence on the FEL radiation.

In an FEL, the different radiation modes have a different wavelength, due to the origin in the spontaneous radiation. Therefore, they can be separated by the spectrometer. Single-shot spectra can be recorded with an intensified CCD camera. The modes can be seen in these spectra (see for example figure 4.19). Furthermore, the average number of modes can be inferred from the statistical variation of the intensity from pulse to pulse. The results have been compared with FEL simulations [Ayv02a] and confirm the high degree of coherence.

Another method to estimate the transverse coherence is to measure the distribution of the intensity in the far field of the FEL. This is determined by the angular distribution of the photons at the undulator exit. If one assumes that the beam is diffraction limited, this is equal to the Fourier transform of the transverse pulse shape [SSY00a]. This can be decomposed in its transverse modes, which gives the degree of coherence.

9.3. Coherence measurement at higher photon energies

Accelerators to generate FEL radiation at shorter wavelengths are currently in the design and commissioning phase. At DESY, the TTF linear accelerator is being extended to drive a free electron laser for wavelengths down to 6 nm [TES02]. In a first stage, the FEL will produce radiation with a wavelength of 30 nm. It will serve as a user facility for various experiments. Since a name for this project has not yet been found, it will be referred to as *VUV-FEL* in this chapter. The layout of the experimental hall is shown in figure 9.1.

Furthermore, an X-ray FEL for wavelengths down to 0.01 nm has been proposed.

The transverse coherence of these FELs can be measured by recording the diffraction pattern of a slit or pinhole pair. The experience from the present set-up shows that the fluorescent crystal and the camera optics degrade the image quality. A much thinner crystal could show improved spatial resolution due to the smaller length the fluorescent light travels through the crystal. Maybe it is even possible to cover the back side of the crystal with an anti-reflex coating for the wavelength of the fluorescent light. The camera can be replaced by microscope optics, achieving much higher resolution. Commercial microscope optics with 30 cm free distance between the front lens and the crystal have been shown to achieve a resolution of $\sigma = 5 \mu\text{m}$ (see section 6.1.3). It has to be noted that this set-up has a much smaller aperture, thus the light yield is inferior to a standard photographic lens.

While the image degradation can be taken into account in the analysis, it would be advantageous to avoid the effects that influence the image quality altogether.

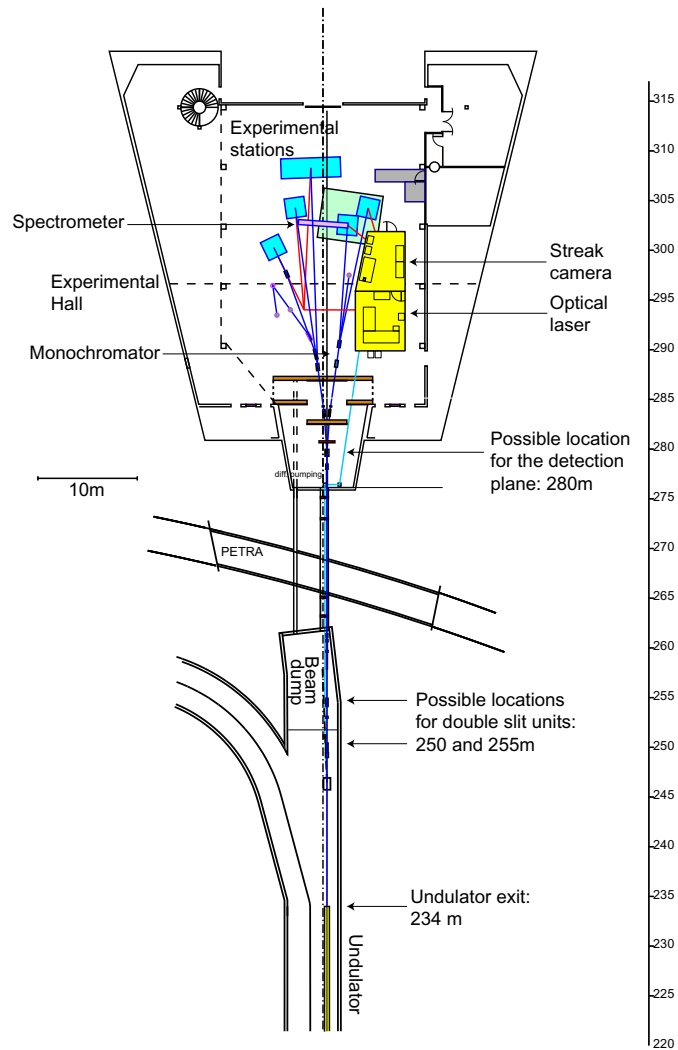


Figure 9.1.: The last part of the accelerator and the experimental hall for the future VUV-FEL at DESY.

This could be achieved by placing a position-sensitive X-ray detector directly into the accelerator vacuum. Back-illuminated CCD sensors show high sensitivity to soft X-rays. Their spatial resolution is given by the pixel size, which is typically $20\ \mu\text{m}$ [Pri02]. The sensitivity would be several orders of magnitude higher than with the fluorescent crystal. However, there is the risk of radiation damage; semiconductors are typically limited to exposure of a few hundred Gray. The detector could also be destroyed immediately by the ablation of its surface if the momentaneous power density is too high.

Figure 9.1 shows possible positions for double slits and observation planes in the future VUV-FEL. A double slit could be inserted at 250 or 255 m on the scale shown in

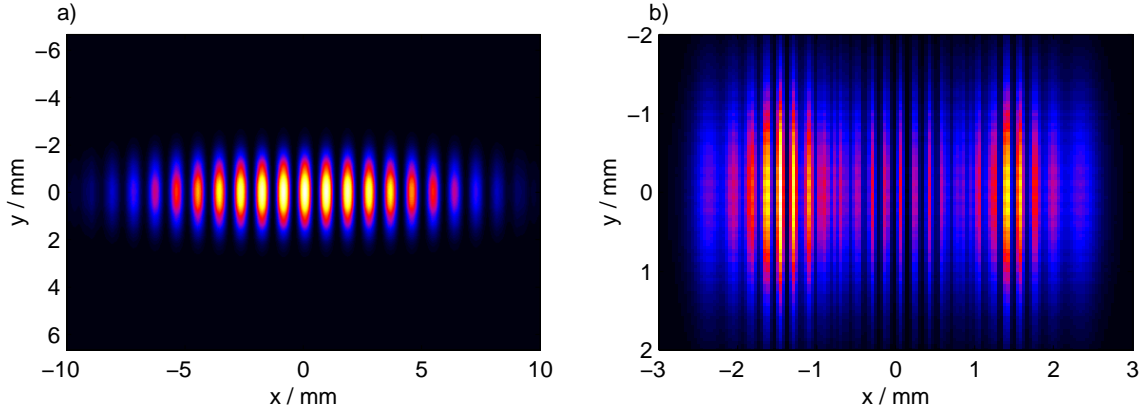
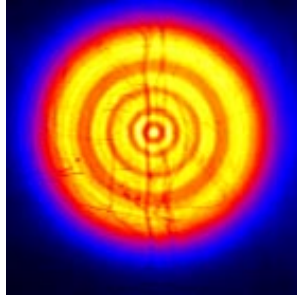


Figure 9.2.: Simulated diffraction pattern that could be observed at the VUV-FEL at DESY. The slit separation has been taken to be 1 mm, the slits are 2 mm long and 100 μm wide. The separation between the double slit and the observation plane is 30 m. a) For a wavelength of 30 nm, b) for a wavelength of 6 nm.

figure 9.1. A smaller distance to the undulator exit seems favourable. This is located at the position 234 m on this scale. In the following, the position at 250 m will be used. The diffraction pattern could be observed at the position 280 m. Such a large separation between the double slit and the observation plane is a great advantage compared to the set-up which is described in this thesis, as the fringe separation is increased and the resolution of the fluorescent crystal and the camera have a smaller influence on the observed image quality.

The angular divergence of the VUV-FEL is expected to range from 24 to 170 μrad FWHM, depending on the operation mode [TES02]. Thus, beam diameters between 0.4 and 2.7 mm FWHM will occur at a position of the double slits. With slit separations between 0.1 and 5 mm, the whole range of the FEL radiation can be covered. For a wavelength of 30 nm, the far field condition is only fulfilled for the smallest slit separations, so the calculation of the diffraction pattern will generally have to be done using Fresnel theory. A slit separation of 1 mm results in a fringe separation of 0.9 mm, which is easy to resolve with standard optics. A diffraction pattern that has been predicted by GLAD is shown in figure 9.2.



Part VI.
Appendices

Figure on the previous page: diffraction at a circular aperture.

A. Mathematical Symbols

Table A.1.: Mathematical Symbols (continued in table A.2).

Symbol	Definition
\mathcal{A}	aperture
α	angle between the z axis and the electron velocity
\vec{B}	magnetic flux density
β	normalised velocity
c	speed of light
\mathcal{C}	coherence
γ	relativistic factor
γ_r	relativistic factor on resonance
$\tilde{\gamma}$	correlation function
Γ	FEL gain parameter
\mathcal{D}	degree of coherence
e	elementary charge
e	Euler's number
\vec{E}	electric field
\tilde{E}	slowly varying complex amplitude of the electric field
f	particle distribution function in phase space
η	relative deviation from resonance energy
I	intensity
\vec{j}	current density
J	Bessel function
\vec{k}	wave number vector
k_u	2π divided by the undulator period
K	undulator parameter
\hat{K}	corrected undulator parameter
ℓ	distance between a point on the aperture and a point on the observation plane
L	distance between aperture and observation plane
L_g	power gain length of the FEL

Table A.2.: Mathematical Symbols (continued).

Symbol	Definition
λ	wavelength
λ_u	undulator period
Λ	power growth rate of the FEL
m_e	(invariant) electron mass
N	number of particles
P	point spread function
Φ	measured image
\vec{r}	space coordinate vector
ρ	charge density
ρ_{Pierce}	Pierce parameter
σ	standard deviation
t	time
ψ	ponderomotive phase
Ψ	real image (as opposed to the measured image)
\vec{u}	unit vector
v	particle velocity
\mathcal{V}	fringe visibility
W	energy
ω	angular frequency
x, y, z	space coordinates
\bar{A}	mean value of A
A^*	complex conjugate of A

B. Imaging with a Tilted Lens

A flat object that is tilted with respect to the optical axis of a camera can be imaged correctly by tilting the lens, too. Optimum focus over the complete image plane is achieved if the planes through object, lens and image intersect in exactly one line. This criterion is derived in this chapter from two rules of geometric optics, namely the thin lens equation (B.1) and the rule that a ray that goes through the centre of the lens proceeds unaltered.

First, a lens without imaging errors whose thickness is negligible will be considered. In this case, the following equation holds:

$$1/f = 1/g + 1/b \quad (\text{B.1})$$

where f is the focal length of the lens, g the distance from the lens to the object and b the distance from the lens to the image.

To ease the derivation, it may be assumed without loss of generality that the lens plane is perpendicular to the optical axis. The three-dimensional problem can be restricted to the plane containing the optical axis where the inclination of the object is highest (figure B.1). The optical axis is taken as x axis, a point in this plane is labelled (x_0, y_0) .

Assuming an object on the line that intersects the optical axis in the point $(-g, 0)$, and with an angle γ to this axis (corresponding to a slope $g' = \tan \gamma$), any point on this line can be represented as

$$(-g + a, ag') \quad (\text{B.2})$$

The image of this point (x_b, y_b) lies on the line that goes through the centre of the lens,

$$x_b \cdot ag' - y_b \cdot (-g + a) = 0 \quad (\text{B.3})$$

its distance to the lens can be derived from Eq. (B.1)

$$\frac{1}{f} = \frac{1}{g - a} + \frac{1}{x_b} \quad (\text{B.4})$$

The solution of equations (B.3) and (B.4) is:

$$x_b = \frac{(a - g)f}{a - g + f} \quad (\text{B.5})$$

$$y_b = \frac{ag'f}{a - g + f} \quad (\text{B.6})$$

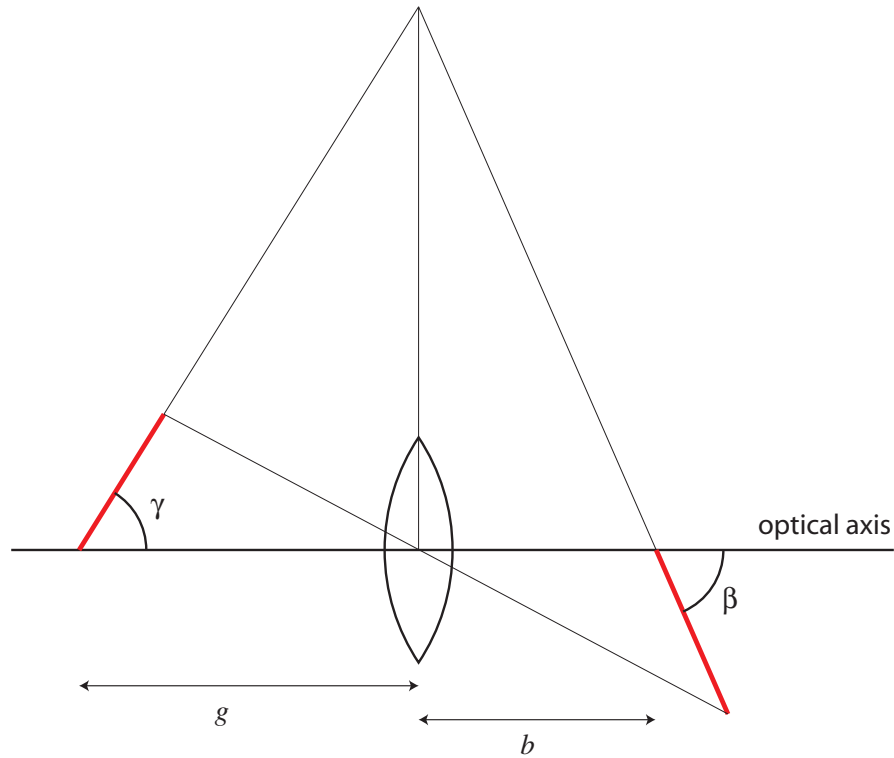


Figure B.1.: Imaging of a tilted object at a distance g that has an angle γ to the optical axis results in an image at a distance b at an angle β .

Varying a leads to the image of an extended object. It intersects the optical axis at the point $(b, 0)$ where

$$b = \frac{g \cdot f}{g - f} \quad (\text{B.7})$$

Since

$$b' := \frac{y_b}{x_b - b} = g' \frac{f - g}{f} \quad (\text{B.8})$$

is independent of a , the image is indeed a straight line. Furthermore, the intersection of the image with the y axis is in the point $(0, g g')$, the same point where the straight line through the object intersects the y axis.

C. The van Cittert-Zernike theorem

Seen from a large distance, the radiation from a spatially incoherent source acquires a certain degree of transverse coherence [Zer38], see also [Fra66]. The coherence depends on the intensity distribution in the source and has for example been used to measure the apparent size of a star.

Consider a radiation source located at a distance L in z direction from the observation plane, as shown in figure C.1. The source is supposed to be pseudo-thermic, consisting for example of a large number N of atoms that emit independently. For simplicity, only the polarisation in \vec{u}_x direction is considered. The transverse coherence between points P_1 and P_2 in the observation plane will be derived. Without loss of generality, one may choose the origin such that $P_2 = (0, 0, L)$.

An atom k , at a position $(x_0, y_0, 0)$ emits an electromagnetic wave:

$$\vec{E}(t) = \tilde{E}_k(t)e^{i\omega t}\vec{u}_x \quad (\text{C.1})$$

At the point T_1 in the observation plane, the electromagnetic field is

$$\tilde{E}_{k1}(t) = \tilde{E}_k(t - \ell_1/c) \frac{e^{i\omega(t - \ell_1/c)}}{\ell_1} \quad (\text{C.2})$$

Similarly for T_2 :

$$\tilde{E}_{k2}(t) = \tilde{E}_k(t - \ell_2/c) \frac{e^{i\omega(t - \ell_2/c)}}{\ell_2} \quad (\text{C.3})$$

The contributions from all atoms in the source are added:

$$\tilde{E}_1(t) = \sum_{k=1}^N \tilde{E}_{k1}(t) = \sum_{k=1}^N \tilde{E}_k(t - \ell_1/c) \frac{e^{i\omega(t - \ell_1/c)}}{\ell_1} \quad (\text{C.4})$$

The coherence function between T_1 and T_2 at the observation plane is:

$$\Gamma_{12} = \left\langle \tilde{E}_1(t) \tilde{E}_2^*(t) \right\rangle_t = \left\langle \sum_{k=1}^N \tilde{E}_{k1}(t) \cdot \sum_{k=1}^N \tilde{E}_{k2}^*(t) \right\rangle_t \quad (\text{C.5})$$

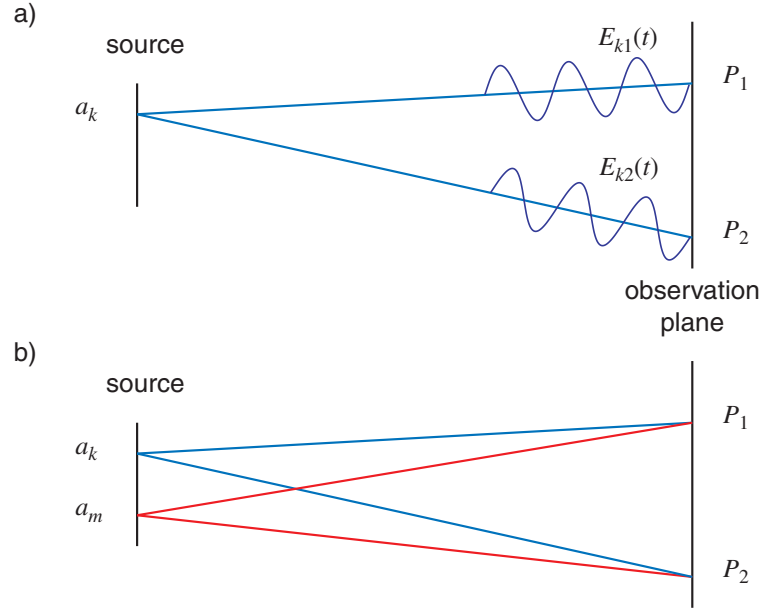


Figure C.1.: Illustration of the van Cittert-Zernike theorem.

Because $\langle \tilde{E}_{k1}(t) \tilde{E}_{m2}^*(t) \rangle = 0$ for $k \neq m$ the product of the two sums may be simplified:

$$\Gamma_{12} = \left\langle \sum_{k=1}^N \left[\tilde{E}_{k1}(t) \tilde{E}_{k2}^*(t) \right] \right\rangle_t \quad (\text{C.6})$$

$$= \left\langle \sum_{k=1}^N \left[\tilde{E}_k(t - \ell_1/c) \tilde{E}_k^*(t - \ell_2/c) \right] \right\rangle_t \frac{e^{i\omega(\ell_2 - \ell_1)/c}}{\ell_1 \ell_2} \quad (\text{C.7})$$

$$= \sum_{k=1}^N \left\langle \tilde{E}_k(t) \tilde{E}_k^*(t - (\ell_2 - \ell_1)/c) \right\rangle_t \frac{e^{i\omega(\ell_2 - \ell_1)/c}}{\ell_1 \ell_2} \quad (\text{C.8})$$

If the source is sufficiently monochromatic, i.e. if its longitudinal coherence length exceeds the path length difference $\ell_2 - \ell_1$, the retardation $(\ell_2 - \ell_1)/c$ in the first term may be neglected and

$$\Gamma_{12} = \sum_{k=1}^N \left\langle \tilde{E}_k(t) \tilde{E}_k^*(t) \right\rangle_t \frac{e^{i\omega(\ell_2 - \ell_1)/c}}{\ell_1 \ell_2} \quad (\text{C.9})$$

The quantity $\langle \tilde{E}_k(t) \tilde{E}_k^*(t) \rangle_t$ is proportional to the intensity J of the radiation that is emitted by the atom k . Due to the large number of atoms in the source, the sum over the atoms may be replaced by an integral over the source:

$$\Gamma_{12} = \iint J(x, y) \frac{e^{i\omega(\ell_2 - \ell_1)/c}}{\ell_1 \ell_2} dx dy \quad (\text{C.10})$$

The denominator can be simplified with $\ell_1 \approx L$ and $\ell_2 \approx L$. In the exponential function, ℓ_1 and ℓ_2 can be expanded similarly to Eq. (3.20):

$$\ell_1 \approx L + \frac{(x_1 - x_0)^2 + (y_1 - y_0)^2}{2L} \quad (\text{C.11})$$

and

$$\ell_2 \approx L + \frac{x_0^2 + y_0^2}{2L} \quad (\text{C.12})$$

Thus,

$$\ell_2 - \ell_1 = -\frac{x_1^2 + y_1^2}{2L} + \frac{x_0x_1 + y_0y_1}{L} \quad (\text{C.13})$$

Using this approximation, the integral (C.10) simplifies to

$$\Gamma_{12} = \iint \frac{J(x, y)}{L^2} \exp \left[i \frac{\omega}{c} \left(-\frac{x_1^2 + y_1^2}{2L} + \frac{x_0x_1 + y_0y_1}{L} \right) \right] dx dy \quad (\text{C.14})$$

Apart from the normalisation, this is just the Fresnel integral, Eq. (3.22), where the aperture function is substituted for the intensity of the source. Thus, *the transverse coherence of a pseudo-thermic monochromatic source is equal to the normalised diffraction pattern that is formed by a coherent source with an aperture that has the same shape as the source.* This relation is the *van Cittert-Zernike theorem*.

D. Data Acquisition

When carrying out experiments on such a large and complex device as a particle accelerator, the need arises to correlate data specific to the experiment itself (i.e. here, the camera images) with measurements from devices designed and operated by other groups. Often, the relevant parameters for the specific experiment become only clear in the analysis process, months after the experiment. It is thus helpful to store data from all available beam diagnostics systems in a central database. This data acquisition (DAQ) system complements the measurements and notes of the operators, stored in the logbook. Such a DAQ system has been implemented for the TTF accelerator. It has operated reliably for more than a year, writing more than 2 TB of compressed data to file. The server programmes are documented in [Lac02]. Various experiments have used these files to cross-check with their measurements. Furthermore, long-term studies, e.g. on the effectiveness of the collimation system and the radiation damage of the undulator, have been carried out.

This chapter describes the existing controls (section D.1.1), how the DAQ was fitted into this system (section D.2.3) and the technical implementation (section D.3).

D.1. Overview of the control system

D.1.1. DOOCS

The TTF accelerator, i.e. the superconducting cavities, the magnets and the beam diagnostics are controlled by a distributed system, the Distributed Object-Oriented Control System (DOOCS). This consists of programmes that are running on a distributed computer system:

- The *front end computers*, mostly VME crates, are the interface to the hardware. Analogue-to-digital converters (ADCs) sample external analogue signals. The standard ADCs at TTF have a sampling rate of 1 MHz. They reside directly in the VME crate. Approximately 400 channels were installed in the phase 1 of the TTF linac. Most diagnostics devices can be easily connected to this ADC. Other devices control the RF regulation or the magnet power supplies. All devices can be accessed through their respective *device servers*. This includes reading values as well as setting the output parameters of the hardware. Different servers exist for the various devices, but the interface to the clients is always the same.

- The *clients* can access these servers with a network call. They then receive an answer. There is a number of different clients at TTF: a graphical user interface, the DOOCS Data Display (ddd) is used by the operators to run the accelerator; many diagnostics are written in MATLAB, and there are also some C++ programmes to perform complex tasks.
- *Gateways* to other systems allow the clients to uniformly access also hardware that is not connected to a DOOCS server.

D.1.2. Object orientation

DOOCS is an object oriented system, i.e. data and the functions that can be applied on it are encapsulated in objects. Object-oriented programming (OOP) has the following advantages as compared to procedural programming:

- *encapsulation* of the data with the functions to access them: this allows to change the internal representation of the data in the servers without the need to redesign the clients that use this data. In addition, this imposes a certain discipline on the programmers.
- Objects can *inherit* properties of their so-called ancestors. One can thus include the code that applies to many different object types (in our case the network communication ability) in a common prototype and then add specific functions to the device server.
- *polymorphism*

Many people see OOP as the only possibility to create large applications that are developed and maintained by many people.

D.1.3. ROOT

ROOT [BR97] is an object-oriented framework for C++ programmes that has been written to effectively handle large amounts of data. The source code is freely available. Pre-compiled versions for a variety of platforms, including Solaris, Linux and Windows, are available. The package was initiated by René Brun and Fons Rademakers; Masuata Guoto has contributed a C++ interpreter, allowing to run programmes in an interactive session.

ROOT includes a database that allows to store objects to a file, independent of the operating system and of the processor architecture. To do so, the objects are streamlined and serialised, resulting in a data stream that can be compressed and sent to the file. Using the same mechanism, objects can also easily be sent over a network. In fact, sending the objects to a special ROOT daemon is more efficient than writing the file through the Network File System (NFS). ROOT takes complete

control over the data flow, optimising it for best performance. The database structure is optimised to provide a fast sequential access to the data.

Additionally, ROOT provides analysis routines for various mathematical tools. Data can be represented in diagrams for screen or printer rendering through plot objects. Owing to its origin in high-energy physics, ROOT has many functions to histogram and fit data. Other areas, as for example image processing, are less well developed.

D.2. A data acquisition for the TTF

D.2.1. Requirements

The requirements for the DAQ system have been formulated in 1999/2000:

- scalability
- extensible
- based on an available system, no home-made database system
- take the data from the DOOCS servers
- encapsulated
- by preference: use the same format as TESLA experiment

D.2.2. Choice of a database

The features of ROOT make it the natural choice for the data acquisition at the TTF accelerator. Its performance for sequential access beats commercial systems by a factor of two, and its freely available source code makes it easy to distribute in the collaboration.

D.2.3. Gateway to the existing control system

The data acquisition system gets all values from the DOOCS servers. These convert the data to physically meaningful units, e.g. the signal height of the beam position monitors to the position in millimetres. ADCs have typically up to 16 bits. A conversion to 32-bit floating point variables, as used by DOOCS, results in an increase in data rate. It would be more efficient to transfer the raw data to the DAQ system. On the other hand, one avoids errors by doing the conversion in exactly one place. Furthermore, one takes advantage of the standardised access to all devices in the accelerator.

The system was implemented and commissioned in a period where the accelerator was running. The reliability of the existing control system had thus the foremost priority.

D.3. Implementation

This section gives a brief overview of the data structures and programmes that constitute the data acquisition system. The implementation is described in detail in [Lac02]. An overview of the system is given in figure D.1.

D.3.1. Data structure

The data is collected in objects that are stored in the ROOT framework. Therefore, these objects, of class `TTFFloatData`, are descendants of `TObject`, a class defined in ROOT. They are arranged in a hierarchical structure, called a *tree*.

The objects have two variables, the time stamp and a data array, receiving for example the values read from the ADC. All channels are stored in the same type of object. The time stamp consists of the time in seconds since the 1970-01-01 00:00 world time and the buffer number of the ADC. The latter is synchronised by a timing signal in the control system. It ranges from 0 to 31 and is incremented with each macro-pulse, i.e. once a second in the present set-up. The data part contains an array of floating-point values. A different number of values is used, depending on the device that is connected to the channel. For example, magnet currents have only one value (the actual current is measured once a second), the amplitude of the RF field is measured 512 times within each macro-pulse, and so on.

D.3.2. ROOT object generators

The ROOT Object Generators [Lac02] are programmes that request the values from the ADC servers, put them into an object derived from `TNamed` and save them into the file. The process, called `adcg` runs on various computers in the middle layer (see also figure D.1). It connects to the DOOCS device servers through an object `TTFDOOCS`.

The protocol that is used by the clients to request data from a DOOCS server is based on the *remote procedure call* (RPC) method. A special function call in the client code opens a network connection to the server, sends the request and then waits for the server to reply (*synchronous mode*). (In a multi-tasking operating system, another process may run during the time where the client waits.) The RPC calls a special function in the server. This does everything necessary to answer the request (e.g. read the values from the ADC, convert them to meaningful units, form averages) and sends the data back to the client.

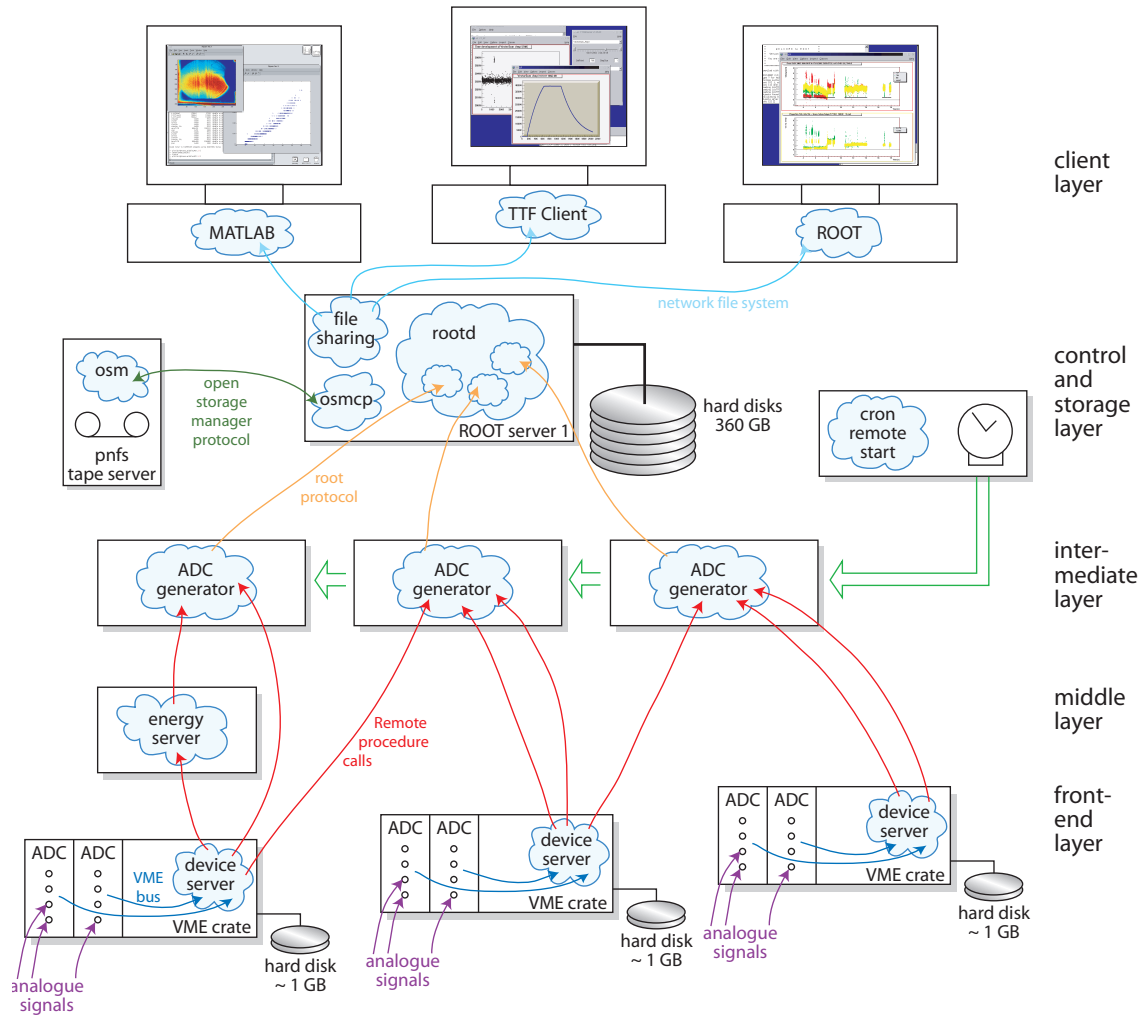


Figure D.1.: A simplified overview of the data acquisition system. The data, represented by arrows, flows from the bottom to the top. Computers are symbolized by boxes, processes by clouds. To simplify the picture, only three front end computers and daq processors are pictured; network components as equipment name servers, routers and switches are not shown.

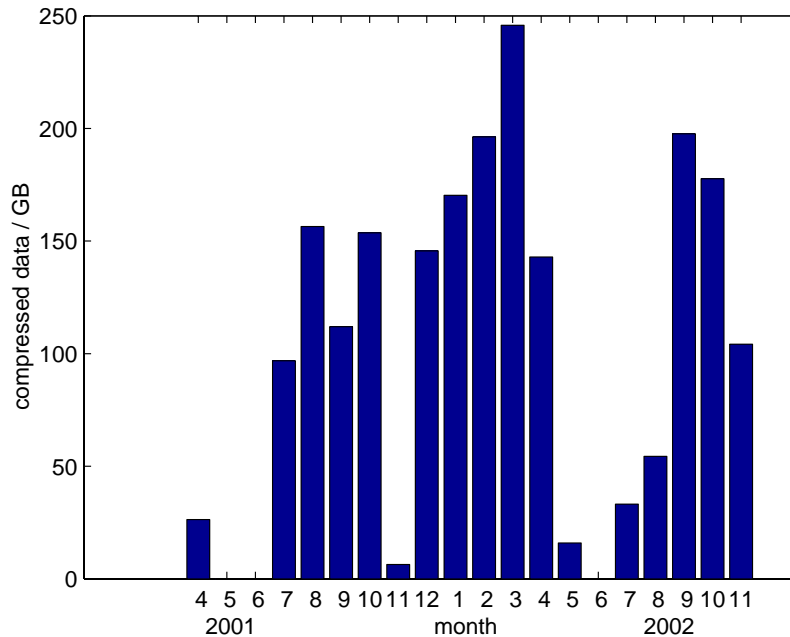


Figure D.2.: Amount of data collected by the TTF DAQ in the years 2001 and 2002.

Remote procedure calls provide a robust way to access data across a network. There are several implementations on the market; TTF uses the Open Network Computing (ONC) RPC, introduced by Sun Microsystems. ONC RPC is also used by Linux.

D.3.3. Network transfer

However, opening a network connection for each object that is to be transferred can be a time-consuming task. Therefore, the access to the ROOT database is implemented with the ROOT daemon, a server based on the Apache webserver. The protocol is well-suited to transfer large amounts of data efficiently. The daemon has been running on the TTF DAQ server for 20 months. It has received more than 2 Terabytes of data without the need to restart it. Figure D.2 shows the amount of data collected each month.

D.3.4. Tape storage

The data are transferred to an automated tape storage machine. For this, the Open Storage Manager (OSM) [Fuh99] is used. The transfer from disk to tape is done once a day, in the early morning hours where the network load is lowest. (As DESY uses a fully switched network, this data transfer does not affect the communication within the accelerator hall.)

D.4. Synchronisation with camera image acquisition

The pictures were acquired and stored independently of the rest of the DAQ system: the camera is connected to a PC running Windows; it is read out by software supplied by the camera manufacturer. This sends the images as 16-bit TIFF¹ files via the Network File System (NFS) to the server `ttfsvr3`. Due to the large amount of data, the image acquisition is only activated for dedicated experiments, running typically for a few 100 seconds, while the rest of the data acquisition, as described above, is running continuously. The images are numbered within one experiment, the date and time of the PC is recorded in the lower part of the image itself. The camera is triggered by the central TTF timing system, which starts also the read-out cycle of the ADCs. The correlation is preserved if both systems run without losing a macropulse.

Synchronisation between the two systems is lost if one of them has to skip a macropulse. This happens from time to time when the network load is high. All network operations are based on asynchronous calls: each process replies to a request as soon as the operating system allocates time for it. The same is true for the network file servers; on some occasions, the recording of data takes then more than one second. The image of the next macropulse can then not be recorded, the programme waits first for the save operation to finish. It is skipped tacitly. A solution is to record the images first to the core memory and to write them to disk at the end of the experiment. The drawback is that the number of images is limited by the amount of memory in the camera server; by recording only the interesting part of the image and by binning several pixels into one, the number of images is increased. The ring buffer of the ADCs allows the DAQ servers to recover from a short congestion in the network. However, sometimes they have to omit macropulses; this is then noted in the files.

To correlate data from the electron beam or the data acquired by the microchannel plate detector, it is necessary to synchronise the two data streams. This was done by making sure that both systems run with the same speed and by synchronizing the start of the measurement.

The internal clock of the PC was adjusted to the central DESY time server by means of the Network Time Protocol (NTP). However, an ambiguity of one second remains. Therefore, the synchronisation of the experiment start was done by switching the injection laser of the accelerator on and off. This is visible in the TTF DAQ system (e.g. the current monitors or the micro channel plate show zero signal); also the image remains completely black. The same procedure was repeated at the end of the experiment, to make sure that the data streams have retained their synchronisation.

The measurement of the FEL brightness by the MCP detector and the CCD camera

¹Tagged Image File Format, an image file format published by Aldus Corporation in 1986

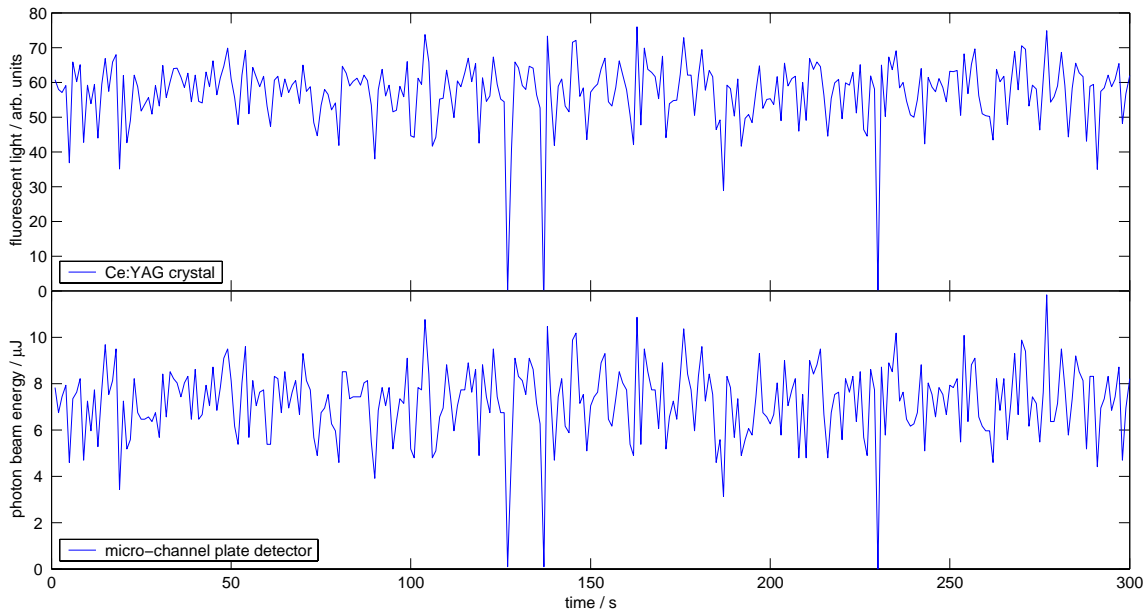


Figure D.3.: Brightness of the FEL pulse, recorded with the camera (top) and the micro channel plate (bottom). The measurements agree, for example the three times where the accelerator failed to deliver a pulse are acquired with the same time stamp. This shows that the synchronisation between the two data acquisition systems has been successful. The correlation plot of these data is shown in Figure 6.3.

shows that this method was successful (Figure D.3); however, it would be desirable to automatize the procedure by integrating the image acquisition completely in the control and data acquisition system of the accelerator.

D.5. Data acquisition of camera images

The control and read-out of the CCD camera is done by the programme *camware* (written by the camera manufacturer PCO) running on a PC under Microsoft Windows. The images are first stored in memory before they are transferred to the file server. Depending on the binning and the region selected for read-out, a few hundred images can be stored. To correlate the images with the TTF DAQ system, a client based on the *network time protocol* has been installed on the PC. Camware stores the time by inserting it in human-readable format in the lower right corner of the image itself. Unfortunately, there is no way to read out the TTF ADC buffer number from the Windows PC, which would allow an unambiguous identification of the macropulse.

Thus, the correlation was done by switching the complete linac off and on several times, searching for this pattern in the data acquired by the two systems.

E. Circular Apertures

Already the circular apertures, installed in the FEL beam line at position 3 in figure 4.12 to reduce the intensity, create a diffraction pattern on the fluorescent crystal.

E.1. Measurements

Circular apertures of 0.5, 1, 3 and 5 mm diameter have been inserted in position 3 in figure 4.12 into the FEL beam, the distance to the detection plane is 3.3 m. An averaged dark image has been subtracted. For each aperture, 79 measurements with 3 bunches have been added to obtain good photon statistics. The resulting diffraction patterns are shown in figure E.1. A wavelength of 99 nm has been measured with the spectrometer. Some imperfections in the fluorescent crystal are visible. The aperture with 5 mm diameter could not be centered completely.

E.2. Analysis

The far field criterion (3.23) is fulfilled for apertures below 0.6 mm. Thus, Fraunhofer diffraction theory (section 3.5) can be applied only for the smallest aperture. The pattern for a 0.5 mm aperture is well described by the Bessel function (3.25), as can be seen in figure E.2. For the larger aperture, the far field criterion is not fulfilled, the calculated curve underestimates the width of the central peak and the height of the side maxima.

The apertures with 3 and 5 mm diameter, on the other hand, create a near field diffraction pattern with several rings that can be described by the Fresnel zones in the aperture (section 3.6). The number of zones calculated from Eq. (3.39) agrees well with the number of extrema in the diffraction pattern (table E.1). The detailed shape of the pattern can be reproduced by numeric simulations. A Gaussian beam with full transverse coherence at the exit of the undulator has been assumed and the wave fronts have been propagated through the aperture to the crystal with the code GLAD. The agreement of the central slices of the simulations with the measurements is shown in figure E.3.

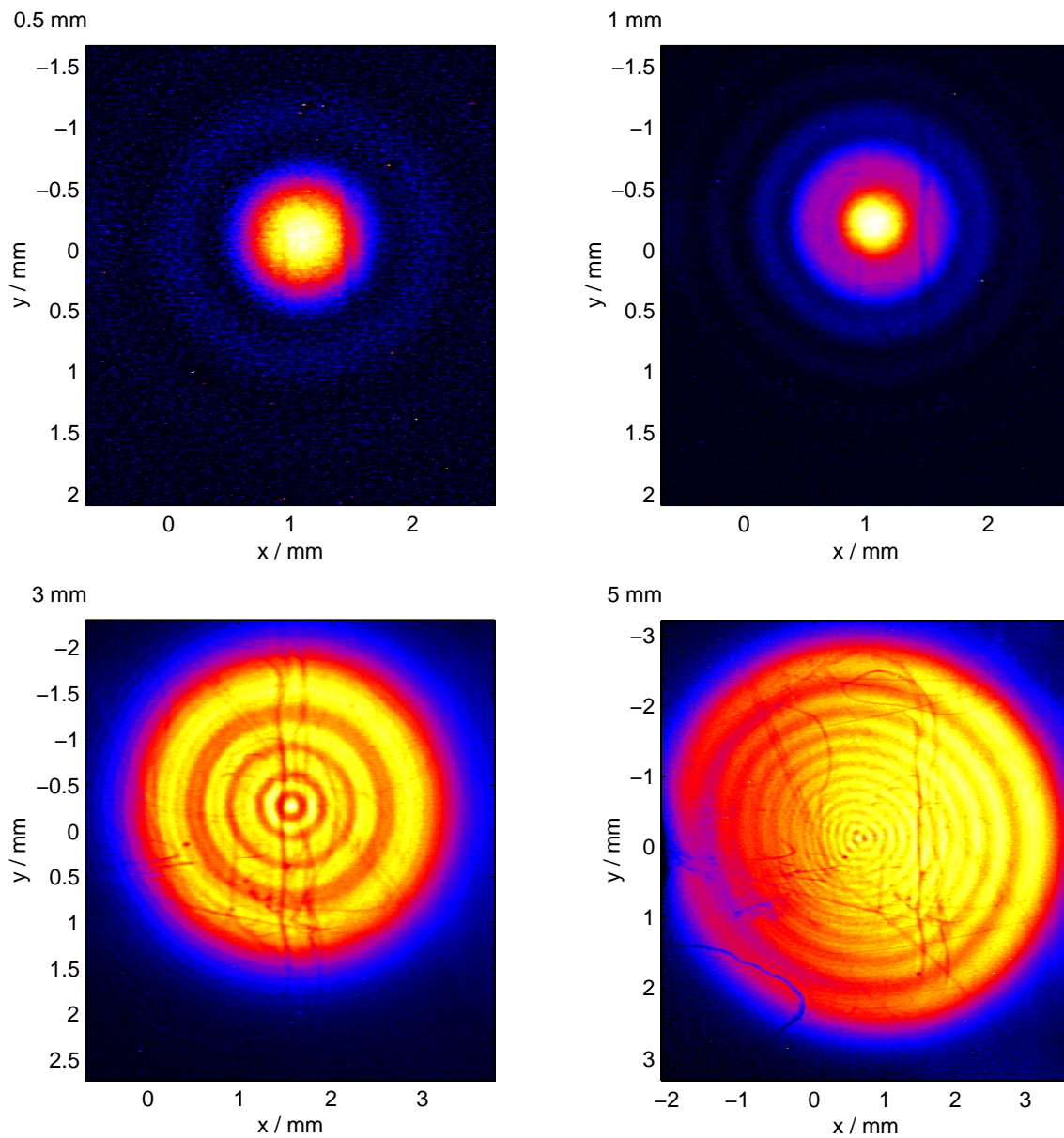


Figure E.1.: Diffraction patterns of circular apertures; a) 0.5 mm, b) 1 mm, c) 3 mm and d) 5 mm diameter. Some scratches on the fluorescent crystal deteriorate the image quality. Note the different scale of the images.

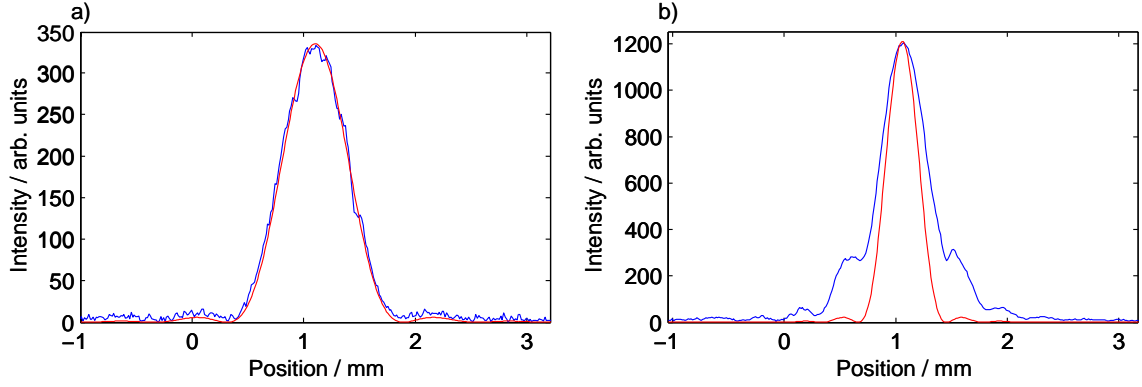


Figure E.2.: Cross section of the diffraction patterns of circular apertures with a) 0.5 mm and b) 1 mm diameter. The measured values are shown in blue, the intensity calculated by Fraunhofer diffraction (Eq. (3.25)) is shown in red.

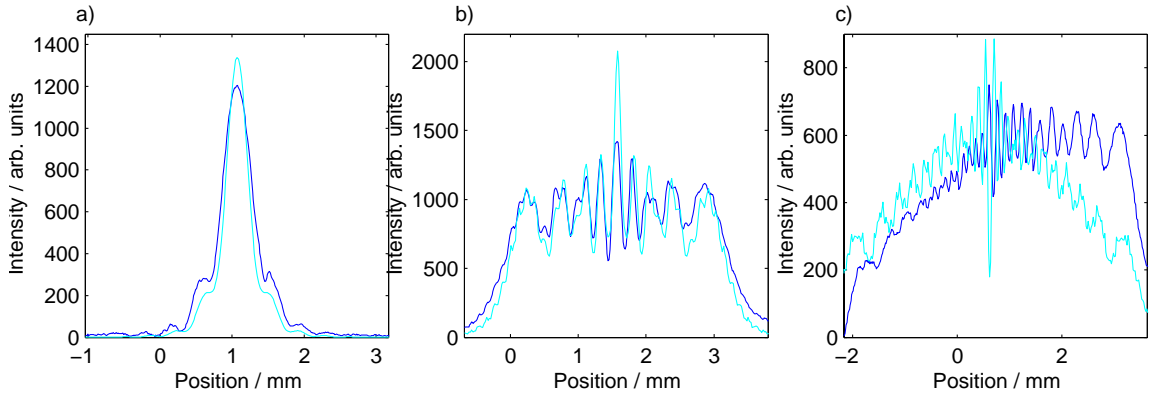


Figure E.3.: Comparison of measured with simulated diffraction patterns of circular apertures with a) 1 mm, b) 3 mm and c) 5 mm diameter. The measurement is shown in a blue line, the simulation in cyan.

Table E.1.: Number of Fresnel zones, calculated from Eq. (3.39) and measured with the FEL. For the calculations, a source position 1 m in front of the exit of the undulator has been assumed.

Aperture	N_F calculated	N_F measured
0.5 mm	0.24	—
1 mm	0.97	—
3 mm	8.7	9
5 mm	24.3	23

F. Analysis Routines for the Double Slit Diffraction Patterns

This appendix lists the procedures that were used to analyse the double slit diffraction patterns in chapter 7. The procedures that generate the plots are not included in this appendix.

F.1. Image procesing

```
% A = processimage(A)
% does the following operations on the image:
% - de-convolute using the Lucy-Richardson algorithm
% - apply non-linearity corrections for the intensity
% - project region of interest
% to operate correctly, please subtract a background image first!

function A = processimage(A)

addpath /home/rasmus/Analyse/Coherence/Calibration

B = A.Image / A.nb_bunches;

% load point spread function for deconvolution
PSF = loadpsf(A.binningx,A.binningy);
% deconvolute
C = deconvlucy(B, PSF, 10);

% crop date and time
D = C(1:end-9,:);

% correct for saturation
spotsizeforcalibration = 0.2; % in cm2
E = - log(1 - D/88.7545) / 0.14685 / spotsizeforcalibration * 100;
indi = find(imag(E)~=0); % find imaginary numbers
E(indi) = E(indi+1);

A.CorrectedImage = E;
```

```
% axes
A.xax = pixel_to_x([1:size(A.CorrectedImage,2)],A.binningx);
A.yax = pixel_to_y([1:size(A.CorrectedImage,1)],A.binningy);

% do projections
A.v = sum(A.CorrectedImage(A.yminpix:A.ymaxpix,A.xminpix:A.xmaxpix), ...
    A.isHori+1);

if A.isHori
    A.vax = A.yax(A.yminpix:A.ymaxpix);
else
    A.v = A.v';
    A.vax = A.xax(A.xminpix:A.xmaxpix);
end

% calculate intensity
A.MaxIntensityRaw = max(mean(A.Image ...
    (A.yminpix:A.ymaxpix,A.xminpix:A.xmaxpix),A.isHori+1))*1.3;
A.MaxIntensity = max(mean(A.CorrectedImage ...
    (A.yminpix:A.ymaxpix,A.xminpix:A.xmaxpix),A.isHori+1))*1.3;
A.TotalIntensity = sum(sum(A.Image(1:end-10,:)));

if A.isHori
    Signal = A.MaxIntensityRaw * sqrt(A.xmaxpix-A.xminpix+1);
    % select an area outside of the diffraction pattern:
    NoiseArea = A.Image(1:end-10,end-10:end);
    Noise = std(NoiseArea(:));
else
    Signal = A.MaxIntensityRaw * sqrt(A.ymaxpix-A.yminpix+1);
    NoiseArea = A.Image(1:10,40:end);
    Noise = std(NoiseArea(:));
end

A.SNR = Signal / Noise;
```

F.2. Analysis method 1: central visibility

```
% analysis_vis.m
% does the analysis 1: smooth the curve, find maxima and minima and
% calculate visibility.

function A = analysis_vis(A);
```

```
% Smooth curve with a butterworth filter.
% This filter cuts away the components with high spatial frequency.
% It has two parameters:
% * the order determines how strong the components are suppressed.
% * the cutoff frequency is given as a ratio to the frequency
%   corresponding to one wavelength over the complete curve.
%   This parameter is more critical.

butterorder = 5;

% the optimum value for the cutoff frequency depends on the slit
% separation ...
switch A.slitsep
    case 0.5e-3, butterfreq = 0.1;
    case 1e-3, butterfreq = 0.17;
    case 2e-3, butterfreq = 0.2;
    case 3e-3, butterfreq = 0.2;
end

% ... and on the binning:
if A.isHori
    binning = A.binningy;
else
    binning = A.binningx;
end
butterfreq = butterfreq * binning;

[butterb,buttera] = butter(butterorder,butterfreq);
A.vsmooth = filtfilt(butterb,buttera,A.v);

if ~isfield(A,'iMax') | isempty(A.iMax)
    % used for the averaged images:
    % find the maxima
    if A.isHori
        binning = A.binningy;
    else
        binning = A.binningx;
    end
    [Max, A.iMax, Min, A.iMin] = find_maxima(A.vsmooth, A.slitsep, ...
        binning, A.isHori);

    % always start and end with a minimum
    if A.iMin(1) > A.iMax(1)
        Min = [A.vsmooth(1) Min];
        A.iMin = [1 A.iMin];
    end
end
```

```
end
if A.iMin(end) < A.iMax(end)
    Min = [Min A.vsmooth(end)];
    A.iMin = [A.iMin length(A.vsmooth)];
end
else
    % used for the single images
    isp('analysis_vis.m: using pre-computed maxima and minima positions')
    Max = A.vsmooth(A.iMax);
    Min = A.vsmooth(A.iMin);
end

MeanMin = mean([Min(2:end); Min(1:end-1)]);

A.Vis = abs((Max-MeanMin) ./ (Max+MeanMin));
A.xax_Vis = A.vax(A.iMax);

indi_central_part = find(A.xax_Vis>-1.5 & A.xax_Vis<1.5);
sortedVis = sort(A.Vis(indi_central_part));
maxi1 = sortedVis(end);
maxi2 = sortedVis(end-1);
if maxi1 <= maxi2*1.1
    A.centralVis = maxi1;
else
    A.centralVis = maxi2;
end
```

F.2.1. Finding maxima and minima

```
function [Max, Maxpos, Min, Minpos] = ...
    find_maxima(vf, slitsep, binning, isHori)
% finds the maxima and minima of the diffraction patterns

if isHori
    switch slitsep
        case 0.5e-3, expected_distance = 64/binning;
        case 1e-3, expected_distance = 32/binning;
        case 2e-3, expected_distance = 15/binning;
        case 3e-3, expected_distance = 10/binning;
        otherwise
            error('Error: unknown slit separation (in find_maxima.m)')
        end
    else
        switch slitsep
```



```

        case 0.5e-3, expected_distance = 45/binning;
        case 1e-3, expected_distance = 22/binning;
        case 2e-3, expected_distance = 11/binning;
        case 3e-3, expected_distance = 7/binning;
    otherwise
        error('Error: unknown slit separation (in find_maxima.m)')
    end
end

% start in the middle
k = round(length(vf)/2);

% look to the right until maximum found
while vf(k+1)>vf(k), k=k+1; end
% now look to the left until maximum found
while vf(k-1)>vf(k), k=k-1; end
% now maximum is at k:
Max = vf(k);
Maxpos = k;
Middle = k;

Min = [];
Minpos = [];

end_reached = 0;
beginning_reached = 0;
Count = 0; % number of maxima to each side
while ~(end_reached & beginning_reached)
    % Look to the right
    if ~end_reached
        % find minimum
        % expected position
        k = round(Middle + (Count+1/2)*expected_distance);
        irstart = k;
        if k>=length(vf), k=length(vf)-1; end
        while vf(k+1)<vf(k)
            k=k+1;
            if k>=length(vf)-1, end_reached = 1; break, end
        end
        while vf(k-1)<vf(k)
            k=k-1;
        end
        % is the deviation from the expected distance too large?
        % then use the expected distance!
    end
end

```

F. Analysis Routines for the Double Slit Diffraction Patterns

```
    if abs(k-istart) > expected_distance / 4, k = istart; end
    % are we inside the range?
    if k<=length(vf), Min = [Min, vf(k)];
        else Min = [Min, vf(end)]; end
    Minpos = [Minpos, k];

    % find maximum
    k = round(Middle + (Count+1)*expected_distance);
    istart = k;
    if k>=length(vf), k=length(vf)-1; end
    while vf(k+1)>vf(k)
        k=k+1;
        if k>=length(vf)-1, end_reached = 1; break, end
    end
    while vf(k-1)>vf(k)
        k=k-1;
    end
    % is the deviation from the expected distance too large?
    % then use the expected distance!
    if abs(k-istart) > expected_distance / 4, k = istart; end
    % are we inside the range?
    if k<=length(vf), Max = [Max, vf(k)];
        else Max = [Max, vf(end)]; end
    Maxpos = [Maxpos, k];
end

% Look to the left
if ~beginning_reached
    % find minimum
    k = round(Middle - (Count+1/2)*expected_distance);
    istart = k;
    if k<=1, k=2; end
    while vf(k-1)<vf(k)
        k=k-1;
        if k<=2, beginning_reached = 1; break, end
    end
    while vf(k+1)<vf(k)
        k=k+1;
    end
    if abs(k-istart) > expected_distance / 4, k = istart; end
    if k>=1, Min = [vf(k), Min]; else Min = [vf(1), Min]; end
    Minpos = [k, Minpos];

    % find maximum
```

```

    k = round(Middle - (Count+1)*expected_distance);
    istart = k;
    if k<=1, k=2; end
    while vf(k-1)>vf(k)
        k=k-1;
        if k<=2, beginning_reached = 1; break, end
    end
    while vf(k+1)>vf(k)
        k=k+1;
    end
    if abs(k-istart) > expected_distance / 4, k = istart; end
    if k>=1, Max = [vf(k), Max]; else Max = [vf(1), Max]; end
    Maxpos = [k, Maxpos];
end

Count = Count + 1;
expected_distance = mean(diff(Maxpos));
end

% Drop maxima and minima outside range

Max = Max(2:end-1);
Maxpos = Maxpos(2:end-1);

while Minpos(end) > length(vf)
    Min = Min(1:end-1); Minpos = Minpos(1:end-1);
    Max = Max(1:end-1); Maxpos = Maxpos(1:end-1);
end

while Minpos(1) < 1
    Min = Min(2:end); Minpos = Minpos(2:end);
    Max = Max(2:end); Maxpos = Maxpos(2:end);
end

```

F.3. Analysis method 2: fit to the intensity

```

% analysis_fit.m
% -----
% does the analysis 2: fit a curve to the intensity
%   para(1) = C;           transverse coherence
%   para(2) = lambda*1e7; wavelength
%   para(3) = mu*1e4;     middle of the pattern
%   para(4) = wcurL*1e5;  wavefront curvature at the left slit

```

F. Analysis Routines for the Double Slit Diffraction Patterns

```
% para(5) = wcurR*1e5;   wavefront curvature at the right slit
% para(6) = Etotal*1e-1; electric field amplitude
% para(7) = Eratio;     ratio of the field amplitudes between the
%                       two slits

function A = analysis_fit(A)

% choose reasonable starting parameters for the fit
if isempty(A.fit_start_para)
    C = 0.5;
    lambda = 100e-9;
    mu = 0;
    wcurL = 0;
    wcurR = 0;
    Etotal = 10;
    Eratio = 1;

    para(1) = C;
    para(2) = lambda*1e7;
    para(3) = mu*1e4;
    para(4) = wcurL*1e5;
    para(5) = wcurR*1e5;
    para(6) = Etotal*1e-1;
    para(7) = Eratio;
else
    para = A.fit_start_para;
end

if isempty(A.fit_bounds)
    lowerbounds = [0  0.80 -10 -10 -10  0.1 0.90];
    upperbounds = [1  1.10  10  20  20 10  1.10];
else
    lowerbounds = A.fit_bounds(1,:);
    upperbounds = A.fit_bounds(2,:);
end

myopt = optimset('LargeScale','on');

% do the fit
[para,resnorm,residual,exitflag,output] = ...
    lsqnonlin(@intenserrvec5, para, lowerbounds, upperbounds, myopt, ...
    [A.vax; A.v'], A.slitsep);

C = para(1); % coherence
```

```

d = A.slitsep; % slit separation
w = 1e-4; % slit width
L = 3.1; % distance slits - screen
lambda = para(2)*1e-7; % wavelength
mu = para(3)*1e-4; % displacement
wcurL = para(4)*1e-5; % left wave front curvature
wcurR = para(5)*1e-5; % right wave front curvature
Etotal = para(6)*1e1; % left E-field
Eratio = para(7); % right E-field

disp(['Coherence C = ',num2str(C),' slit separation d = ', ...
      num2str(d*1e3),'mm, slit width w = ',num2str(w*1e6),'um,', ...
      'distance to screen L = ',num2str(L),'m, '])
disp(['wavelength lambda = ',num2str(lambda*1e9),'nm, ', ...
      'middle = ',num2str(mu*1e3),'mm, wavefront curvature wcurL = ', ...
      num2str(wcurL)])
disp(['wavefront curvature wcurR = ',num2str(wcurR), ...
      ', average E-field = ',num2str(Etotal), ...
      ' E-field ratio = ',num2str(Eratio)])

if size(A.v,1)<size(A.v,2), A.v = A.v'; end

A.fit_error = sum(intenserrvec4(para, [A.vax; A.v'], A.slitsep).^2);
disp(['fit error = ',num2str(A.fit_error)])

A.fit_para = para;

% prepare plots
x = A.vax;

% single slit diffraction patterns
argL = pi*w*(x+d/2+wcurL*L-mu)/(lambda*L);
argL(argL==0) = eps;
argR = pi*w*(x-d/2-wcurR*L-mu)/(lambda*L);
argR(argR==0) = eps;

E1 = sin(argL)./argL * Etotal * Eratio;
E2 = sin(argR)./argR * Etotal / Eratio;

% intensities
I1 = E1.^2;
I2 = E2.^2;
S = I1 + I2;

```

```

% intensities in the maxima and minima
Iex1 = (E1+E2).^2;
Iex2 = (E1-E2).^2;

% visibility
V = (Iex1-Iex2)./(Iex1+Iex2);
% correction when the fields at the slits are not equal
Vcor = 2/(Eratio^2 + 1/Eratio^2);

% total double slit diffraction pattern
Icalc = S .* (1 + C * V * Vcor .* cos(2*pi*d/(lambda*L) * (x-mu)));

A.xax_vfit = x;
A.vfit = Icalc;

% the most important parameter of the fit, the transverse coherence:
A.fitC = A.fit_para(1);

```

F.3.1. fitted function

```

function errvec = intenserrvec5(para, data, slitsep);
% calculates the deviation from the expected pattern

C = para(1); % coherence
d = slitsep; % slit separation
w = 1e-4; % slit width
L = 3.1; % distance slits - screen
lambda = para(2)*1e-7; % wavelength
mu = para(3)*1e-4; % displacement
wcurL = para(4)*1e-5; % wave front curvature
wcurR = para(5)*1e-5; % wave front curvature
Etotal = para(6)*1e1; % left E-field
Eratio = para(7); % right E-field

x = data(1,:);
Iref = data(2,:);

% single slit diffraction patterns
argL = pi*w*(x+d/2+wcurL*L-mu)/(lambda*L);
argL(argL==0) = eps;
argR = pi*w*(x-d/2-wcurR*L-mu)/(lambda*L);
argR(argR==0) = eps;

E1 = sin(argL)./argL * Etotal * Eratio;

```

```
E2 = sin(argR)./argR * Etotal / Eratio;

% intensities
I1 = E1.^2;
I2 = E2.^2;
S = I1 + I2;

% intensities in the maxima and minima
Iex1 = (E1+E2).^2;
Iex2 = (E1-E2).^2;

% visibility
V = (Iex1-Iex2)./(Iex1+Iex2);
% correction when the fields at the slits are not equal
Vcor = 2/(Eratio^2 + 1/Eratio^2);

% total double slit diffraction pattern
Icalc = S .* (1 + C * V * Vcor .* cos(2*pi*d/(lambda*L) * (x-mu)));

% deviation from expected pattern
errvec = Icalc-Iref;
```

Bibliography

- [Åbe95] T. Åberg et al. A VUV free electron laser at the TESLA test facility at DESY – conceptual design report. Technical report, DESY, 1995. TELS-FEL 95-03.
- [ABE02] R. Akre, L. Bentson, and P. Emma. Bunch length measurements using a transverse RF deflecting structure in the SLAC linac. In *Proceedings of the EPAC2002 conference*, 2002.
- [Ama99] Lorenzo Amati. Crab nebula 240 channels spectrum. <http://tonno.tesre.bo.cnr.it/~amati/tesi/node73.html>, 1999.
- [And00] J. Andruszkow et al. First observation of self-amplified spontaneous emission in a free-electron laser at 109 nm wavelength. *Physical Review Letters*, 85(18), October 2000.
- [App01a] Applied Optics Research. *GLAD Theory Manual*, 4.7 edition, 2001.
- [App01b] Applied Optics Research. *GLAD User's Manual*, 4.7 edition, 2001.
- [Aun00] B. Aune et al. Superconducting TESLA cavities. *Physical Review Special Topics – Accelerators and Beams*, 3, 2000.
- [Ayv02a] V. Ayvazyan et al. Generation of GW radiation pulses from a vuv free-electron laser operating in the femtosecond regime. *Physical Review Letters*, 88(104802), 2002.
- [Ayv02b] V. Ayvazyan et al. A new powerful source for coherent VUV radiation: Demonstration of exponential growth and saturation at the TTF free-electron laser. *European Physical Journal D*, 20:149–156, 2002. <http://dx.doi.org/10.1140/epjd/e2002-00121-4>.
- [BA97] David S.C. Biggs and Mark Andrews. Acceleration of iterative image restoration algorithms. *Applied Optics*, pages 1766–1775, March 1997.
- [BGG⁺03] M. Brunken, H. Genz, P. Göttlicher, C. Hessler, M. Hüning, H. Loos, A. Richter, H. Schlarb, P. Schmüser, S. Simrock, D. Suetterlin, M. Tonutti, and D. Türke. Electro-optic sampling at the TESLA Test Accelerator: Experimental setup and first results. Technical report, DESY, 2003. TESLA 2003-11.
- [BHE00] I. Bloch, T. W. Hänsch, and T. Esslinger. Measurement of the spatial coherence of a trapped bose gas at the phase transition. *Nature*, 403:166–170, 2000.

- [BPG⁺02] Randy A. Bartels, Ariel Paul, Hans Green, Henry C. Kapteyn, Margaret M. Murnane, Sterling Backus, Ivan P. Christov, Yanwei Liu, David Attwood, and Chris Jacobsen. Generation of spatially coherent light at extreme ultraviolet wavelengths. *Science*, 297:376ff., July 2002.
- [BR97] Rene Brun and Fons Rademakers. ROOT – an object oriented data analysis framework. Technical report, CERN, May 1997.
- [Bra90] C. A. Brau. Free electron lasers. *Boston, USA: Academic (Advances in electronics and electron physics, Suppl. 22)*, 1990.
- [BRHM96] A.F. Boden, D.C. Redding, R.J. Hanisch, and J. Mo. Comparative results with massively parallel spatially-variant maximum likelihood image restoration. *J. Opt. Soc. of America A*, 13(7):1537–1545, 1996.
- [Cas96] M. Castellano et al. OTR measurements for the TTF commissioning. In *Proceedings of the EPAC conference*, 1996.
- [Cas02] Pedro Castro. Performance of the TESLA Test Facility linac. In *EPAC*, page 876ff., 2002.
- [Che95] R. Chehab et al. Progress in the study and construction of the TESLA Test Facility injector. In *Proceedings of the 16th IEEE Particle Accelerator Conference (PAC 95) and International Conference on High Energy Accelerators (IUPAP)*, Dallas, Texas, May 1995.
- [CL94] T.F. Coleman and Yuying Li. On the convergence of interior-reflective Newton methods for nonlinear minimization subject to bounds. *Mathematical Programming*, 67(2):189–224, 1994.
- [CL96] T.F. Coleman and Yuying Li. An interior trust region approach for nonlinear minimization subject to bounds. *SIAM J. Optimization*, 6(2):418–445, 1996.
- [CL99] Czech Republic Crytur Ltd, Turnov. http://www.crytur.cz/scintillator_e.htm, 1999.
- [Col97] E. Colby. *Design, construction, and testing of a radiofrequency electron photoinjector for the next generation linear collider*. PhD thesis, UCLA, 1997. FERMILAB-THESIS-1997-03, UMI-98-07655-mc.
- [CPR90] W.B. Colson, C. Pellegrini, and A. Renieri (Editors). *Laser Handbook – Free Electron Lasers*, volume 6. North-Holland, 1990.
- [DeL89] Lawrence J. DeLucas et al. Protein crystal growth in microgravity. *Science*, 246(4930), 1989.
- [Det00] Universität Gießen Detektorlabor. <http://www.physik.uni-giessen.de/Detektorlabor/Bilder/Szintillatoren%20tabelle.PDF>, 2000.

- [DR02] Martin Dohlus and Jörg Rossbach. High-gain free-electron laser, 2002. CERN-US-Japan Accelerator School, Long Beach.
- [Edw95] D.A. Edwards (Editor). TESLA test facility linac – design report. Technical report, DESY, 1995. TESLA 95-01.
- [Faa01] B. Faatz et al. Use of micro-channel plate for nondestructive measurement of VUV radiation from the SASE FEL at the TESLA Test Facility. In *Contributions to the FEL2001 Conference*, pages 62–67, 2001. DESY-FEL 2001-09.
- [Faa03] Bart Faatz. Private communication, 2003.
- [FJ96] Jean Fusellier and Jean Marc Joly. Beam intensity monitoring and machine protection by toroidal transformers on the TESLA Test Facility. In *Proceedings of the 5th European Particle Accelerator Conference (EPAC 96)*, Sitges, Spain, Jun 1996.
- [FK02] Hartmut Frommert and Christine Kronberg. Supernova remnant M1 (NGC 1952) in Taurus – crab nebula. <http://www.maa.agleia.de/Messier/E/m001.html>, 2002.
- [FP99] B. Faatz and J. Pflüger. Magnet sorting for the TTF-FEL undulator using simulated annealing. Technical Report 1999-01, DESY / HASYLAB, 1999.
- [Fra66] M. Françon. *Optical Interferometry*. Academic Press, New York and London, 1966.
- [Fuh99] Patrick Fuhrmann. <http://mufasa.desy.de/>, 1999.
- [Gei99] Marc Geitz. Investigation of the transverse and longitudinal beam parameters at the TESLA Test Facility linac. Doktorarbeit, Universität Hamburg, 1999.
- [Ger03] Christopher Gerth. Private communication, 2003.
- [GFH⁺03] Ch. Gerth, J. Feldhaus, K. Honkavaara, K.D. Kavanagh, Ph. Piot, L. Plucinski, S. Schreiber, and I. Will. Bunch length and phase stability measurements at the TESLA test facility. *Nuclear Instruments and Methods in Physics Research A*, 507:335–339, July 2003.
- [GFL⁺01] Ch. Gerth, B. Faatz, T. Lokańczyk, R. Treusch, and J. Feldhaus. Photon diagnostics for the study of electron beam properties of a VUV SASE-FEL. *NIM A*, 475:481–486, 2001.
- [Goo85] J. Goodman. *Statistical Optics*. John Wiley and Sons, 1985.
- [GSSY03] G.A. Geloni, E.L. Saldin, E.A. Schneidmiller, and M.V. Yurkov. A method for ultrashort electron pulse shape-measurement using coherent synchrotron radiation. Technical report, DESY, 2003. arXiv:physics/0303113, DESY 03-031.

-
- [Hah00] U. Hahn et al. Design and performance of the vacuum chambers for the undulator of the VUV FEL at the TESLA Test Facility at DESY. *Nuclear Instruments and Methods in Physics Research A*, 445:442–447, 2000.
- [HBF⁺03] K. Honkavaara, A. Brenger, R. Fischer, D. Nölle, K. Rehlich, L. Cacciotti, M. Castellano, G. DiPirro, M. Raparelli, R. Sorchetti, L. Catani, and A. Cianchi. Design of OTR beam profile monitors for the TESLA Test Facility, phase 2 (TTF2). In *Contributions to the PAC2003 Conference*, 2003.
- [Hec94] Eugene Hecht. *Optik*. Addison-Wesley, 3 edition, 1994.
- [HPS01] M. Hüning, Ph. Piot, and H. Schlarb. Observation of longitudinal phase space fragmentation at the TESLA Test Facility free-electron laser. *Nuclear Instruments and Methods in Physics Research A*, 475:348–352, 2001.
- [HS03] M. Hüning and H. Schlarb. Measurement of the beam energy spread in the TTF photo-injector. In *Contributions to the PAC2003 Conference*, 2003.
- [HSGP03] K. Honkavaara, S. Schreiber, Ch. Gerth, and Ph. Piot. Electron bunch shape measurements at the TTF-FEL. In *Contributions to the PAC2003 Conference*, 2003.
- [HT73] R.H. Hardin and F.D. Tappert. Applications of the split-step fourier method to the numerical solution of nonlinear and variable coefficient wave equations. *SIAM Review*, 15:423, 1973.
- [Hün02] Markus Hüning. Analysis of surface roughness wake fields and longitudinal phase space in a linear electron accelerator. Doktorarbeit, Universität Hamburg, 2002.
- [Jac98] John David Jackson. *Classical Electrodynamics*. John Wiley and Sons, 1998.
- [Kam00] Thorsten Kamps. Monitoring the electron beam position at the TESLA Test Facility free electron laser. Doktorarbeit, Humboldt-Universität zu Berlin, 2000.
- [KH00] Kwan-Je Kim and Z. Huang. Physics of high-gain free-electron-lasers, 2000. United States Particle Accelerator School, Stony Brook.
- [KLLZ00] M. Kirm, A. Luschchik, Ch. Luschchik, and G. Zimmerer. Investigation of luminescence properties of pure and Ce³⁺ doped Y₃Al₅O₁₂ crystals using VUV radiation. *ECS Proceedings*, 99-40:113–122, 2000.
- [KSK92] J.L. Krause, K.J. Schafer, and K.C. Kulander. High-order harmonic generation from atoms and ions in the high intensity regime. *Physical Review Letters*, 68(24):3535, 1992.
- [Lac02] Christian Lackas. Datennahme und Analyse der Beschleunigerdaten der TESLA-Testanlage zur Verbesserung und Stabilisierung der Strahlqualität. Diplomarbeit, RWTH Aachen, 2002.

- [Lam83] Robert L. Lamberts. Use of sinusoidal test patterns for mtf evaluation. Technical report, Sine Patterns LLC, 1983.
- [LBS⁺99] B. Leissner, Ch. Berger, R. Siedling, M. Tonutti, M. Geitz, G. Schmidt, and P. Schmüser. Bunch length measurements using a Martin Puplett interferometer at the TESLA Test Facility linac. In *Proceedings of the IEEE Particle Accelerator Conference (PAC 99)*, New York, NY, Mar–Apr 1999.
- [LBYW98] A.H. Lumpkin, W.J. Berg, B.X. Yang, and M. White. Time-resolved imaging for the APS linac beams. Technical report, Argonne National Laboratory, 1998.
- [Lie98] Matthias Liepe. Regelung supraleitender Resonatoren mit Strahlbelastung am TESLA-Test-Linearbeschleuniger. Doktorarbeit, Universität Hamburg, August 1998.
- [Lor97] R. Lorenz et al. First operating experiences of beam position monitors in the TESLA Test Facility linac. In *Proceedings of the PAC97 conference*, 1997.
- [Luc74] L.B. Lucy. An iterative technique for the rectification of observed distributions. *The Astronomical Journal*, page 745ff., June 1974.
- [LZPR94] H. Lengfellner, S. Zeuner, W. Prettl, and K.F. Renk. Thermoelectric effect in normal-state YBa₂Cu₃O_{7- δ} films. *Europhys. Lett.*, 25:375–378, 1994.
- [Mad70] John Madey. PhD thesis, Stanford University, 1970.
- [Mag98] C. Magne et al. High resolution bpm for future colliders. In *Proceedings of the 19th International Linear Accelerator Conference (Linac 98)*, Chicago, Illinois, Aug 1998.
- [Mat01a] The MathWorks. *Image Processing Toolbox*, 3.1 edition, 2001.
- [Mat01b] The MathWorks. *Optimization Toolbox*, 2.1.1 edition, 2001.
- [Mat01c] The MathWorks. *Signal Processing Toolbox*, 5.1 edition, 2001.
- [McD99] David McDowell. Standards update. *IS&T Reporter “The Window on Imaging”*, 14(4), August 1999.
- [Men03] Jan Menzel. Private communication, 2003.
- [Mey00] C. Meyer-Kobbe, 2000. MeKo Laser, <http://www.meko.de>.
- [MRY⁺00] A. Murokh, J. Rosenzweig, V. Yakimenko, E. Johnson, and X.J. Wang. Limitations on the resolution of YAG:Ce beam profile monitor for high brightness electron beam. *World Scientific*, 2000.
- [MT01] G. Materlik and Th. Tschentscher (Editors). TESLA technical design report part V: The X-ray free electron laser. Technical report, DESY, March 2001. DESY 2001-011.

- [N.02] N. N. Selection guide CCD. <http://www.sony.net/Products/SC-HP/SG/CCD/superhad-ccd.html>, 2002.
- [Ng96] Johnny S.T. Ng. A beam trajectory monitor using spontaneous undulator radiation at the TTF-FEL. 1996. DESY-TESLA-FEL-96-16.
- [Nil01] Norman B. Nill. Conversion between sine wave and square wave spatial frequency response of an imaging system. Technical Report MTR01B0000021, MITRE, July 2001.
- [NSK⁺97] P. V. Nickles, V. N. Shlyaptsev, M. Kalachnikov, M. Schnrer, I. Will, and W. Sandner. Short pulse X-ray laser at 32.6 nm based on transient gain in Ne-like titanium. *Physical Review Letters*, 78(14), 1997.
- [OS92] Alan V. Oppenheim and Ronald W. Schafer. *Zeitdiskrete Signalverarbeitung*. Oldenbourg, 1992.
- [PAM⁺01] D. Paterson, B.E. Allman, P.J. McMahon, J. Lin, N. Moldovan, K.A. Nugent, I. McNulty, C.T. Chantler, C.C. Retsch, T.H.K. Irving, and D.C. Mancini. Spatial coherence measurement of X-ray undulator radiation. *Optics Communications*, 195:79–84, 2001.
- [PCO02] PCO Computer Optics GmbH. *SensiCam, SensiCamQE Operating Instructions*, 07/2002 edition, 2002.
- [Pér96] J.-Ph. Pérez. *Optik*. Spektrum Akademischer Verlag, 1996.
- [Pri02] Princeton Instruments. *PI-MTE:1300B data sheet*, co edition, 2002. <http://www.roperscientific.com>.
- [Rei99] Sven Reiche. Numerical studies for a single pass high gain free-electron laser. Doktorarbeit, Universität Hamburg, 1999.
- [RGK⁺03] M. Richter, A. Gottwald, U. Kroth, A.A. Sorokin, S.V. Bobashev, L.A. Shmaenok, J. Feldhaus, Ch. Gerth, B. Steeg, K. Tiedtke, and R. Treusch. Measurement of gigawatt radiation pulses from a VUV/EUV free-electron laser. 2003.
- [Ric72] William Hadley Richardson. Bayesian-based iterative method of image restoration. *Journal of the Optical Society of America*, page 55ff., January 1972.
- [Rön96] Wilhelm Konrad Röntgen. Eine neue Art von Strahlen. Technical report, Verlag und Druck der Strahl'schen Hof- und Universitäts- Buch- und Kunsthandlung, 1896.
- [RR96] M. Razeghi and A. Rogalski. Semiconductor ultraviolet detectors. *J. Appl. Phys.*, 79:7433–7473, 1996.
- [RST⁺94] J.J. Rocca, V. Shlyaptsev, F.G. Tomasel, O.D. Cortázar, D. Hartshorn, and J.L.A. Chilla. Demonstration of a discharge pumped table-top soft-X-ray laser. *Physical Review Letters*, 73(16), 1994.

- [RSTW01] F. Richard, J. R. Schneider, D. Trines, and A. Wagner (Editors). TESLA technical design report. Technical report, DESY, March 2001. DESY 2001-011.
- [Sal03] Evgeny Saldin. Private communication, 2003.
- [SCG⁺02] S. Schreiber, J.-P. Carneiro, C. Gerth, K. Honkavaara, M. Hüning, J. Menzel, P. Piot, E. Schneidmiller, and M. Yurkov. Performance of the TTF photoinjector for FEL operation. In *Contributions to the ICFA2002 Conference*. World Scientific, 2002.
- [Sch00] Siegfried Schreiber. Performance status of the RF-gun based injector of the TESLA Test Facility linac. In *EPAC*, page 309ff., 2000.
- [Sch01a] Holger Schlarb. Collimation system for the VUV free-electron laser at the TESLA Test Facility. Doktorarbeit, Universität Hamburg, 2001.
- [Sch01b] Peter Schmüser. Vorlesung über Freie-Elektronen-Laser, 2001. Universität Hamburg.
- [Sch02] Holger Schlarb et al. Expansion of the fast linac protection system for high duty cycle operation at the TESLA Test Facility. In *Proceedings of the 8th European Particle Accelerator Conference (EPAC 2002), Paris, France*, Jun 2002.
- [Sch03a] Peter Schmüser. Superconductivity in high energy particle accelerators. Technical report, Institut für Experimentalphysik, Universität Hamburg, 2003.
- [Sch03b] Siegfried Schreiber. Private communication, 2003.
- [SMK⁺96] K. Solt, H. Melchior, U. Kroth, P. Kuschnerus, V. Persch, H. Rabus, M. Richter, and G. Ulm. PtSi-*n*-Si Schottky-barrier photodetectors with stable spectra responsivity in the 120–250 nm spectral range. *Appl. Phys. Lett.*, 69:3662–3664, 1996.
- [SSY99] E.L. Saldin, E.A. Schneidmiller, and M.V. Yurkov. FAST: a three-dimensional time-dependent FEL simulation code. *Nuclear Instruments and Methods in Physics Research A*, 429:233, 1999.
- [SSY00a] E.L. Saldin, E.A. Schneidmiller, and M.V. Yurkov. Diffraction effects in the self-amplified spontaneous emission FEL. *Optics Communications*, 186:185–209, 2000.
- [SSY00b] E.L. Saldin, E.A. Schneidmiller, and M.V. Yurkov. *The Physics of Free Electron Lasers*. Springer, 2000.
- [SSY03] E.L. Saldin, E.A. Schneidmiller, and M.V. Yurkov. Coherence properties of the radiation from SASE FEL. *Nuclear Instruments and Methods in Physics Research A*, 507:106–109, July 2003. [http://dx.doi.org/10.1016/S0168-9002\(03\)00848-9](http://dx.doi.org/10.1016/S0168-9002(03)00848-9).
- [Ste03] Bernd Steffen. Private communication, 2003.

-
- [Stö99] Horst Stöcker. *Taschenbuch mathematischer Formeln und moderner Verfahren*. Verlag Harri Deutsch, 4 edition, 1999.
- [Stu02] Nikolay Sturm. Energie-Stabilisierung für den Freien Elektronlaser an der TESLA-Test-Anlage. Diplomarbeit, RWTH Aachen, 2002.
- [Sug01] Toru Sugitate. The photon spectrometer for RHIC and beyond. hiroh2.hepl.hiroshima-u.ac.jp/phx/slides/phx031/phx031.pdf, 2001.
- [SWS⁺00] S. Schreiber, I. Will, D. Sertore, A. Liero, and W. Sandner. Running experience with the laser system for the RF gun based injector at the TESLA Test Facility linac. *NIM A*, 445:427–431, 2000.
- [Szö99] Abraham Szöke. Time-resolved holographic diffraction at atomic resolution. *Chemical Physics Letters*, 313:777–788, 1999.
- [Tec02] Applied Scintillation Technologies. <http://www.apace-science.com/ast/phosphor.htm>, 2002.
- [TES02] The TESLA Test Facility FEL team. SASE FEL at the TESLA Facility, phase 2. Technical report, DESY, 2002. TESLA-FEL-2002-01.
- [TLF98] R. Treusch, T. Lokajczyk, and J. Feldhaus. Photon beam diagnostics for the TTF phase I VUV SASE-FEL. *HASYLAB Annual Report*, 1998.
- [TLX⁺00] R. Treusch, T. Lokajczyk, W. Xu, U. Jastrow, U. Hahn, L. Bittner, and J. Feldhaus. Development of photon beam diagnostics for VUV radiation from a SASE FEL. *NIM A*, 445:456–462, 2000.
- [Tre01] Rick Trebino. Diffraction and the fourier transform. Technical report, Georgia Tech, 2001. <http://www.physics.gatech.edu/gcuo/UltrafastOptics/>.
- [Tür02] Diana Türke. Elektro-optische Abtastung von Elektronenpaketen an der TESLA-Test-Anlage - aufbau eines experiments. Diplomarbeit, RWTH Aachen, 2002.
- [TW57] B.J. Thompson and E. Wolf. *J. Opt. Soc. Am.*, 47:895, 1957.
- [UB81] A. Unsöld and B. Baschek. *Der neue Kosmos*. Springer, 3 edition, 1981.
- [Wab02] Hubertus Wabnitz et al. Multiple ionization of atom clusters by intense soft X-rays from a free-electron laser. *Nature*, 420, December 2002.
- [WC53] James Watson and Francis Crick. A structure for deoxyribose nucleic acid. *Nature*, 171, April 1953.
- [You04] Thomas Young. Experimental demonstration of the general law of the interference of light. *Philosophical Transactions of the Royal Society of London*, 94, 1804.
- [Yur02] Mikhail Yurkov. Private communication, 2002.

Bibliography

- [Yur03] Mikhail Yurkov. Private communication, 2003.
- [Zer38] F. Zernike. The concept of degree of coherence and its application to optical problems. *Physica*, 5:785, 1938.
- [ZPL95] S. Zeuner, W. Prettl, and H. Lengfellner. Fast thermoelectric response of normal state $\text{YBa}_2\text{Cu}_3\text{O}_{7-\delta}$ films. *Appl. Phys. Lett.*, 66:1833–1835, 1995.

Acknowledgements

I would like to thank all my colleagues at DESY, RWTH Aachen and Universität Hamburg, who contributed to the formation of this thesis. My work would not have been possible without them. Through their help in the measurements, interesting discussions and their support in the preparation of this document, they have helped me a lot.

First of all, I would like to thank my advisors, *Prof. Dr. Peter Schmüser* and *Prof. Dr. Manfred Tonutti*, who got me excited for the TTF project and who supported the measurements, analysis and the writing of this document with many constructive ideas. They always found time for fruitful discussions and helped me to refine my thoughts.

Furthermore, I show my gratitude to *Josef Feldhaus*, with whom I discussed many details of the experimental set-up and the analysis of the measurements. Special thanks to *Jörg Roßbach*, who discussed many details of the FEL theory with me.

The measurements for this thesis were done with the SASE FEL photon diagnostics group. Together, we have set up the devices used to measure the transverse coherence of the FEL beam. It was a great joy to work with them. I would like to thank *Christopher Gerth*, who contributed to the analysis of the data with many helpful ideas. Special thanks also to *Kai Tiedtke*, with whom I discussed the numerical methods of the near field diffraction. I am grateful to *Rolf Treusch* and *Fini Jastrow* for their contributions to the experimental set-up and for their help during the measurements. Many thanks also to *Bernd Sonntag* and *Barbara Steeg* for helpful discussions. *Elke Plönjes* and *Stefan Düsterer* have joined the photon diagnostics group recently and have corrected many mistakes in this document.

I had many fruitful discussions with *Mikhail Yurkov*. He provided me with simulation data of the FEL process and helped me understand the processes of coherence development. Furthermore, he took a close look at the theory chapter in this work and straightened out my errors. I am also thankful to *Evgeny Schneidmüller* and *Evgeny Saldin* for numerous discussions on the details of the FEL process.

I have spent a wonderful time in the FDET group with my fellow students who do their diploma or their Doktorarbeit, and I am grateful for the delighting atmosphere in the group. I would like especially *Siggi Schreiber* and *Holger Schlarb* for introducing me to the TTF accelerator. I thank Siggi also for his proofreading of this thesis, correcting my mistakes and straightening my line of thought. *Christian Lackas* helped me develop the data acquisition system for TTF, redesigned and implemented all the computer programmes to make it run reliably. I have also had many joyful hours with *Nikolay Sturm*, who worked on the stabilisation of the beam energy and with *Diana Türke*, who set up a femtosecond laser to measure the bunch length. I am grateful to *Bernd Steffen*, who started as a summer student and worked with me on the Beam Trajectory Monitor. *Axel Winter* joined our group a

short time ago, and I thank him for many stimulating discussions. I have had many fruitful discussions with my fellow PhD students, *Jan Menzel*, *Markus Hüning*, *Lutz Lilje* and *Jürgen Scheins*. *Axel Knabbe* joined our group and I have had many fruitful discussions, improving the clearness of my thoughts. Special thanks also to *Marc Geitz*, who spent many nights to introduce me to the operation of the TTF linac and to *Stefan Simrock* for many stimulating discussions.

Michiko Minty has proofread this document, helped to improve the document structure and corrected my mistakes in the the English language. I thank also *Dirk Nölle* for correcting many mistakes in the description of the TTF FEL. Many thanks to *Bart Faatz*, who always found beam time for my experiments in the tight schedule for the TTF linac.

For my work on the Beam Trajectory Monitor, a device invented by *Johnny Ng*, I would like to thank the following people: *Sven Karstensen*, *Stefan Roth*, *Heinz Thom*, *Ute Carina Müller*, *Sonja Hillert*, *Peter Göttlicher* and *Uli Kötz*.

Thank you also to all the TTF team, those who contributed to the enormous success of our FEL, working in many different areas of the project, especially *Winni Decking*, *Klaus Flöttmann*, *Pedro Castro*, *Philippe Piot*, *Hans Weise*, *Ryszard Sobierajski*, *Katja Honkavaara*, *Luciano Catani*, *Alessandro Cianchi*, *Daniele Sertore*, *Dieter Trines*, *Gerald Schmidt* and *Kirsten Zapfe*.

The value of a good computer system sometimes appears only when it fails. Despite of its complexity with file servers, front end computers and office terminals, the TTF system is exceptionally stable. I want to thank especially *Kay Rehlich*, *Olaf Hensler*, *Gerhard Grygiel*, *Thomas Bruns*, *Elke Sombrowski*, *Raimund Kammering*, *Martin Staack*, *Valeri Ayvazyan*, *André Gössel* and *Vitali Kocharyan*. Many thanks also for numerous discussions on the data acquisition system.

To *Marco Kirm* I owe a fruitful discussion on the properties of the scintillating crystals. *Kirill Sytchev* helped me with the calibration of the light yield of the Ce:YAG crystal. Many special thanks also to *Ingrid Nikodem* for her support in all areas of the DESY administration. In his summer school course, *Quang-Je Kim* has taught me a lot about free electron lasers. For many helpful discussions, adding the view from the outside, I am thankful to *Peter Wienemann*.

I would like to thank especially my family, *Tini* and *Friedrich*, *Moritz*, *Till* and *Eckhard Ischebeck*, and last, but not least *Simone Söntges* for their tremendous support.

Hiermit versichere ich, diese Arbeit selbständig ausgeführt und nur die angegebenen Quellen verwendet zu haben.

Hamburg, im Oktober 2003

Curriculum Vitae

Rasmus Ischebeck
born May 23, 1973, in Münster, Germany

University Studies

1999	RWTH Aachen Diploma in Physics Cumulative grade: with distinction (mit Auszeichnung) Title of the diploma thesis: Construction of a Twin Microstrip Gas Detector to determine the second Spatial Coordinate in the CMS Forward Tracker
1995–1996	Universit de Genève Study of Physics
1993–1999	RWTH Aachen Study of Physics

Community Service

1992–1993	Biological Station “Rieselfelder Münster”
-----------	---

School

1983–1989	Pascalgymnasium Münster
1989–1990	Highland High School, Albuquerque, New Mexico
1990–1992	Pascalgymnasium Münster Bilingual German / French Abitur Cumulative grade: very good (1.2)

Languages

German	Native Language
French	Fluent
English	Fluent
Italian	Basic knowledge